Instability processes and optimisation in multi-kilowatt coaxial CO_2 lasers

Viktor Granson

Submitted for the degree of Engineering Doctorate in Photonics

Heriot-Watt University

School of Engineering and Physical Sciences

February 2014

Abstract

This thesis presents research carried out on a high power diffusion-cooled CO_2 laser excited by a radiofrequency (RF) electric discharge in the annular configuration, and with a folded hybrid optical resonator. The main objective of the research was to investigate certain key aspects of the laser, so as to optimise overall performance while increasing power stability and reproducibility and ensuring safe and reliable operation at minimum cost. The work presented in the thesis contributed significantly to introduce the TruCoax Version 6 laser, which has 40% lower cost compared to the preceding version.

The technological challenges encountered are divided into four main research areas as follows:

The *first area* relates to RF discharge stability especially during the discharge ignition process and in the region of the RF feed-through, where an improved design eliminated damage due to electric breakdown and suppressed the occurrence of local γ-type RF discharge.

Secondly, experimental acoustic measurements matched with a theoretical characterization of the acoustic properties of the annular CO_2 laser vacuum vessel were used to generate information on the acoustic resonant frequencies and standing-wave patterns. Implementation of laser control algorithms based on this information prevented from laser damage due to acoustic resonances.

Thirdly, the impact of thermal lensing in a gas laser gain medium located within a free-space stable resonator has been studied. The results show that the thermal lensing is an integral part of resonator configuration in the stable direction and can be applied towards a unified design for a range of RF input power levels.

In the *fourth* key research area, temporal fluctuations in the laser output power (of order of 100 W) which were observed to occur on a timescale of minutes have been investigated for a laser with a power output of ~3.5 kW. Small power fluctuations in the range of ± 25 W could be attributed to increases in the coupling losses of rotational lines, and this was confirmed experimentally.

Acknowledgements

I am sincerely grateful for the great support I received over the duration of the work reported in this thesis. People surrounding me at all levels have provided various kinds of help, which I regard with the deepest appreciation.

I would like to thank my industrial supervisor Dr. Francisco Villarreal for the many technical discussions which have been very fruitful for me, as well as his suggestions and active help in designing and setting up some of the experiments. Francisco's broad experience and unending, deep fascination for the subject has enabled him to be an excellent tutor and industrial supervisor.

I appreciate highly the continuing support and suggestions from my academic supervisor Prof. Denis Hall, and also his suggestions for the thesis structure and style of writing.

I thank the former president and CEO, Mr. Rolf Biekert for supporting the EngD programme at TRUMPF Inc. I also would like to thank the manager of Laser Development Department at TRUMPF Inc., Dr. Jochen Deile and co-workers from the Development Group, especially Mr. Peter Daniel and Dr. Shadi Sumrain for the great support they have given me over the years of collaboration. A special thank to Dr. Fernando Monjardin for the helpful discussions and help to obtain experimental data.

Last, but not least I would like to thank my wife Nina for her enduring support and understanding during the late evening and weekends I have spent working on the thesis.

Declaration Statement

List of publications

[1] B. Ehlers, J. Deile, S. Sumrain, V. Granson, F. Villarreal, V. Negoita "Experimental and theoretical study of a coaxial, hybrid-stable-unstable resonator for high power lasers", Proc. SPIE 6452, 64520G (2007)

[2] V. Granson, S. Sumrain, P. Daniel, F. Villarreal, J. Deile "Power scaling issues of diffusion cooled annular CO_2 laser in the multi-kilowatt region", Proc. SPIE 6872, 687209 (2008)

[3] F. J. Villarreal-Saucedo, J. Deile, S. Sumrain, V. Granson, J. F. Monjardin-Lopez, P. Daniel, , "Laser having distributed inductances", US patent 7,778,303 (2010)

[4] V. Granson, F. J. Villarreal, J. Deile, J. F. Monjardin, S. Sumrain "Comprehensive analysis of thermal lensing effects on the coaxial resonator of a high power RF-excited CO_2 laser", Proc. SPIE 6236, 623606 (2012)

[5] F. J. Villarreal-Saucedo, J. F. Monjardin-Lopez, P. Daniel, J. Deile, S. Sumrain, V. Granson "RF-excited laser assembly", US patent application 0106586 (2012)

[6] V. Granson, F. J. Villarreal, J. Deile, J. F. Monjardin, S. Sumrain "Optimization of the intra-cavity optical flux in the unstable direction in RF excited annular CO_2 laser in terms of power stability", Proc. SPIE 8600, 86004 (2013)

Table of Contents

List of Symbols

Symbol	*Unit*	*Description*	*Section*
α	$\frac{1}{m}$	first Townsend coefficient (ionisation)	2.2.4 3.2.1
	$\frac{C\ m^2}{V}$	molecular polarizability	5.2
α_P, α_R	$\frac{\%}{cm}$	laser gain in P- and R-branch respectively	7.2.3
β	$\frac{1}{m}$	second Townsend coefficient (recombination)	2.2.4
	dimensionless	luminance scaling factor	5.4
Γ	*dimensionless*	modified third Townsend coefficient	3.2.1
	dimensionless	voltage reflection coefficient	3.5.1
γ	*dimensionless*	third Townsend coefficient (ionisation)	3.2.1
	$\frac{1}{m}$	transmission line propagation constant	3.5.1
	dimensionless	specific heat ratio	4.2.3
Δv	*Hz*	laser emission linewidth	7.2.2
ε	*dimensionless*	dielectric constant	2.2.4, 3.3
η	$Pa\ s$	gas viscosity	5.2
θ	*dimensionless*	relative pressure rise	5.6
	dimensionless	rotational line degeneracy factor	7.3.5
κ	$\frac{1}{K}$	linear expansion coefficient	7.3.2
Λ	*N/A*	diagonal matrix	6.2
λ	*dimensionless*	eigenvalue	6.2
	$\frac{W}{m\ K}$	thermal conductivity	5.2, 5.5
	m	wavelength	6.5
μ	$\frac{cm^2}{V\ s}$	electron mobility	3.2.3

μ	$\frac{V\ s}{A\ m}$	vacuum permeability	3.3
ν	Hz	laser emission frequency	7.3.1
ν_i	Hz	ionisation frequency	3.2.3
v_1,v_2	N/A	eigenvectors	6.2
v	*dimensionless*	vibrational mode quantum number	7.2
ξ	m	particle displacement	4.2.1
ρ	$\frac{1}{m^3}$	charge density	3.3
	$\frac{kg}{m^3}$	gas density	4.4
σ	S	electric conductivity	2.2.4
	dimensionless	variance	4.7.2
τ	s	time constant	4.4
υ	*dimensionless*	vibrational state of the molecule	7.2.1
Φ	$\frac{Pa\ s\ m^3}{kg}$	velocity potential of a gas particle	4.3
φ	V	electric field potential	3.3
χ	*dimensionless*	dimension across RF discharge gap	2.2.3
	dimensionless	auxiliary integration variable	7.3.1
Ψ	*dimensionless*	wave function variable	4.2.2
Ω	Ω	DC discharge resistance	2.3.2
ω	$\frac{1}{s}$	circular frequency	3.5.1, 4.2.1
A	$\frac{1}{cm\ Pa}$	gas specific electric breakdown coefficient	3.2.1
	cm	electron oscillation amplitude in a RF discharge	3.2.3
B	$\frac{V}{cm\ Pa}$	gas specific electric breakdown coefficient	3.2.1
	MHz	fitting coefficient of rotational spectrum	7.2.1
b	*dimensionless*	integration range of the Voigt integral	7.3.1

C	$\frac{F}{m}$	shunt capacitance per unit length of a transm. line	3.5.1
c	$\frac{m}{s}$	speed of sound	4.2.1
	$\frac{J}{kg\ K}$	specific heat capacity	4.2.3
D	$\frac{cm^2}{s}$	electron diffusion coefficient	3.2.3
		electric displacement field	3.3
d	m	RF discharge gap	5.4
	m	length of a transmission line section	3.5.1
dc	%	duty cycle	4.6
e	C	elementary charge of an electron	2.2.2
E	$\frac{V}{m}$	electric field vector	3.2.1, 5.4
E_0	$\frac{V}{m}$	electric field amplitude	2.2.4, 3.2.3
EV	*dimensionless*	exposure value	5.4
F	N	Coulomb force	3.3
f	Hz	frequency	4.2.4, 4.6
	dimensionless	Boltzmann function	2.2.2
	dimensionless	degree of freedom of a molecule	4.2.3
G	$\frac{S}{m}$	shunt conductance per unit length of a transm. line	3.5.1
G_{iRF}	*dimensionless*	thermal instability growth	2.3.2
h	%	relative humidity factor	4.2.3
	$\frac{W}{K\ m^2}$	heat transfer coefficient	4.4
H	MHz	fitting coefficient of rotational spectrum	7.2.1
I	A	electric current	3.5.1
I_2	*dimensionless*	identity matrix of size 2×2	6.2
i	*dimensionless*	index variable	6.4.3

J	*dimensionless*	rotational quantum number of a molecule	7.2.1
j	*dimensionless*	imaginary unit	3.5.1
	dimensionless	rotational line number	7.2.3
k	$\frac{1}{cm}$	wave number	2.3.2
L	m	length of thermal lensing medium	6.2
	$\frac{H}{m}$	inductance per unit length of a transmission line	3.5.1
	$\frac{cd}{m^2}$	luminance	5.4
L_{cav}	m	cavity length	6.5, 7.3.2
M	*N/A*	2x2 matrix	6.2
M_i	*dimensionless*	relative molecular mass of gas species *i*	4.2.3
m	*dimensionless*	stability value of ray transfer matrix	6.4.1
N	$\frac{1}{cm^3}$	neutral gas density	2.2.2, 3.2.1
N_f	*dimensionless*	Fresnel number	6.5, 7.3.4
N_{ap}	*dimensionless*	lens aperture	5.4
n	*dimensionless*	refractive index	5.3
	dimensionless	integer number	7.3.1
	$\frac{1}{m^3}$	electron density	2.2.4, 3.2.3
P	W	electric power	2.2.2
	Pa	absolute gas pressure	4.2.1
	dimensionless	rotational line in P-branch	7.2.1
p	Pa	relative gas pressure	4.2.1
Q	*dimensionless*	resonator quality factor	4.5
q	C	electrostatic charge	3.3
	m	complex beam parameter	6.4.1
R	m	radius	2.3.2

R	$\frac{\Omega}{m}$	resistance per unit length in a transmission line	3.5.1
	dimensionless	rotational line in R-branch	7.2.1
	$\frac{J}{mol\ K}$	gas constant	4.2.3
ROC	m	radius of curvature	5.7
r	$\frac{J}{kg\ K}$	specific gas constant	4.2.3
	m	position in polar and cylindrical coordinate system	3.4.2
T	K	temperature in Kelvin	4.2.3, 7.2.3
t	s	time variable	4.2.1
$\boldsymbol{u}$	m	space vector	3.3
u	*dimensionless*	parameter variable	3.5.2
	$\frac{m}{s}$	particle velocity	4.2.1
V	m^3	volume	4.2.4
	V	electric voltage	2.2.4
	dimensionless	Voigt profile function	7.3.1
V_{br}	V	electric breakdown voltage in DC field	3.2.1
V_{br2}	V	electric breakdown voltage in RF field	3.2.3
V_{in}	V	electric voltage at the feed point of the transm. line	6.4.3
V_{gap}	V	inter-electrode voltage in a RF discharge	6.4.3
V_n	$\frac{cm^3}{mol}$	molar volume	2.2.2
w	$\frac{W}{m^3}$	volumetric power density	4.6, 5.4
x	m	position in Cartesian coordinate system	2.2.3
x_i	*dimensionless*	mole fraction of gas species *i*	5.2
y	m	pos. in Cartesian/polar/cylindrical coord. system	3.4.2
Z	Ω	electric impedance	3.5
Z_0	Ω	characteristic transmission line impedance	3.5
z	m	position in Cartesian/cylindrical coordinate system	6.4.3

Chapter 1

ANNULAR RF EXCITED DIFFUSION-COOLED CO_2 LASERS

1.1 Historical Overview

Since its discovery in 1964 [1.1], the CO_2 laser has became the laser of choice for many important industrial applications. It is the combination of some key properties of the CO_2 laser that has made it so popular from an early stage in its development. The main benefits offered include its high beam quality, the capability to scale power to the multi-kilowatt region, its low cost per Watt compared to other laser sources and the fact that the infrared emission is well suited for dielectric and metal cutting and welding.

Typical high power lasers in the 1970s employed DC discharges where the high voltage electrodes are placed along the beam propagation path. High powers required larger gain lengths which in turn demanded longer spacing between the electrodes so that the applied inter-electrode DC voltage must be increased to (many) tens of kV in order to sustain a satisfactory electric field magnitude. With the "re-discovery" of gas discharge excitation at RF frequencies, a variety of discharge volumes and therefore novel optical resonators became a possibility, since the discharge could be excited in the (transverse) direction perpendicular to the beam propagation direction. RF excited CO_2 lasers were developed to the point where they became of particular interest for material processing applications in the second half of 1980s.

Two distinctive types of RF excited high power CO_2 lasers have been developed, based on the principle used for the removal of excess heat. Fast flow lasers employ a gas recirculation system to cool the gas convectively, whereas lasers with static gas and actively cooled discharge surfaces rely on cooling by heat diffusion.

A diffusion cooled CO_2 laser with an annular RF discharge geometry was developed in the second half of 1980s ([1.2], [1.3], [1.4]) delivering 65 W output power. The setup

consists of a stable resonator where the Herriott cell [1.5] is used as a folding element to extract the power from an annular gain medium.

Around the same time a stable-unstable optical resonator design [1.6] was successfully applied in a RF excited CO_2 laser with the slab geometry [1.7], [1.8], [1.9]. The hybrid stable-unstable resonator with a waveguide stable resonator in the dimension across the discharge gap and an unstable confocal resonator in the much larger lateral dimension was a major technological milestone, allowing efficient power extraction from high-aspect ratio gain volume and high output beam quality at the same time.

The foundation of the annular diffusion cooled laser with a hybrid stable-unstable resonator, which is the platform of this thesis, was laid by research work at the Fraunhofer Institute for Laser Technology (ILT) in Aachen, Germany, in the late 1980s to mid 1990s. In contrast to a multipass, Herriott cell-type resonator, the researchers [1.10], [1.11] propose a resonator with two torus mirrors. The torus geometry allows one to focus the beam in the radial direction and a slight tilt in one of the tori makes the resonator azimuthally unstable. Two beams are "driven" in two semi-circles, until they are outcoupled through an aperture in the tilted torus mirror. The principal benefit of this type of design is that the whole volume of the annular gain medium can be fully exploited for laser action, unlike in a multipass resonator, which, though it produces classical modes, is wasteful of the excited gain medium.

Ehrlichmann [1.12], [1.13] applied the stable-unstable resonator to the annular geometry to pursue a high beam quality option, especially in the azimuthal direction. This work realised a helix-torus resonator with 1 kW output power and a beam quality (M^2) parameter in the azimuthal direction of 2.1.

The annular laser technology was acquired in 1996 from ILT by TRUMPF in order to commercialise the product, and was initially intended for a medical application [1.14]. Following a research and development phase in Germany, which resulted in many features employed in the current product, including the axicon mirror in place of the torus and the inclusion of a beam-shaping telescope [1.15], the system was further developed since 2000 at the TRUMPF subsidiary in the US.

The first commercial version of the annular laser, which has been branded as "TruCoax" since 2007, was introduced in 2004 in a 2 kW version. Since that time, the TruCoax laser has been expanded into a product family, with output powers ranging from 1- 3.2 kW.

1.2 Optical Configuration of the TruCoax Resonator

The internal beam propagation of a helix-axicon resonator is shown schematically in figure 1.1. The intra-cavity propagation path can be visualised using the ray tracing method. In this context, the beam starts propagating from one of the helix mirror-halves until it reaches the axicon mirror. The axicon mirror then images the beam to the other helix mirror half, where it is reflected with some inclination due to the slope in the helix mirror. The point of incidence of the beam then advances with each roundtrip making its way towards the aperture in the helix mirror.

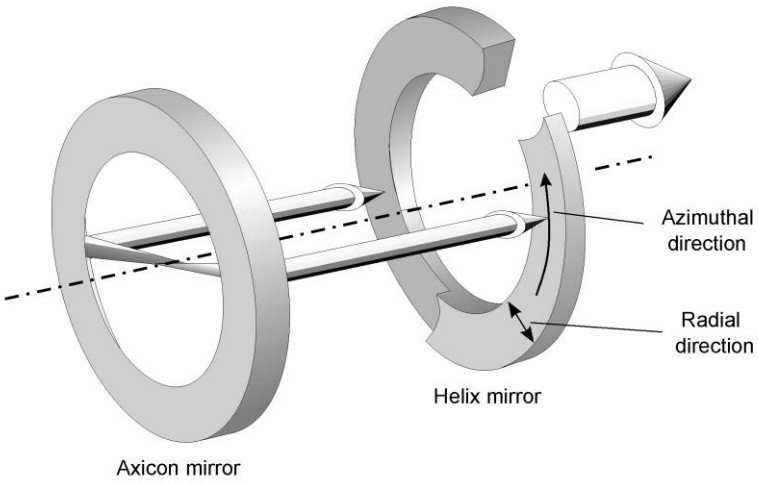

Figure 1.1 Schematic representation of the beam propagation in a helix-axicon resonator [1.15]

When discussing geometrical details in the helix-axicon resonator it is often helpful to regard the stable and unstable directions independently in a two-dimensional representation as shown in figure 1.2.

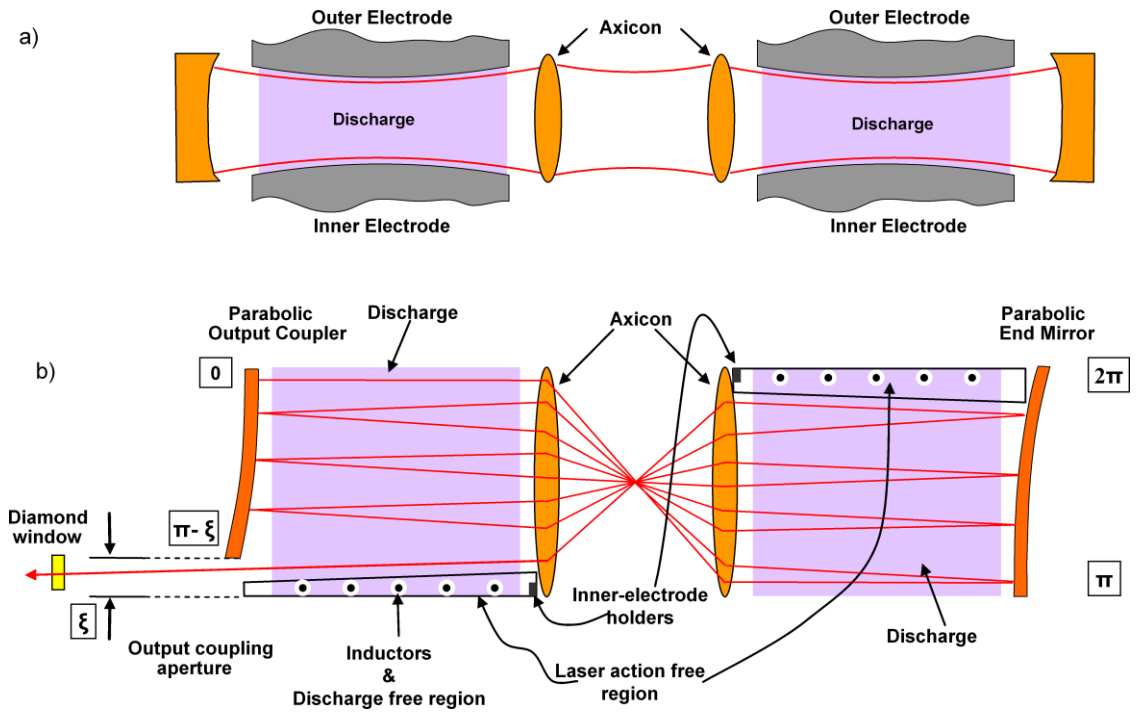

Figure 1.2 Schematic representation of the helix-axicon resonator [1.19]:
a) radial direction
b) azimuthal direction

1.2.1 Resonator in stable (radial) direction

In a cross-sectional view of the resonator where the 45° reflections of the axicon are represented by transmissive optics, it becomes apparent that the halves of the helix mirrors act as end mirrors and the superimposed torroid on the axicon refocuses the beam in-between the end mirrors as seen in figure 1.2(a). The resonator is designed to be a free space resonator, where the interaction of the beam with (structural) apertures and the electrodes is minimal. However, the selection of the magnitude of the discharge gap and its geometry are critical so that, on the one hand the diffraction losses of the fundamental radial mode are minimised, and on the other hand the diffraction losses are large enough to inhibit oscillation of higher order radial modes. The optimization of the caustic-shaped electrode gap was a major development effort, where numerical Fox and Li simulations as well as empirical results were used to determine the optimal discharge gap geometry [1.16]. Both electrodes feature machined grooves with a pitch of the order of 0.7 mm [1.17], the so-called "optical thread" to extinguish undesired stray light amplification.

1.2.2 Resonator in the unstable (azimuthal) direction

The beam propagation in the azimuthal direction can be mapped onto a 2-dimensional plane, where the azimuthal angle is plotted in the vertical direction (figure 1.2(b)). The two helix mirror halves act as the end mirrors. The inclination of both helix mirror-halves allows one to have a much smaller profile height compared to the known unstable confocal resonators. Ehrlichmann [1.12] has shown that the magnification, *M* of the helix resonator is defined by the profile height in the azimuthal direction, and not by its shape. A typical value for the magnification, *M* is 1.05 for this resonator and is limited by diffraction losses on the electrodes since the beam starts to interact with the electrodes if the azimuthal inclination angle is too large. The first helical slope mirror was realised by mechanically stretching a torus mirror with a cut-out segment for the outcoupling aperture [1.7]. Later, the evolution of diamond turning technology allowed a linear helical profile to be machined into the mirror. Subsequent tests showed, however, that a parabolic profile, as indicated in figure 1.2(b), makes the internal beam propagation much more resilient as compared to a linear profile to mitigate against slight mirror distortions caused by water pressure fluctuations or heat load variations [1.16].

1.2.3 Beam reformatting telescope

Given that the principal commercial application of this laser is for sheet metal cutting, it is essential that the beam has circular symmetry, high beam quality, reproducible beam size from laser to laser and is circular polarised. For this purpose, the outcoupled beam needs to be formatted by a number of optical elements (OEs), and a schematic representation of the beam reformatting telescope used in the TruCoax laser is depicted in figure 1.3. As shown, cylindrical lenses are used to separate the functions of the optical elements between the two directions. Higher order mode content is filtered in the far field of a Keppler telescope configuration in the azimuthal direction, while the beam size and convergence in the radial direction are corrected by a Galilean telescope in the radial direction.

Unlike the situation illustrated in figure 1.3, the actual optical elements are dielectrically coated and actively cooled metal mirrors which are able to handle the high power beams. Another advantage of reflective optics is the option to fold the propagation path to be able to mount the telescope setup onto the optical resonator structure. The mechanical design allows the position of the optical elements to be adjusted so that the beam parameters in

both axes can be matched for each individual laser in spite of possible variations of the outcoupled beam due to manufacturing tolerances.

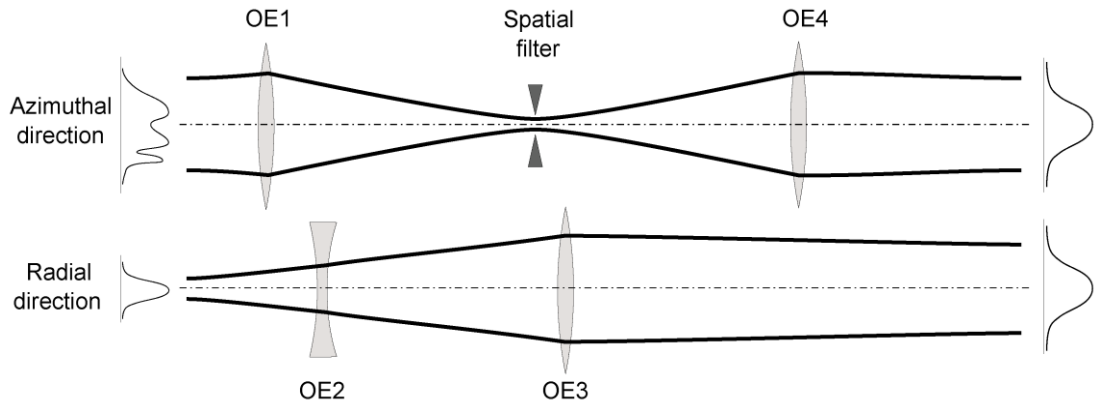

Figure 1.3 Formatting of the outcoupled beam to achieve a diffraction-limited anastigmatic circular beam. The optical elements (OE1 to OE4) are shown for illustration as transmissive optics. [1.15]

1.2.4 State of polarization

In addition to producing an astigmatic beam in the working range, the laser emission also needs to be circularly polarised so as to inhibit directionality in metal cutting due to the difference in absorption of *s*- and *p*-polarization.

The outcoupled beam is azimuthally polarised, but because of the low magnification in the unstable direction, a relatively small circular segment is produced which is taken up by the outcoupling aperture, so in practice the polarization state is very close to being linearly polarised. One of the telescope mirrors includes an absorbing thin-film reflector (ATFR) coating, thereby eliminating residual polarization components, which are not linearly polarised. A reflective phase retarder (RPR) located in the beam delivery system of the cutting machine converts the linearly polarised beam to a circular beam.

In summary, the TruCoax laser provides a high power, high quality beam with $M^2<1.1$, which is circular, anastigmatic and circularly polarised making it a particularly suitable laser source for sheet metal cutting application.

1.3 Electrical Configuration of TruCoax Resonator

The RF power is delivered conventionally by a 50Ω coaxial cable from the 27.12 MHz RF power supply to the laser head. An LC impedance-matching circuit is used to achieve optimal power transfer from the supply to the (operational) RF discharge.

In the TruCoax 2000, the first commercial product in this line, the inner electrode was fed with RF power from one end, and the only means available to control the longitudinal voltage distribution was by adjusting the value of the termination inductor at the other end of the inner electrode. Although the longitudinal variation in the transverse voltage is relatively small at the (low) 27.12 MHz excitation frequency, such small changes can still play a role over a 1 metre RF discharge length, as in the TruCoax 2000 laser. A commonly-used technique to even out the voltage distribution is to insert multiple shunt inductor along the discharge length, which though they can be easily attached to the sides of the discharge in a slab laser, the typical annular discharge geometry does not provide such easy access for the shunt inductors. However, as shown by Knupfer [1.18], the laser action "shadow", provided by the inner electrode holders (as shown in figure 1.2(b)), was successfully used to provide space to add inductors along the discharge length. By adding four inductors in the shadow region, the improved longitudinal RF discharge homogeneity resulted in a 20% increase in output power compared to a setup without inductors.

The technique of using distributed parallel inductances, introduced in 2007, allowed the laser output power to be increased from 2 kW to over 3 kW, as measured after the reformatting telescope [1.19], [1.20]. This was achieved by extending the RF discharge length to 1.3 m while keeping the discharge diameter and by increasing the RF input power from 18 kW to 30 kW. The electrical configuration of this high power TruCoax laser, which will be denoted here as TruCoax V5 (version 5), is shown schematically in figure 1.4. In this version of the laser, the RF voltage is fed through the central void space in the helical mirror to one end of the inner electrode, and the inner electrode is electrically insulated from the grounded outer electrode by alumina spacers on either end, which support the inner electrode. An inductor is attached between the axicon mirror and the inner electrode to provide additional control over the transverse voltage distribution. Not shown in figure 1.4 are the coaxial water channels around the RF feed-through for inner electrode cooling.

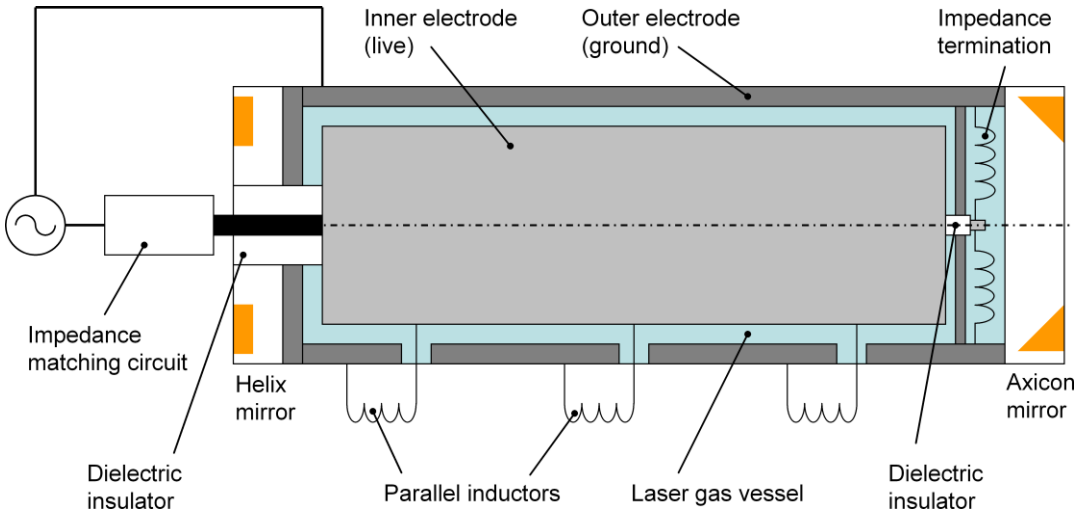

Figure 1.4 Electrical setup of TruCoax V5 laser. The inner electrode is electrically insulated from the grounded outer electrode except for an adjustable termination inductor.

The configuration of the TruCoax V5 offers good performance in terms of RF power delivery and distribution. However, in order to strengthen its market competitiveness, the TruCoax laser underwent a major mechanical and electrical design update in 2009, while maintaining the basic optical design unchanged.

To simplify the assembly and part count, the RF feed point was moved to one of the outer electrode ports as shown in figure 1.5, and the cooling water supply was done introduced through the inner electrode holders in the axicon mirror end. Without the complicated RF feed-through and water feed assembly in the helix mirror, both resonator mirrors can be replaced in a matter of minutes.

The ceramic holders on the ends of the inner electrode, which had provided both mechanical support and electric insulation, were removed in the TruCoax V6 design as another significant step towards cost reduction. The inner electrode is terminated electrically by all-metal inductors, where the termination at the helix end is spiral-shaped to increase its inductance [1.21].

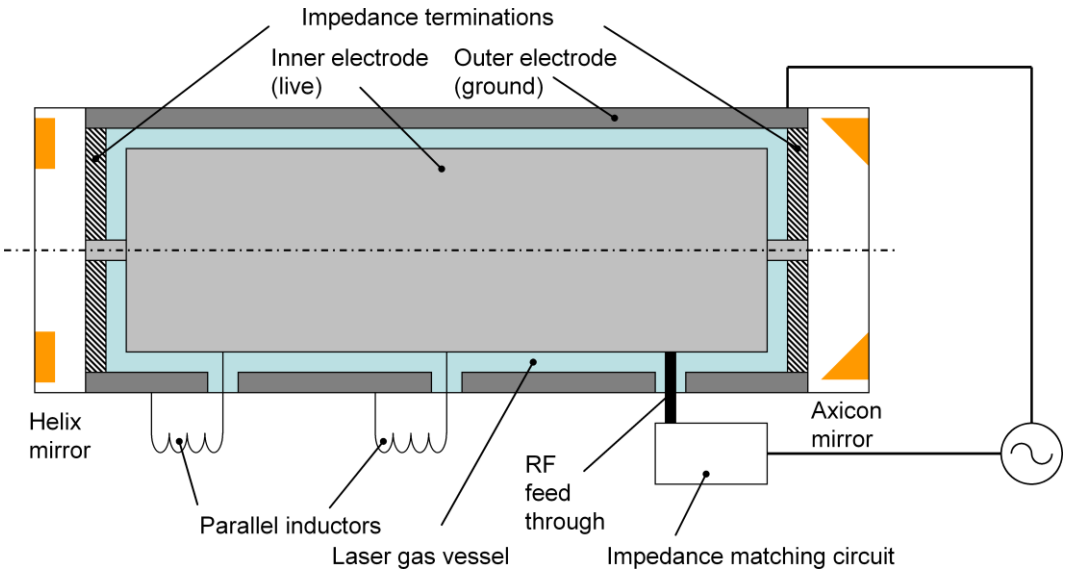

Figure 1.5 Electrical setup of the TruCoax V6 laser. One of the outer electrode ports is used for RF power delivery, and the mechanical structure supporting the inner electrode is electrically conductive.

1.4 Goals of the Thesis

The work described in this thesis has aimed to present key parts of the laser science and technology which delivers underpinning for the development of the TruCoax V6 laser. Many important laser-related topics have needed to be revisited and new aspects considered, so as to provide the backing to enable the laser to undergo a major redesign of the RF electrical, thermo-optical and acoustic configurations.

The challenges encountered in this work have been distributed over a number of scientific and engineering disciplines, to address problems in electric field and RF power engineering (e.g. RF feed-through design), the generation and impact of acoustic resonances, opto-thermal effects (thermal lensing) and laser physics (e.g. laser output power fluctuations and resonator design). The topics covered in this work are organised into chapters, which can be treated as relatively independent units. An exception to this relates to Chapters 5 and 6; in Chapter 6 the thermal lensing results which had been reported in the preceding Chapter 5 are used to estimate beam expansion and guide resonator design. The problem definitions of the individual chapters will be briefly introduced here.

The delivery of RF power to the discharge is implemented through an opening in the outer electrode envelope structure. The RF feed needs to run through the laser gas medium, which is designed for RF discharge operation (see figure 1.5), and given the additional space constraints, the goal is to use modelling and experiment to come up with a RF feed-through design that allows safe laser operation without any occurrence of RF discharge instabilities (arcing, γ-type discharge). This topic is addressed in Chapter 3.

Just as problems with RF power delivery arise through having values of the electric fields which are too high, fluctuations in gas pressure can also lead to RF discharge instabilities. Pressure variations can be caused by *pulsed* RF discharge operation in the kHz range, a situation in which acoustic standing wave patterns are built up in the laser gas vessel. The values for the unwanted acoustic *resonant* frequencies need to be determined and techniques developed to avoid the production of potentially-damaging discharge-instability effects. The acoustic resonance issues are tackled in Chapter 4.

Significant transverse gas-temperature gradients which occur across the RF discharge gap have the effect of producing divergent thermal lensing in the radial direction of the annular laser. The impact of such thermal lensing therefore needs to be taken into consideration when designing the stable resonator configuration, especially since the TruCoax laser employs a free space optical resonator. The magnitude of the thermal lensing needs to be estimated for a given set of boundary conditions as discussed in Chapter 5. Knowledge of the magnitude and relative weighting of operating conditions such as discharge gap, gas pressure and RF power density are required to provide input data for the design of the optical resonator. In this context it is also beneficial to understand the effect of thermal lensing on the internal beam propagation in the radial direction. This topic is elaborated further in Chapter 6.

The final topic covered relates to instabilities in the laser output power on the time scale of several minutes, which will be addressed in Chapter 7. The preliminary measurements obtained indicate that output power fluctuations of up to ±3% are accompanied by a change of vibrational-rotational emission spectrum, reflecting the effects of the so-called "laser signature". The selection mechanism of the CO_2 infrared spectrum will be applied to the boundary conditions of the TruCoax laser to develop insight into the measured laser signature. From here, the goal is to find a correlation between the laser signature and output power instability.

The significant achievements are recapped in Chapter 8 for the thesis as a whole as well as in more detail for Chapters 3 to 7 individually. Discussion of work that could be continued in context of each chapter is also included in Chapter 8. The discussions comprise two parts, where the work that could not be carried out due to time constraints is discussed in the first part and possible continuation of the individual topics are given in the second part.

1.5 References

[1.1] C. K. N. Patel "Interpretation of CO_2 optical maser experiments", Phys. Rev. Lett., vol. 12, pp. 588-590 (1964)

[1.2] J. G. Xin, D. R. Hall "A multipass off-axis resonator CO_2 laser", Lasers 1985 Conference, Las Vegas (1985)

[1.3] J. G. Xin, D. R. Hall "Multipass coaxial radiofrequency CO_2 laser", Opt. Commun., vol. 58, pp. 420-422 (1986)

[1.4] J. G. Xin, D. R. Hall "Compact, multipass, single transverse mode CO_2 laser", Appl. Phys. Lett., vol. 51, pp. 469-471 (1987)

[1.5] D. Herriott, H. Kogelnik, R. Kompfner "Off-axis paths in spherical mirror interferometers", Appl. Opt., vol. 4, pp. 523-526 (1964)

[1.6] O. L. Bourne, P. E. Dyer "A novel stable-unstable resonator for beam control of rare-gas halide lasers", Opt. Comm., vol. 31, pp. 193-196 (1979)

[1.7] P. E. Jackson, H. J. Baker, D. R. Hall "CO_2 large-area discharge laser using an unstable-waveguide hybrid resonator", Appl. Phys. Lett., vol. 54, pp. 1950-1952 (1989)

[1.8] K. M. Abramski, A. D. Colley, H. J. Baker, D. R. Hall "Power scaling of large-area transverse radio frequency discharge CO_2 lasers", Appl. Phys. Lett., vol. 54, pp. 1833-1835 (1989)

[1.9] J. Tulip "Large area laser", US patent 6,704,333 (2004)

[1.10] K. Du, P. Loosen, U. Habich "Laserresonator", German patent DE 41 23 024 (1995)

[1.11] U. Habich "Diffusionsgekühlte CO_2 Laser für die industrielle Materialbearbeitung", dissertation RWTH Aachen, ISBN 3-86073-009-6 (1992)

[1.12] D. Ehlichmann "Azimutal instabile Resonatoren und Ringresonatoren für Hochleistungslaser", dissertation RWTH Aachen, ISBN 3-8265-0190-X (1994)

[1.13] D. Ehrlichmann, U. Habich, H.-D. Plum, P. Loosen, G. Herziger "Azimuthally unstable resonators for high-power CO_2 lasers with annular gain media", IEEE J. Quant. Electron., vol. 30, pp. 1441-1447 (1994)

[1.14] H. Schlüter "The long journey from idea to industrial success", Proc. SPIE 6874, 687402 (2008)

[1.15] J. Schulz "Diffusionsgekühlte, koaxiale CO_2-Laser mit hoher Strahlqualität", dissertation RWTH Aachen (2001)

[1.16] J. Deile "Power scaling of high brightness multi-kilowatt coaxial CO_2 lasers", dissertation Heriot-Watt University (2012)

[1.17] J. Deile "Diffusion-cooled laser system", US patent 6,879,616 (2005)

[1.18] S. Knupfer "Optimization of the gas discharge characteristics on a high power CO_2 coaxial laser", Dipl. Ing. (FH) thesis, University of Applied Sciences Esslingen (2007)

[1.19] V. Granson, S. Sumrain, P. Daniel, F. Villarreal, J. Deile "Power scaling issues of diffusion cooled annular CO_2 laser in the multi-kilowatt region", Proc. SPIE 6872, 687209 (2008)

[1.20] F. J. Villarreal-Saucedo, J. Deile, S. Sumrain, V. Granson, J. F. Monjardin-Lopez, P. Daniel "Laser having distributed inductances", US patent 7,778,303 (2010)

[1.21] F. J. Villarreal-Saucedo, J. F. Monjardin-Lopez, P. Daniel, J. Deile, S. Sumrain, V. Granson "RF-excited laser assembly", US patent application 0106586 (2012)

Chapter 2

LITERATURE SURVEY: DIFFUSION COOLED HIGH POWER CO_2 LASERS

2.1 Introduction

The invention of the CO_2 laser changed its environment as has few other laser types. The scalability potential of this laser to high output powers was quickly identified and the CO_2 laser and its application became an important subject of research for decades. The first industrial applications were already being tested at the time when the fundamental research on the laser was still being conducted. For example first laser metal cutting was tested in 1967 at the British Services Electronics Research Laboratory, just three years after demonstration of the first CO_2 lasers [2.1].

In the following decades the laser was optimised for particular applications such as cutting and welding, molecular spectroscopy, medical and military applications and even data communication. Retrospectively, it is clear today that some of the applications had a limited lifetime, for example the gas dynamic lasers with continuous wave output power of tens of kilowatts was once a candidate for laser weapon programs, whereas other applications like some sectors of industrial material processing are still dominated by CO_2 lasers. Since the introduction of the first commercial CO_2 laser cutting machines in the 1970s, the demands and the laser system performance have been increased steadily, and laser cutting is now regarded as a standard industrial process. The metal cutting industry is still dominated by CO_2 lasers, in spite of the development of other high power laser types. To indicate the volume of the market, the reported monthly average sales orders amounted to $190M in the US alone in the period from 2009 to 2010 [2.2].

The highly competitive situation in this industry has resulted in ever growing customer expectation from the CO_2 lasers in terms of cost of ownership including initial capital cost per kW, the system reliability or continuing maintenance costs. A profound

understanding of the overall CO_2 laser technology in general and especially the discharge excitation processes which may lead to instabilities are very important in order to keep up with the ongoing development requirements for high power CO_2 lasers. The main objective of this literature survey is to describe the current state-of-the-art and recent research results relating to instabilities in the radiofrequency discharge which is the basic excitation process for modern CO_2 lasers. Here, particular importance is attached to RF excited lasers which are diffusion-cooled, since this represents a significant fraction of modern industrial CO_2 lasers.

This chapter is divided into six sections. The historical development of CO_2 lasers including important technological milestones since its pioneering era is outlined in the first part. In the second section the basic physics of the CO_2 laser are briefly summarised to provide a basic understanding of the laser operation. As described below, efficient management of the electric discharge is a necessity for effective generation of the population inversion. For this reason the next two subsections are dedicated to research on the basic RF discharge cell and to studies of the reduced electric field, since this parameter is key to generating efficient population inversion. The generation of RF discharges at high power densities in an efficient and temporally stable manner can only be achieved with spatially homogeneous discharges, and the methods for achieving a homogeneous distribution of the RF discharge are described in the next section. Publications which cover instability processes are the subject of discussions in the final section.

2.2 Background Science and Current State-of-the-art

2.2.1 Historical background

The early history of the laser is closely associated with two research groups, one in USA (Townes/Schawlow) and in USSR (Prokhorov/Basov). Working in the field of electromagnetic radiation in the microwave range they were each successful in developing ammonia “molecular” amplifiers (MASERs) and oscillators in the mid 50s. Important laser-related terms such as population inversion, coherent radiation and electromagnetic beam resonators were well known to these people several years before the first laser was demonstrated experimentally by Maiman in 1960.

The history of origins of the carbon dioxide (CO_2) laser is often equated with the publication of an important paper several years later in 1964 by C. Kumar Patel [2.3]. The importance of his discovery is hard to over-estimate given the unique importance of this laser and the multiple technologies it has spawned over the past half century. Nevertheless it is useful to view the evolution of this laser in the context of the time. The idea of an "open" resonator, where two mirrors confine the optical cavity in contrast to the volumetric microwave resonators and the creation of population inversion by optical pumping lead to the development of new laser types. The group around Patel started research on gas lasers after the demonstration of the first gas laser (HeNe laser, 1961 [2.4]). Following reports of laser transitions with electronically excited noble gases, Patel was able to achieve laser action with excitation of vibrational-rotational of CO_2 molecules. The initial power of 1 mW was very low, so the potential of CO_2 laser to become the dominant industrial high power laser was not realised. However, huge improvements in the laser power were achieved in the early years by optimizing the gas chemistry. The huge importance for efficient upper laser level excitation of the addition of nitrogen to the gas mixture was recognised by Patel, who in 1965 reported over 10 W power from a laser with a N_2-CO_2 mixture. He correctly attributed this multifold power increase to the proximity of key N_2 and CO_2 levels and the efficient electronic excitation of the N_2 molecule [2.5].

Moeller and Ridgen reported slight improvement of a CO_2-He mixture compared to CO_2-N_2 mixture, whereas a tertiary CO_2-N_2-He mixture gives a four fold improvement in power over the binary mixtures, recognizing the importance of He in this gas mixture [2.6]. The beneficial effect of He to the power was thought to be the extension of the diffusion time of the excited CO_2 molecules, whereas the importance of more efficient heat transport in Helium-rich mixtures due to the cooling effect of He was better understood rather later.

Several decades of research followed, aimed at improving the sealed-off lifetime of CO_2 lasers. For example, Witteman noted that the addition of small amounts of water vapour resulted in higher laser output power, which he explained in terms of the accelerated relaxation of lower level 10^00, since the vibrational mode of H_20 is close to it [2.7]. Experiments showed that the output power increases by adding water vapour up to a critical point (0.2 torr added to 10.7 torr He-N_2-CO_2 mix). After this point the power

decreases abruptly with added water vapour content. Water also was shown to be a major factor for a long term operation in a sealed off system. A small amount of H_2O was necessary in order to maintain laser action over 1500 hours of operation [2.8].

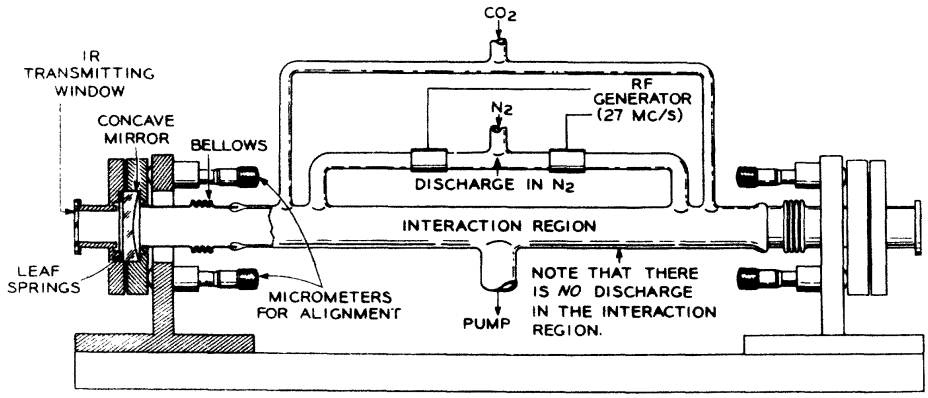

Figure 2.1 CO_2 laser setup used for the first laser [2.3]

However, in the first decade following the discovery of the CO_2 laser, the main emphasis was focused on maximizing the laser output power, mainly in the context of possible military applications. Already in 1965 C. Kumar Patel was able to produce 106 W in a slow flow system with 230 cm discharge length in a water cooled quartz tube in a design similar to that shown in figure 2.1. Additional power scaling could be achieved by increasing the discharge length, with an optimal scaling factor of about 80 W/m.

The high voltage for the DC discharge is applied parallel to the optical axis. Longer distance between the electrodes requires higher voltage, which means that the maximum distance is limited for practical reasons, for example the occurrence of arcs between the electrode and surroundings.

High output power with the technology accessible in the 1960s was realised by adding many discharge cells to a long resonator [2.9]. Roberts *et al*. at Redstone Arsenal reported 2.3 kW laser power from 36 discharge cells with the overall length of more than 50m. However, such installations are not practical because of their size and alternative designs with high power extraction per unit length have been subject of research.

An annular plano-plano resonator with both DC and RF discharge excitation was able to produce significantly higher gain compared to DC excited systems [2.10]. The high voltage for the DC excitation was fed in the longitudinal direction of the 1.2 m long

discharge. The outer tube was divided into insulated sections which served as electrodes for RF excitation at 36 MHz, which improved the homogeneity of the discharge distribution. The hybrid principle of excitation, water cooled silica tubes and the constant flow of the laser gas attributed to a specific power of 210 W/m.

In 1964 Marcatili and Schmeltzer [2.11] proposed a mathematical model which showed that the transmission losses in a hollow dielectric tube can be as low at few dB/km if the radius is chosen appropriately to establish so-called "waveguide" modes. The first waveguide CO_2 laser was realised by Bridges *et al*. [2.12] with a 1 mm diameter quartz glass tube. The small transversal dimension was beneficial in many aspects to produce significantly higher gain per unit volume. The quartz tube capillary provides efficient cooling of the gas so that the operating pressure can be increased from 12 torr to about 150 torr. Higher ratio of the area to the gain volume accelerates the lower laser level de-excitation of the CO_2 molecules by wall collision. Altogether, the waveguide laser design improves the power extraction per volume and the saturation intensity even more when using dielectric materials with high thermal conductivity such as BeO.

For almost two decades, until about 1980, DC discharge excitation was the method of choice for pumping CO_2 lasers. However, towards the end of 1970s researchers realised that RF excitation techniques can have multiple advantages over DC discharge excitation, including the fact that high voltages and dissipative stabilizing ballast resistance are not required for the transverse geometry, and power modulation at kHz frequencies is simple to achieve, which are important features for some applications such as material processing. Lachambre *et al*. were one of the first groups to report results on RF excitation of waveguide CO_2 lasers in 1978 [2.13]. Despite a number of additional issues that needed to be addressed, for example the need of impedance matching, RF shielding enclosures and voltage distribution techniques, the advantages of the RF excited lasers were soon seen to justify any additional research effort needed to understand some areas peculiar to this technology. The authors of [2.14] analyzed these advantages some fifteen years later in a retrospective way. Since the RF voltage is applied in the direction transverse to the laser axis, much lower voltages are needed. Moreover, the electrodes can be covered with a dielectric layer which reduces the electrode degradation and consequent deleterious effects on the gas mixture stability. One of the main fundamental benefits of the RF excitation is due to its discharge structure, consisting of neutral gas

layers which act as stabilizing capacitances, so that not only is the ballast resistor used for DC discharge stabilization not required, but in addition the instability threshold is much higher for transverse RF discharges, so that much higher power densities can be achieved in a stable manner.

With better understanding of the physics involved, such as the RF discharge and the longitudinal voltage distribution, more efficient RF excited waveguide lasers were developed in the first half of the 1980s. He and Hall reported an increase in the specific power to 0.83 W/cm, a significant step towards ultra-compact lasers, with saturation intensity values of 10.5 kW/cm^2, which is double that of comparable DC excited lasers. Thus it was shown that cw power levels of 30 W could be extracted from a 37 cm long electrode structure with a 2.25 mm square cross-section [2.15].

As one particular application of CO_2 lasers, namely laser cutting began to gain importance in the mid 1980s, the demand for higher power became more pronounced.

The heat removal capacity can be regarded as one of the bottlenecks in achieving higher output powers. The approach to remove the excess heat by convection, where the gas is circulated either in the axis parallel to the beam direction (axial flow) or perpendicular to it (transverse flow) are collectively called (fast) flow lasers. Fast flow lasers with multi-kilowatt laser power were already demonstrated in early 1970s ([2.16], [2.17]). The available power from the early flow laser design provided a testing ground for development of material processing applications such as metal cutting and welding. In spite of the important role of convectively cooled lasers for industrial applications, the emphasis of the chapter is placed on diffusion cooled high power CO_2 lasers.

The discharge of diffusion cooled CO_2 lasers could be scaled up only to a certain point both in the lateral direction and in length. The solution for even higher powers was explored by either combining many beams from parallel discharge cells or use a folded single optical resonator design with discharge cells in series [2.18]. This way of scaling the power in linear fashion was superseded with introduction of RF excited CO_2 lasers where the power is scaled with the discharge area. The large discharge area compared to linear waveguide lasers made compact high power possible which could not be achieved before.

A hybrid resonator with a stable resonator in one axis and unstable resonator in the other axis was first suggested and demonstrated by Bourne and Dyer [2.19] for excimer lasers meant a breakthrough in the specific power output by applying the idea to the waveguide CO_2 laser. The hybrid resonator approach was developed in the second half of 1980s, where the resonator was constructed in a way that the resonator was a conventional waveguide in the transverse direction and an unstable positive branch resonator in lateral direction [2.20], [2.21]. Thus, from a discharge length of 37 cm, 240 W output power could be extracted from a hybrid waveguide-unstable resonator. This type of slab CO_2 laser turned out to be highly adaptable for compact laser designs with several hundred watts of output power, making them attractive for material processing applications.

One desirable direction has been to "roll-up" the slab laser to form an annular laser which is compact and offers a rigid structure. A technological issue of RF excited CO_2 lasers are the transmission line effects in lateral direction of the discharge. A distributed parallel resonance (DPR) technique is required to equalise the voltage distribution, which is accomplished in channel and slab waveguides by adding inductors in equidistant spaces between the live and ground electrodes outside the discharge region. The access to those regions is problematic in annular lasers. Bethel *et al*. [2.22] tackled this issue not by regarding the inner and outer electrodes as live and ground for the RF voltage but to split the outer tube in insulated sections where the applied voltage is shifted by π and the inner electrode is left as a floating ground. The two electrodes, basically extruded semi-circles were connected in the axial direction with several DPR conductors. This annular waveguide laser produced 465 W out of 260x36 mm discharge dimension. The specific power could be increased from 14 kW/m^2 in [2.21] to 16.8 kW/m^2. The plano-plano optical resonator is able to extract high power from the discharge, but in order to obtain diffraction limited beam quality more sophisticated resonator annular designs are needed.

Lapucci *et al*. [2.23] developed for example an external beam quality control. An annular waveguide with plane mirrors forms a simple resonator and beam reformatting in the azimuthal direction is done by introducing circular apertures around the gap. The apertures form a periodic beam profile in the near field with distinct spacing between the apertures. The half-Talbot length of the features is designed to be close to the resonator round-trip. A phase-modulated mirror is used to filter the higher order azimuthal modes.

In 1994 results were published by Ehrlichmann *et al*. [2.24] on an annular CO_2 laser, where the beam is free space propagated. The optical resonator consisted of a hybrid stable-unstable resonator, similar to the one suggested in [2.19], [2.21], but in cylindrical coordinate system. The resonator consisted of two toric mirrors, one of which was tilted to form an unstable resonator in azimuthal direction. The researchers used RF frequency of 27 MHz. The relatively low frequency made the setup unsuitable for waveguide operation but on the other hand the longer RF wavelength made longer and uniform discharge structure possible without the need of use parallel inductances to overcome the transmission line effects. The 1.8 m long discharge aluminium tube were used as a live and ground electrode.

In summary, a large variety of different CO_2 laser types was developed, which were specialised to serve in various applications. The object of the following sections of the chapter is to give an overview of development of high power diffusion cooled RF excited CO_2 lasers used for material processing. Furthermore, strategies that have been employed to suppress the occurrence of discharge instabilities are described in further sections.

2.2.2 Optimization of E/N ratio

A key objective with regard to parameters such as the discharge geometry, gas mixture and pressure or applied voltage is to adjust them so as to optimise the output power of the CO_2 laser. These parameters, even though they are different in their nature have significant impact on the key properties of discharge-excited CO_2 lasers, but can be gathered together in a single highly influential parameter - the ratio of the applied electric field amplitude to the density of the neutral particles. This ratio, which is also called the reduced field strength, can be described in the classical view on the atomic scale. Free electrons in the plasma are accelerated by the Coulomb force induced by the applied voltage on the electrodes, and after gaining kinetic energy in the field, the electrons collide with the gas molecules. Thus, the ratio *E/N* is a measure of average energy of the electrons in a discharge. The kinetic theory of gases developed in the 20^{th} century is a useful tool to understand the physics of the discharges that underpin the operation of the CO_2 lasers.

The Boltzmann equation (2.1) is one of the most important relations used to calculate the electron density distribution function *f*.

$$\frac{\partial f}{\partial t} - \frac{eE}{m}\frac{\partial f}{\partial v} = \left(\frac{\partial f}{\partial t}\right)_c \tag{2.1}$$

Frost and Phelps [2.25] include in the Boltzmann equation the terms for inelastic and elastic collisions of the electrons with the molecules as well as the collisions of the second kind (where low energy electrons are accelerated by excited molecules). The density distribution function can be calculated numerically for a given *E/N* and momentum transfer coefficients $Q_m(E)$ based on experiments as described in [2.26]. Lowke *et al.* [2.27] calculated the distribution function for various CO_2 laser gas mixtures (see figure 2.2). The results can be used to obtain transport coefficients like drift velocity and the average electron energy. More importantly, the power input to individual vibrational levels of N_2 and CO_2 was calculated similarly to the work of Nighan and Bennett [2.28], but with updated data for the cross-section coefficients.

Ultimately, the optimization of a given CO_2 laser system means that the goal is to select the *E/N* parameter of the system so as to maximise the fractional power transferred to the CO_2 (001) level (indicated as II in figure 2.2), thereby achieving conditions for the highest laser efficiency.

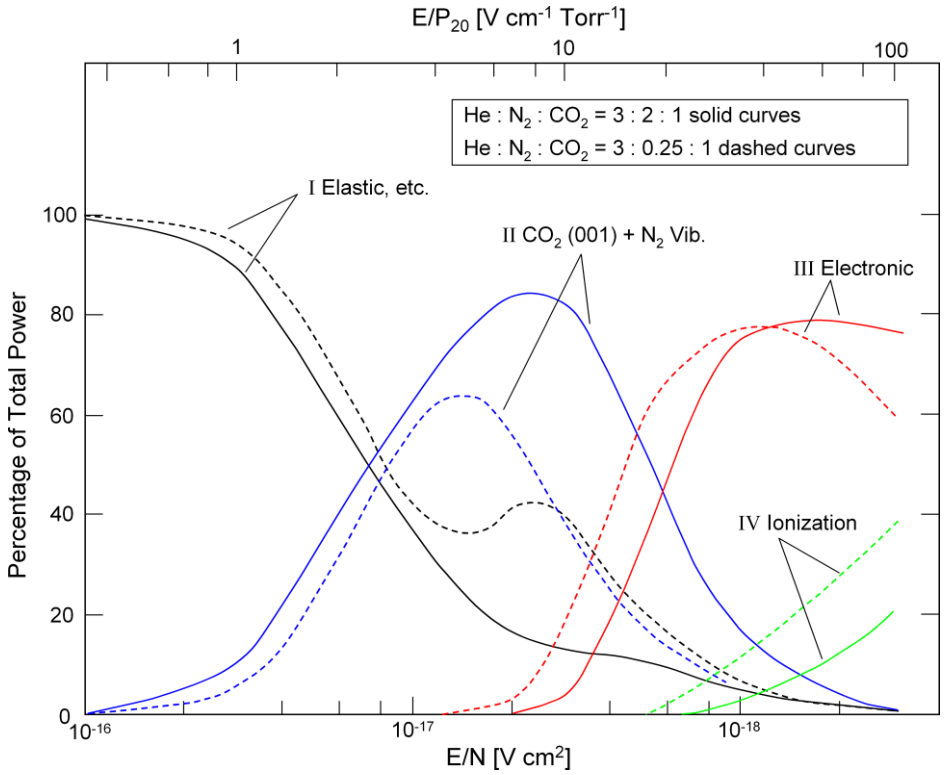

Figure 2.2 Calculated percentage of power transferred to individual vibrational levels as function of E/N (adapted from [2.27])

As seen from a comparison of dashed and solid lines in figure 2.2, the outcome of the calculation is strongly dependent of the gas mixture. Subsequently, Lowke *et al.* [2.27] observed a shift of the maximal fractional power towards smaller *E/N* values by the addition of Helium to the gas mix. The results clearly demonstrate the many degrees of freedom that are available when optimizing a laser discharge for best performance.

The selection of parameters to optimise the *E/N* ratio and maximise the power transfer to the CO_2 (001) level of a laser system is a basic general goal when a laser design is being considered. The correlation of *E/N* ratio and the maximum of the power transfer to CO_2 (001) level can be estimated during the concept phase to find if a design generally makes sense. An example of such an estimation is mentioned in [2.15]. The electric field strength is calculated based on available RMS-voltage of the RF power supply and the discharge gap:

$$E = \frac{V_{rms}}{d} = \frac{\sqrt{P \cdot R_d}}{d} == 737 \frac{V}{cm} \tag{2.2}$$

with d = discharge gap, P = dissipated electric power and R_d = lumped resistance of the discharge.

The neutral gas density N is a function of pressure:

$$N = \frac{N_a}{V_n} = 3.8 \times 10^{18} \frac{1}{cm^3} \tag{2.3}$$

where V_n in the above equation is the molar volume:

$$V_n = \frac{R \cdot T}{p} \tag{2.4}$$

with R = gas constant, T = gas temperature, N_a = Avogadro constant.

This example results in an *E/N* ratio of $1.9 \times 10^{-16} V\,cm^2$ which exhibits a suitable discharge condition for a 3:1:1 He:N_2:CO_2 mixture (compare with figure 2.2).

2.2.3 RF discharge cell

Experiments with RF discharges in a test cell date as far back as 60 years before the invention of masers ([2.29], [2.30]). A typical setup for RF discharges consists of two parallel electrodes in the shape of disks with adjustable separation and geometrical dimensions of several centimetres within a vacuum chamber (e.g. [2.14]). The discharge behaviour depends on many factors including the gas composition and electrode material

even if the geometrical dimensions are kept constant. The measurement of the current-voltage-characteristics (CVC) can provide important insights into the properties of the discharge for a given geometric setup and gas composition. Generally, the lateral dimensions of the discharge grow with increasing applied voltage in order to keep the current density constant in the so-called normal α-type discharge. Once the full electrode area is occupied, the current density rises in the subnormal α-type mode of operation up to an abrupt transition to the γ-type discharge.

Wester *et al.* [2.31] calculated CVC for RF discharges at different pressures and frequencies taking account of the continuity equations for electrons and positive ions, the electrostatic continuity (Poisson) and heat conduction. The contribution of capacitive sheaths and voltage drop across discharge are seen to play the major role in forming the CVC.

A lump-component equivalent diagram for the discharge may be postulated, where the ion sheath is represented by a capacitance and resistance in series and the plasma column as a resistance. Vitruk *et al.* [2.32] showed how to convert the measurement of the voltage between live electrode and ground and between electrodes and the current through a capacitor between ground and ground electrode into equivalent values of sheath capacitance and plasma resistance (see figure 2.3). As can be seen in figure 2.3, the sheath voltage increases linearly with higher currents and plasma voltage staying fairly constant, which indicates a shrinkage of the ion sheath thickness. The authors concluded that for the α-type discharge the ion sheath capacitance is dominating over the voltage drop in the plasma column which is the reason for the influence of the sheath on the discharge stability. The accuracy of suggested model is higher at RF frequencies above 100 MHz, where the ohmic losses in the ion sheath can be neglected. The equivalent model was refined by Baker [2.33] resulting in higher accuracy of the measurement and somewhat higher values of the plasma voltage.

Vitruk *et al*. describe a set of differential equations for the RF discharge comprising the continuity equations for electron density and negative ions, the Poisson's equation and the heat flow equation [2.34]. The variables are transformed into dimensionless variables, for example the space coordinate x is replaced by a dimensionless variable $\chi = x$ / discharge space scale a_0. The constants of the scaled differential equations contain the information about the invariance or scaling laws of the RF discharge. The similarity laws (see

table 2.1) include among geometrical dimensions, the electrical properties also the excitation frequency as a scaling parameter. These help to clarify the dependencies of the operating parameters and allow researchers to make comparisons between RF lasers of various configurations.

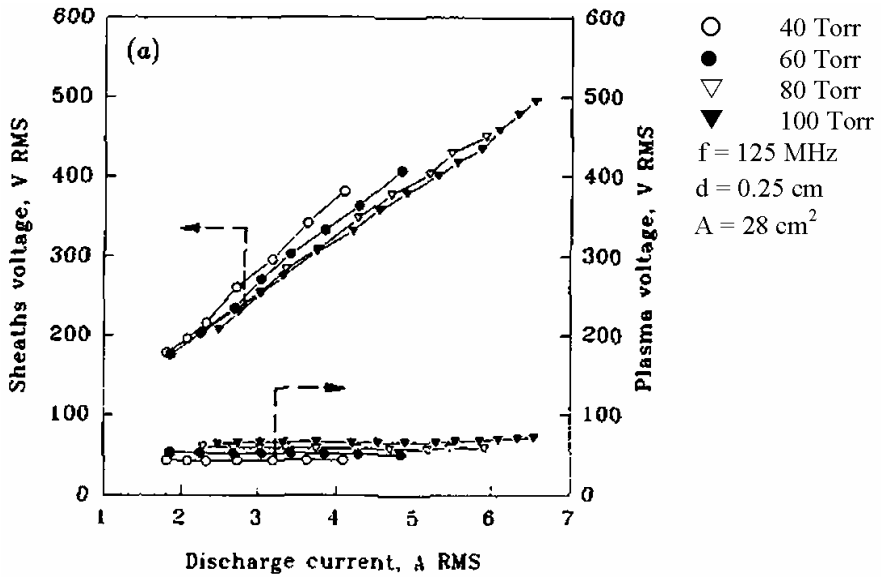

Figure 2.3 Measured current-voltage characteristics for the plasma column and ion sheath at various operating pressures for 3:1:1+5% (He:N_2:CO_2+Xe) gas mix (taken from [2.32])

However, the presented scaling laws have some boundaries where they can be applied. The authors put emphasis on the discharges with frequencies above 100 MHz, where the ion sheath region can be approximated as a capacitance without a resistive component. However, especially at lower frequencies the ohmic losses in the discharge boundaries cannot be neglected. The other limitation is that the gas mixture of (3:1:1 of He:N_2:CO_2 + 5% Xe) is kept constant in the studies, but additional Helium content can reduce the optimal discharge gap and extend the optimal excitation frequencies in the lower end.

Table 2.1 Similarity laws for RF discharges (taken from [2.34]). The scaling variables are defined as $a = D_2 / D_1$ and $b = S_1 / S_2$, where D denotes the discharge gap and S the lateral discharge area.

Parameter	Invariants	Similarity Relations
Excitation Frequency f	fD	$f_2 = f_1/a$
Gas Temperature T	T	$T_2 = T_1$
Electron Temperature T_e	T_e	$T_{e2} = T_{e1}$
Gas Pressure p	p/f, pD	$p_2 = p_1/a$
Electron Density n_e	n_e/f, n_e/p, n_eD	$n_{e2} = n_{e1}/a$
Discharge Current Density j	j/f, j/p, jD	$j_2 = j_1/a$
Discharge Current I	I/fS, I/pS, ID/S	$I_2 = I_1/ab$
Plasma Electric Field E_p	E_p/f, E_p/p, E_pD	$E_{p2} = E_{p1}/a$
Plasma Column Voltage V_p	V_p	$V_{p2} = V_{p1}$
Plasma Column Resistance R_p	R_pfS, R_ppS, R_pS/D	$R_{p2} = R_{p1}ab$
Plasma Column Capacitance C_p	C_p/fS, C_p/pS, C_pD/S	$C_{p2} = C_{p1}/ab$
Ion Sheath Voltage V_s	V_sf, V_sp, V_s/D	$V_{s2} = V_{s1}a$
Ion Sheath Capacitance C_s	C_s/fS, C_s/pS, C_sD/S	$C_{s2} = C_{s1}/ab$
Ion Sheath Resistance R_s	R_sfS, R_spS, R_sS/D	$R_{s2} = R_{s1}ab$
Specific RF Power Deposition in Plasma jE_p	jE_p/f^2, jE_p/p^2, jE_pD^2	$(jE_p)_2 = (jE_p)_1/a^2$
Total RF Power Deposition in Plasma W_p	W_p/fS, W_p/pS, W_pD/S,	$W_{p2} = W_{p1}/ab$
Power Losses in Ion Sheaths W_s/W_p ($\ll 1$)	$(W_s/W_p)f^2$, $(W_s/W_p)p^2$, $(W_s/W_p)/D$	$(W_s/W_p)_2 = (W_s/W_p)_1 a^2$
Gain g	g	$g_2 = g_1$
Saturation G	G/f^2, G/p^2, GD^2	$G_2 = G_1/a^2$
Laser Efficiency $q = W_L/W_p$	q	$q_2 = q_1$
Laser Output Power W_L	W_L/fS, W_L/pS, W_LD/S	$W_{L2} = W_{L1}/ab$

2.2.4 Longitudinal distribution of RF discharge

The RF cell model may be simplified to a one dimensional problem, with the processes analyzed across the discharge gap. However, the electrodes in RF excited CO_2 lasers have length or area dimensions such that the inter-electrode applied voltage is not constant over the entire length or area. Detailed understanding and control of the longitudinal distribution of the discharge is of particular importance for high power CO_2 lasers, since any significant variation of transverse voltage may lead to instabilities and is detrimental to the overall efficiency of the laser system.

The transmission line theory proved to be a powerful tool to represent the voltage distribution of waveguide lasers. He *et al.* [2.15] could show that the transmission line effect cause a voltage variation which is much shorter than expected from a standing wave effect of the RF excitation. The authors could improve the homogeneity by adding an inductor as electric termination.

The use of inductors which are added parallel to the discharge as suggested by Chenausky and Newman [2.35] proved to be effective to equilibrate the voltage distribution. The values of the inductors are adjusted in a way that they form a resonance circuit with the

adjacent capacitance of the electrode structure, so that this technique is also called Distributed Parallel Resonance (DPR).

The equivalent circuit model representing the RF discharge [2.32] can be extended to the longitudinal dimension as described in [2.36]. An analytical solution of the transmission line setup as shown in figure 2.4 can be obtained. Considering that the plasma voltage, R_p and the sheath capacitance, C_s also depend on the voltage at each point x along the electrode, the authors solved the transmission line equations for the current and voltage distribution numerically. It could be confirmed by experiment that it is necessary for the distributed impedances to be matched not only to the capacitance of the electrode surface but also to the ion sheath capacitance.

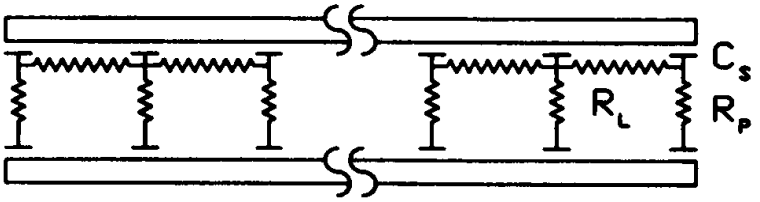

Figure 2.4 Equivalent electric circuit to calculate the longitudinal voltage distribution [2.36]

The authors of [2.37] introduce the stability parameter a defined as the ratio of plasma conductivity ion sheath admittance which has to be equal or larger than one. The dependence of the frequency is taken into account by having a effective ion sheath thickness d_{eff} given by

$$d_{eff} = \frac{6.37 \times 10^4 m/s}{f_{RF}} \tag{2.5}$$

The results show that the capacitance of the electrode structure is higher than the ion sheath capacitance for frequencies $f_{RF} < 40$ MHz. The voltage distribution can be then calculated for the "cold" gap, which means without taking into account the discharge properties. Furthermore, Akimov *et al.* point out that voltage distribution and energy deposition distribution cannot be both homogeneous at the same time.

Raizer and Shneider [2.38] introduced the influence of the current-voltage-characteristics to the transmission line model. Their approach is based on a condition that the ionisation rate α and recombination rate β are in balance:

$$\nu_{iRF}(E_0) = \beta n \tag{2.6}$$

with ν_{iRF} = ionisation frequency, E_0 = electric field amplitude, n = electron density.

Based on equation (2.6) the electric field strength E_0 can be found for a given value of electron density n. As shown in [2.14], E_0 can be related to the current density $j_a \approx e\mu_e n E_0$. Knowing the CVC, the critical voltages, if they exist for given parameters, V_{min} and j_{min} are calculated for each longitudinal position. Below these values the CVC has a negative slope and the discharge becomes unstable. The system, consisting of series of parallel inductances, could be then optimised for given parameters, so that the voltage V along the electrode is always larger than V_{min} for any point along the electrodes.

The DPR technique can also be applied to annular lasers to improve the voltage homogeneity. Whereas in the planar waveguide lasers the inductor can be attached on either side of the electrodes, this is not possible in an annular structure. The accessibility problem is solved in [2.22] by dividing the outer electrode into two halves isolated from each other. The halves act as positive and negative electrodes and the inner electrode has a floating potential. This way, the DPR circuit can be attached outside of the structure between the outer electrode sections. Villarreal *et al*. [2.39] used the "laser beam-free" zone which is in the shadow of the output coupler mirror to add distributed impedance to provide a more uniform voltage distribution, thereby making it possible to achieve uniform discharges at higher input powers (over 30 kW) and longer electrode structures compared to previous designs reported in [2.24].

Similar to [2.36], Strohschein *et al.* [2.40], [2.41] replaced the transmission line elements per unit length with lump components of the plasma R_p and ion sheaths C_s based on the earlier work of Vitruk *et al.* [2.32]. The electrode is divided into sub-sections and each section is solved analytically based on the neighbouring boundary conditions.

The model introduced by Vitruk *et al*. is valid for RF excitation frequencies f above 100 MHz, where the losses in the ion sheath are neglected. Using the fact that the power dissipated in the ion sheath is proportional to $1/f^2$, the model in [2.41] is extended to lower excitation frequencies by introducing an effective plasma resistance as follows:

$$R_d^{'} = R_d\left(1 + P_s \big/ P_p\right) \tag{2.7}$$

with R_d' = reduced discharge resistance, P_s = power deposited in the ion sheath, P_p = power deposited in the plasma column.

The models described here using lossy and lossless transmission line theory are primarily suited for one-dimensional structures, i.e. waveguide lasers. The so-called finite integral technique (FIT) developed by Weiland [2.42] was applied by Spindler [2.43] to calculate the voltage distribution. In the FIT, Maxwell's equations are solved in a discrete form in a staggered mesh where the electric and magnetic field vectors are perpendicular to each other (see figure 2.5). Each cell is assigned the material properties (dielectric constant ε and electric conductivity σ) which are calculated based on the discharge lump component model suggested by Vitruk [2.32] and extended by Baker [2.33]:

$$\varepsilon = \mathrm{Im}\left(\frac{1}{Z_d}\right)\frac{d}{\omega S} \tag{2.8}$$

$$\sigma = \mathrm{Re}\left(\frac{1}{Z_d}\right)\frac{d}{S} \tag{2.9}$$

with d = discharge gap, S = electrode area per cell, Z_d = discharge impedance.

The FIT-calculated results are at least qualitatively very similar to those calculated with the transmission line theory. The advantage is that the FIT model can easily be extended to two-dimensional structures to calculate the voltage distribution of slab lasers or even modified to arbitrarily shaped discharges.

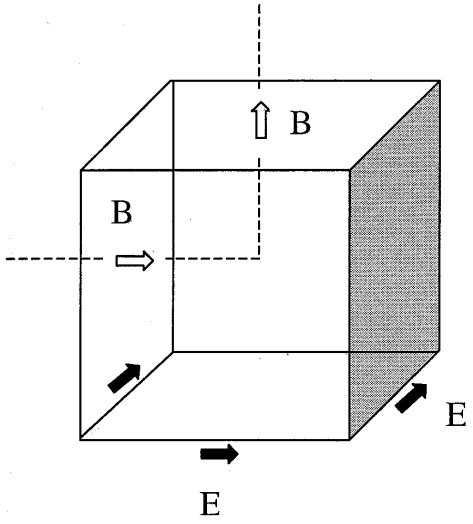

Figure 2.5 Grid cell used in FIT (Finite Integral Technique) [2.43]. The electric field and magnetic flux are perpendicular to each other and calculated on different positions of the cell.

2.3 Discharge Stability

2.3.1 Transition of α- to γ-type RF discharges

Sergei Levitskii was one of the first researchers to observe the existence of two distinct stable regimes of RF discharges and attribute their characteristics to different ionisation mechanisms [2.44]. A regime where the ionisation of the gas is sustained by the electron in the bulk plasma was called the α-type discharge following the naming convention of the first Townsend ionisation coefficient. With higher pressure and voltage another regime was observed where the discharge is brighter in the vicinity of the electrodes. The ionisation of this regime was attributed to the secondary electron emission and hence it was named the γ-type discharge associated with the Townsend secondary ionisation coefficient γ.

Since the 1980s a considerable amount of work has been done in studying the effects of α- to γ-discharge transition, because the electron temperature in the α-type discharge is preferable for the CO_2 laser operation, but the maximum power deposition into the discharge is limited with the occurrence of γ-type discharge.

The authors of [2.14] attribute the rapid transition from α- to γ-type discharge to the spontaneous breakdown of electrons through the ion sheaths then creating an avalanche effect of secondary emitted electrons on the electrodes. By integrating numerically the continuity equations for the electrons and anions, continuity equations of densities of drift charges and the Poisson's equation, the authors were able to show that either the α- or the γ-discharge distribution could be generated by an appropriate selection of the three main parameters: the neutral particle density n, electric field amplitude E_a and the current density j_a.

Raizer *et al.* studied the mechanism of the abrupt change of α-type discharge to γ-type discharge as the applied RF voltage is increased over a threshold value. They attributed the transition to the voltage breakdown between the electrically non-conducting ion sheath and the electrode surface. The breakdown leads to the emission of secondary electrons which in turn establish the γ-type discharge.

The threshold voltage V_t at which the transition occurs was estimated using the Townsend's breakdown criterion where the breakdown distance d is set equal to the thickness of the ion sheath of the RF discharge:

$$V_t = \frac{B\ pd}{C + \ln(pd)} \tag{2.10}$$

with p = operating gas pressure, B and C = experimentally determined constants.

Based on experimental measurements, Vitruk *et al*. [2.32] report that the transition is dominated by the ion sheath voltage at RF frequencies which are typically used in linear waveguide lasers (125 MHz). The sheath voltage in this case is much higher than the discharge voltage. A model is used where the time is calculated for an electron entering the plasma until a gamma electron is emitted from the electrode. Qualitative results for the α-to-γ transition show increasing threshold with increasing excitation frequency.

The reason for the self-stabilizing effect of either α- or γ-type discharge is examined in [2.45]. The authors introduce a reproduction factor which is defined as the ratio of the production and removal rate of charged particles. The discharge is assumed to be stable when both rates are equal. In figure 2.6 the reproduction rates for α- and γ-discharges are shown. The ion sheath thickness moved at any given position either to α_s or γ_s so that the overall reproduction factor is unity and its slope is positive to stabilise the ionisation. This mechanism can be used to find the transition point between the discharge type and the hysteresis effect, once one of the extrema in the reproduction factor curve reaches value of 1 and the stability criterion is broken.

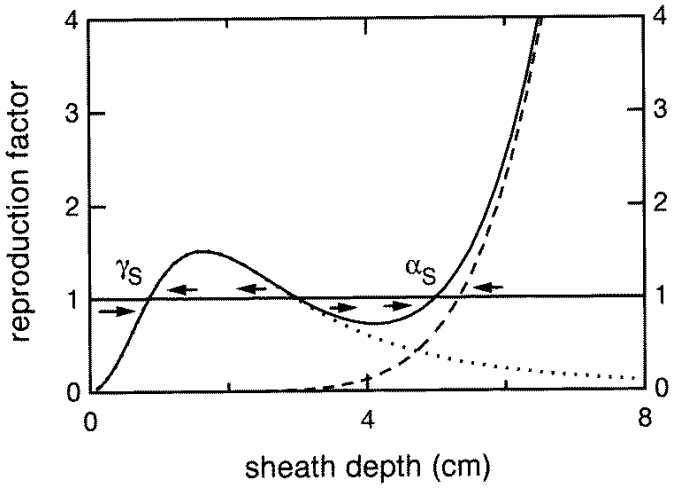

Figure 2.6 The reproduction factors for α-type (dotted curve), γ-type discharge (dashed curve) and overall factor (solid curve). The arrows indicate progression over time. Taken from [2.45]

2.3.2 Thermal instabilities

When designing high power discharge-excited gas lasers, researchers are often confronted with a critical or "threshold" input power that can be deposited into the discharge volume, above which the discharge becomes unstable. In the case of the RF excitation, this threshold is exceeded when the discharge regime undergoes a transition to the γ-type discharge due to an avalanche of secondary electron emission as discussed in the section above, or alternatively it can transform into an arc due to local thermal instabilities. Raizer [2.46] describes the process as follows: The local increase in the gas temperature means an increase in the local gas density, *N* which in turn shifts the *E/N* ratio towards higher values and electron temperatures. The higher *E/N* ratio leads to higher current densities and Joule heat release. As a result, the gas is heated even more, eventually leading to the formation of arcs or striations. This instability process can be regarded as a closed loop and the process can be initiated at any point in the chain of events. Raizer emphasises that the term "arc" used here should not be confused with an electric arc at atmospheric pressures. The electron and gas temperatures are in thermal equilibrium at 6000-10000 K whereas the arc in the discharge has low electron energy of 1-3 eV and the gas temperature is in the region of 2000-3000 K.

An early investigation of the thermal instability mechanism in DC discharges was carried out by Ecker *et al*. [2.47] in the 1960s. The plasma is defined by a set of differential equations based on the transport equations for particle density, momentum and energy. The authors regard only atomic species so the energy transport to rotational and vibrational excitation levels of molecules cannot by analyzed in this model.

The basic idea is that the disturbances, which lead to particle creation and particle loss might be out of balance so that more particles are created, thereby leading to instabilities. The results are shown in figure 2.7. The product of the discharge radius *R* and pressure *p* is plotted on the *x*-axis, while on the *y*-axis the critical product of discharge current *I* and pressure *p*, above which thermal instabilities will occur is plotted. The set of curves show that the discharge is unstable without the presence of an external resistance ($\sigma \rightarrow 0$) and for any value of external resistance for large product of tube diameter and pressures. Indeed, it became common practice for DC discharge CO_2 lasers to be stabilised with a ballast resistor of several MΩ. The results are qualitative, but the work shows a valuable descriptive approach for handling thermal instabilities in high power discharges.

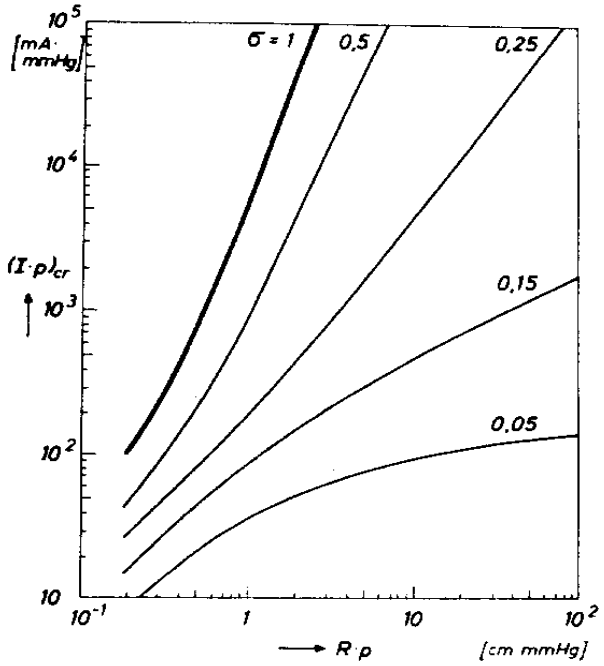

Figure 2.7 The critical current as a function of tube radius R with $\sigma = (1 + \Omega_i/\Omega_0)^{-1}$, Ω_i internal resistance, Ω_0 external ballast resistance (taken from [2.47])

When going to higher power densities in DC discharges it was noticed in 1970s that the gas cooling itself via fast circulation through heat exchangers still could not prevent discharge instabilities from occurring. A comprehensive model of the fluid with, overall, fourteen differential equations including the momentum and energy continuity, translational and vibrational energy of single diatomic species and Maxwell's equations was established by Haas [2.48]. The time constants of the system response were introduced and analyzed and nine different modes of instability with the time constants varying from nanoseconds (space-charge relaxation) to sub-milliseconds (fluid vorticity). Three modes were identified as being critical for CO_2 laser stability: the ionisation mode and negative-ion production which evolve in microseconds and the vibrational relaxation with the time constant of some milliseconds.

Nighan and Wiegand [2.49] studied the implications of the thermal and vibrational stability processes which were derived by Haas [2.48], who had introduced a disturbance growth rate v_g given by

$$v_g = -\frac{1}{2}b \pm \frac{1}{2}\sqrt{b^2 - 4c} \tag{2.11}$$

where b and c are abbreviations for the differential equations describing the thermal and vibrational stability respectively.

In the case where instabilities occur, these coefficients have negative values. Nighan and Wiegand calculated the reciprocal value of v_g representing a time constant for instabilities to occur as a function of the gas pressure, power density and dimension of the disturbances for DC excited CO_2 lasers. The results show that at a gas temperature of 300 K the thermal mode is stable and instability of the vibrational mode is the limiting factor. At a gas pressure of 20 torr the shortest instability growth time is in order of milliseconds which the author sees as manageable time when using fast flow design where the residence time of the gas in the discharge chamber can be reduced to less than one millisecond. On the other hand, when using higher pressure of 200 torr and higher power density of above 10 W/cm^3, the instability growth time becomes too short to be stabilised by convection. As the gas temperature is increased to 600 K in the calculation, the authors report that the thermal mode also becomes unstable. The calculated growth times of the instabilities were confirmed by measurements.

Another modification of the model from [2.48] was made by Nighan [2.50] to estimate the instability processes in externally sustained discharge with high pressures of hundreds of torr and power densities of 100 W/cm^3. It could be shown that the discharge is generally unstable and thus knowledge of the instability growth time can give a measure of required circulation rate of the gas.

As researchers shifted their attention from DC to RF excited high power lasers, the understanding of thermal instabilities in RF discharges also gained in importance. The occurrence of instabilities in the form of filaments in the fast flow CO_2 lasers was studied by Wester *et al*. [2.31]. In the model they developed, the electric field was calculated using the Poisson's equation and the neutral gas density with the Navier-Stokes equations. The time-dependent development of filaments could then be simulated on the basis of fluctuations of the electron and neutral gas density. The filament current is limited by the dielectric placed between the electrodes and the gas thus stabilises the discharge. This result is in agreement with the work of Raizer *et al*. [2.14] where it is shown that the plasma column is stabilised by the dielectric if its thickness d/ε_r is larger than the ion sheath thickness. The filaments are built up within few hundred microseconds and form highly conductive stripes reaching from one electrode to the other. The calculation by Wester and colleagues show that the filaments cease to exist after about 1.5 milliseconds, when the gas reaches its steady hot temperature and the neutral gas density dilutes accordingly.

The model for evaluation of thermal instabilities in DC discharges [2.51] was extended by Wester [2.52] for RF discharges. Additionally to the reduced field *E/N* characterizing the discharge, a frequency-dependent term was added which is the ratio of excitation frequency to the momentum transfer frequency. The differential equations describing the continuity of the density of neutral gas, its energy and momentum as well as rate coefficients for electron ionisation and attachment are calculated for a steady state assuming that the time constants of the processes described by these equations are much smaller than the time constant of thermal instabilities. The system of equations is then linearised around the steady state. For this some mathematical manipulations are required (the Fourier transform of the lateral dimension, describes the linear system of equations by a matrix and calculate the eigenvalues using the characteristic equation) as already applied by Jacob and Mani for a DC discharge [2.51]. The procedure delivers eigenvalues λ for the thermal and acoustic stabilities mode. An example of the resulting eigenvalues as a function of the Fourier transform of the position (the wave number k) is shown in figure 2.8. The mode is stable when the eigenvalue is negative. As can be seen, the acoustic mode λ_3 is stable for most of the wave number range except for small k (large discharge gap). The thermal mode λ_2 is always stable whereas the thermal mode λ_1 becomes unstable in the range between k = 0.5 - 12 cm^{-1}. The stability is explained by the response of the absorption of power as a function of the neutral gas density. For low wave numbers the thermal mode λ_1 is stabilised by field reduction and for high wave numbers (small discharge gap) by diffusion and heat conduction.

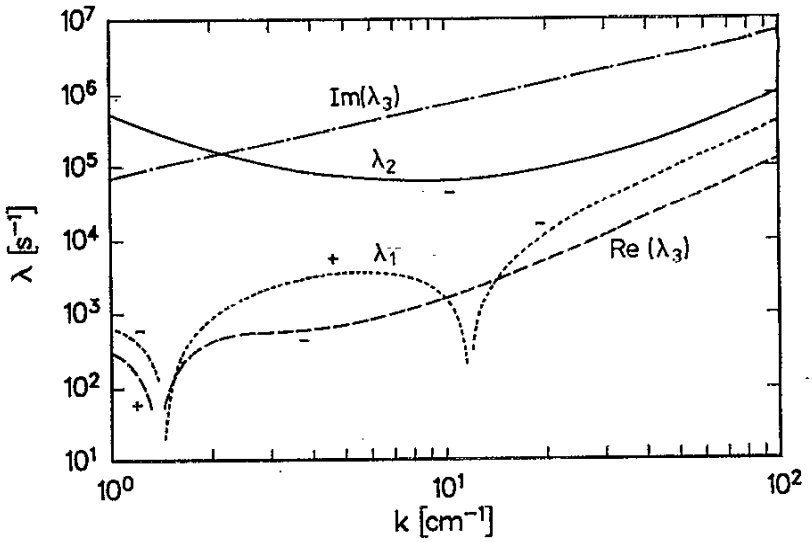

Figure 2.8 Example of the results from calculation of the eigenvalues for thermal modes (λ_1, λ_2) and acoustic modes (λ_3) for 30 MHz, d = 30 mm. Abscissa is the Fourier transformed of the gap dimension, positive values of λ lead to instabilities. The figure is taken from [2.31].

The analysis method described in [2.52] is further extended by Loosen and Wester [2.53] but also work in the field of RF discharge stabilities by Menshikov and Yatsenko is mentioned. Note that Loosen *et al*. disregard the sheaths, which is accurate enough down to 10 MHz. By using the continuity equations for electron density and neutral gas they derive two stability equations:

$$dN_0 = \sqrt{\frac{\lambda_0 T_0 \pi^2}{2|\alpha|\varepsilon_0 \omega \left(E/N_0\right)^2}} \tag{2.12}$$

$$w = \frac{\lambda_0 T_0 \pi^2}{2d^2|\alpha|} \tag{2.13}$$

with λ_0 = thermal conductivity of the gas, T_0 = temperature of the gas, ω = excitation circular frequency, d = discharge diameter, α = short term of an expression of stability growth.

The equation (2.12) states that for a given product of discharge gap d and neutral gas density N_0 the term on the right hand side must not be exceeded. The equation (2.13) gives the optimal power density w for given discharge parameters in the case that the operation is close to the limit of the first equation. The calculation was compared with the results of fast flow lasers, with the outcome that the measured values were 3-4 times higher than expected by the theory. This difference was attributed to the effect of gas turbulences and the exclusion of the plasma sheath in the model.

The studies of thermal stabilities in RF discharge were summarised by Vitruk *et al.* [2.34] and also an approach was shown which would explain the stabilizing effect of the α-type discharge. As described in previous results for DC discharges, the plasma column is always unstable without the presence of a ballast resistor due, among other things to the positive slope in the current-voltage characteristic as discussed in [2.46]. The RF discharge is expected to be also always unstable for the same reason if it were not for the presence of the ion sheaths. If the electric properties of the ion sheath are approximated as a purely capacitive passive element and the plasma column as a resistor, the complex voltage of the discharge can be calculated using the Pythagorean Theorem:

$$V_d^2 = V_p^2 + V_s^2 \tag{2.14}$$

with V_d = voltage on the discharge, V_p = voltage on the plasma column, V_s = voltage on the ion sheath.

By differentiating the discharge voltage in equation (2.14) with respect the current density the authors obtain the slope of the current-voltage characteristic. Vitruk *et al*. state an equation for the thermal instability growth G_{iRF} assuming that the instability occurs if the heat release rate in the discharge v_h is larger than heat removal rate v_c:

$$G_{iRF} = \nu_h \frac{1+R+\nu^* R}{1+R+\nu^*} - \nu_c \text{ with } R = \frac{V_p^2}{V_s^2} \tag{2.15}$$

According to equation (2.15), the discharge is on the stability limit for $v_h = v_c$ and $V_p = V_s$. Thermal stability is improved by having a higher heat removal rate v_c than v_h, or if the voltage drop on the ion sheath V_s is larger than the voltage drop on the plasma column V_p. The latter tendency provides an explanation as to why the RF discharge is shown to be more stable at higher excitation frequencies. Analogous to the results of [2.31], the equation for G_{iRF} also shows that thermal instabilities are amplified for larger discharge gaps because of the voltage drop on the plasma column.

2.3.3 Discharge stabilization in atmospheric pressure CO_2 lasers

There are some applications such as photolithography that require high pulse energies rather than high average power. The logical approach for achieving this is by increasing the operating pressure since higher gas density means more gain and also faster relaxation of rotational-vibrational modes by higher collision rates of molecules. Since the threshold for discharge instabilities is very low for high pressures and high power densities, many technological issues had to be solved so as to make possible the realization of transversely excited atmospheric pressure CO_2 lasers (TEA).

The first TEA laser setup demonstrated by Beaulieu in 1970 [2.54] consisted of a flat anode and a cathode surface was replaced by series of pins with 1 kΩ resistance in series for each pin. The pin design and short excitation duration was achieved by discharging a capacitor allowed the operation at atmospheric pressure. Further methods which were developed in the early 1970s to prevent arc formation in TEA laser were summarised by Wood [2.55]. Two effective techniques have been evolved, the first being the optimization of the electrode shape for electric field distribution and the other preionisation of discharge. The so-called Rogowski profile electrodes are curved in the outer regions so the electric field lines are penetrating the electrodes in a perpendicular way. This shape decreases the local electric field strength and allows designs with higher

power densities and discharge volumes. The ignition process of the discharge is stabilised if the gas is ionised before voltage is applied to the electrodes. Preionisation can be accomplished for example by electron beams or by radiation from radioactive reactions, but also more practical solution like direct UV light radiation or UV light radiation from auxiliary discharges proved to be effective. Richardson *et al*. [2.56] presented results of a TEA laser where both electrode shape optimization (termed as "double Rogowski" profile since both electrodes had this profile) and a double discharge setup were employed. Remarkable pulse energy of 300 Joules could be achieved.

2.4 Summary

The CO_2 laser has come a long way since its pioneer years in terms of the diversity of the laser technology and the breadth of applications. Within the first few years after its invention, it became clear that the CO_2 laser has the potential to generate high output power. Despite its success there were also cases where the CO_2 laser has been superseded by other technologies. For example it was decided to use a chemical laser instead of a gasdynamic CO_2 laser at the US Airborne Laser project. Another example would be the decision to use solid state lasers for laser induced fusion tests. In other applications, such as sheet metal processing, the CO_2 laser technology has still maintained a dominating role for 30 years.

For the first 15 years the discharge excitation method for high power lasers was by direct current. The mechanism of formation of thermal instabilities was understood thanks to works by Ecker [2.47], Nighan [2.49], Raizer [2.46] to name a few. Starting in the 1980s, as the technology changed to RF excited CO_2 lasers researchers occupied themselves with processes leading to α- to γ-discharge formation for example by Odrobina [2.45]. When the research activity would be measured by the frequency of publications, one would find a steady decline of research in the field of high power CO_2 lasers beginning in the middle of the 1990s. Arguably two significant publications of this era are the representation of the RF discharge by electric lump components in 1992 [2.32] and formulation of similarity laws of RF discharges in 1994 [2.34].

2.5 References

[2.1] J. C. Ion "Laser processing of engineering materials: principles, procedure and industrial application", Elsevier Butterworth-Heinemann Amsterdam, ISBN 075-0660-791 (2005)

[2.2] P. Borden, P. McGibon "Manufacturing technology consumption up 58.9% in 2010", U. S. Manufacturing Technology Consumption News Release September 2010, WWW.AMTonline.org (2010)

[2.3] C. K. N. Patel "Interpretation of CO_2 optical maser experiments", Phys. Rev. Lett., vol. 12, pp. 588-590 (1964)

[2.4] A. Javan, W. R. Bennett, D. R. Herriott "Population inversion and continuous optical maser oscillation in a gas discharge containing a He-Ne mixture", Phys. Rev. Lett., vol. 6, pp. 106-110 (1961)

[2.5] C. K. N. Patel "CW high power N_2-CO_2 laser", Appl. Phys. Lett., vol 7, pp. 15-17 (1965)

[2.6] G. Moeller, J. D. Ridgen "High-power laser action in CO_2-He mixtures", Appl. Phys. Lett., vol. 7, pp. 274-276 (1965)

[2.7] W. J. Witteman "Rate determining processes for the production of radiation in high power molecular lasers", IEEE J. Quantum Electron., vol. 2, ppp. 375-378 (1966)

[2.8] W. J. Witteman "The CO_2 laser", Springer-Verlag Berlin, ISBN 3-540-17657-8 (1987)

[2.9] T. G. Roberts, G. J. Hutcheson, J. J. Ehrlich, W. L. Hales, T. A. Barr "High-power N_2-CO_2-He laser development", IEEE J. Quantum Electron., vol. 8, 605-609 (1967)

[2.10] A. Crocker "Carbon-dioxide laser with high power per unit length", Electron. Lett., vol. 5, p. 63-64 (1969)

[2.11] E. A. Marcatili, R. A. Schmeltzer "Hollow metallic and dielectric waveguides for long distance optical transmission and lasers", Bell Syst. Tech. J., vol. 43, pp. 1783-1809 (1964)

[2.12] T. J. Bridges, E.G. Burkhardt, P. W. Smith "CO_2 waveguide lasers", App. Phys. Lett., vol. 20, pp. 403-405 (1972)

[2.13] J.-L. Lachambre, J. Macfarlane, G. Otis, P. Lavigne "A transversely re-excited CO_2 waveguide laser", App. Phys. Lett., vol. 32, pp. 652-653 (1978)

[2.14] Y. P. Raizer, M. N. Shneider, N. A. Yatsenko "Radio-frequency capacitive discharges", CRC Press Roca Baton, ISBN 0-8493-8644-6 (1995)

[2.15] D. He, D. R. Hall "A 30-W radio frequency excited waveguide CO_2 laser", Appl. Phys. Lett., vol. 43, pp. 726-728 (1983)

[2.16] A. E. Hill "Role of thermal effects and fast flow power scaling techniques in CO_2-N_2-He lasers", Appl. Phys. Lett., vol. 16, pp. 423-426 (1970)

[2.17] P. A. Hilton "Early days in laser cutting", Proc. 11th Nordic Laser Materials Processing Conference Lappeenranta (1997)

[2.18] J. G. Xin, D. R. Hall "Compact, multipass, single transverse mode CO_2 laser", Appl. Phys. Lett., vol. 51, pp. 469-471 (1987)

[2.19] O. L. Bourne, P. E. Dyer "A novel stable-unstable resonator for beam control of rare-gas halide lasers", IEEE Opt. Commun., vol. 31, pp. 193-196 (1979)

[2.20] K. M. Abramski, A. D. Colley, H. J. Baker, D. R. Hall "Power scaling of large-area transverse radio frequency discharge CO_2 lasers", Appl. Phys. Lett., vol. 54, pp. 1833-1835 (1989)

[2.21] P. E. Jackson, H. J. Baker, D. R. Hall "CO_2 large-area discharge laser using an unstable-waveguide hybrid resonator", Appl. Phys. Lett., vol. 54, pp. 1950-1952 (1989)

[2.22] J. W. Bethel, H. J. Baker, D. R. Hall "A new scalable annular CO_2 laser with high specific output power", Opt. Commun., vol. 125, pp. 352-358 (1998)

[2.23] A. Lapucci, M. Ciofini, S. Mascalchi "Beam quality enhancement for a radio-frequency excited annular CO_2 laser", Appl. Phys. Lett., vol. 73, pp. 2549-2551 (1998)

[2.24] D. Ehrlichmann, U. Habich, H.-D. Plum, P. Loosen, G. Herziger "Azimuthally unstable resonators for high-power CO_2 laser with annular gain media", IEEE J. Quantum Electron., vol. 30, pp. 1441-1447 (1994)

[2.25] L. S. Frost, A. V. Phelps "Rotational excitation and momentum transfer cross sections for electrons in H_2 and N_2 from transport coefficients", Phys. Rev., vol. 127, pp. 1621-1633 (1962)

[2.26] G. J. Schulz "Measurement of excitation of N_2, CO, and He by electron impact", Phys. Rev., vol. 116, pp. 1141-1147 (1959)

[2.27] J. J. Lowke, A. V. Phelps, B. W. Irwin "Predicted electron transport coefficients and operating characteristics of CO_2-N_2-He laser mixtures", J. Appl. Phys., vol. 44, pp. 4664-4671 (1973)

[2.28] W. L. Nighan, J. H. Bennett “Electron energy distribution functions and vibrational excitation rates in CO_2 laser mixtures”, Appl. Phys. Lett., vol. 14, pp. 240-243 (1969)

[2.29] F. Paschen “Ueber die zum Funkenübergang in Luft, Wasserstoff und Kohlensäure bei verschiedenen Drucken erforderliche Potentialdifferenz”, Ann. Phys., vol. 273, pp. 69-75 (1889)

[2.30] J. S. Townsend “The theory of ionization of gases by collision”, Constable & Company, ISBN 1-1125-6602-3 (1910)

[2.31] R. Wester, S. Seiwert, R. Wagner “Theoretical and experimental investigations of the filamentation of high-frequency excited CO_2 laser discharges”, J. Phys. D: Appl. Phys., vol. 24, pp. 1796-1802 (1991)

[2.32] P. P. Vitruk, H. J. Baker, D. R. Hall “The characteristics and stability of high power transverse radio frequency discharges for waveguide CO_2 slab laser excitation”, J. Phys. D: Appl. Phys., vol. 25, pp. 1767-1776 (1992)

[2.33] H. J. Baker “Direct measurement of the electrical impedance of the narrow gap radio frequency gas discharges in the 100 MHz region”, Meas. Sci. Technol., vol. 7, pp. 1631-1635 (1996)

[2.34] P. P. Vitruk, H. J. Baker, D. R. Hall “Similarity and scaling in diffusion-cooled RF-excited carbon dioxide lasers”, IEEE J. Quantum Electron., vol. 30, pp. 1623-1634 (1994)

[2.35] P. P. Chenausky, E. H. Drinkwater, L. M. Laughman “Tuned-circuit RF-excited laser”, US Patent, 4,363,126 (1982)

[2.36] A. Lapucci, F. Rossetti, M. Ciofini, G. Orlando “On the longitudinal voltage distribution in radio-frequency-discharged CO_2 lasers with large-area electrodes”, IEEE J. Quantum Electron., vol. 31, pp. 1537-1542 (1995)

[2.37] A. G. Akimov, D. N. Zybin, N. I. Lipatov, S. M. Nefedov, D. E. Protsenko, T. A. Tikhomirova “Effect of the spatial structure of the radio-frequency discharge on the impedance of a laser head”, Laser Phys., vol. 3, pp. 980-988 (1993)

[2.38] Y. P. Raizer “Radio-Frequency Capacitive Discharge in a Long Strip Line”, IEEE Trans. Plasma Sci., vol. 26, pp. 1017-1021 (1998)

[2.39] F. J. Villarreal-Saucedo, J. Deile, S. Sumrain, V. Granson, P. Daniel “Laser having distributed inductances”, US patent 7,778,303 (2010)

[2.40] J. D. Strohschein, W. D. Bilida, H. J. J. Seguin, C. E. Capjack “Enhancing discharge uniformity in a multi-kilowatt radio frequency excited CO_2 slab laser array”, Appl. Phys. Lett., vol. 68, pp. 1043-1045 (1996)

[2.41] J. D. Strohschein, W. D. Bilida, H. J. J. Seguin, C. E. Capjack “Computational model of longitudinal discharge uniformity in RF-excited CO_2 slab lasers”, IEEE J. Quantum Electron., vol. 32, pp. 1289-1298 (1996)

[2.42] T. Weiland “Eine Methode zur Lösung der Maxwellschen Gleichungen für sechskomponentige Felder auf diskreter Basis”, AEÜ, vol. 31, pp. 116-120 (1977)

[2.43] G. Spindler “Two-dimensional computational model of discharge uniformity in radio-frequency-excited CO_2 slab lasers with high aspect ratio electrodes”, IEEE J. Quantum Electron., vol. 39, pp. 343-349 (2003)

[2.44] S. M. Levitskii “An investigation of the sparking potential of a HF discharge in a gas in the transition range of frequencies and pressures”, Sov. Phys. – Tech. Phys., vol. 2, pp. 887-893 (1957)

[2.45] I. Odrobina, M. Kando “Discontinuous transitions between alpha and gamma regimes of rf capacitive discharge”, Plasma Sources Sci. Technol., vol. 5, pp. 517-522 (1996)

[2.46] Yu.P. Raizer “Gas discharge physics”, Springer, ISBN 3-540-19462-2 (1997)

[2.47] G. Ecker, W. Kröll, O. Zöller “Thermal instability of the plasma column”, Phys. Fluids, vol. 7, pp. 2001-2006 (1964)

[2.48] R. A. Haas “Plasma stability of electric discharges in molecular gases”, Phys. Rev. A, vol. 8, pp. 1017-1043 (1972)

[2.49] W. L. Nighan, W. J. Wiegand “Causes of arcing in cw CO_2 convection laser discharges”, Appl. Phys. Lett., vol. 25, pp. 633-636 (1974)

[2.50] W. L. Nighan “Causes of thermal instability in externally sustained molecular discharges”, Phys. Rev. A, vol. 15, pp. 1701-1720 (1977)

[2.51] J. H. Jacob, S. A. Mani “Thermal instability in high-power laser discharges”, Appl. Phys. Lett., vol. 26, pp. 53-55 (1975)

[2.52] R. Wester “Frequency dependence of thermal volume instabilities in high-frequency CO_2 laser discharges”, J. Appl. Phys., vol. 70, pp. 3449-3454 (1991)

[2.53] P. Loosen, R. Wester “Parameter limits of thermal instabilities in high-frequency CO_2 laser discharges”, J. Phys. D: Appl. Phys., vol. 28, pp. 849-855 (1995)

[2.54] A. J. Beaulieu “Transversely excited atmospheric pressure CO_2 lasers”, Appl. Phys. Lett., vol. 16, pp. 504-505 (1970)

[2.55] O. T. Wood “High-pressure pulsed molecular lasers”, Proc. IEEE, vol. 62, pp. 355-397 (1974)

[2.56] M. C. Richardson, A. J. Alcock, K. Leopold, P. Burtyn “A 300-J Multigigawatt CO_2 laser”, IEEE J. Quant. Electron., vol. 9, pp. 236-243 (1974)

Chapter 3

SUPPRESSION OF DISCHARGE INSTABILITIES IN THE RF FEED REGION

3.1 Introduction

The RF power delivery in a TruCoax V6 laser was designed to pass through a port in the outer electrode, in a region in which the beam is shadowed by the metallic webs supporting the inner electrode. The design enables a relatively effortless exchange of resonator mirrors during the manufacturing process. However, the outer electrode port is limited in its size so that this configuration is attended by high electric fields around the RF feed as well as high current density. In addition to these limiting issues, the RF feed-through is located inside the laser vacuum vessel, thereby increasing the risk of possible voltage breakdown between the RF feed shaft and the surrounding grounded outer electrode. Consequent detrimental effects, including discharge instabilities can range from leaving marks on the metal surface to the formation of localised γ-type discharge or ultimately to catastrophic damage of the RF feed assembly.

The goal of this chapter is to develop a design for the RF feed-through, that provides an acceptably-low level of risk of voltage breakdown in regions other than the desired inter-electrode discharge gap. The plan of this chapter is first to introduce the theory of electrical breakdown in gases for DC and RF voltages for the simple case of a homogeneous electric field, after which in the following section a method will be described for the calculation of the electrostatic potential field, allowing one to determine the electric field for conductors of arbitrary shape. The model can then be applied to the task of improving the geometrical design of the RF feed, the dielectric insulator and the shape of the interface between the RF feed shaft and the inner electrode in subsequent sections.

3.2 Electrical Breakdown in Gases

3.2.1 Electrical breakdown with applied DC voltage

A model describing electrical breakdown when a DC voltage is applied between electrodes was provided by Townsend [3.1]. Free electrons are accelerated by the Coulomb force and after travelling some average distance, collide with atoms or molecules. Such collisions are a source of ionisation in a neutral gas. The frequency of ionisations per unit length along the electric field lines is expressed by the so-called first Townsend coefficient α. Electrons are also able to ionise the gas after striking the anode, and the ionisation rate following collisions of electrons and anions with the anode is another ionizing mechanism. This rate is quantified by the third Townsend coefficient, sometimes called the secondary emission coefficient γ. The threshold condition for electric breakdown is called the Townsend criterion [3.2], which can be written as:

$$\gamma[\exp(\alpha d) - 1] = 1 \tag{3.1}$$

where α is first coefficient, and d is the discharge gap.

The dependence of the first Townsend ionisation coefficient α of the ratio E/p was derived for noble gases using the kinetic gas theory [3.1] so that:

$$\alpha = pA\exp\left(-\frac{B}{E/p}\right) \tag{3.2}$$

Here, the variable p is the gas pressure, A and B are experimentally-determined gas-specific coefficients. In a homogeneous electric field, which implies flat parallel electrode with large lateral dimension, the relationship between the field E and voltage V is:

$$E = \frac{V}{d} \tag{3.3}$$

where d is the inter-electrode spacing.

After introducing a substitute variable Γ for the product αd, we can rearrange equation (3.1) yielding:

$$\Gamma = \ln\left(\frac{\gamma + 1}{\gamma}\right) \tag{3.4}$$

Inserting equations (3.2), (3.3) and (3.4) into equation (3.1) yields the breakdown criterion including coefficients A and B:

$$pdA\exp\left(-\frac{Bpd}{V_{br}}\right) = \Gamma \tag{3.5}$$

After rearranging equation (3.5), we obtain an expression for the breakdown voltage:

$$V_{br} = \frac{-Bpd}{\ln\left(\frac{\Gamma}{pdA}\right)} \tag{3.6}$$

Equation (3.6) shows, that the breakdown voltage V_{br} is a function of the product of the pressure p and discharge gap d, if the functional relationship (3.2) holds true. The relationship of the breakdown voltage V_{br} as function of the product pd is commonly referred as the Paschen curve.

In general, the coefficient α is a function of the ratio of the electric field E to the neutral gas density N. If this function $\alpha(E/N)$ is known, one can find the breakdown voltage by finding the electric field E needed to satisfy the Townsend criterion (equation (3.1)) without using the analytical expression in equation (3.2).

3.2.3 Electrical breakdown with applied RF voltage

Electrical breakdown caused by RF voltages can be described using diffusion theory as shown by Brown and McDonald [3.3]. The change of the electron density $\partial n/\partial t$ is affected according to [3.3] by volumetric ionisation and by a diffusion term:

$$\frac{\partial n}{\partial t} = \nu_i n + D\frac{\partial^2 n}{\partial x^2} \tag{3.7}$$

where n is the electron density, ν_i is the ionisation frequency, D is the diffusion coefficient, x is the dimension across the electrode gap.

At the threshold for the electrical breakdown the temporal change in electron density n is zero so that the number of ionised charges is in balance with the reduced number of carriers due to diffusion. Kihara [3.4] introduced a third term describing the transport of electric charges by drift, as follows:

$$\frac{\partial n}{\partial t} = \nu_i n + D\frac{\partial^2 n}{\partial x^2} - \mu E_0 \cos\omega t \frac{\partial n}{\partial x} \tag{3.8}$$

where μ is the electron mobility and E_0 is the electric field amplitude.

Electrons are absorbed by the electrode, once they are in contact with matter. The boundary condition for the differential equation (3.7) is therefore:

$$n\left(\pm\frac{d}{2}\right) = 0 \tag{3.9}$$

Kihara [3.4] derived an analytical solution for the equation (3.8):

$$\frac{1}{\pi^2}\left[d - \frac{2\mu \mathrm{E}_0}{\omega}\right]^2 \frac{\nu_i}{D} = 1 \tag{3.10}$$

According to equation (3.10), the breakdown criterion depends on the conditions defined by easily-quantifiable parameters (discharge gap, RF frequency, electric field), but also on swarm parameters, which describe the collective properties of electrons in the gas medium and which depend on the mixture. The values for the electron mobility $\mu(E/p)$, anisotropic electron diffusion constant $D(E/p)$, and the first Townsend coefficient $\alpha(E/p)$ were calculated using a numerical Boltzmann function solver BOLSIG [3.5], which is based on algorithms described in [3.6]. The last quantity in equation (3.10), which depends on the E/p ratio, is the ionisation frequency by collisions, ν_i. This frequency can be found from the product of the electron mobility μ, electric field magnitude E and the first Townsend coefficient α [3.7]:

$$\nu_i = \nu_{dr}\alpha = \mu E \alpha \tag{3.11}$$

where ν_{dr} is the electron drift velocity.

The implementation of a numerical evaluation of the breakdown voltage in RF fields, V_{br2} from equation (3.10) is shown in Appendix I. The space between the data points of swarm parameters was linearly interpolated to obtain continuous and stepwise differentiable functions which then allowed one to apply Newton's method for numerical root-finding. The solutions of equation (3.10) as a function of pressure p and spacing d show that the breakdown curves are not a function of pd product but of p and d independently. In figure 3.1 the breakdown voltage as function of pressure p was calculated for nitrogen gas using the criterion (3.10) and the data obtained from BOLSIG software.

For comparison, measurement results for the same conditions are taken from [3.7], and Kihara's model shows good agreement for pressures above 2 hPa in this example. For small gaps or low pressures, the creation of charge carriers due to secondary emission starts to play a non-negligible role in the electrical breakdown process. Kihara recognised that the missing term for the surface ionisation introduces an error for smaller gaps. The value for the third Townsend coefficient γ describing this process is, however, difficult to quantify. The coefficient γ depends on a number of conditions, such as the electrode surface finish, material and reduced electric field E/N [3.8].

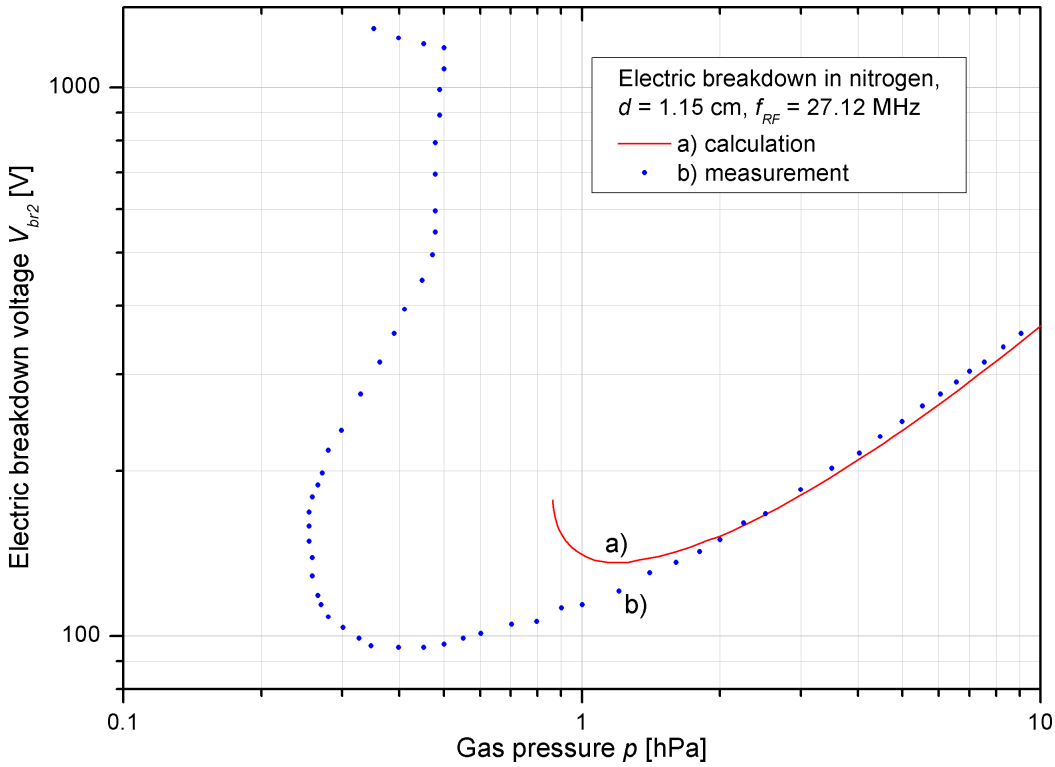

Figure 3.1 Comparison of calculated breakdown voltage in N_2 at 27.12 MHz with measurements taken from [3.7]

As can be seen from figure 3.1, the mechanism for electrical breakdown due to applied RF voltages can be described sufficiently using diffusion theory. An analogy to the breakdown mechanism for applied DC voltages, which is described by the Townsend's criterion, can also be observed at certain RF voltages for sufficiently low pressure-gap products *pd*. In the measurement (dots (b) in figure 3.1), this region can be seen in the top part, where the breakdown curve forms horizontal lines for small gaps and high voltages. Lisovskiy [3.8] referred to these two regions as the diffusion-drift curve and the Paschen curve. However, the gas pressure in typical CO_2 lasers is generally large enough such that the Paschen region of the RF breakdown curve can be neglected.

In spite of the limited accuracy for small pressure-gap products, the strength of the Kihara's method lies in its flexibility. The breakdown curves can be calculated for a given RF frequency and with the data supplied from the BOLSIG code, the electron swarm parameters become available for gas mixtures. In figure 3.2 the breakdown curves are calculated for three different RF excitation frequencies. The CO_2 laser gas mixture is represented by a tertiary He:N_2:CO_2 mixture of 77:13:10, as BOLSIG is limited to three input gas species in a mixture.

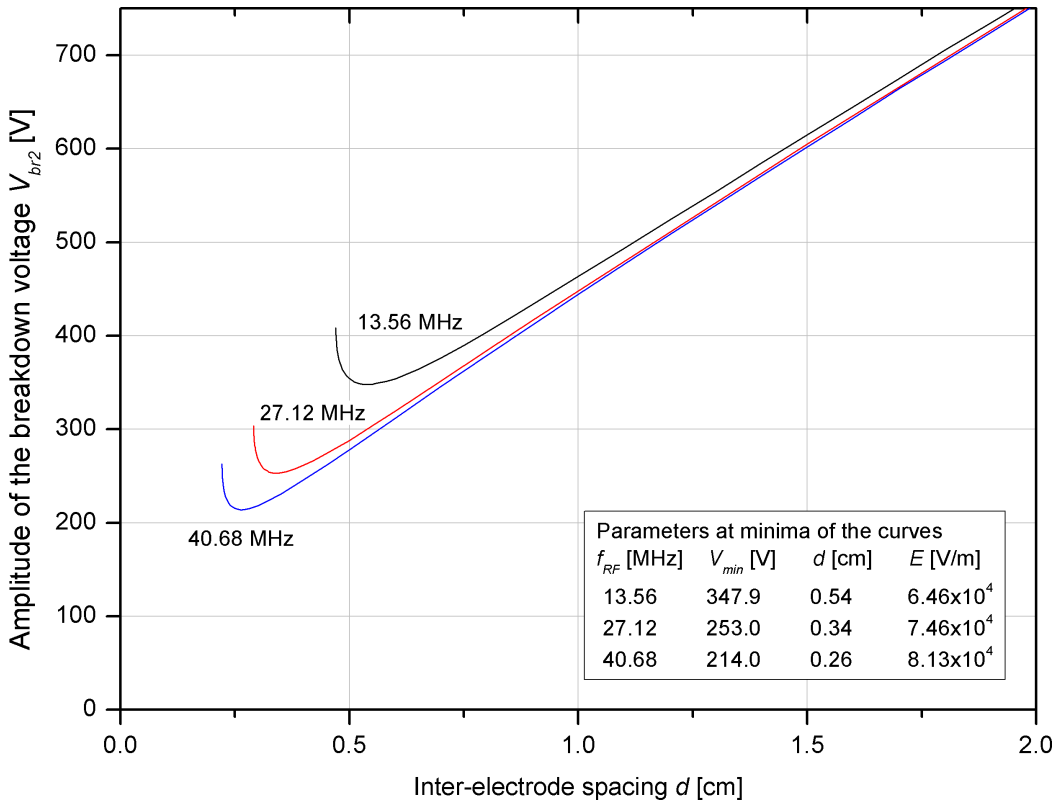

Figure 3.2 Calculated gas breakdown at RF excitation for an approximated CO_2 laser gas mixture 77% He: 13% N_2:10% CO_2 at p = 60 hPa

It can be seen from the figure 3.2, that the minima of the breakdown voltage curves decrease with high RF frequencies. The electrode spacing at the minimum is also smaller with increasing RF frequency. We note that the breakdown curves are limited on the left hand side by a point of singularity, and the difference term in equation (3.10) converges at towards zero this point so that:

$$d_{LHS} = \frac{2\mu E_0}{\omega} \tag{3.12}$$

The amplitude A of the free electron oscillation in a RF field is given by [3.2]:

$$A = \frac{\mu E_0}{\omega} \tag{3.13}$$

The left-most point in the breakdown curves (figures 3.1 and 3.2) occurs when the electrode spacing is twice the oscillation amplitude of free electrons:

$$d_{LHS} = \frac{A}{2} \tag{3.14}$$

The voltage at this point, where the slope of the breakdown voltage curve becomes vertical, is also called the turning point voltage V_t [3.8].

3.2.3 Penning effect by addition of xenon

In the TRUMPF TruCoax laser system two additional gas species are added to the $He:N_2:CO_2$ gas mix, namely, carbon monoxide and xenon. Carbon monoxide does not alter the breakdown characteristics significantly, whereas a small fraction of xenon (of the order of 5%) when added to the gas mixture *both* increases the laser output power and has a substantial impact on the breakdown voltage. The helium atom has a metastable state, with a very long life time of several hours [3.9]:

$$2^3s_1 \rightarrow 1^1s_0 \tag{3.15}$$

An energy of 19.8 eV is released after the electron relaxation via photon radiation. The photon energy is large enough to ionise xenon atoms with an ionisation energy of 12.1 eV:

$$He + Xe \rightarrow He + Xe^+ + e_0 \tag{3.16}$$

Significantly, the breakdown voltage in a He-Xe mixture due to this effect is lower in comparison to that of pure helium or xenon gas. Reflecting this effect, the He-Xe mixture is sometimes described as a "Penning mixture" [3.10]. The model in the BOLSIG code takes into account the ionisation potential of the included gases, which makes the results applicable for Penning-effect calculations as reported, for example in [3.11]. The RF breakdown voltage is shown in figure 3.3 for a varying proportion of helium and xenon. The transition of the breakdown voltage to a minimum can be seen in the graphs as the xenon content is increased to about 6%.

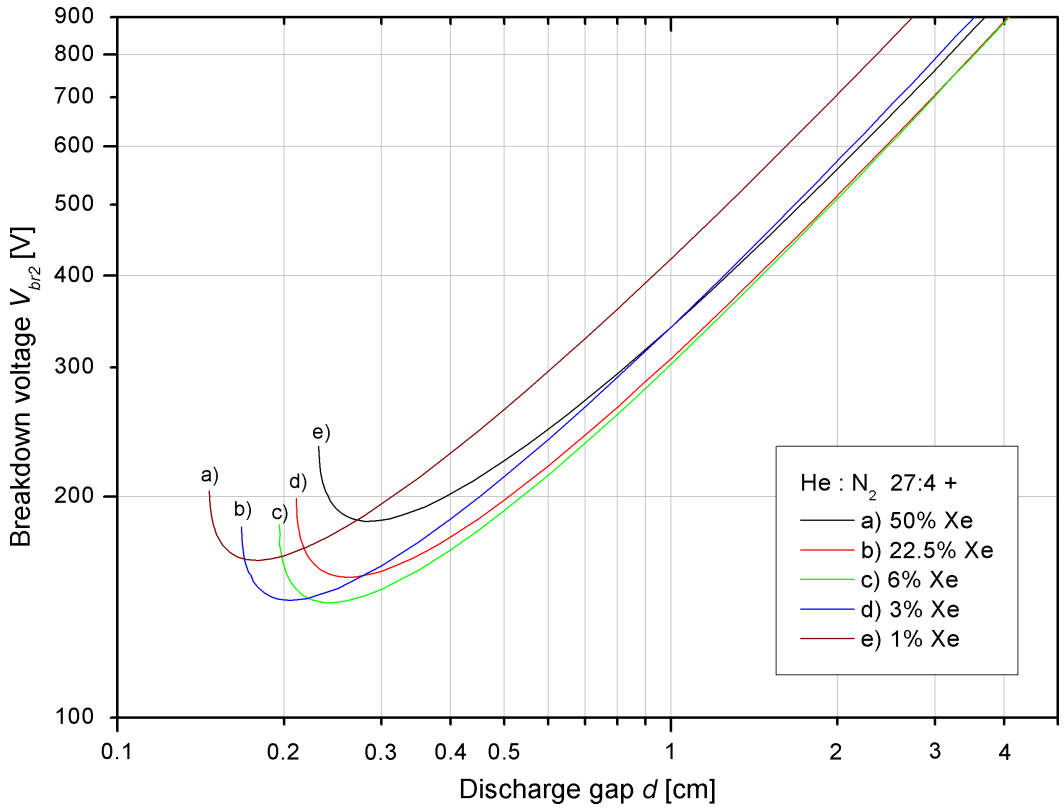

Figure 3.3 Variation of breakdown voltage due to Penning effect, f_{RF} = 27.12 MHz, p = 60 hPa

3.3 Electric Field Distribution as Means to Locate Breakdown Regions

In the analysis presented so far, the electrodes have been considered as flat surfaces with the lateral dimension being much larger than the inter-electrode spacing. The electric field is assumed to be distributed homogeneously between the electrodes with the field gradient directed only towards the electrode surface so that in our discussion so far breakdown has been treated as a one-dimensional phenomenon (see equation (3.7)).

However, electrical breakdown can also be studied for arbitrarily-shaped electrodes, if the electric field is known at each position *E(x,y,z)*. For this more general case, we can turn to the field of electrostatics as described in [3.12].

The Coulomb force, F between two charges q and q' with their location described by space vectors u and u' is:

$$F(x,y,z) = \frac{qq'}{4\pi\varepsilon_0}\frac{u-u'}{|u-u'|^3} \tag{3.17}$$

The electric field E represents the potential Coulomb force acting on a charged particle towards the charge q for an arbitrarily small charge q':

$$E(x, y, z) = \lim_{q' \to 0} \frac{F(x, y, z)}{q} \tag{3.18}$$

It can be shown [3.12] that the gradient of the electric field is the quotient of the charge density ρ and the vacuum permittivity ε_0 (Gauss' law):

$$div(E) = \frac{\rho}{\varepsilon_0} \tag{3.19}$$

The relationship between the electric field E and electric field potential φ is:

$$grad(\varphi) = -E \tag{3.20}$$

Taking divergence on both sides of equation (3.20):

$$div(grad(\varphi)) = div(-E) \tag{3.21}$$

with the annotation:

$$div(grad(\varphi)) \equiv \nabla^2 \varphi \tag{3.22}$$

and the equation (3.19), we arrive at the Poisson's equation:

$$\nabla^2 \varphi = -\frac{\rho}{\varepsilon_0} \tag{3.23}$$

Poisson's equation is the governing differential equation describing the electric potential distribution and (via equation (3.20)), also provides an expression for the electric field distribution. In the absence of electric charges, the equation is further simplified to Laplace's equation:

$$\nabla^2 \varphi = 0 \tag{3.24}$$

The area of interest for the electric field in the case of the RF feed geometry is the space between the electrodes. In the time before discharge ignition, we note that no electric charges are present in this volume. Laplace's equation can now be applied to this situation. The electric field distribution including regions incorporating dielectric materials which are used as electric insulators, are included in the calculation by adding an auxiliary electric displacement field D. For small values of the amplitudes of the electric field E, the displacement vector can be regarded as the product of the electric field E with a scalar number [3.12]:

$$D = \varepsilon_r \varepsilon_0 E \tag{3.25}$$

where ε_r is the relative permittivity and ε_0 is the vacuum permittivity.

By solving equations (3.20) and (3.25) it is possible to find the electric displacement field $D(x, y, z)$. The electric potential φ is calculated as a function of the location system by

numerically calculating the Laplace's equation (3.24) in FEA software (FlexPde [3.13]). The boundary conditions, defined by the electric potential of the live and ground electrodes and the relative permeability ε_r are shown in figure 3.4.

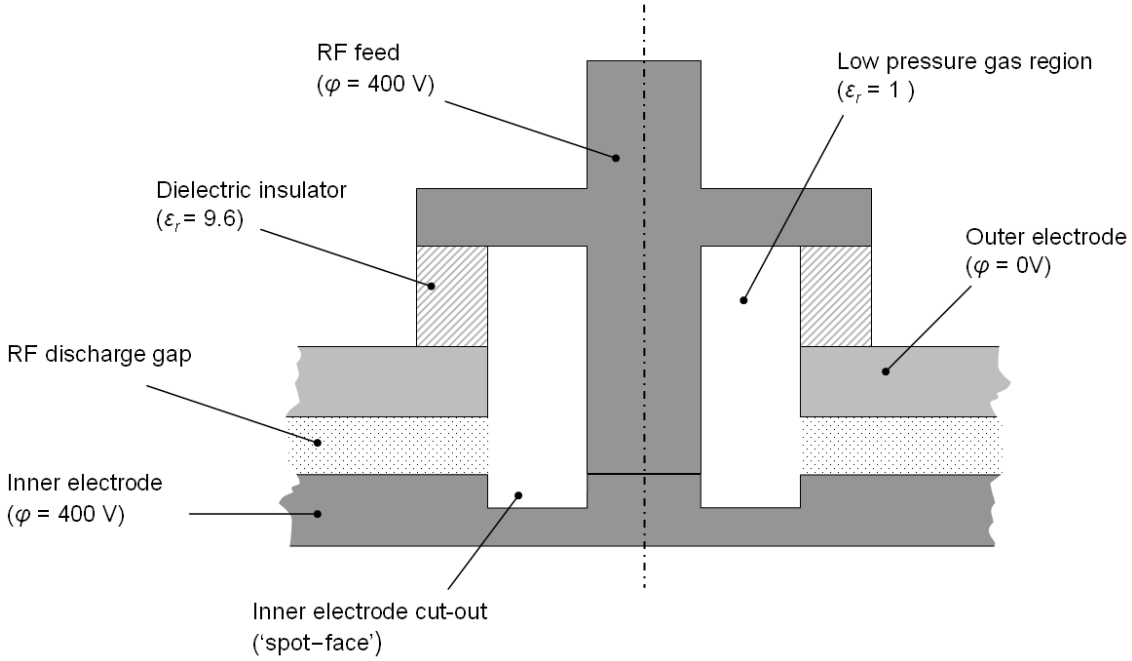

Figure 3.4 Boundary conditions applied for electric field distribution

The calculation is applied to the RF feed geometry as illustrated in figure 3.4. The RF feed assembly consists of a shaft which delivers the input RF power to the inner electrode. The shaft is electrically insulated from the grounded outer electrode by a dielectric insulator ring. Another important feature of the assembly is a machined concentric pocket around the RF feed shaft. This pocket will be referred as the "spot-face" in the subsequent section, where its function is to prevent RF discharge formation by effectively increasing the RF discharge gap.

The coaxial design of the RF feed simplifies the modelling, since it is possible to use a cylindrical coordinate system. Once the electric potential $\varphi(r, y)$ is found for given boundary conditions, the data can be used to determine the direction of the electric or displacement field. An example of the calculated results is shown in figure 3.5. The Coulomb force acts on the charged particles parallel to the electric field lines (blue curves), which run perpendicular to the equipotential lines (red curves). The electrical breakdown occurs along the electric field lines with the shortest path, where the electric

field is the strongest. In the case of figure 3.5 the shortest path is in the RF discharge gap region.

The gas pressure and gas mixture composition are tuned for the discharge gap at the relevant RF excitation frequency so that after the electrical breakdown in the gap, an α-type discharge is established. Once the RF discharge is ignited, the potential on the RF feed is reduced and electrical breakdown is unlikely to occur. However, there is a (non-zero) statistical probability of the ignition process taking place between the RF feed and the grounded outer electrode port. This is the environment in which the goal is to optimise conditions such that the likelihood of electrical breakdown occurring is reduced to as low value as possible.

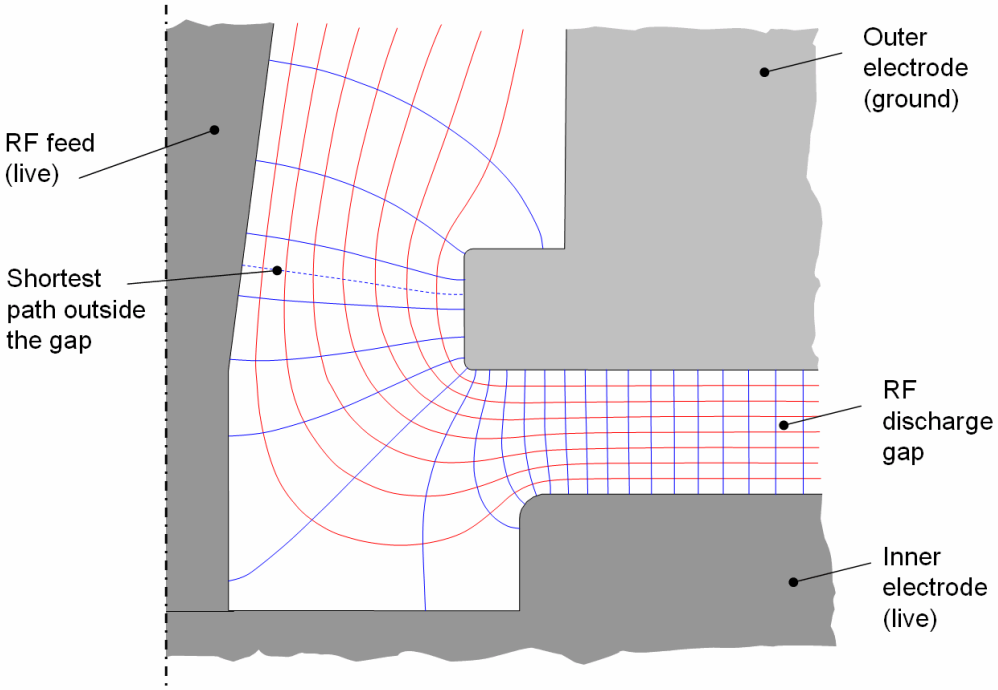

Figure 3.5 Calculated equipotential lines with 50 V spacing (red curves) and the direction of the electric field (blue curves)

The relationship between the electrical breakdown curves calculated in the previous section and the electric potential distribution $\varphi(r, y)$ can be established by integrating the electric potential φ over a path parallel to the electric field lines (blue curves in figure 3.5). A method for obtaining the breakdown voltage and the likely location of electrical breakdown is to find the electric field line with the shortest path outside the RF discharge gap region. The location of the electric field line with the shortest path between the

electrodes is indicated as a dotted curve in figure 3.5. The voltage *V* along this field line can easily be calculated if we integrate the values of electric potential φ. The result is shown in figure 3.6(c) together with the RF breakdown curves for the He:N_2:CO_2 (77:13:10) gas mixture and the He:N_2:Xe mixture (84.5:12:3). It can be assumed that electrical breakdown occurs if the integrated potential curve (voltage curve) crosses the breakdown curve. It can be seen from figure 3.6 how the voltage along the electric field lines compares with the breakdown curves, since breakdown may easily be achieved in the case of the line across the discharge gap (figure 3.6 (c)). In the case of the shortest field line outside the gap (figure 3.6 (d)), the RF breakdown curve for a mixture including xenon is only about 5% larger than the calculated voltage.

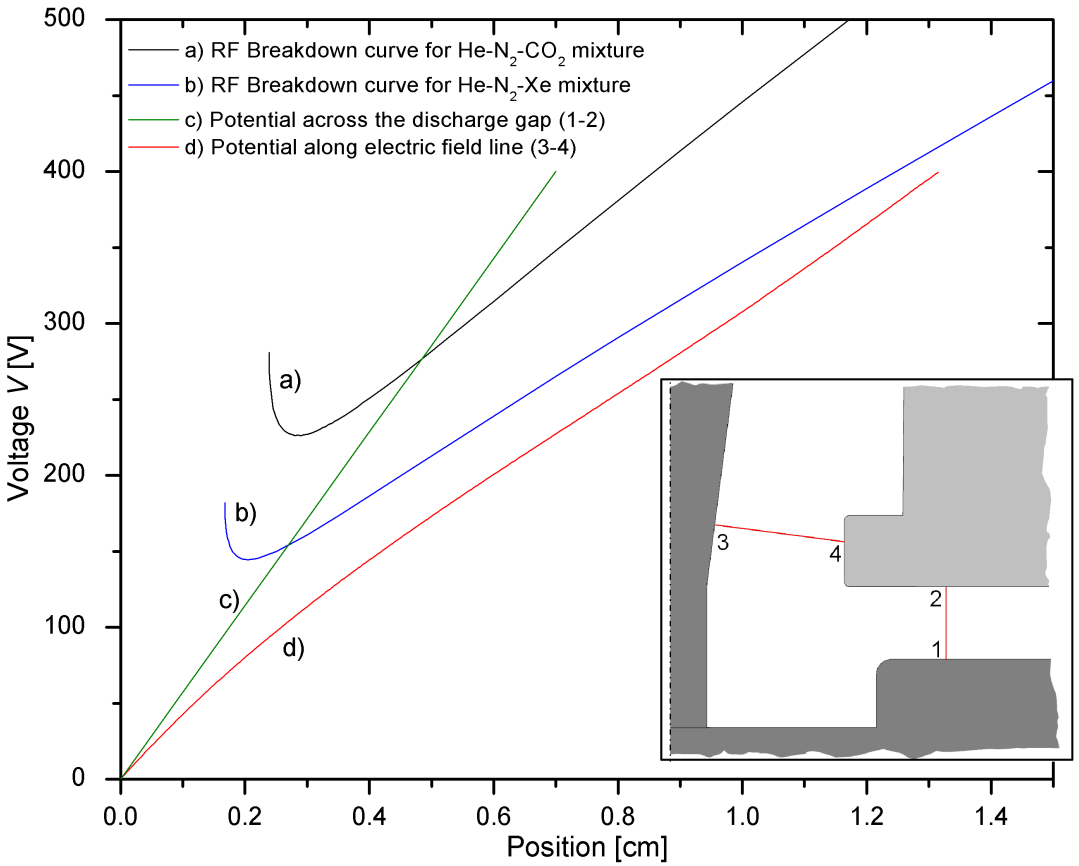

Figure 3.6 RF breakdown curves for two gas mixtures (a) and (b) and integrated electric potential (c) and (d) for evaluation of electric arc occurrence

3.4 Optimization of RF Feed Geometry to Avoid Damage due to Breakdown

3.4.1 RF feed shaft

It was shown in the previous section that the threshold for electrical breakdown outside the discharge gap is not reached according to the evaluation method that was described, but that the threshold is of the same order of magnitude as the voltages reached outside the gap region.

The critical areas of RF feed design were analyzed by plotting the electric field magnitude $|E(r, y)|$, which can be obtained from the electric potential $\varphi(r, y)$ using equation (3.20). The resulting electric field contour plot is shown in figure 3.7(a). The experimental results (see figure 3.7(b)) show that the RF feed shaft was damaged in the region where the electric field exceeds a value of 5×10^4 V/m in the proximity of the feed surface. The identification of this location is also in agreement with the 'short electric field line approach' described in the previous section (figure 3.6).

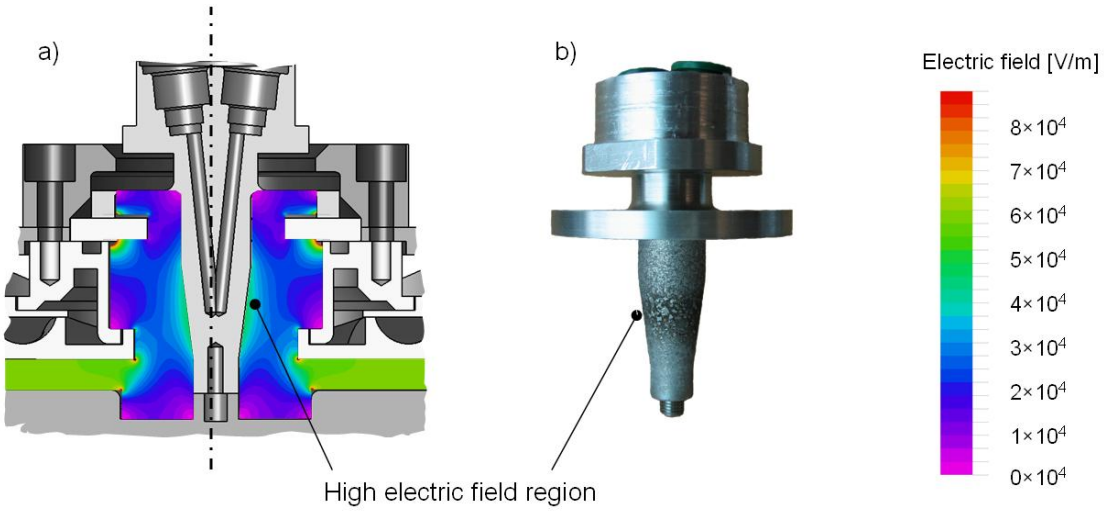

Figure 3.7 Correlation of predicted high electric field region:
a) The electric field contour plot based on Laplace's equation solution
b) The failure mode of the RF feed

The use of field contour plots allows faster assessment of the RF feed design as compared to the method of finding the shortest electric field lines. The configuration of components, such as the shape of the RF feed shaft and the width of the outer electrode opening was modified to find a setup with a larger "safety margin" for electrical breakdown occurrence. An evaluation of this design showed that the potential for

possible improvements turns out to be minimal, because the diameter of the outer electrode opening is limited due to manufacturing constraints. One proposed solution [3.14] is to reduce the gap between the RF feed shaft and the outer electrode opening to only about 200 µm. In this way, the voltage in this narrow gap will be on the far right of the breakdown curve, where the required voltage for breakdown is high. The gas in this narrow gap will also be depleted of free electrons, since the gap is narrower than the free electron oscillation amplitude (equation (3.14)). However, a significant disadvantage of such a design is the required high precision of the RF feed location.

The choice of the RF feed material is another option to reduce the likelihood of electrical breakdown. As was mentioned in section 3.3, the amount of secondary electron emission, which is expressed by the Townsend's γ coefficient, depends on the electrode material. The dependence of the electrode material is shown in table 3.1 for an applied DC voltage in high vacuum, where free charges are only introduced by secondary emission.

The initially-employed aluminium RF feed shaft was replaced by one fabricated in copper, because of the higher value of the breakdown voltage (see table 3.1). Although other metals have higher breakdown voltages compared to copper, cost and machinability considerations favour the use of it. In addition, the higher electrical conductance of copper reduces ohmic losses in the RF power transfer.

Table 3.1 DC breakdown voltage in dependence of electrode materials, d = 75 mm, high vacuum [3.15]

Material	W	Mo	Fe	Ni	Cu	Al	Graphite
Breakdown voltage V_{br} [kV]	87	76	72	72	68	57	52

The breakdown voltage within dielectric insulators (dielectric strength) is much larger than values in gases. The dielectric strength for alumina is 1.34×10^7 V/m for applied DC voltage [3.16], a value which is safe to assume will never be reached in the RF feed assembly. We can use this property to shield the critical area of the RF feed as shown in figure 3.8(b). The area above the insulator is surrounded by air at atmospheric pressure. The breakdown voltage for air at atmospheric pressure is also much larger when compared to the laser gas mixture at a tenth of an atmosphere and can therefore be neglected in design considerations.

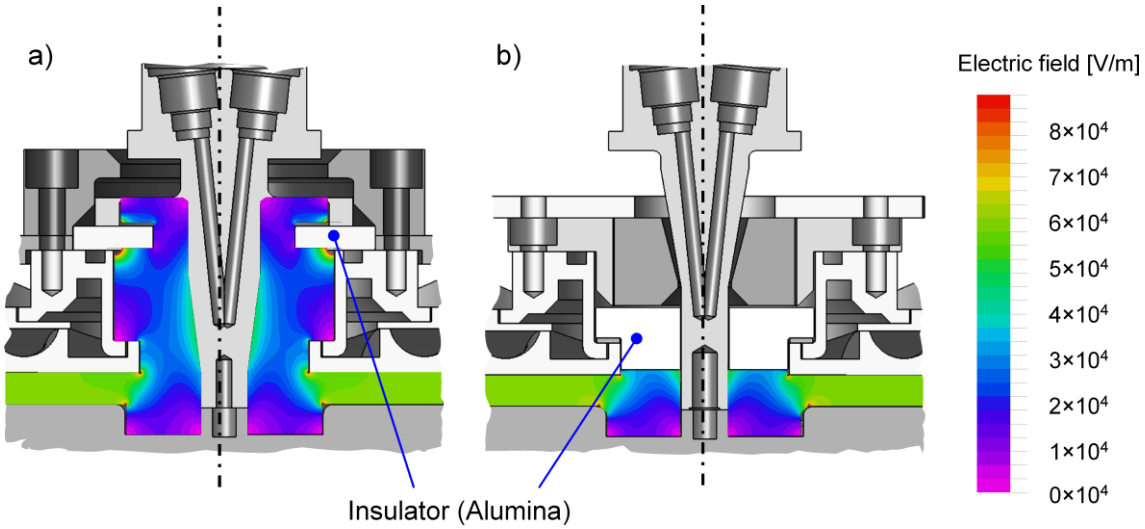

Figure 3.8 Electric field contour plots:
a) initial RF feed design
b) optimised design

Together with the modified RF feed shaft material (changed from aluminium to copper) and the relocation of the dielectric insulator, the occurrence of electrical breakdown outside the RF discharge gap could be reduced drastically. The lifetime of the RF feed assembly was extended from several hours in the initial design to several weeks with the (partially) optimised configuration.

3.4.2 Dielectric insulator

It can be seen in the figure 3.8(b), that the RF feed shaft is still partially surrounded by a region high electric field up to of 5×10^4 V/m, and analyzed RF feed shafts still showed signs of pitting from arcs in this region, as was identified from the contour plots.

To further assess the problem, the electric field distribution was evaluated by performing a numerical solution of Laplace's equation as described in section 3.3, as a function of the geometry of the dielectric insulator. One option is the introduction of a circular step in the dielectric is shown in figure 3.9.

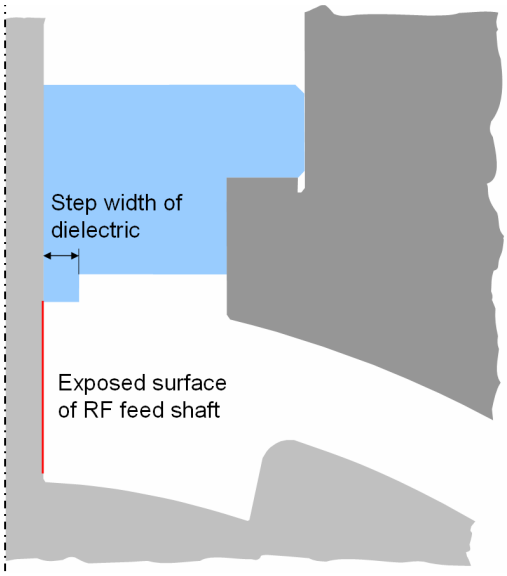

Figure 3.9 Geometry of a dielectric insulator (blue shape) shown in a cross-sectional cut perpendicular to the optical axis

As well as an effective definition of the geometry, a technique to evaluate the calculated data is also important. The numerical calculation delivers a two-dimensional matrix of the electric potential field $\varphi(r, y)$ which needs to be processed to be able to quantify the results.

A proposed optimization method is shown in figure 3.10. The electric field amplitude on the surface of the RF feed shaft, which is indicated by the red line in figure 3.9, is plotted on the *y*-axis. At the same time the dielectric step width is modified in the *x*-axis. The results show that in this scenario there is an optimum with a step width of about 2.5 mm, in which position the electric field on the RF feed shaft is minimal. This procedure can also be re-iterated by fixing the step width and modifying the step height.

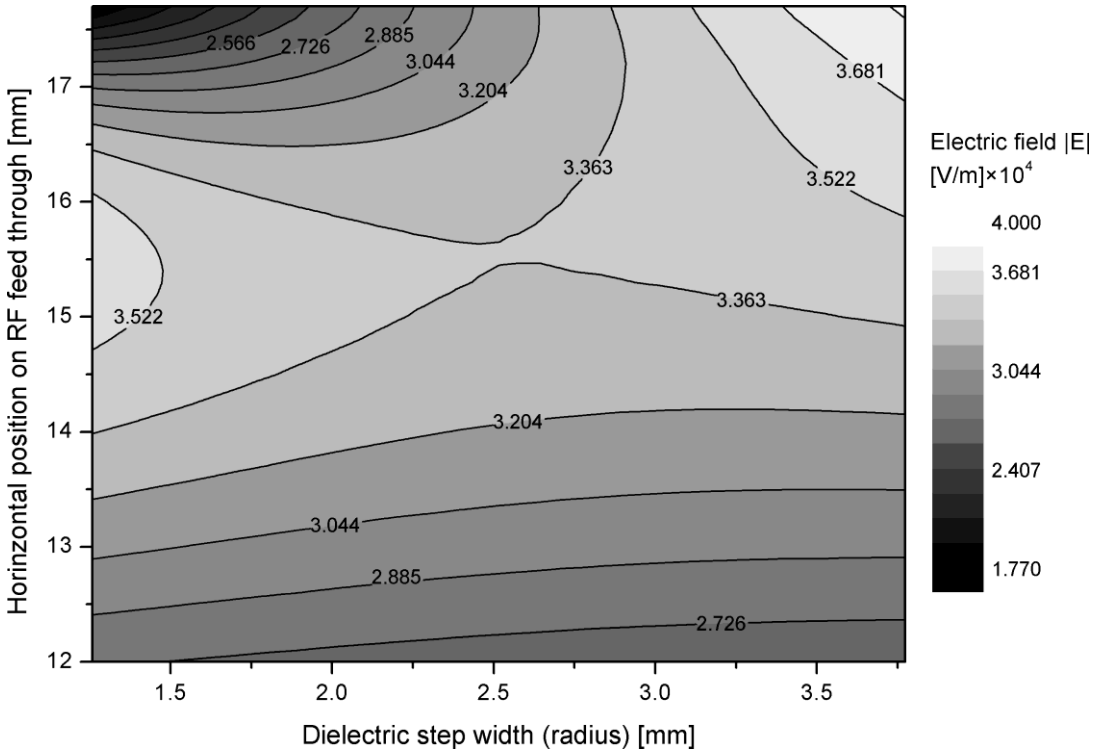

Figure 3.10 Calculated electric field magnitude on the RF feed shaft (*y*-axis) for a dielectric with a step as shown in figure 3.9. The step width is plotted in *x*-axis. The step height is fixed to 2.5 mm.

These calculations show that by modifying the geometry of the dielectric insulator it is possible to redistribute the high electric field from the RF feed shaft towards the insulator. In order to further shift high electric field away from the RF feed shaft, additional features can be added to the dielectric insulator. Examples of calculated electric field magnitude plots are shown in figure 3.11.

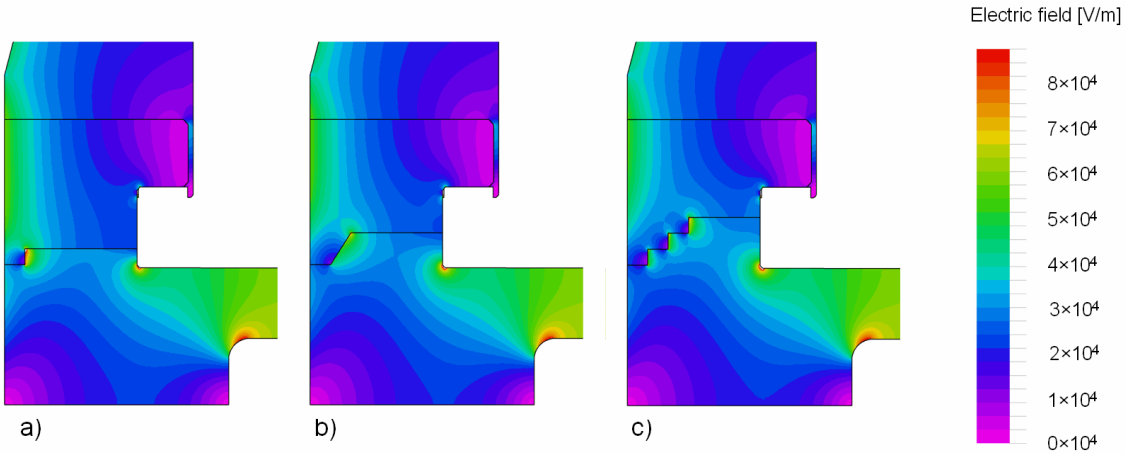

Figure 3.11 Electric field magnitudes for different dielectric insulator geometries: a) one step dielectric, b) conical step dielectric, c) dielectric with three steps

The extent to which the electric field is reduced by adding dielectric steps can be observed by plotting the electric field amplitude on the surface of the RF feed shaft (figure 3.11). Even with a single step, the electric field is lower than the value of 5×10^4 V/m, which was identified earlier as a critical point for observed surface damage by arcing. In figure 3.12 it can also be seen how effectively the dielectric insulator is able to concentrate high electric fields. The electric field on the surface covered by the insulator is over 50% higher than that on the bare surface.

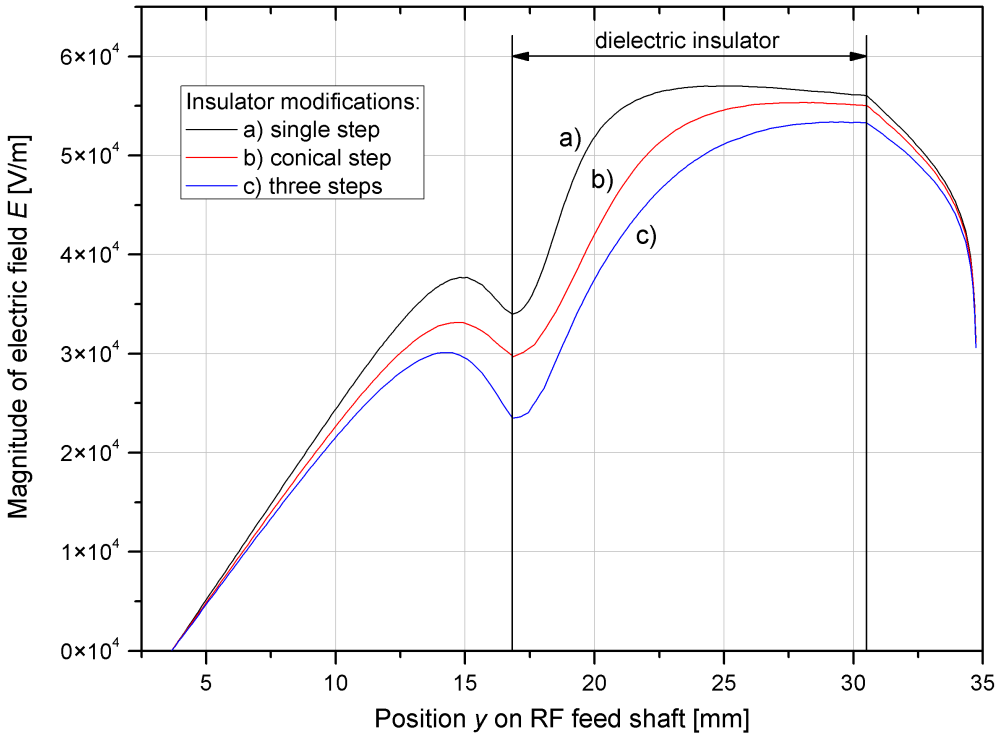

Figure 3.12 Electric field on the RF feed shaft (*x*-axis) for dielectric insulator geometries shown in figure 3.11

In the final RF feed design a single step with a conical chamfer was implemented as shown in figure 3.11(b). The copper RF feed-through the shaft did not show any signs of damage after endurance runs of several weeks with an RF input power loading of 20 kW.

3.5 Optimization of Design to Avoid Localised γ-type Discharge

The RF feed-through assembly, having undergone the described optimization process did not show signs of damage after endurance runs with an RF input power 20 kW. During the operation of the feed-through at increased RF input power of 30 kW another intermittent failure mode was observed. If the discharge cell is switched on and off for

several minutes, a bright localised discharge area occurred in the vicinity of the inner electrode spot-face during discharge ignition (see figure 3.13). The calculated electric field amplitudes showed increased values at the ring surface, where the spot-face blends in to the inner electrode (see red coloured area in figure 3.11). The observed bright discharge flashing is attributed to γ-type discharge formation which is mostly localised both temporally and spatially. However, this type of instability prevents the ignition and spreading of an α-type discharge, a consequence which must be avoided.

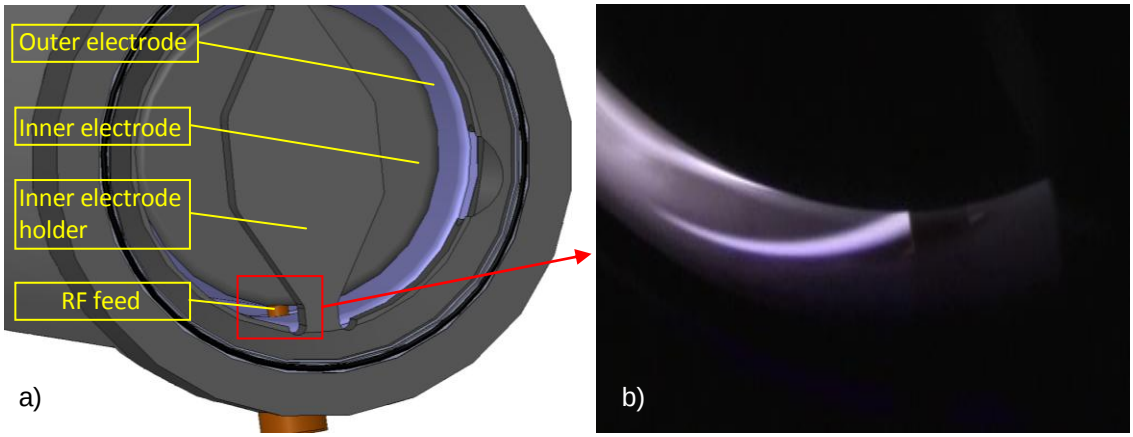

Figure 3.13 Formation of localised γ-type discharge in RF feed region:
a) View at the RF feed at the axicon mirror end using a simplified CAD drawing
b) Photograph of γ-type discharge after 16 ms since RF voltage is turned on

The work undertaken to solve this problem is divided into two sections. The phenomenon of the occurrence of a γ-type RF discharge will be analyzed in the first subsection by studying the longitudinal voltage distribution before and after formation of stable α-type RF discharge. The optimization of the inner electrode geometry in the vicinity of RF feed will be discussed in the second section.

3.5.1 Estimation of longitudinal voltage distribution

As was already described in Chapter 2, transmission line theory has proven to be a useful tool to calculate the voltage distribution in waveguide RF-excited CO_2 lasers. At this frequency and electrode dimensions, the width of the strip-line RF discharge in waveguide lasers is much smaller than the length, making one-dimensional transmission line theory a suitable mathematical description. When applying the one-dimensional theory to the TruCoax laser structure, we should be aware that lateral discharge variation will be neglected. Thus, transmission line theory should not be regarded as a rigorous

tool for calculations of voltage distribution of the TruCoax laser, but the results are expected to provide useful information on observed phenomena.

The complex voltage V and current I as function of propagation distance z are described for a lossy transmission line with harmonic oscillation by a system of two differential equations [3.17]:

$$\frac{dV(z)}{dz} = -(R + j\omega L)I(z) \tag{3.26}$$

$$\frac{dI(z)}{dz} = -(G + j\omega C)V(z) \tag{3.27}$$

where j is the imaginary unit, ω is the circular frequency of the excitation wave. The parameters R and L describe the series resistance and inductance of the transmission line per unit length. The parameters G and C represent the shunt elements describing the conductance and capacitance per unit length respectively.

Initially, the transmission line parameters for the TruCoax laser are not known and so they need to be estimated from impedance measurements. Once defined, the parameters can be inserted into a general solution of equations (3.26) and (3.27) to obtain the standing wave patterns of complex voltage and current distributions. A very similar problem has been described by Engelbrecht *et al.* [3.18].

An electric circuit diagram representing the model of the TruCoax V6 laser is shown in figure 3.14. A shunt inductor in the centre improves the longitudinal voltage homogeneity, consistent with the distributed parallel resonance (DPR) technique described in Chapter 2.

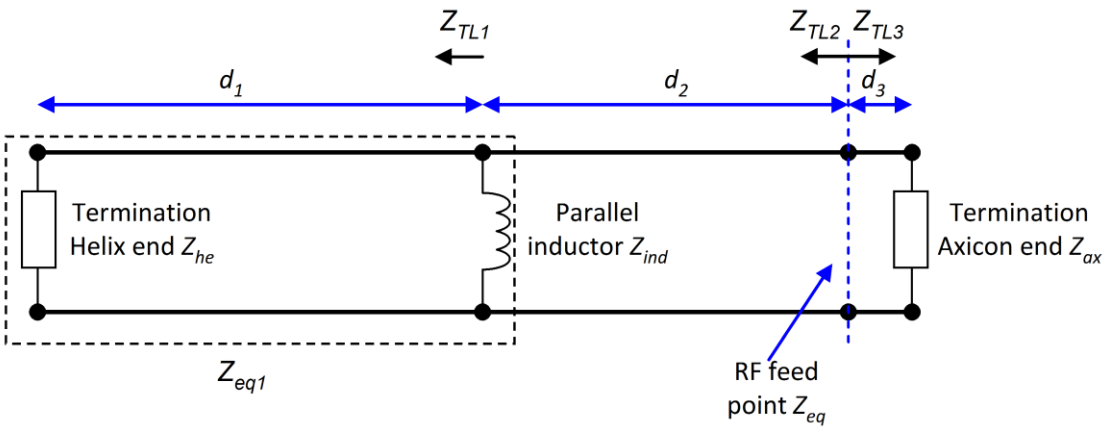

Figure 3.14 Electric circuit representing the transmission line model of the TruCoax resonator

The TruCoax V6 resonator was matched for zero reflected RF power at typical operating condition (30 kW RF input power, 60 hPa fill pressure). The impedance was measured with a vector impedance metre at the RF feed point from the matching circuit side. The complex conjugate of the measurement is the input impedance Z_{eq} to the circuit in figure 3.14. Additionally, the impedances on either end of the electrode structure Z_{he} and Z_{ax} as well as the inductance of the parallel coil Z_{ind} were measured on a disassembled structure.

The equivalent impedance Z_{eq} of the electrical network can be described as a function of the electrical components, but first we have to specify some important transmission line definitions. The characteristic impedance Z_0 of the transmission line is [3.17]:

$$Z_0 = \sqrt{\frac{R + j\omega L}{G + j\omega C}} \tag{3.28}$$

The propagation constant γ, which should not be confused with Townsend's ionisation coefficient (for which the same symbol is traditionally used) is [3.17]:

$$\gamma = \sqrt{(R + j\omega L)(G + j\omega C)} \tag{3.29}$$

The impedance Z_{TL} of a lossy transmission line element of length d terminated with impedance Z_{term} as shown in figure 3.15 is [3.17]:

$$Z_{TL} = Z_0 \frac{Z_{term} + Z_0 \tanh(\gamma d)}{Z_0 + Z_{term} \tanh(\gamma d)} \tag{3.30}$$

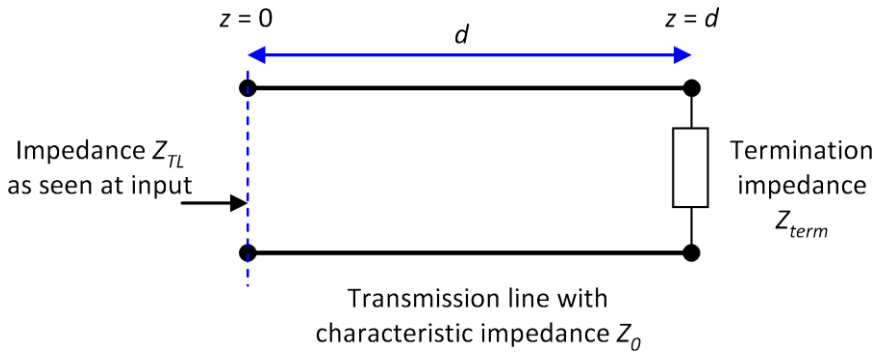

Figure 3.15 Transmission line element of length *d*

We can calculate the impedances Z_{TL1} and Z_{TL3} using equation (3.30):

$$Z_{TL1} = Z_0 \frac{Z_{he} + Z_0 \tanh(\gamma d_1)}{Z_0 + Z_{he} \tanh(\gamma d_1)} \tag{3.31}$$

$$Z_{TL3} = Z_0 \frac{Z_{ax} + Z_0 \tanh(\gamma d_3)}{Z_0 + Z_{ax} \tanh(\gamma d_3)} \tag{3.32}$$

The termination impedance Z_{eq1} of the transmission line 2 can be represented as a parallel circuit of Z_{TL1} and Z_{ind} (see figure 3.14):

$$Z_{eq1} = \frac{1}{\frac{1}{Z_{TL1}} + \frac{1}{Z_{ind}}} \tag{3.33}$$

The impedance Z_{TL2} as seen at the input of transmission line 2 can be found with equations (3.30) and (3.33):

$$Z_{TL2} = Z_0 \frac{Z_{eq1} + Z_0 \tanh(\gamma d_2)}{Z_0 + Z_{eq1} \tanh(\gamma d_2)} \tag{3.34}$$

Finally, we can calculate the equivalent impedance Z_{eq} of the entire network, which consists of Z_{TL2} and Z_{TL3} in parallel:

$$Z_{eq} = \frac{1}{\frac{1}{Z_{TL2}} + \frac{1}{Z_{TL3}}} \tag{3.35}$$

The cross-section of the TruCoax laser can be regarded as a coaxial transmission line. The value for the transmission line inductance L per unit length can be calculated as [3.17]:

$$L = \frac{\mu_0}{2\pi} \ln\left(\frac{b}{a}\right) \tag{3.36}$$

where μ_0 is vacuum permeability, b and a are radii of the outer and inner electrode. The contribution of the RF discharge to inductance is too small to be considered here.

The series resistance R per unit length is a very small number, since the metallic electrode has a large cross-section, so the resistance value R will be set to zero, as was done for other RF excited CO_2 lasers [3.18], [3.19].

The remaining two unknown transmission line parameters C and G were found by adjusting the values, until the deviation from the calculated impedance Z_{eq} in equation (3.35) and the measured input impedance was minimal.

The standing wave voltage function $V(z)$ in a transmission line of length d as shown in figure 3.15 can be derived from basic transmission line equations.
The overall voltage is made up of the forward and backward travelling waves [3.17]:

$$V(z) = V^{+}(z) + V^{-}(z) = V_0^{+}\exp(-\gamma z) + V_0^{-}\exp(\gamma z) \tag{3.37}$$

where superscripts "+" and "-" denote the forward and backward direction respectively.

The reflection coefficient Γ is defined as the ratio of voltages [3.17]:

$$\Gamma(z) = \frac{V^{-}(z)}{V^{+}(z)} \tag{3.38}$$

Note that the letter Γ has no relation to Γ in Townsend's electric breakdown theory (equations (3.4) to (3.6)).

The forward travelling voltage in a transmission line is reflected at a boundary to an impedance *Z*, which is different to the characteristic impendence Z_0 [3.17]:

$$\Gamma(z) = \frac{Z - Z_0}{Z + Z_0} \tag{3.39}$$

Using (3.37) and (3.38):

$$V(z) = V^{+}(z) + \Gamma(z)V^{+}(z) \tag{3.40}$$

Based on equation (3.38), the forward wave in the denominator is taken from (3.37). The reflected wave in the nominator is the forward wave propagated to point *d*, reflected with Γ_{out} at point *d* and propagated backwards by *(z-d)*:

$$\Gamma(z) = \frac{V_0^{+}(z)\exp(-\gamma d)\Gamma_{term}\exp(\gamma(z-d))}{V_0^{+}(z)\exp(-\gamma z)} = \Gamma_{term}\exp\left(2\gamma(z-d)\right) \tag{3.41}$$

where Γ_{term} is the reflection coefficient at termination impedance Z_{term} according to equation (3.38).

From equation (3.40), the voltage at the transmission line input V_{in} is the sum of the forward and backward travelling waves:

$$V_0^{+} + \Gamma_{in}V_0^{+} = V_{in} \tag{3.42}$$

where Γ_{in} is the reflection coefficient at the input of the transmission line. The impedance immediately before entering the transmission line is Z_{in} and the voltage is V_{in}.

By inserting $\Gamma(z)$ from (3.41) and V_0^{+} from (3.42) in (3.40) yields the equation describing the voltage in the transmission line:

$$V(z) = V_0^{+}\exp(-\gamma z) + V_0^{-}\exp\left(\gamma z\right) \tag{3.43}$$

with

$$V_0^+ = \frac{V_{in}}{1+\Gamma_{in}} \tag{3.44}$$

$$V_0^- = \frac{V_{in}}{1+\Gamma_{in}} \exp(-2\gamma d)\Gamma_{term} \tag{3.45}$$

After factoring out the common terms in equation (3.43) we arrive at the equation as the one given for example in [3.18]:

$$V(z) = \frac{V_{in}}{1+\Gamma_{in}} \exp(-\gamma z)(1+\Gamma(Z_{term}) \exp(2\gamma(z-d))) \tag{3.46}$$

The voltage distribution for the entire structure as shown in figure 3.14 can now be calculated by applying the equation (3.33) to each transmission line section with adjustment of values for V_{in}, Z_{in}, Z_{term} and d.

The voltage distribution for the un-ignited state of the RF discharge can be modelled by modifying the transmission line parameters. The shunt capacitance value C becomes the capacitance of a coaxial capacitor with electrode spacing of the TruCoax laser. The shunt conductance G is zero, since there are no conducting charges in the gas in the first approximation, and the parameters L and R are kept the same as for the case before ignition.

In addition to the different transmission line parameters, the power supply delivers RF power in the first 1 to 2 ms due to the transient response of its closed loop control. The increased initial voltage can be measured with an oscilloscope connected to the reflectometer. The increased voltage can be expressed in the model by using a larger voltage magnitude V^+ at the RF feed point.

The results for the calculated transmission line voltages, which correspond to the case before the RF discharge ignition and after a stable α-type discharge has been formed, are plotted in figure 3.16. The results show that the voltage drop from the RF feed point to the termination impedances is much larger for the case of the un-ignited RF discharge. The initial voltage is already high because of the power supply, which can exceed the α- to γ-type discharge transition threshold, whereupon a local region of γ-type discharge in the vicinity of the RF feed can be formed. As another complication, the longitudinal voltage drop of the initial distribution (curve (a) in figure 3.16) hinders the fast spreading of the RF discharge. Also, the localised γ-type discharge can be sustained for a time

longer than the initial voltage spike, as long as the α-type discharge is not formed over the entire length.

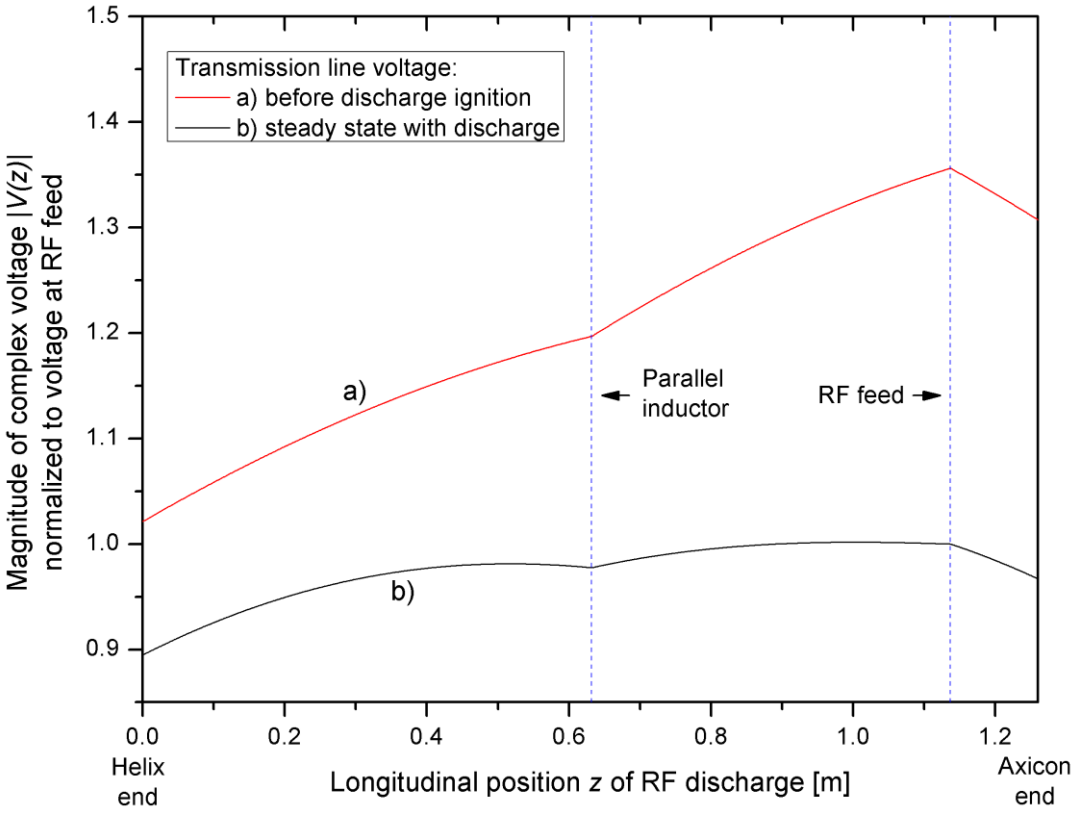

Figure 3.16 Voltage distribution along the RF discharge length

a) before discharge ignition

b) after the α-type is established and stabilised based on data for 60 hPa and 30 kW RF input power

An option to improve the ignition behaviour would be to increase the inductance of the termination impedances from the measured 50 nH to about 200 nH, whereupon the increased voltage at each end would promote faster spreading of the discharge. However, there are design limits with the all-metal termination structure (see section 1.4), which complicates the situation.

Instead, we can improve the design of the inner electrode pocket in the vicinity of the RF feed-through which was previously defined as the "spot-face". Minimization of the high local electric field will be discussed in the next subsection.

3.5.2 Inner electrode design around RF feed-through

The goal here is to avoid γ-type discharge formation by homogenizing the electric field distribution, in a manner conceptually-similar to the design of Rogowski profile electrodes [3.20] which are frequently used in TEA lasers. In the intermediate step, a chamfer and a larger radius can be machined to the spot-face. A more desirable spot-face design with the geometry of a constantly decreasing radius of curvature starting out from a flat surface on the inner electrode and reaching a final curvature in the bottom of the spot-face. The radius of curvature R of such a curve is a function of its length s:

$$R = \frac{const}{s} \tag{3.47}$$

The geometrical shape formed by this function has many applications and is described as a 'clothoid' or 'Euler spiral'. In the field of optics this function is referred to as a Cornu spiral. The shape can be calculated in the parametric form by using the Fresnel integrals [3.21]:

$$C(u) = \int_0^u \cos\left(\frac{1}{2}\pi x^2\right) dx \tag{3.48}$$

$$S(u) = \int_0^u \sin\left(\frac{1}{2}\pi x^2\right) dx \tag{3.49}$$

with x being an auxiliary integrand variable and u the parameter variable, u = [0, 1.25].

By normalizing and scaling we can calculate the coordinates x and y of a Cornu spiral as a function of the parameter u:

$$x(u) = \left(1 - \frac{C\left(u\sqrt{\frac{2}{\pi}}\right)}{C\left(1.25\sqrt{\frac{2}{\pi}}\right)}\right) L_x \tag{3.50}$$

$$y(u) = \left(1 - \frac{S\left(u\sqrt{\frac{2}{\pi}}\right)}{S\left(1.25\sqrt{\frac{2}{\pi}}\right)}\right) L_y \tag{3.51}$$

where L_x and L_y denote the dimensions (width and height) of the spiral.

Three spot-face geometries are compared in figure 3.17, where we also show the contour plots of the electric field magnitude as well as the equipotential line plots. The

equipotential lines help to visualise the effect of homogenization of the electric field by using smooth transitions in the electrode geometry.

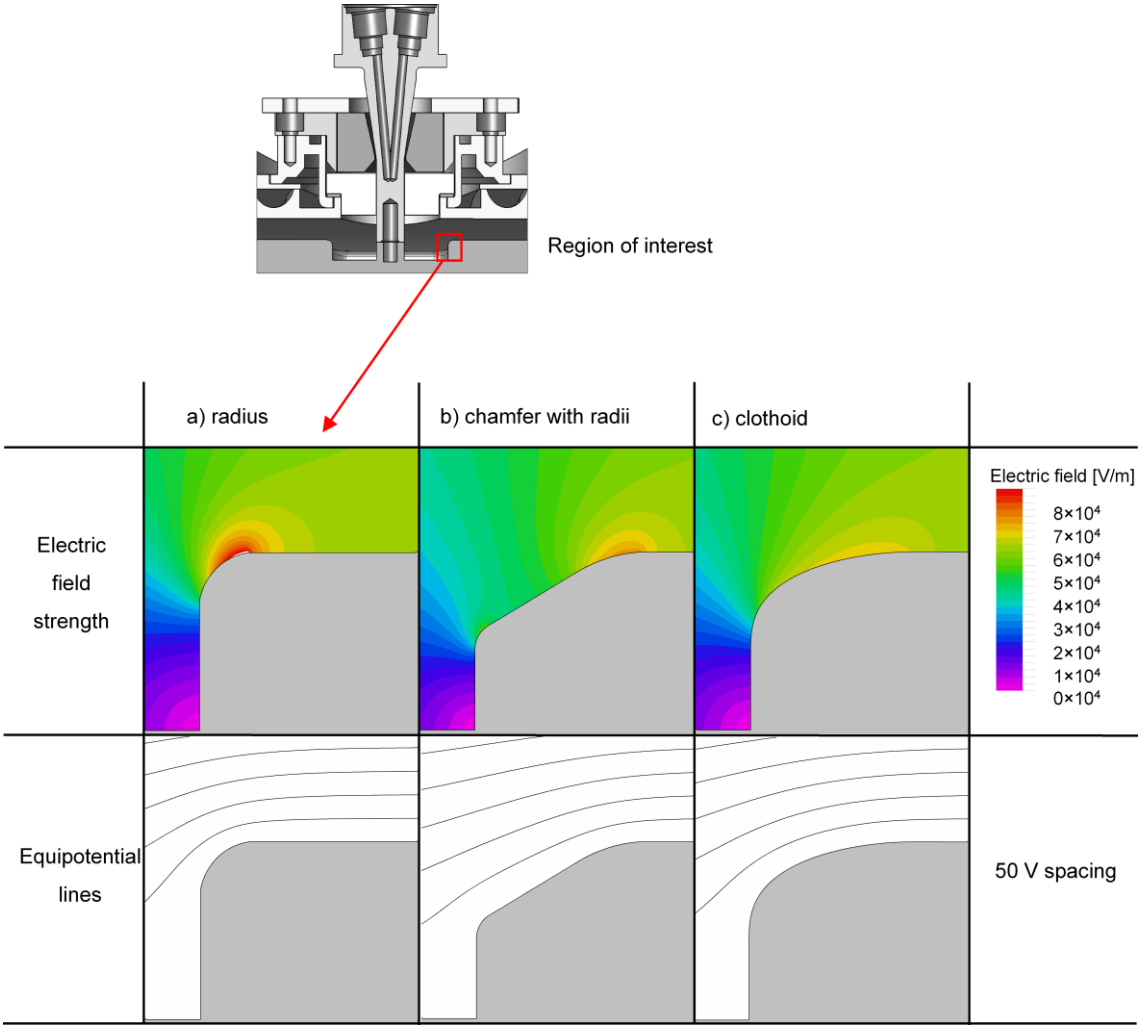

Figure 3.17 Electric field amplitude in the first row and equipotential lines in the second row for different spot-face geometries:
a) initial design with a radius
b) chamfer and radii
c) clothoid shape

The electric field amplitude on the path parallel to the inner electrode surface is plotted in figure 3.18. The peak electric field found in the spot-face with a radius could be avoided in the clothoid-shaped design.

This geometry was implemented in the TruCoax design and successfully tested in the 30 kW version of the laser.

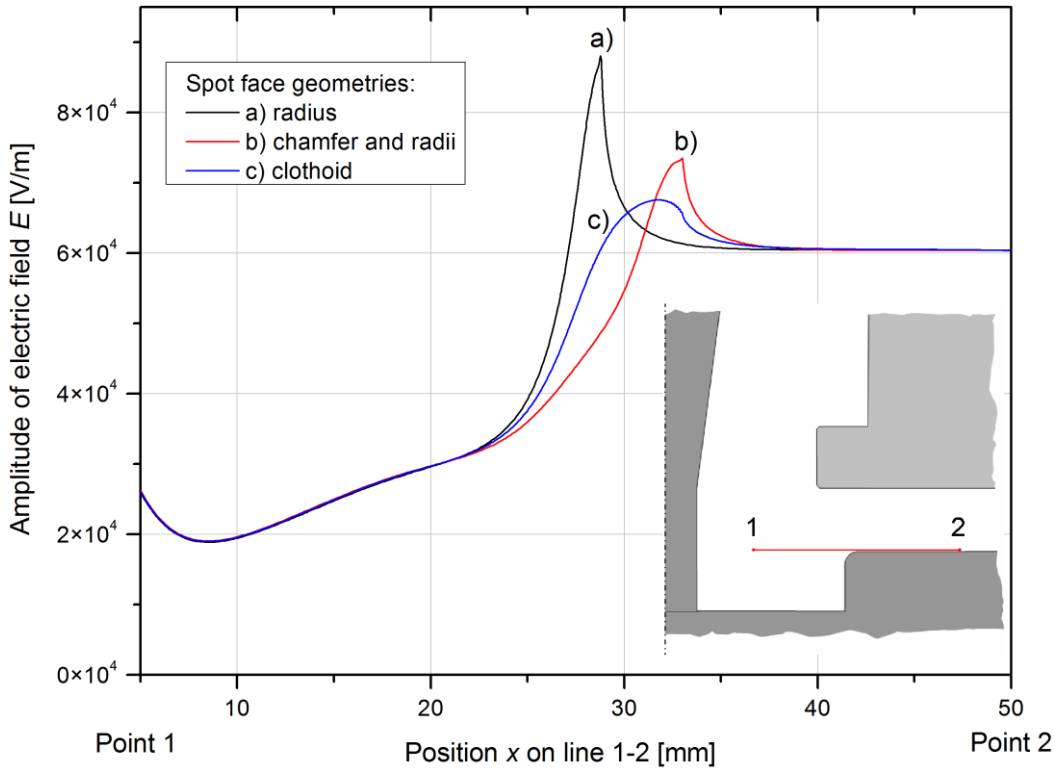

Figure 3.18 Comparison of the electric field amplitudes

3.6 Summary

Breakdown curves are calculated for typical CO_2 laser gas mixtures with applied RF voltages. A procedure based on a calculation of the Laplace's equation is demonstrated for the optimization of RF feed geometry so as to avoid electrical breakdown. A modification of this design which includes changes to the dielectric insulator shape, its location and the spot-face geometry is then developed.

A new design was then proposed and has been implemented enabling stable RF power delivery. The life time of the feed-through components, which were subject to concern, is now *not* a limiting factor in the final design. In the latter work the voltage distribution of the entire electrode design can be taken into consideration in the cold case and in the case of a fully-developed plasma. The location of the RF feed and its design can be further improved to enable easier ignition and lateral spreading of α-type discharge in the inter-electrode space.

3.7 References

[3.1] J. S. Townsend "The theory of ionization of gases by collision", Constable & Company, London (1910)

[3.2] Yu.P. Raizer "Gas discharge physics", Springer, ISBN 3-540-19462-2 (1997)

[3.3] S. C. Brown, A. D. MacDonald "Limits for the diffusion theory of high frequency gas discharge breakdown ", Phys. Rev., vol. 76, pp. 1629-1633 (1949)

[3.4] T. Kihara "The mathematical theory of electrical discharges in gases", Rev. Mod. Phys., vol. 24, pp. 45-61 (1952)

[3.5] BOLSIG, "Electron Boltzmann equation solver", version 1.05, CPAT Toulouse & Kinema Software (1996)

[3.6] L. C. Pitchford, J. P. Boeuf, W. L Morgan "User-friendly Boltzmann code for electrons in weakly ionized gases", IEEE Intl. Conf. on Plasma Science, Boston (1996)

[3.7] V. Lisovskiy, J. - P. Booth, K. Landry, D. Douai, V. Cassagne, V. Yegorenkov "Similarity law for RF breakdown", Eur. Phys. Lett., vol. 82, p. 15001 (2008)

[3.8] V. A. Lisovskiy, V. D. Yegorenkov "RF breakdown of low-pressure gas and a novel method for determination of electron-drift velocities in gases", J. Phys. D: Appl. Phys., vol. 31, pp. 3349-3357 (1998)

[3.9] H. W. Moos, J. R. Woodsworth "Observation of the forbidden $2^3S_1 \rightarrow 1^1S_0$ spontaneous emission line from helium and measurement of the transition rate", Phys, Rev. Lett., vol. 30, pp. 775-778 (1973)

[3.10] G. Veronis, U. S. Inan, V. P. Pasko "Fundamental properties of inert gas mixtures for plasma display panels", IEEE Trans. Plas. Sci., vol. 28, pp. 1271-1279 (2000)

[3.11] O. B. Postel, M. A. Cappelli "Parametric study of the vacuum ultraviolet emission and electrical characteristics of a He-Xe microdischarge", J. Appl. Phys., vol. 89, pp. 4719-4726 (2001)

[3.12] B. Thidé "Electromagnetic field theory", Dover Publications, ISBN 0-486-4773-2 (2011)

[3.13] FlexPDE, "A flexible solution system for partial differential equations", version 6.14, PDE Solutions Inc. (2010)

[3.14] F. J. Villarreal-Saucedo, J. F. Monjardin-Lopez, P. Daniel, J. Deile, S. Sumrain, V. Granson "RF-excited laser assembly", US patent application publication US2012/0106586 A1 (2012)

[3.15] V. Yu. Ushakov “Insulation of high voltage equipment”, Springer Berlin, ISBN 3-540-20729-5 (2004)

[3.16] D. R. Lide “CRC Handbook of chemistry and physics, 85th edition”, CRC Press, ISBN 0-849-304857 (2004)

[3.17] D. K. Cheng “Field and wave electromagnetics”, Addison-Wesley, 2nd edition, ISBN 0-201-01239-1 (1983)

[3.18] R. Engelbrecht, R. Schulz, G. Seibert, J. Hagen, L.-P. Schmidt “Gas discharge impedance and transmission line voltages in a RF excited CO_2 slab laser”, Frequenz, vol. 59, pp. 154-157 (2005)

[3.19] A. Rauf, Bingxin Zhang, Jianguo Xin “Longitudinal power distribution and corresponding temperature distribution in a RF waveguide CO_2 laser”, Piers Online, vol. 2, pp. 619-623 (2006)

[3.20] J. A. Harrison “A computer study of uniform-field electrodes”, Brit. J. Appl. Phys., vol. 18, pp. 1617-1627 (1967)

[3.21] E. Hecht “Optics”, Addison Wesley San Francisco, ISBN 0-321-18878-0 (2002)

Chapter 4

ACOUSTIC RESONANCES IN THE LASER VACUUM VESSEL

4.1 Introduction

In laser applications such as sheet metal cutting, accurate control of the power delivered is mandatory in order to obtain high quality cuts over a larger range of material thicknesses and cutting speeds. When using RF excited lasers this is achieved by operating the laser in pulse mode at frequencies faster than the thermal response time of the material being treated, which is usually in the range of kilohertz. In this way, the need to vary RF impedance matching conditions is minimised, allowing a fixed matching circuit. However, the repetitive pulsing of the laser discharge can excite acoustic waves in the medium, created by gas heating following RF discharge ignition. Depending on the mechanical enclosure, these acoustic waves can add up to form standing waves. The consequent spatial pressure variation may have detrimental effects on laser operation including power loss, discharge length shrinkage or even electrode surface damage by arc breakdown in the ionisation phase.

The aim of this work has been to establish a model of the TRUMPF TruCoax laser gas chamber acting as an acoustic resonator. Once the values of resonant frequencies as well as their relative severity are known, we can define a set of so-called forbidden regions for pulsed laser operation, which avoid such resonances.

The chapter is organised into several sections. After describing fundamental acoustic theory in the first part, a finite element model will be introduced. The third section contains the results of calculated standing wave frequencies compared with measurement results as well as a map of standing wave severity in the duty cycle – frequency operational space. The final section provides an overview of methods to counter acoustic resonances in the TRUMPF TruCoax laser.

4.2 Theoretical Background

4.2.1 Acoustic wave equation

The derivation of the Acoustic Wave Equation, which plays a central role in understanding the acoustic phenomena, is the starting point of textbooks on the subject, such as [4.1], [4.2]. The acoustic wave is described in terms of a small perturbation of the known state of a fluid with pressure P_0 and density ρ_0. In order to satisfy the small perturbation approach, the following conditions have to be met: a) values of unperturbed quantities are known, b) the perturbation is small compared to unperturbed values, and c) no temperature gradient is introduced into the system, i.e. we assume a strictly adiabatic process. By following the fundamental physical laws of conservation of mass, momentum, energy, and the equation of state, four equations are set, which, when combined define the state of the fluid in three dimensional spatial coordinates and time. The acoustic wave equation in Cartesian coordinate system is:

$$\frac{\partial^2 p}{\partial t^2} = \frac{1}{c^2}\nabla^2 p \tag{4.1}$$

where c is the speed of sound and $p = P\text{-}P_0$ is the relative pressure. The acoustic wave can alternatively be also represented by other fluid quantities, for example the particle velocity u, the particle displacement ξ, or the density ρ. The specific quantity to be used can be chosen depending on the problem definition. Once the solution of any quantity is found, the result can be converted to other quantities.

4.2.2 Helmholtz equation

Assuming that the variable $p(x,y,z,t)$ can be separated into two parts, where the part Ψ is only dependent on spatial coordinates and the time dependent part has the form of complex trigonometric function, we can write:

$$p(x,y,z,t) = \Psi(x,y,z)\exp(i\omega t) \tag{4.2}$$

Inserting equation (4.2) into (4.1) allows us to eliminate the time-dependent term and we arrive at an ordinary differential equation, which is called the Helmholtz equation:

$$\nabla^2\Psi + k^2\Psi = 0 \tag{4.3}$$

where the wave number k is the speed of sound c divided by the circular frequency ω:

$$k = \frac{c}{\omega} \tag{4.4}$$

Analytical solutions of the Helmholtz Equation can be found in textbooks for simple cases. For example we can calculate solutions for standing waves in one dimension in a system of length L. One general solution of equation (4.3) in one dimension is [4.3]:

$$\Psi(x) = A\exp\left[j(\omega t - kx)\right] + B\exp\left[j(\omega t + kx)\right] \tag{4.5}$$

where the two summands describe two one-dimensional waves travelling in opposite direction. Coefficients A, B are the amplitudes of these waves and j is the imaginary unit.

If we substitute Ψ with particle velocity u, we are able to define the boundary conditions for the standing wave:

$$u(0) = 0 \tag{4.6}$$

$$u(L) = 0 \tag{4.7}$$

Inserting equations (4.6) and (4.7) in (4.5) delivers two equations, from which A and B can be determined. After some manipulation we arrive at

$$\frac{1}{\exp\left[jkL\right]} - \exp\left[jkL\right] = 0 \tag{4.8}$$

which yields the following expression for the circular frequency ω of the standing wave:

$$\omega_n = c\pi\frac{n}{L} \tag{4.9}$$

where c is the speed of sound and n is an integer indicating the order of the mode.

An equation for resonances in three-dimensional Cartesian coordinate system takes a similar form for a rectangular cuboid with edge lengths L_x, L_y and L_z [4.1]:

$$\omega_{n,l,m} = c\pi\sqrt{\left(\frac{n}{L_x}\right)^2 + \left(\frac{l}{L_y}\right)^2 + \left(\frac{m}{L_z}\right)^2} \tag{4.10}$$

Analytical solutions can be found for simple geometrical shapes such as a cylinder or a sphere if the Helmholtz equation is transformed to the corresponding coordinate system.

4.2.3 Speed of sound in gas mixtures

As was shown in the previous section, knowledge of the speed of sound creates a link between the eigenmodes of an acoustic cavity and the actual resonant frequency. For an ideal gas the speed of sound can be expressed as [4.1]:

$$c = \sqrt{\gamma\ rT} \tag{4.11}$$

where γ is the specific heat ratio, r is the specific gas constant and T is the temperature. According to equation (4.11), the speed of sound is not dependent on the pressure. Note that the specific gas constant r is the gas constant R divided by the molar mass M of the gas species:

$$r = \frac{R}{M} \tag{4.12}$$

The specific heat capacity for constant pressure c_p divided by the specific heat capacity for constant volume c_v yields the specific heat ratio γ as follows:

$$\gamma = \frac{c_p}{c_v} \tag{4.13}$$

The relationship between the specific heat capacities for an ideal gas is given by [4.4]:

$$c_p = c_v + R \tag{4.14}$$

It can be shown that the specific heat capacity can also be expressed in terms of the number of degrees of freedom f of a molecule [4.4]:

$$c_v = \frac{f}{2} R \tag{4.15}$$

The specific heat ratio γ becomes a simple function of the number of degrees of freedom f from the equations (4.13), (4.14) and (4.15) as follows:

$$\gamma = \frac{f+2}{f} \tag{4.16}$$

Monatomic molecules have three degrees of freedom for translation in *x*-, *y*- and *z*-axes. Additional degrees of freedom appear in polyatomic molecules due to rotation and vibration. The vibrational energy levels are usually higher than the kinetic energy of molecules at room temperature. These energy levels are said to be "frozen out". The figure 4.1 compares the specific heat ratio of gases found in the gas mixture of the TruCoax laser with the measured values provided by NIST Webbook [4.6]. The graphs

show that the specific heat ratio based on equation (4.16) is decreasing in accuracy for more complex molecules and for higher temperatures.

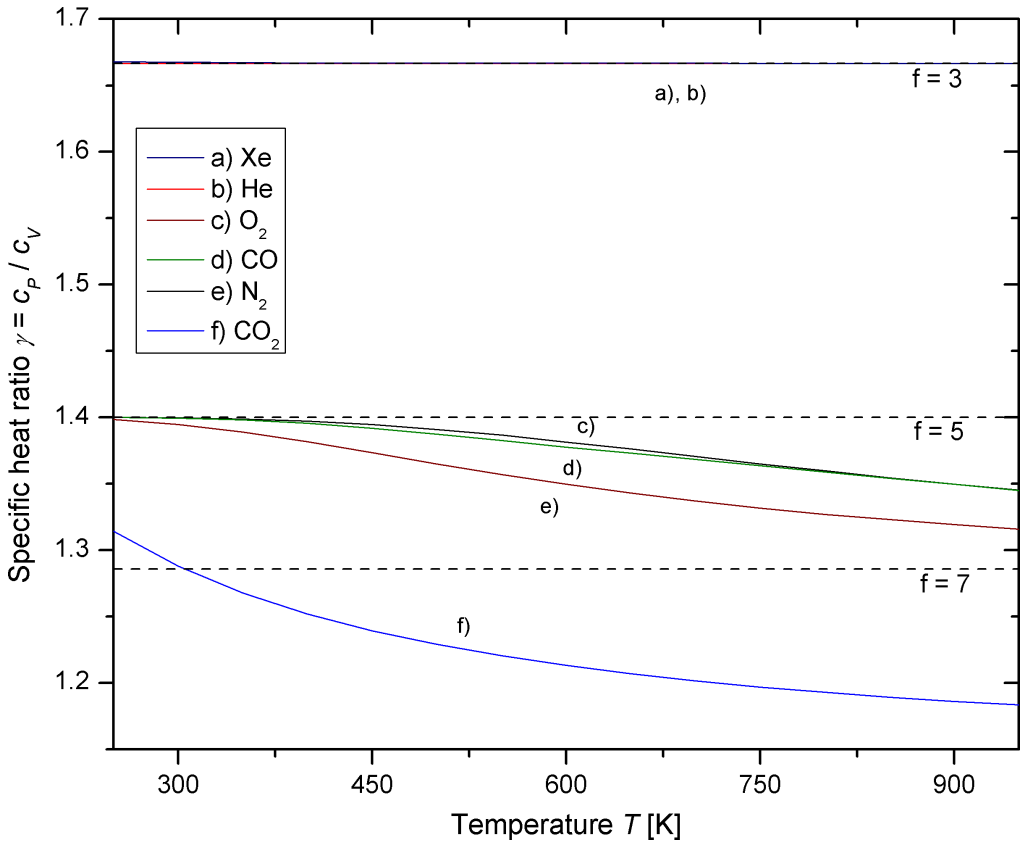

Figure 4.1 Specific heat ratio γ in dependence of temperature at pressure of 75 hPa [4.6]. Dashed lines represent the heat ratios based on degrees of freedom for monatomic ($f = 3$), diatomic ($f = 5$) and triatomic molecules ($f = 7$).

The gas mixture composition of n gas species can be described by the mol fraction x_i of each species, so that:

$$\sum_{i=1}^{n} x_i = 1 \tag{4.17}$$

The specific heat ratio of the mixture γ_{mix} is [4.7]:

$$\gamma_{mix} = \sum_i x_i \gamma_i \tag{4.18}$$

The gas mixture of the TruCoax laser is dominated by monatomic (77%) and diatomic gases (18%). The calculated γ_{mix} using the equation (4.18) is for this reason a good approximation for this mixture. The deviation of the results is less than 1% compared to a calculation based on measurement data from [4.6].

The specific gas constant of the mixture r_{mix} is calculated in a manner analogous to equation (4.18) [4.7]:

$$r_{mix} = R\sum_i \frac{x_i}{M_i} \tag{4.19}$$

where R = 8.314 J/molK is the gas constant, M_i is the molar mass of gas species i.

The speed of sound in air can be computed based on the approach described here. Knowledge of the speed of sound in air is of interest for various applications and has been studied extensively by many workers. Bohn [4.5], for example, derived and verified an equation of the speed of sound as a function of temperature T and relative humidity RH:

$$c_{air} = 331.45\frac{m}{s}\sqrt{\frac{T}{273}}\left[4.5513\sqrt{\frac{7+h}{(29-11h)(5+h)}}\right] \tag{4.20}$$

In equation (4.20), h is defined as:

$$h = RH \cdot \frac{p_{H_2O}(T)}{p_{air}} \tag{4.21}$$

The vapour pressure p_{H2O} as a function of temperature can be found from an experimental data fit in the form [4.8]:

$$p_{H_20}(T) = p_c \exp\left[\frac{T_c}{T}\sum_{j=1}^{6}\left(A_i\left(1-\frac{T}{T_c}\right)^{B_j}\right)\right] \tag{4.22}$$

where the coefficients A_j, B_j, T_c and p_c are summarised in the table 4.1.

Table 4.1 Coefficients for the vapour pressure calculation using equation (4.22) [4.8]

A_1	A_2	A_3	A_4	A_5	A_6	p_c
-7.85951783	1.84408259	-11.7866497	22.68074011	-15.9618719	1.80122502	22.064 MPa
B_1	B_2	B_3	B_4	B_5	B_6	T_c
1	1.5	3	3.5	4	7.5	647.096 K

4.2.4 Helmholtz resonator

An acoustic device made of a volume V connected with its surroundings via a tube with cross section A as shown in figure 4.2(a) produces a sound wave of a specific frequency f_H once air is blown into the opening. This setup is called the Helmholtz resonator.

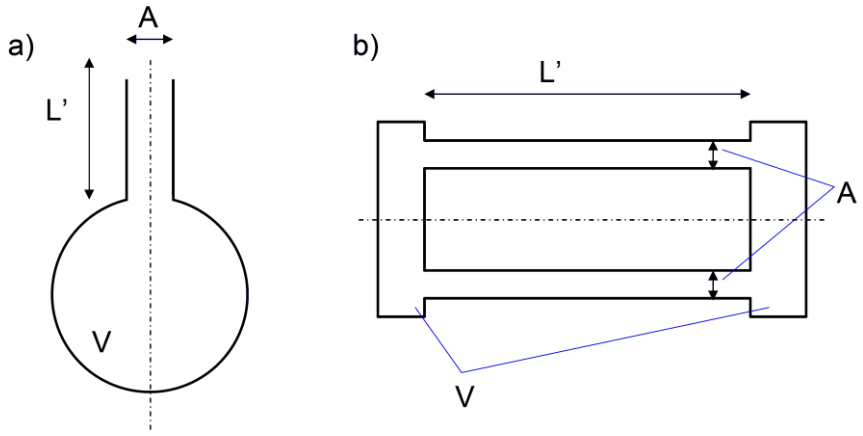

Figure 4.2 a) Geometry of the Helmholtz resonator
b) Simplified cross-sectional cut through the TruCoax resonator

It can be shown [4.1] that the differential equation for the displacement ξ of the gas in the neck of the resonator can be written as:

$$\rho_0 L' \frac{\partial^2 \xi}{\partial t^2} + \frac{\rho_0 c k^2 A}{2\pi} \frac{\partial \xi}{\partial t} + \frac{\rho_0 c^2 A}{V} \xi = P \exp(j\omega t) \tag{4.23}$$

where ρ_0 is the unperturbed gas density, c is the speed of sound and P is the pressure amplitude of the excitation wave. The equation (4.23) shows that the Helmholtz resonator is the acoustical equivalent to driven oscillator in mechanics or an RLC circuit in electrical engineering. In the Helmholtz resonator case the kinetic energy of the gas in the neck is transformed into potential energy by compression of the gas in the volume V. The solution for the resonant frequency f_H of the system is:

$$f_H = \frac{c}{2\pi} \sqrt{\frac{A}{L'V}} \tag{4.24}$$

The design of the gas cavity of the TruCoax laser contains a region of geometry with high aspect ratio as shown schematically in the cross-sectional view in figure 4.2(b), which is the volume taken by the RF discharge.

An important feature of the vacuum vessel in terms of acoustic resonances is the existence of ballast volumes of several litres on either side of the electrodes, which will be referred as resonator mirror blocks further in the text. These ballast volumes are created to separate the resonator mirrors from the RF discharge to prevent damage.

Thus, the vessel can be regarded as a Helmholtz resonator (see figure 4.2(b)). Taking the cross section A of the RF discharge volume perpendicular to the optical axis, the discharge length as reduced neck length L' and the combined volume V in the TruCoax blocks, we find an estimate for the Helmholtz resonance at 35.6 Hz for air or 54.0 Hz for the laser gas mixture.

The Helmholtz resonance is one of the most disruptive frequencies for the TruCoax laser. The gas pressure is lowered at the helix mirror, or at the axicon mirror end of the electrode over durations over several milliseconds. The gas movement during this time is minimal. However, the duration is long enough so that discharge instabilities may be established at either end of the electrodes.

4.3 Resonator Finite-Element Analysis

The analytical solution for standing waves and the Helmholtz resonances provides an estimate of frequency values. However, it should be recognised that the accuracy of the estimate is limited, since for example the ballast volumes in the mirror blocks cannot be neglected therefore preventing the application of standing wave theory in a purely cylindrical geometry. The shape of the ballast volumes in the case of the Helmholtz resonance is not important as long as the ballast volume is smaller than the acoustic wavelength. The effective or reduced length of the "neck" is, however, not known.

A solution of the eigenmodes may be calculated numerically by solving the Helmholtz equation (equation (4.3)). As stated previously, the choice of the variable does not affect the result of the solution as long as the boundary conditions are adjusted accordingly. Backstrom [4.9] suggests using the velocity potential Φ as an independent variable, because the solution allows a simple conversion to pressure and particle velocity solution. The functional relationship of the velocity potential is derived in [4.1]. Under the assumption, that the fluid has negligible viscosity, no rotational flow takes place and the rotation of particle velocity must be zero:

$$\nabla \times u = 0 \tag{4.25}$$

We now introduce a new variable u, defined as the gradient of the velocity potential Φ:

$$u = \nabla \Phi \tag{4.26}$$

Using Euler's equation:

$$\rho_0 \frac{\partial u}{\partial t} = -\nabla p \tag{4.27}$$

and inserting equation (4.27) into equation (4.26), we obtain:

$$\nabla\left(\rho_0 \frac{\partial \Phi}{\partial t} \right) = -\nabla p \tag{4.28}$$

From equation (4.28) it follows that the pressure p can be found from the velocity potential Φ:

$$p = -\rho_0 \frac{\partial \Phi}{\partial t} \tag{4.29}$$

The boundary conditions indicate that the particle velocity is zero at the walls:

$$\nabla \Phi = 0 \tag{4.30}$$

The excitation of an acoustic wave is sufficient if the particle velocity of one of the walls is set to be not equal to zero, as suggested in [4.9]. The frequencies of the eigenmodes can be determined by the FlexPDE approach of subspace iteration methods as described in [4.10], [4.11]. Alternatively the solution of the velocity potential can be solved for a range of acoustic wavelengths λ_i.

Two methods to model the acoustic resonator volume were chosen. Simple geometrical elements, which are cylinders for the ballast volumes on either end plus a rolled-up slab section representing the discharge area were used to model the cavity in a 3-dimensional coordinate system. A solution of the Helmholtz resonance mode from this model is shown in figure 4.3(a). One quarter of the volume is hidden to show the structure of the approximated cavity. The volumes of the cylinders are adjusted to fit the actual volume in the helix mirror and the axicon mirror blocks. The gas cavity of the TruCoax laser, if we disregard minor details, has a rotational-symmetric symmetry along the centre line of the coaxial optical resonator. This property is used for the second approach to be able to model the gas cavity in two-dimensional cylindrical coordinate system. The modelled region including an example of one of the eigenmodes is shown in figure 4.3(b).

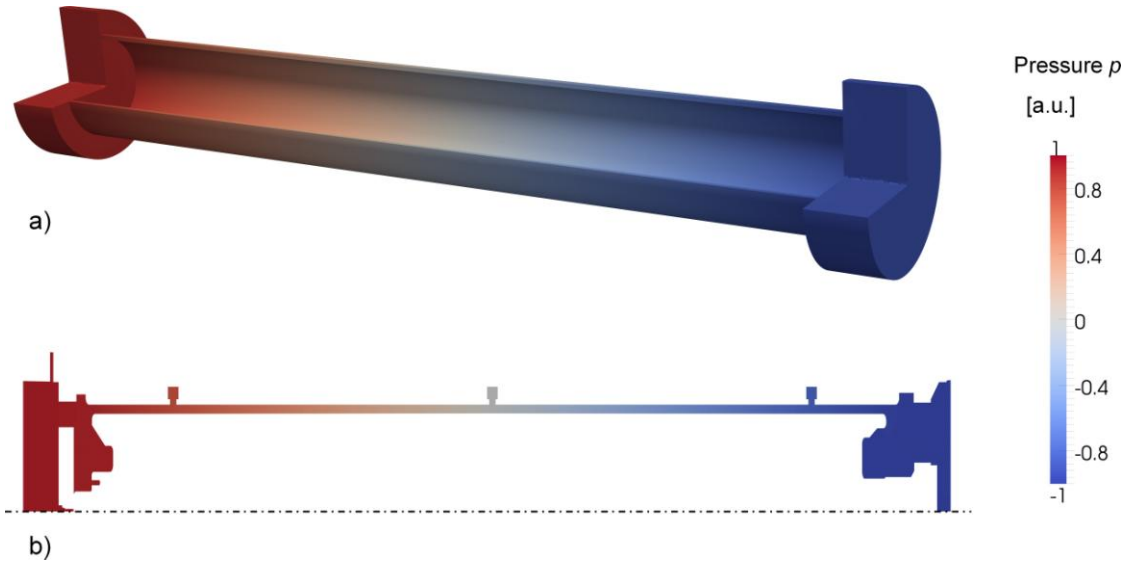

Figure 4.3 Pressure distribution for Helmholtz resonance at t=π/2 in 3d and 2d model. One quarter of the 3d model was hidden for illustration. Absolute pressure *P* is one atmosphere.

Each model has advantages and drawbacks. The 3-dimensional model is far less detailed than the 2-dimensional model but it allows modelling of the eigenmodes in the azimuthal direction or eigenmodes with mixed axial-azimuthal orders. However, details, such as gas pockets for the outer electrode ports may be included in the 2-d model, though lower order solutions of the eigenmodes, the details do not affect the results since the acoustic wavelength is comparable to the length of the whole cavity. However, the accuracy of solutions of the higher order axial modes does become dependent on the level of the detail, as will be shown in the next section.

4.4 Measurement of Eigenmodes by Harmonic Excitation

The numerical calculations deliver solutions of eigenmodes, and the results are mutually consistent in that the resonant frequencies match within the calculation error when the same geometries are used for both the 2-d and 3-d models. The verification of the calculations with actual resonances in the cavity is, however, just as important.

The excitation of acoustic modes occurs due to expansion of hot gas in the RF discharge region. It was stated earlier that the acoustic wave equation was derived under the assumption of adiabatic conditions. However, the adiabatic process, in which the acoustic wave does not exchange thermal energy with the fluid needs to be differentiated from the case where gas heating is an external effect caused by RF power input. The time constant

τ_{therm} of the thermal expansion, and therefore the speed of an imaginary piston moving the gas can be estimated by taking the heat transfer equation [4.12]:

$$\tau_{therm} = \frac{\rho c_p V}{hA} \tag{4.31}$$

where ρ is the gas density, c_p the specific heat capacity, V the gas volume, h the heat transfer coefficient and A the electrode surface area. The heat transfer coefficient is the ratio of the heat flux q to the temperature difference ΔT between electrodes and the gas [4.12]:

$$h = \frac{q}{\Delta T} \tag{4.32}$$

Taking the electrode geometry of the TruCoax laser, the gas parameters r and c_p of the laser gas mix and heat dissipation of 20 kW, the thermal time constant of the gas, τ_{therm} is equal to 1.8 ms. The excitation of the pressure wave is periodic but not harmonic. In the limit of low frequencies, where the period of the gating frequency is much longer than the thermal time constant, the excitation wave function approaches a rectangular pulse shape. In this case the excitation frequency may be a sub-multiple of one of the acoustic resonance frequencies.

For the case of excitation frequencies, the period T_{exc} is much shorter than the time constant τ_{therm}, the shape of the amplitude of the excitation wave becomes more and more triangular. For either case the excitation wave can be regarded as a sum of sinusoidal excitation frequencies (Fourier decomposition). If one of these sinusoidal excitation frequencies is close to one of the acoustic resonance frequencies, a resonant mode will be excited even if the RF gating frequency does not correspond to a resonant frequency. For both reasons, excitation of resonances with sub-multiples of resonance and excitation of resonances by higher order harmonics, the analysis of acoustic resonance frequencies is problematic when using non-harmonic oscillation.

Instead, an experimental configuration was prepared as shown schematically in figure 4.4. The axicon mirror was replaced by a loudspeaker, which is used to excite a single acoustic mode when driven by a sinusoidal signal. The speaker acoustic volume is lowered so that the cone displacement is linearly proportional to the signal, creating a harmonic oscillator. A conventional electret microphone was placed in different locations in the gas cavity. The measurement procedure involved sweeping through a relevant frequency range with the loudspeaker and recording the corresponding microphone RMS signal.

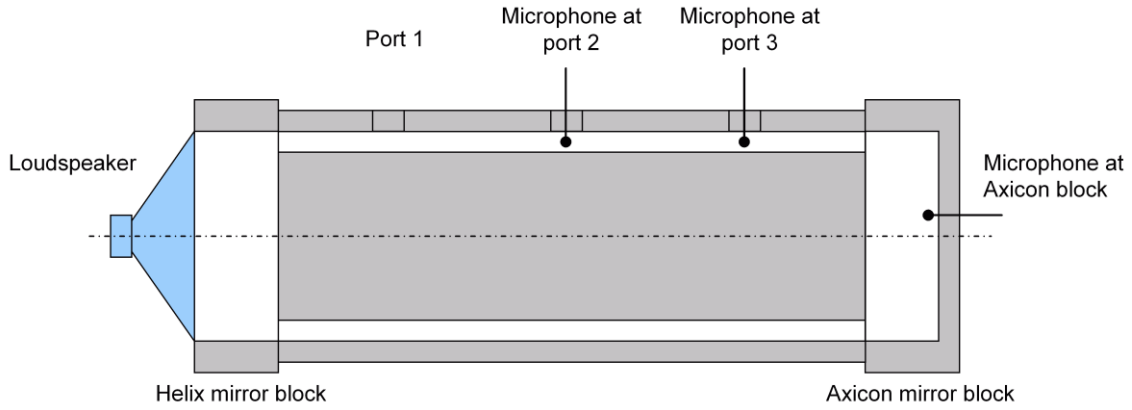

Figure 4.4 Experimental setup for the acoustic resonances measurement

Measurement results were taken for the three microphone positions shown in figure 4.5 and during the experiment the gas cavity was filled with air at atmospheric pressure. In addition to information about the values of the resonance frequencies, an analysis of the relative heights of the peaks to each other gives clues about the eigenmode shape. For example, at 290 Hz mode, the port 2 signal (curve (a) in figure 4.5) has a minimum but the curves for port 3 and axicon mirror block (curves (b) and (c) in figure 4.5) have a maximum in this position. The pressure node of this mode must therefore be in the centre, indicating a second order axial mode. Another example would be the two modes with high peaks at 140 Hz and 400 Hz, measured in port 2. The peaks are much higher than in other cases. The pressure antinode positions must be closely lined up with the microphone position, which indicated that these are axial modes with mode numbers 1 and 3.

The recorded curves give also information about the frequency width of the resonance curves. The full width at half maximum is about 40 Hz.

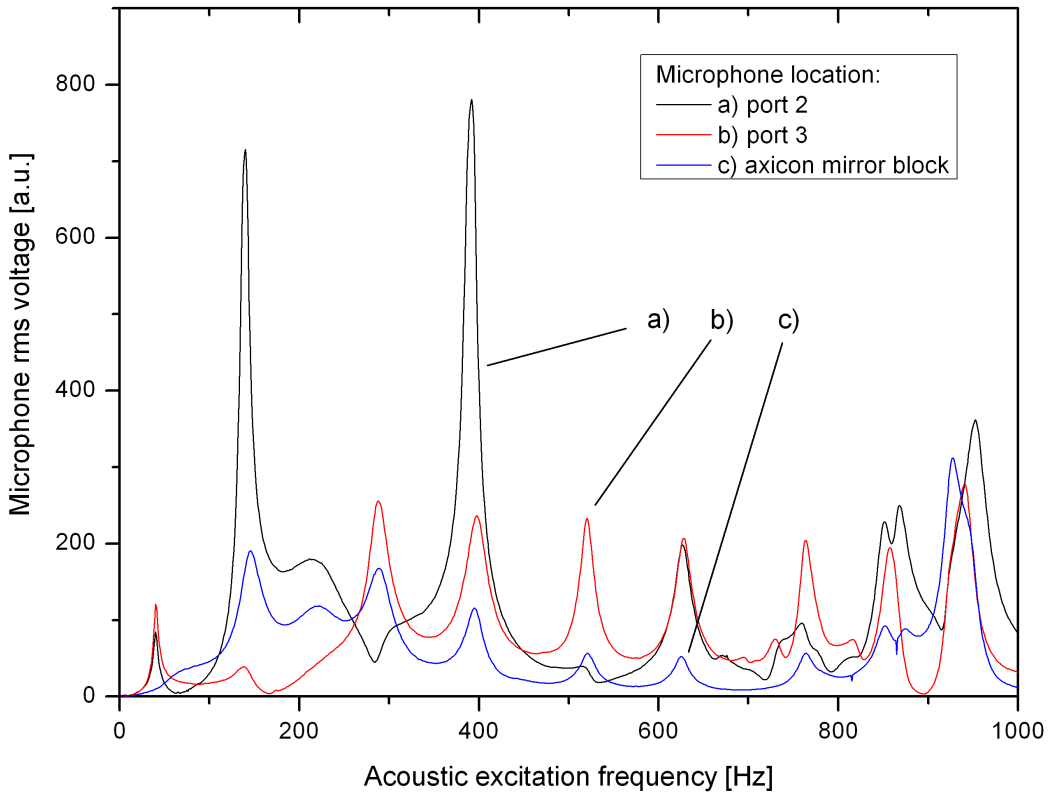

Figure 4.5 Measured microphone RMS signal as function of loudspeaker excitation frequency in air. The microphone locations are indicated in figure 4.4.

The results for the calculations of the 2-d rotational-symmetric modes, the 3-d model and the measurement results are summarised in the table 4.2. In general, the 3-d model is much more demanding in terms of convergence towards a solution. The calculation time is not only an order of magnitude longer compared to 2-d model, but also the high aspect ratio of the geometry requires an increasingly dense mesh to be able to find higher order modes. No axial mode of order higher than six was calculated, which already takes a PC several hours. The modes (g), (h) and (j) in figure 4.6 could be attributed to azimuthal acoustic modes. The 3-d model, however, does not include the six pockets of the outer electrode ports. These are located close to the positions of the antinodes for the 1st order azimuthal mode (port 2 at the top and bottom as shown in figure 4.4) and for the 2nd order mode (ports 1 and 3 at the top and bottom). Such geometrical coincidences are expected to have impact on the values of the resonant frequencies.

Table 4.2 Summary of determined resonance frequencies and mode shapes

Mode	Measured peak [Hz]	Resonant frequency 2-d model [Hz]	Resonant frequency 3-d model [Hz]	Pressure distribution 3-d model
a) Helmholtz resonance	40	37	63	
b) axial 1 azimuthal 0	138	156	158	
c) axial 2 azimuthal 0	288	282	274	
d) axial 3 azimuthal 0	397	393	396	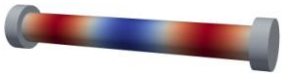
e) axial 4 azimuthal 0	520	521	521	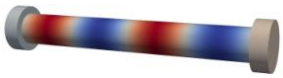
f) axial 5 azimuthal 0	628	629	647	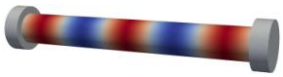
g) axial 0 azimuthal 1	695	n/a	725	
h) axial1 azimuthal 1	731	n/a	757	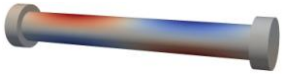
i) axial 6 azimuthal 0	764	777	771	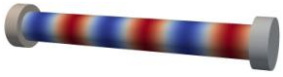
j) axial 2 azimuthal 1	816	n/a	806	
k) axial 7 azimuthal 0	857	882	Too large mesh required to perform 3-d calculation	
l) axial 8 azimuthal 0	941	952	Too large mesh required to perform 3-d calculation	

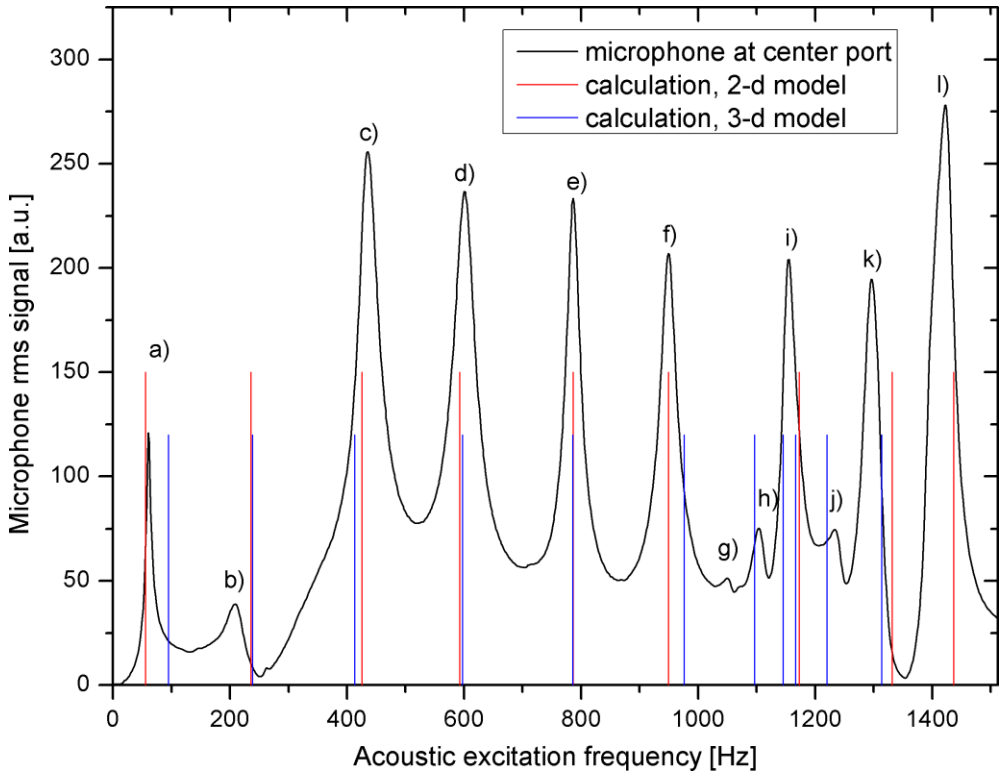

Figure 4.6 Comparison of calculated resonance frequencies for the two models (red and blue lines) with resonance measurement in air. The height of the lines from the calculations is set arbitrarily. The letters indicate the eigenmodes from table 4.2.

4.5 Pressure Wave Measurement

A complementary measurement of acoustic resonances was devised with a gas cavity under operating conditions including an actual laser 5-gas mixture. The gas chamber is enclosed and laser gas mixture is filled at an operating pressure of 70 hPa. Pulse widths in the order of 0.1 ms or longer are observed to excite the medium twice. First, the pressure wave is initiated from gas expansion, while the second pressure wave, excited from the contraction of the gas after the RF voltage is turned off interacts with the first pressure wave. An UV lamp used as a discharge ignition aid makes it possible to ignite the discharge in the region of the feed-through with a RF voltage pulse of 10 µs duration.

The response of such a short shock wave is picked up by a microphone placed inside the helix mirror block. The relaxation time constant, τ of the acoustic wave taken from the microphone membrane trace (figure 4.7) was observed to show a value of 7 ms.

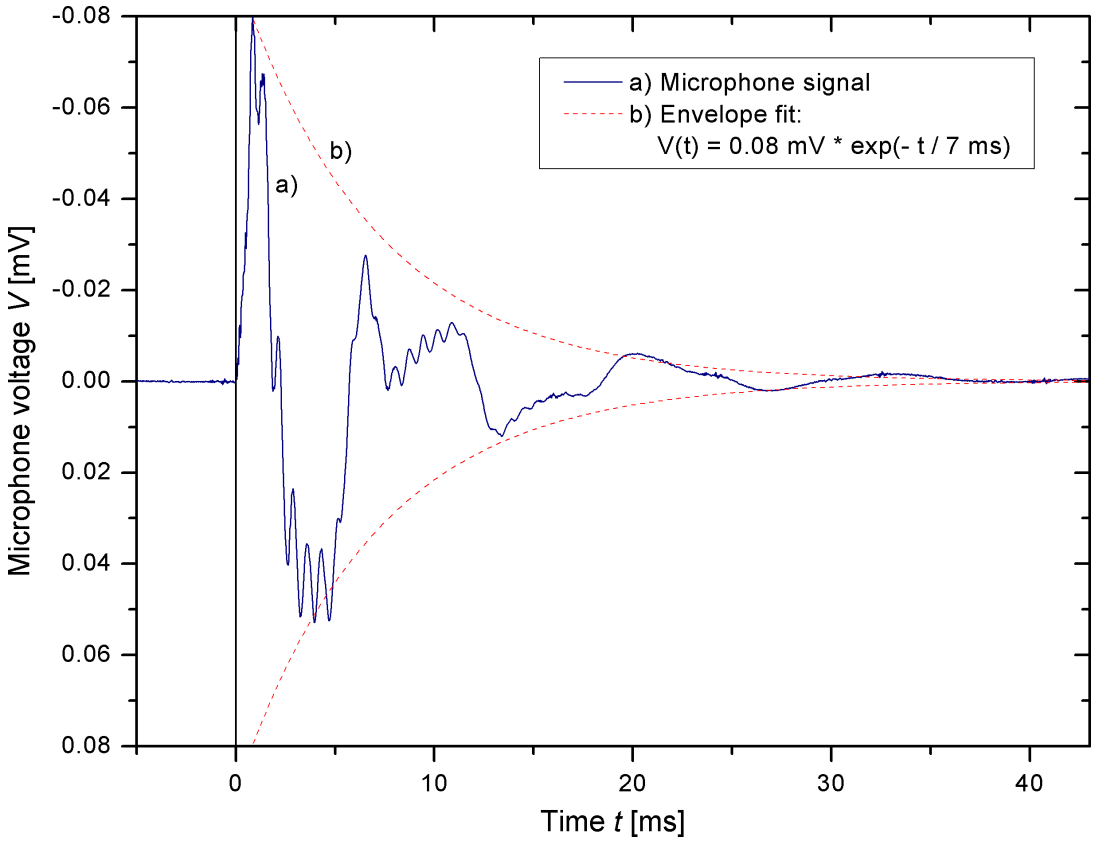

Figure 4.7 Measured pressure after an acoustic wave was excited by RF discharge ignition in laser gas mixture. The duration of RF voltage pulse is 10 µs.

The resonator quality factor Q is related to the relaxation time by the expression [4.1]:

$$Q = \frac{1}{2}\omega_0 \tau \tag{4.33}$$

where ω_0 is the circular resonance frequency and τ the relaxation time. The quality factor Q is also defined as a ratio of the resonance frequency ω_0 to the frequency full width at half maximum $\Delta\omega$ as follows [4.1]:

$$Q = \frac{\omega_0}{\Delta\omega} \tag{4.34}$$

The relations (4.33) and (4.34) allow an estimate to be made of the width of the resonance peak for a known relaxation time, given by:

$$\Delta f = \frac{1}{\tau\pi} \tag{4.35}$$

The width of the resonance frequency was observed to be 45 Hz, which correlates well to the widths observed from the measurements with the loudspeaker (see figure 4.5). The

results show that the modification of one of the walls, where the rigid metal wall (the helix mirror) was replaced by a loudspeaker did not distort the results significantly.

The modal content caused by the pressure wave can be analyzed by Fourier-transformation of the signal, as indicated by the graph in figure 4.8. The pressure wave signal (figure 4.7) in conjunction with its Fourier-transform (figure 4.8) reveals some information of the acoustic modal content, which should be discussed in more detail. The mode with the highest amplitude has at the same time the lowest frequency of about 90 Hz. Because of its frequency the mode is attributed to the Helmholtz resonance. The oscillation period of about 11 ms is larger than the estimated relaxation time of 7 ms, making accurate estimate of the frequency value impossible. The amplitude of axial modes decreases with increasing mode order as can be seen in figure 4.8. The peak at 1385 Hz is seemingly an exception, but we can attribute it to an eigenmode in the axicon mirror block rather than an axial mode. This assumption is supported by the fact that the axicon block diameter corresponds to a half-wavelength of 19 cm at the speed of sound in the laser gas mixture and at 1385 Hz.

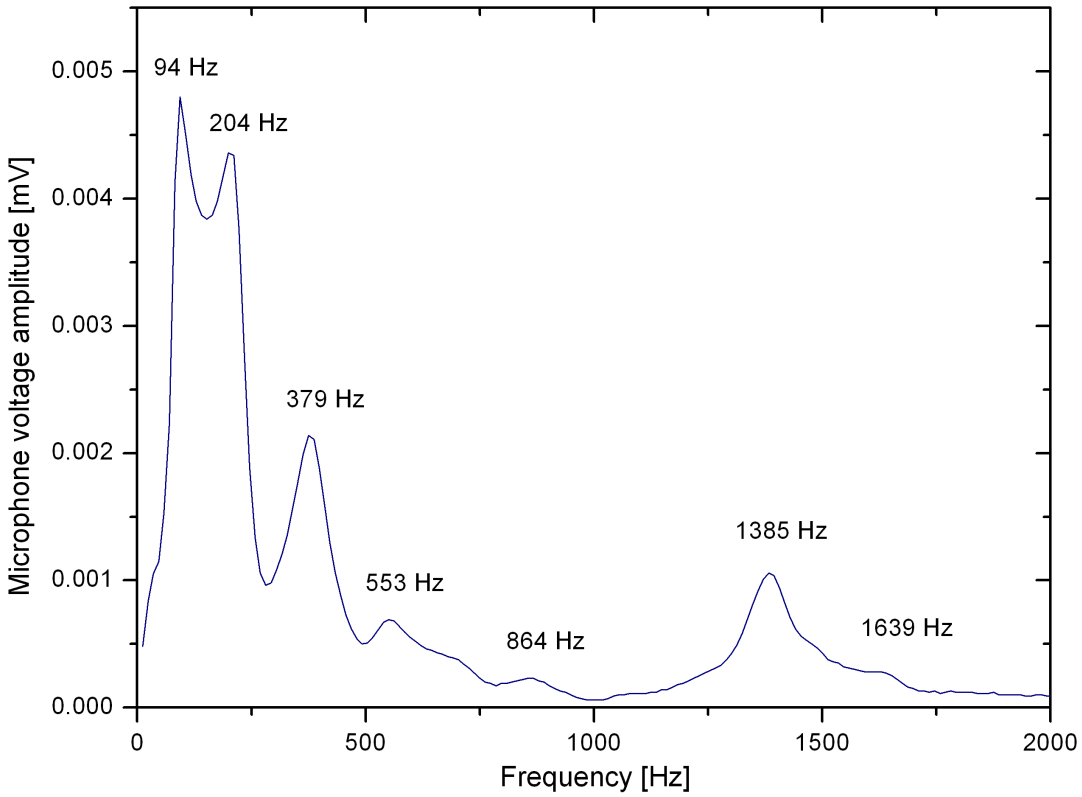

Figure 4.8 Fast Fourier Transform of the signal from figure 4.7

The frequency values of the axial modes measured with laser 5-gas mixture can be compared with loudspeaker measurements performed in air (section 4.4) by scaling with the speed of sound as follows:

$$f_{5gas}\frac{c_{air}}{c_{5gas}} = f_{5gas}\frac{344\,m/s}{522\,m/s} = f_{air} \tag{4.36}$$

The best correlation between the two measurement techniques was achieved in measuring the 1st order axial mode (see table 4.3). The data taken from the loudspeaker harmonic wave excitation is expected to deliver more reliable data, since the higher order modes could be sustained by the large speaker throughout the measurement range, whereas the damped pressure wave delivers a low signal to noise ratio.

Table 4.3 Comparison of measured axial resonant frequencies in air

Axial mode order	Frequency from loudspeaker tests	Scaled frequency from pressure wave tests
1	138 Hz	134 Hz
2	288 Hz	249 Hz
3	397 Hz	364 Hz
4	520 Hz	569 Hz

4.6 Acoustic Resonances in Operational Region of the TruCoax Laser

The acoustic resonances were treated as harmonic oscillations or as a pressure wave problem in order to analyze the modal content. The output power in the TruCoax laser is controlled by RF pulse width modulation, where the gating frequency is determined by the specific application. In this section the response of the acoustic resonator to the RF discharge operating conditions is considered.

An approximation of the thermal time constant τ_{therm} of the gas in the discharge volume was discussed in section 4.4. Since the acoustic pressure wave is excited by thermal expansion, it is reasonable to assume that for sufficiently high pulsing frequencies *f*:

$$\frac{1}{f} << \tau_{therm} \tag{4.37}$$

Under such conditions, the gas approaches a time-independent steady state and no acoustic wave will be excited. For sufficiently low or high cycles one of the switched on or switched off durations, respectively, will also be much shorter than the thermal time

constant. For low duty cycles, the duration for which the RF power is switched on is shorter than the thermal time constant:

$$T_{on} << \tau_{therm} \tag{4.38}$$

On the other hand, at high duty cycles the off time becomes shorter than the thermal time constant:

$$T_{off} << \tau_{therm} \tag{4.39}$$

These assumptions create the three boundary conditions (low duty cycles, high duty cycles and high pulsing frequencies), at which the acoustic resonances are expected to extinguish. The heat equation is used as a tool to study the extent of these boundaries.

The temperature profile across the discharge gap can be calculated by solving the steady state heat equation:

$$\frac{d^2T}{dx^2} = -\frac{w}{\lambda} \tag{4.40}$$

where w is the power density, λ is the thermal conductivity and x is the coordinate across the discharge gap. The gas temperature profile will be discussed in more detail in Chapter 5 in the context of the thermal lensing effect.

The transient of the temperature can be calculated by adding a time-dependent term [4.12]:

$$\frac{\partial^2 T}{\partial x^2} - \frac{c_p \rho}{\lambda}\frac{\partial T}{\partial t} = -\frac{w}{\lambda} \tag{4.41}$$

where c_p is the specific heat capacity and ρ is the gas density. The released power density w is not only a function of x as shown in Chapter 5, section 5.4, but also a function of time, representing the RF power gating signal. We can design the pulse width modulated signal, which will switch with desired duty cycle represented by symbol *dc*, and frequency f as function of time. An example of such function would be:

$$RF_{on}(t) = \frac{1}{2}\left(sign\left(dc - \frac{1}{\pi} a\cot\left(\cot\left(t \cdot f \cdot \pi\right)\right)\right) + 1\right) \tag{4.42}$$

Inserting equation (4.42) into (4.41) gives the time-dependent heat equation as function of pulsing parameters:

$$\frac{\partial^2 T}{\partial x^2} - \frac{c_p \rho(T)}{\lambda(T)}\frac{\partial T}{\partial t} = -\frac{w(x) \cdot RF_{on}(t)}{\lambda(T)} \tag{4.43}$$

One example for such a temperature transient calculation is shown in figure 4.9 for a low pulsing frequency, with the period being longer than the thermal time constant and, another example is used for high frequency. It can be seen that for low duty cycles the gas temperature region extends over the entire range from room temperature to the steady state temperature corresponding to full RF input power. As the pulsing frequency is increased, the temperature fluctuation decreases. The temperature variation for 50% and 25% duty cycles are also plotted in the figure 4.9, which shows that at high pulsing frequencies (e.g. 960 Hz) the duty cycle has a strong impact in both magnitude of the temperature variation and the average temperature.

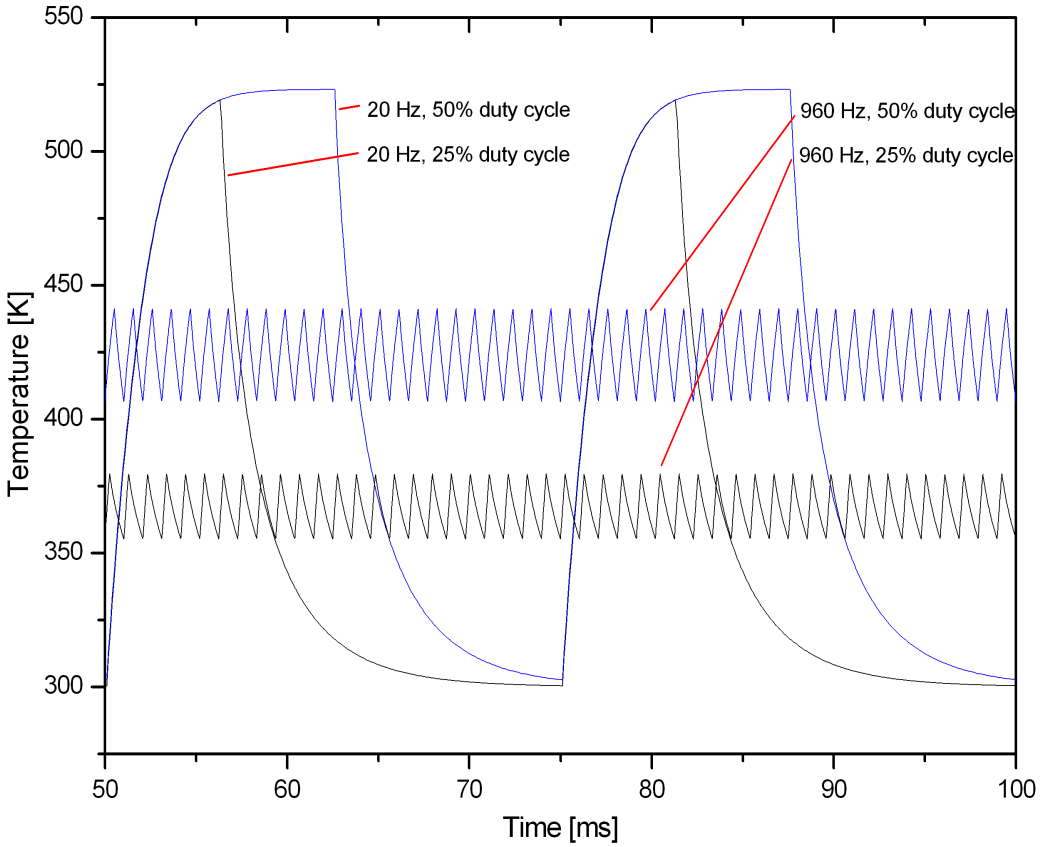

Figure 4.9 Examples of calculated average temperature progression for a low frequency (20 Hz) and high frequency (960 Hz) at two duty cycles

The temperature variation causes expansion and contraction of the gas, which in turn is the source for the acoustic wave excitation. We can define the peak-to-peak value of the temperature variation as the modulation function *m(f, dc)*, normalised to the maximal temperature range T_{cw}-T_{room}. The modulation function is a measure of a weighting factor for acoustic resonances at a given operating point in frequency – duty cycle space, and

this function converges towards zero for 0% and 100% duty cycle and towards high frequencies. At about 250 Hz and 50% duty cycle the temperature range is half of the range compared to 10 Hz, while at 1500 Hz the temperature range is 10% and acoustic effects become negligible.

It can be seen in the eigenmode patterns (right column in table 4.2) that the volume in the discharge is also, to a large extent, the region in which standing waves occur. For this reason the average temperature in the discharge region is assumed to be the only dependent variable for calculation of the speed of sound (according to equation 4.11) in the cavity as function of pulsing frequency and duty cycle *c(f, dc)*. The modulation function *m(f, dc)* and the speed of sound function *c(f, dc)* were calculated numerically by using equation 4.41 for a series of frequencies and duty cycles in the operation range.

An analysis of the electrode surface following arcing damage when the laser is operated at resonant frequencies shows that the electrode end towards the axicon mirror is the more likely region to become damaged. It should be noted that the ballast volume in the axicon mirror block is almost twice as large as that in the helix mirror block. For this reason the pressure amplitude is higher at Helmholtz resonance at the axicon mirror, which supports the observed asymmetric failure mode.

We can model the temperature variation (see figure 4.9), which is the driver for the generation of acoustic waves as a piston, where its displacement is proportional to the temperature. The content of higher order harmonics of the *T(t)* signal was analyzed for a range of frequencies at 50% duty cycle, and the first ten harmonics are plotted in figure 4.10; the amplitudes were scaled relative to the fundamental mode.

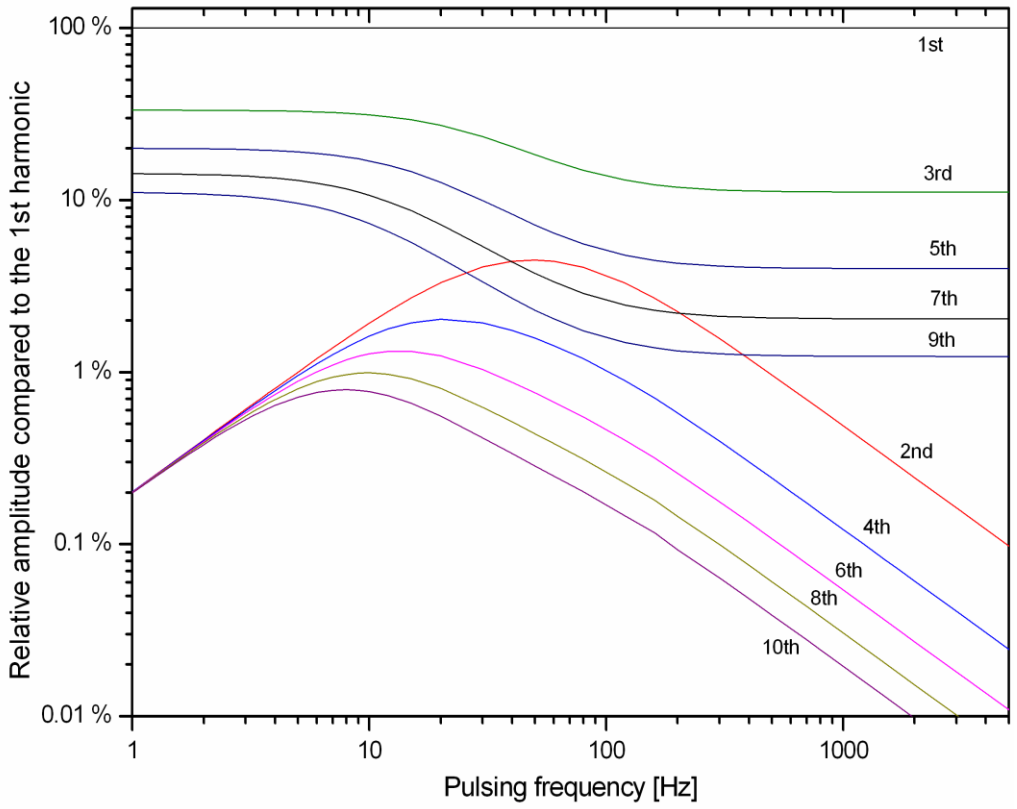

Figure 4.10 Relative amplitude of higher order harmonics of the gas temperature *T(t)* due to pulsing at 50% duty cycle. Only first ten harmonics are shown.

The temperature variation function takes a form of a rectangular wave for frequencies lower than 10 Hz, and only odd harmonics are present in the spectrum. The even-numbered harmonics start to appear in the transitional range between 10 Hz and 500 Hz, and for frequencies above 500 Hz the temperature variation increasingly resembles a triangular wave form (see figure 4.9). The odd-numbered harmonics are present in the high frequency of the spectrum, and their relative amplitude decreases to a larger extent compared to frequencies <10 Hz, which is typical of triangular wave forms. The 3rd and 5th harmonics are the first two higher order harmonics observed throughout the pulsing range at 50% duty cycle. As the duty cycles is changed towards 0% or 100%, the relative amplitudes of harmonics are increasingly evenly distributed, which is expected from a wave form approaching a delta function.

For analysis of the operational region, the fundamental mode together with the 3rd order harmonic mode at 20% relative amplitude and 5th order harmonic mode with 10% amplitude were taken into account. The recorded resonance signal *s(f)* measured from the loudspeaker tests in air was combined with the functions *c(f, dc)* and *m(f, dc)* to create

a map of the severity of the standing wave in the operational range of the TruCoax laser (figure 4.11):

$$res(f,dc) = s(f)\frac{c(f,dc)}{c_{air,300K}}m(f,dc) \tag{4.44}$$

The data presented in figure 4.11 allows one to make some general observations:

a) Acoustic resonances are extinguished towards 0% and 100% duty cycle. The duty cycle range is larger in terms of resonances at low frequencies.
b) At frequencies above 2 kHz the acoustic resonances become negligibly small.
c) The values of resonant frequencies become dependent of the duty cycle towards higher pulsing frequencies.

However, an actual map including additional higher order harmonics would have more resonance regions with reduced amplitude.

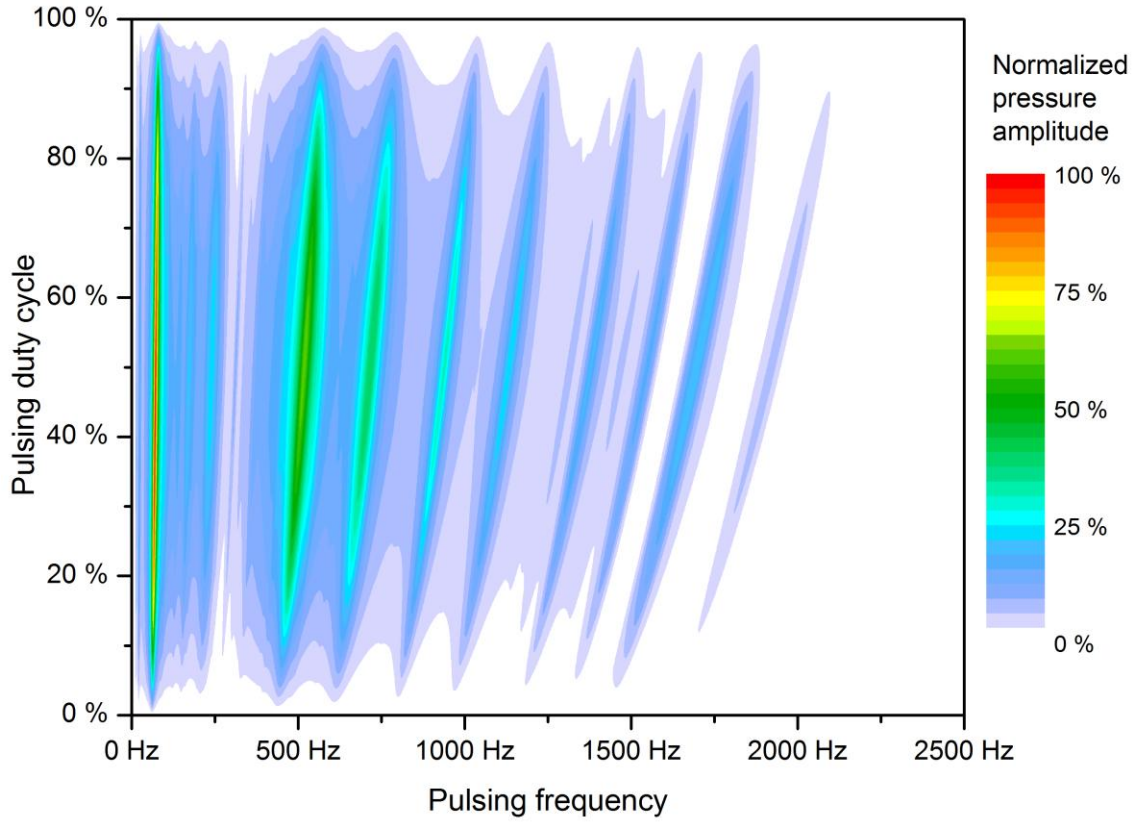

Figure 4.11 Severity of acoustic resonances of the RF discharge at the axicon end. 1st, 3rd and 5th harmonics were included.

The frequency values for the resonances were observed to increase at higher duty cycles as the gas gets hotter while the speed of sound increases. The speed of sound increases according to equation (4.44) in proportion to the pulsing frequency, so that the slope of acoustic resonance vs. duty cycle lines is shallower for higher pulsing frequencies. It should be noted that the most destructive resonance is the Helmholtz resonance, which is confined to a small frequency region with small dependency on the duty cycle. The first axial mode located at around 250 Hz is almost not present, because it has an antinode at the end of the electrode.

4.7 Methods to Minimise Acoustic Resonance Effects in the TruCoax Resonator

Once the operating parameters with high risk have been identified in the preceding sections, we can focus on producing a laser design where the detrimental effects are at least minimised. There are several different options available for tackling acoustic resonance problems, including:

a) Altering the gas cavity design and shifting the acoustic resonance frequencies

b) Blocking pulsed operation at the resonant frequencies

c) Designing software algorithms that minimise the standing wave effects

An example of option (a) being implemented in a patent by Hart *et al.* [4.13], in which the waveguide excitation regions in a z-fold waveguide CO_2 laser were connected by channels in two locations. This technique reduced the build-up of pressure in the standing wave pattern by allowing the gas to flow through the channels between the waveguides. However, the coaxial system does not allow such an easy access around the discharge as in a waveguide or slab laser, since in our case the cross-sectional area of the discharge volume is much larger than for the a 1-d waveguide structure. In practice, the cross-section of the bypass channel must be of the same order as the discharge area, which is also difficult to realise.

The second option would be to block pulsing frequencies in the range of acoustic resonances.

The third option, on which most attention is devoted here, is to influence the resonances by laser control algorithms, as discussed below.

4.7.1 Two-frequency modulation

Initial tests with the TruCoax laser model V4 showed that the RF discharge becomes unstable mostly at the Helmholtz resonance and the 1st axial mode. When increasing the RF input power from 20 kW to 30 kW, the discharge exceeds the stability level (figure 4.12(a)) and filaments begin to extend from the inter-electrode gap (figure 4.12(b)) as the power density at the low pressure point of the acoustic resonance becomes too high. Randomly the discharge can collapse to form a region of so-called γ-type discharge (see Chapter 2, section 2.2.1), which eventually, after the electrode surface is heated up, promotes arc breakdown between the electrodes.

A remedy to prevent from this catastrophic instability is to minimise the pressure wave at those resonant frequencies. This was accomplished by replacing the pulses in the pulse-width modulated signal with *bursts* of pulses of higher frequency. The frequency of the embedded high frequency pulses is set to be high enough so that for the acoustic wave the two-frequency modulation acts like a low frequency signal with reduced amplitude. In practice, it was determined that a frequency of 20 kHz produced the desired effect. The benefit of this switching technique is that the amplitude of the pressure wave can be adjusted by reducing the duty cycle of the 20 kHz signal without the need to modify the RF matching and voltage distribution setup.

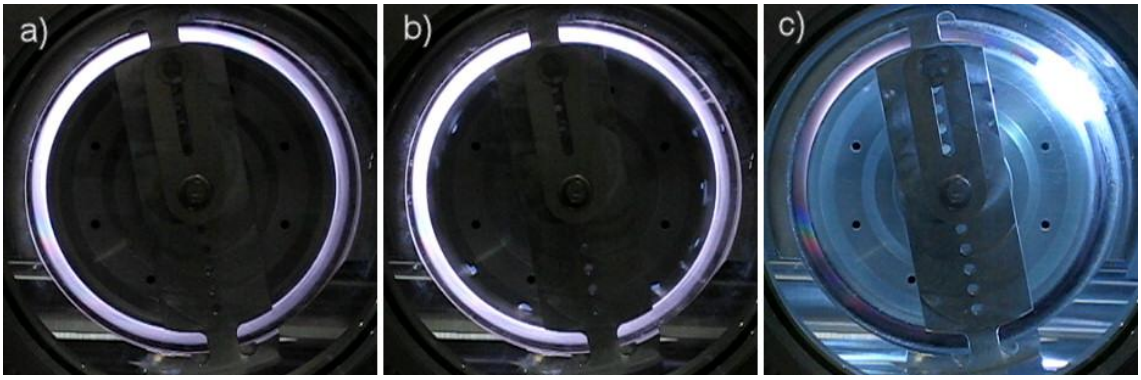

Figure 4.12 Photographs of the discharge at the axicon mirror end, looking through a glass lid.
a) stable operation
b) discharge filaments formation
c) γ-type discharge before arc breakdown

4.7.2 Frequency dithering

The application for which the TruCoax laser is designed, does not require high adherence to the commanded pulsing frequency. Based on the assumption that a certain magnitude of the difference between the actual and requested frequency can be allowed, a frequency modulation algorithm can be implemented to reduce acoustic resonance effects.

The fundamental issue for discharge instabilities as shown in figure 4.12(b) and (c) is the formation of acoustic standing wave. In such situation, the pressure wave matches the resonance frequency so that at each period the pressure wave builds up to form a standing wave pattern. Thus, if the frequency f_0 is changed by a random amount Δf after each period, the chance of a build-up of a standing wave is minimised. Such a variation of the pulsing frequency can be for example normal-distributed around the centre frequency. For example the method of Box and Muller [4.14] provides a simple way to obtain normal-distributed random numbers with a variance σ^2 of one.

$$y = \sqrt{-2\ln x_1}\cos(2\pi x_2) \tag{4.45}$$

The advantage of this method is the straightforward implementation in the laser control logic and the fact that the laser output power should not be affected by the algorithm.

4.8 Summary

The objective of this study has been to derive a solid theoretical understanding of the development of acoustic resonances which derive from the pulsed RF discharge excitation of the laser gas mixture. Moreover, an equally important objective has been to determine regimes of laser operation which facilitate the avoidance of damaging effects of acoustic resonances in the performance of the laser in practical industrial processing application.

The study of resonance standing waves is a classical problem in acoustics. However, the information about a comparative extensive acoustic analysis for CO_2 lasers or gas lasers in general is apparently not present in the literature.

4.9 References

[4.1] L. E. Kinsler, A. R. Frey, A. B. Coppens, J. V. Sanders “Fundamentals of acoustics”, John Wiley & Sons, New York, ISBN 0-471-02933-5 (1982)

[4.2] D. R. Raichel “The science and applications of acoustics”, Springer New York, ISBN 0-387-26062-5 (2006)

[4.3] F. Jacobsen, T. Poulsen, J. H. Rindel, A. C. Gade, M. Ohlrich “Fundamentals of acoustics and noise control”, Technical University of Denmark, lecture note 31200 (2011)

[4.4] R. Fitzpatrick “Thermodynamics and statistical mechanics”, University of Austin, Texas, lecture note (2006)

[4.5] D. A. Bohn “Environmental effects on speed of sound”, J. Audio Eng. Soc., vol. 36, pp. 223-231 (1988)

[4.6] E. W. Lemmon, M. O. McLinden, D. G. Friend “Thermophysical properties of fluid systems”, NIST Standard database 69, http://webbook.nist.gov (2012)

[4.7] J. R. Belcher, W. V. Slaton, R. Raspet, H. E. Bass, J. Lightfoot “Working gases in thermoacoustic engines”, J. Acoust. Soc. Am., vol. 105, pp. 2677-2684 (1999)

[4.8] W. Wagner, A. Pruss “International equations for the saturation properties of ordinary water substance”, J. Phys. Chem. Ref. Data, vol. 22, pp. 783-787 (1993)

[4.9] G. Backstrom “Simple deformation and vibration by Finite Element Analysis”, GB Publishing Malmo, ISBN 9-197-55532-0 (2006)

[4.10] FlexPDE, “A flexible solution system for partial differential equations”, version 6.14, PDE Solutions Inc. (2010)

[4.11] K.-J. Bathe, S. Ramaswamy “An accelerated subspace iteration method”, Comp. Meth. Appl. Mech. Eng., vol. 23, pp. 313-331 (1980)

[4.12] J. Lienhard IV, J. Lienhard V “A heat transfer textbook”, Phlogiston Press Cambridge, ISBN 0-971-38352-9 (2002)

[4.13] R. A. Hart, J. T. Kennedy, E. R. Mueller, L. A. Newman “RF excited waveguide laser”, DeMaria Electrooptics Systems, US patent 6-192-061 (2001)

[4.14] G. E. P. Box, M. E. Muller “A note on the generation of random normal deviates”, Ann. Math. Statist., vol. 29, pp. 610-611 (1958)

Chapter 5

FUNDAMENTALS OF THERMAL LENSING IN GAS LASERS

5.1 Introduction: Motivation and Overview of Calculation Procedure

A comprehensive analysis of an optical resonator requires attention not only to the direct factors such as mirrors, lenses, windows and apertures, but also to those factors that affect the properties of the medium through which the beam propagates. Indirect factors, such as temperature profiles and discharge morphology play an important role in determining both the laser beam characteristics and the process for optimization of the optical resonator.

A common property of diffusion-cooled gas lasers is the temperature gradient across the discharge gap, where the gas is hottest in the centre of the discharge gap and is coldest next to the electrode walls. The temperature profile across the gap leads to a refractive index variation, which is referred as thermal lensing.

The objective of this chapter is to evaluate the magnitude of thermal lensing based on boundary conditions of the TruCoax laser. The calculation procedure to estimate the thermal lensing effect is divided into work packages as illustrated by the flow-chart in figure 5.1. At each work package either information is fed into the system or calculation based on data from previous work packages is performed.

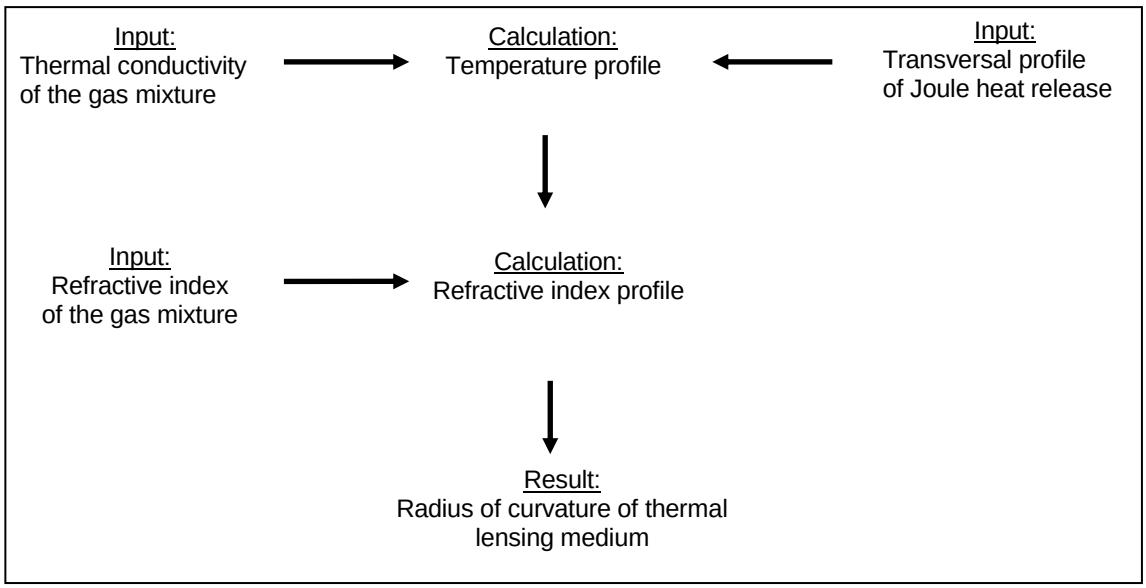

Figure 5.1 Strategy for estimating the thermal lensing effect

5.2 Temperature-dependent Thermal Conductivity of a Gas Mix

The thermal conductivity of pure gases was measured for various pressures and temperatures and has been published in various handbooks of physical properties as, for example in [5.1]. The measurement points are fitted by a polynomial function in [5.2] in order to obtain a continuous function of temperature T for the thermal conductivity λ and the viscosity η for pure gases:

$$\lambda_i(T) = A_i \times 10^{-4} T^{B_i} + a_i \times 10^{-2} + b_i T \times 10^{-5} + c_i T^2 \times 10^{-8} \tag{5.1}$$

$$\eta_i(T) = K_i \times 10^{-6} T^{L_i} + k_i \times 10^{-5} + l_i T \times 10^{-8} + m_i T^2 \times 10^{-11} \tag{5.2}$$

Thermal properties of gas mixtures cannot be computed directly based on their relative concentrations, because the interaction between the atoms or molecules depends on their mass or their molecular velocities. The thermal conductivity λ_{mix} of binary and ternary mixtures was evaluated and a formula for a mixture with j gases is given in [5.3] as:

$$\lambda_{mix} = \sum_{i=1}^{j} \lambda_i \left[1 + \sum_{k=1,\ k \neq i}^{j} G_{i,k} \frac{x_k}{x_i} \right]^{-1} \tag{5.3}$$

where j is the number of gases, i and k are index variables, λ_i is the thermal conductivity of gas species i, x_k and x_i are mole fractions of gas species k and i respectively.

The matrix $G_{i,k}$ in the above formula is calculated as:

$$G_{i,k} = \frac{1.065}{2\sqrt{2}}\left(1+\frac{M_i}{M_k}\right)^{-\frac{1}{2}}\left[1+\left(\frac{\eta_i M_k}{\eta_k M_i}\right)^{\frac{1}{2}}\left(\frac{M_i}{M_k}\right)^{\frac{1}{4}}\right]^2 \tag{5.4}$$

with M_i being the molecular mass of gas species *i*.

The thermal conductivity of the gas mix used in the TruCoax laser is calculated using the coefficients in the table 5.1 for the equations (5.1) and (5.2).

Table 5.1 Thermal conductivity and viscosity coefficients [5.2]

	CO_2	CO	N_2	He	Xe
A	0.4255	2.6251	2.9625	24.8795	0.5039
B	1.0631	0.8009	1.0631	0.7187	0.8349
a	-0.8537	-0.04679	0.2459	0.1279	-0.0438
b	2.698	0.143	-0.8075	-0.4273	0.143
c	-1.591	-0.08529	-1.591	0.2576	-0.0853
K	0.2052	0.3596	0.4706	0.4139	0.2518
L	0.7589	0.6877	0.6417	0.6777	0.801
k	-0.2928	-0.1049	-0.167	0.0204	-0.3915
l	0.9581	0.3473	-0.552	-0.0652	1.2738
m	-0.5762	-0.209	-0.3348	0.0403	-0.0768

5.3 Refractive Index of a Gas

The temperature dependence of the refractive index *n* can be calculated using the Clausius-Mossotti equation [5.4]:

$$a_0 = \frac{3}{4\pi N}\frac{n^2-1}{n^2+2} \tag{5.5}$$

where α_0 is the molecular polarizability and *N* is the gas density.

Since the refractive index *n* is nearly unity, the denominator in equation (5.5) simplifies to:

$$n^2+2 \approx 3 \tag{5.6}$$

The gas density *N* for an ideal gas is:

$$N = \frac{p}{k_B T} \tag{5.7}$$

where k_B is the Boltzmann constant, p is the gas pressure and T is the gas temperature.

After solving equation (5.5) for n, inserting the equations (5.6) and (5.7) and using the first term of the Taylor series:

$$\sqrt{1+x} \approx 1+\frac{1}{2}x \tag{5.8}$$

we arrive at the description of the refractive index of a gas as follows:

$$n = 1 + 2\pi \frac{p}{k_B T}\alpha_0 \tag{5.9}$$

Equation (5.9) contains only the molecular polarizability α_0 as a gas species-specific variable. The values of the polarisabilities of the gases used can be found in [5.5]. They are shown in table 5.2.

Table 5.2 Molecular polarisabilities in SI units [5.5]

	CO_2	CO	N_2	He	Xe
α [m^2C/V]	2.911×10^{-30}	1.95×10^{-30}	1.7403×10^{-30}	0.204956×10^{-30}	4.044×10^{-30}

Attention must be paid here to the units of polarizability. The units for polarizability are often expressed in ESU (electro-static units), where the Coulomb charge is defined without the factor $1/4\pi\varepsilon_0$. In electro-static units, the polarizability has units of a volume (cm^3 or $Å^3$) and is quoted as α' [5.6]. The polarizability for the gas mixture α_{mix} used in the TruCoax laser is calculated by adding the molar fraction of each gas species. The resulting function $n(T)$ in figure 5.2 is used for later calculations.

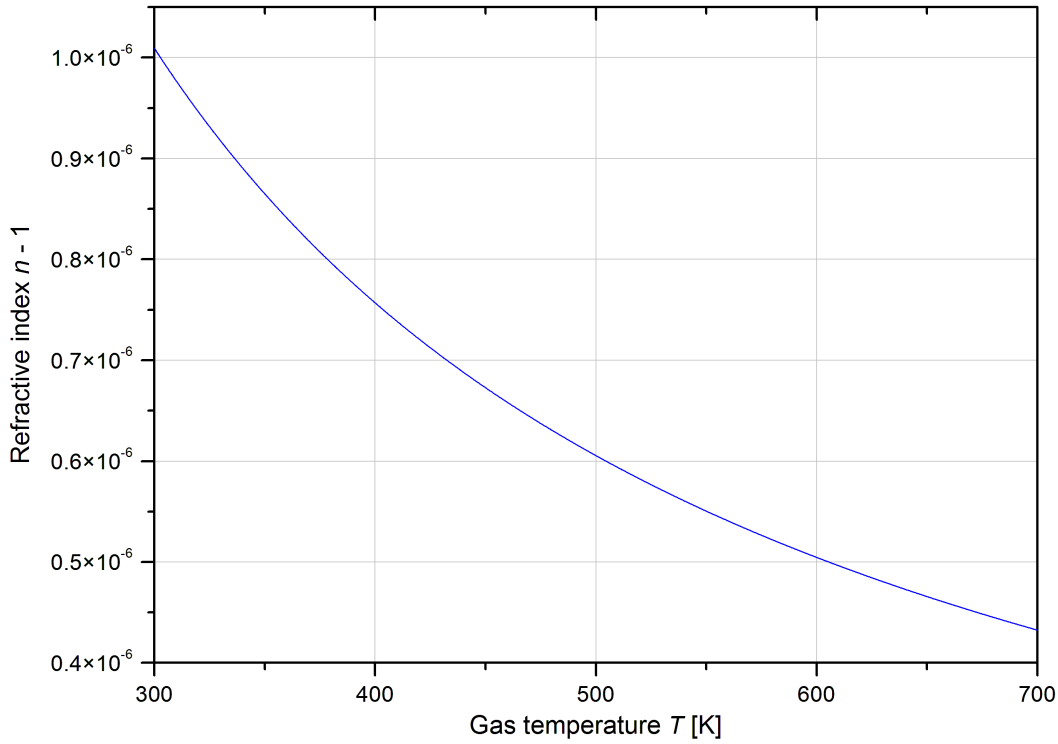

Figure 5.2 Refractive index for the 5 gas mix (α_{mix} = 0.731×10^{-31} m^{2}C/V) at 91 hPa

5.4 Measurement of Lateral Luminance Distribution

The Joule heat release w in the RF discharge has been studied for both inductively-coupled [5.7] and capacitively-coupled radiofrequency discharges [5.8]. It was found that the heat release has two maxima at the boundary between the ion sheaths and the positive column. The reason for this is that on the one hand the positive column has high current density j but low voltage (or electric field E), but on the other hand the ion sheath has high field strength but low current. At the boundary between these two regions there is a point where $w = jE$ has a maximal value. The Joule heat release jE is proportional to the local ionisation rate of the gas and this phenomenon is observed by the typical luminance distribution of the α-type discharge with its two bright regions.

An experimental setup was put in place to measure the luminance profile of the RF discharge which can be used as a basis of the power density profile for thermal lensing calculations. The axicon mirror was replaced for this measurement with a glass window so that the RF discharge can be observed along the inter-electrode gap. A digital SLR camera was placed 3.5 meters away from the resonator and aligned parallel to the inter-electrode gap. The RF feed-through, which is separated by 115 mm from the end of the

electrodes, acted as a background for the photograph of the discharge. The brightness levels of digital cameras are not linearly dependent on the luminance because there are designed to represent the object as it would be perceived by the human eye. Recognizing this, the relationship of output pixel values and luminosity was established by taking a series of measurement of the same object with a number of exposure durations t. The exposure value EV was then calculated as [5.9]:

$$EV = \log_2\left(\frac{N_{ap}{}^2}{t}\right) \tag{5.10}$$

where the lens aperture N_{ap} is the reciprocal of the camera lens f/#. Thus, the output of the camera was calibrated so that the exposure value EV is known as a function of the pixel brightness.

In the second step the known exposure values EV are converted to luminance L_{EV} using the relationship [5.9]:

$$L_{EV} = 2^{EV-3} \tag{5.11}$$

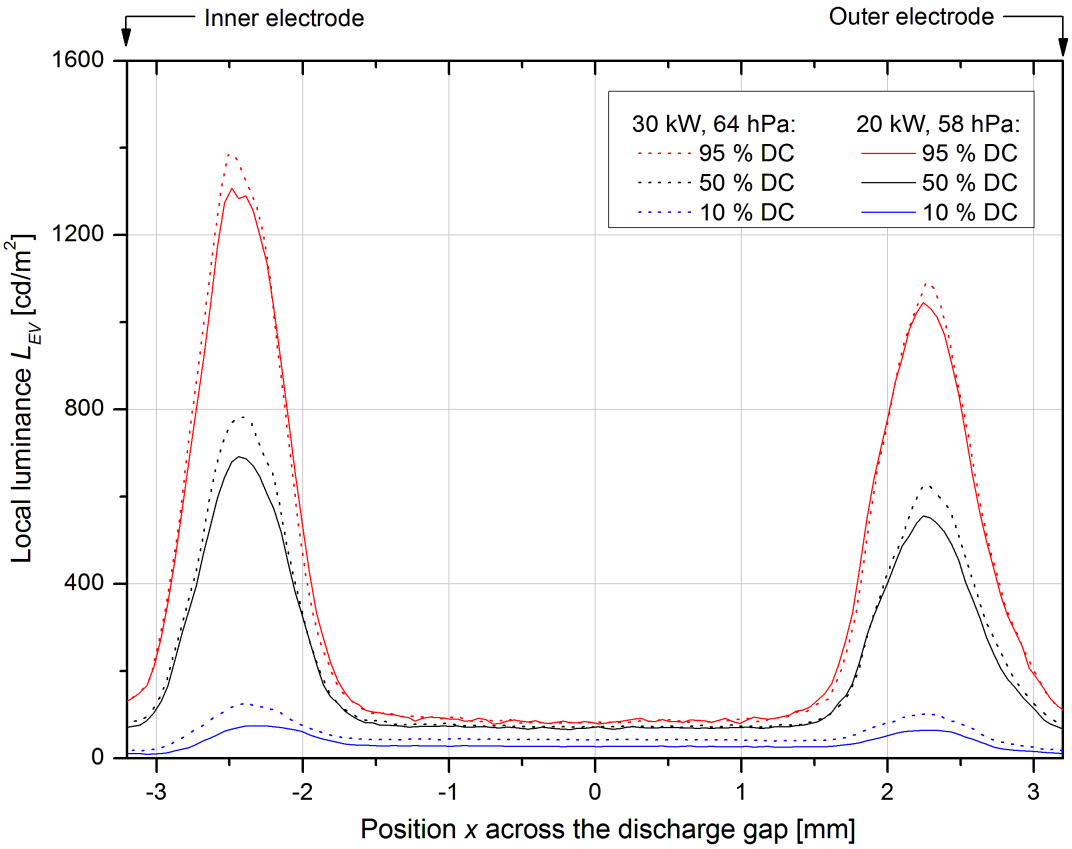

Figure 5.3 Measured discharge luminance across the gap as function of operating parameters.

The luminance distributions were recorded for two RF discharge power amplitudes (20 kW and 30 kW) and for three pulsing duty cycles (10%, 50% and 95%) at a 10 kHz gating frequency, using the procedure outlined above (see figure 5.3). The operating pressure was adjusted at both RF amplitude levels to keep similar discharge brightness distribution along the length. The results show that the RF amplitude has a minor effect on the discharge luminance. At 95% duty cycle the luminance of the peaks increases only by 5% to 6% when going from 20 kW to 30 kW. Consistent with the literature data, for example in [5.10], figure 4(b), the ion sheath thickness decreases with RF input power. The difference in ion sheath thickness for 20 kW and 30 kW is comparatively small and is of the order of 30 μm. A remarkable feature in the measurements is the difference of the height of the peaks by 20% with the left peak being closer to the inner electrode. The reason for this lies in the difference of surface area of the two electrodes due to the annular geometry:

$$\left(\frac{R+d/2}{R-d/2}\right)^2 = \left(\frac{77.5mm+3.5mm}{77.5mm-3.5mm}\right)^2 = 1.198 \tag{5.12}$$

However, the intra-cavity laser beam propagates twice through the discharge region but where the axicon mirror reverses the symmetry. In this way, the wedge effect of the gas in the discharge region due to the asymmetric power deposition is cancelled out. The average of the two peaks is taken for the Joule heat release profile *w(x)* to reflect the fact that the net power deposition is symmetric. Then the heat release profile is obtained by scaling the luminance profile $L_{EV}(x)$ with a scaling factor β, where x is the position across the discharge gap:

$$w(x) = \beta\, L_{EV}(x) \tag{5.13}$$

The constant factor β is calculated so that the average power density for the discharge gap d equals the power density based on the input power P and discharge volume V:

$$\beta = \frac{P/V}{\int_0^d L_{EV}(x)dx} \tag{5.14}$$

5.5 Temperature Profile Across the Discharge Gap

The steady-state heat distribution of the gas across the gap *d* can be calculated by solving the steady state heat equation [5.11]:

$$\nabla \bullet \left(-\lambda \nabla T\right) = w \tag{5.15}$$

where *w* is the Joule heat density and λ is the thermal conductivity.

The power density *w* in the above equation is *dW/dV* deposited into the gas. The equation (5.15) can be solved analytically if the thermal conductivity λ and power density *w* are constants. For the one dimensional case, with *x* being the coordinate variable, the equation (5.15) reduces to:

$$\frac{d^2T}{dx^2} = -\frac{w}{\lambda} \tag{5.16}$$

Double integration of the left and right hand side of equation (5.15) yields:

$$\iint T''(x)dx^2 = T(x) = -\frac{wx^2}{2\lambda} + c_2 x + c_1 \tag{5.17}$$

where c_1 and c_2 are integration constants.

If we assume that the temperature is the same for both left and right walls, we will have a symmetric temperature profile *T(x)*. In that case the integration constant c_2 needs to be zero:

$$c_2 = 0 \tag{5.18}$$

The boundary conditions are the known gas temperatures at the water cooled walls with temperature T_0:

$$T\left(-\frac{d}{2}\right) = T_0 \tag{5.19}$$

$$T\left(+\frac{d}{2}\right) = T_0 \tag{5.20}$$

The integration constant c_1 is found by inserting equation (5.19) or (5.20) into equation (5.17):

$$c_1 = \frac{8T_0\lambda + wd^2}{8\lambda} \tag{5.21}$$

With c_1 described by equation (5.21) and with equation (5.18), the temperature profile can be written as:

$$T(x) = -\frac{w}{2\lambda}x^2 + \frac{8T_0\lambda + wd^2}{8\lambda} \tag{5.22}$$

The analytical solution (equation (5.22)) is useful for estimating the influence of the parameters. However, as the thermal conductivity λ and the power density w are not constants but functions of temperature and space respectively, the analytical solution for the more realistic case does not exist. Instead, the temperature profile is calculated numerically using the mathematical software package (FlexPDE) with the boundary conditions $T_0 = 300$ K at $x = -d/2$ and at $x = d/2$. The comparison of temperature profiles using the analytical solution and the numerical calculation is shown in figure 5.4. The temperature in the centre of the gap is much lower for the numerical calculation (curve (b) in figure 5.4) mostly because of the applied power density function $w(x)$.

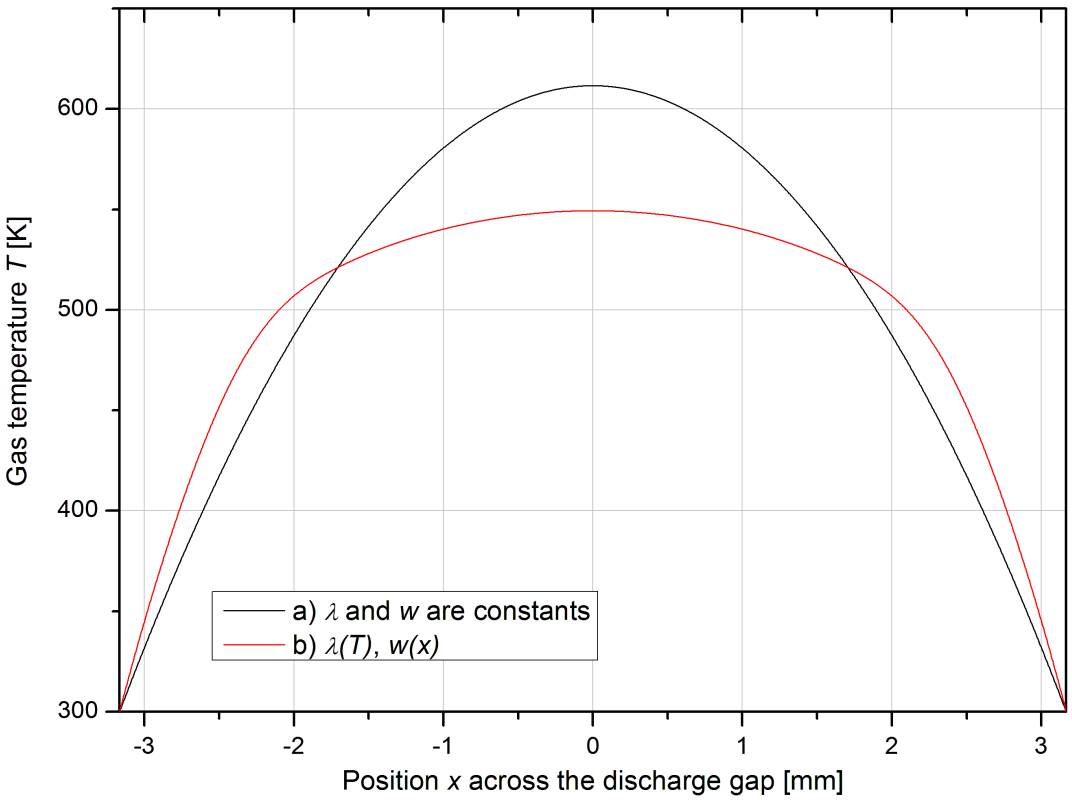

Figure 5.4 Gas temperature profile for a constant heating power release of 7.8 W/cm^3

This comparison reveals one reason why the RF discharge is advantageous for the excitation of CO_2 lasers, as explained here. According to the heat equation (5.16), the increase of the gas temperature is proportional to the applied power density w, the

distance x from the cooled wall and inverse proportional to the thermal conductivity λ. If the first moment of the applied heat is shifted from the centre of the discharge gap closer to the cooled walls, then the average gas temperature is expected to be lower for a constant w and λ. Therefore, higher power densities can be achieved in RF discharges compared to a constant Joule heat release across the gap.

5.6 Pressure in the Resonator as Function of RF Duty Cycle

The measurement of the pressure rise within the TruCoax laser due to gas heating by the RF discharge can be used to confirm the temperature profile calculation method. After making the link between the gas temperature obtained from calculations and the pressure increase in the vacuum vessel, the theoretical results will be compared with experimental data.

The overall volume V of laser gas within the laser vacuum vessel is occupied partly by the discharge volume V_{dis} and partly by the rest volume V_{rest} outside the discharge region. This relation can be expressed in terms of the amount of gas before and after ignition:

$$\frac{p_{cold}V}{T_{cold}} = \frac{p_{hot}V_{dis}}{T_{avg}} + \frac{p_{hot}V_{rest}}{T_{cold}} \tag{5.23}$$

The average gas temperature T_{avg} is calculated from the temperature profile and the ambient temperature T_{cold} is assumed to be 300 K. The volumes occupied by the discharge V_{dis} and the volume V_{rest} outside the discharge region but still within the vacuum vessel are estimated based on the CAD model. The magnitude of the pressure rise due to gas heating can be described by a scaling variable θ:

$$\theta = \frac{p_{hot}}{p_{cold}} \tag{5.24}$$

Equation (5.23) is solved for the scaling variable θ, yielding an expression for the pressure increase as a function of the dissipated power P:

$$\theta(P) = \frac{p_{cold}V\,T_{avg}(P)}{V_{rest}T_{avg}(P) + V_{dis}T_{cold}} \tag{5.25}$$

The measurement of the gas pressure at different duty cycles was performed on a TruCoax laser with RF input power magnitude of 32 kW. However, the discharge

impedance varies with the duty cycle, thereby affecting the matching network so that the mean reflected power P_{rm} should be subtracted from the incident RF power P_i.

The comparison of the data shows good correlation (figure 5.5), which confirmed that the assumption of the spatial power density $w(x)$ on one hand and also the boundary conditions for the calculations on the other hand were valid for the given setup. The initially-estimated volume of about 11.0 *l* had to be adjusted to 11.5 *l* to achieve a better fit to the measurements.

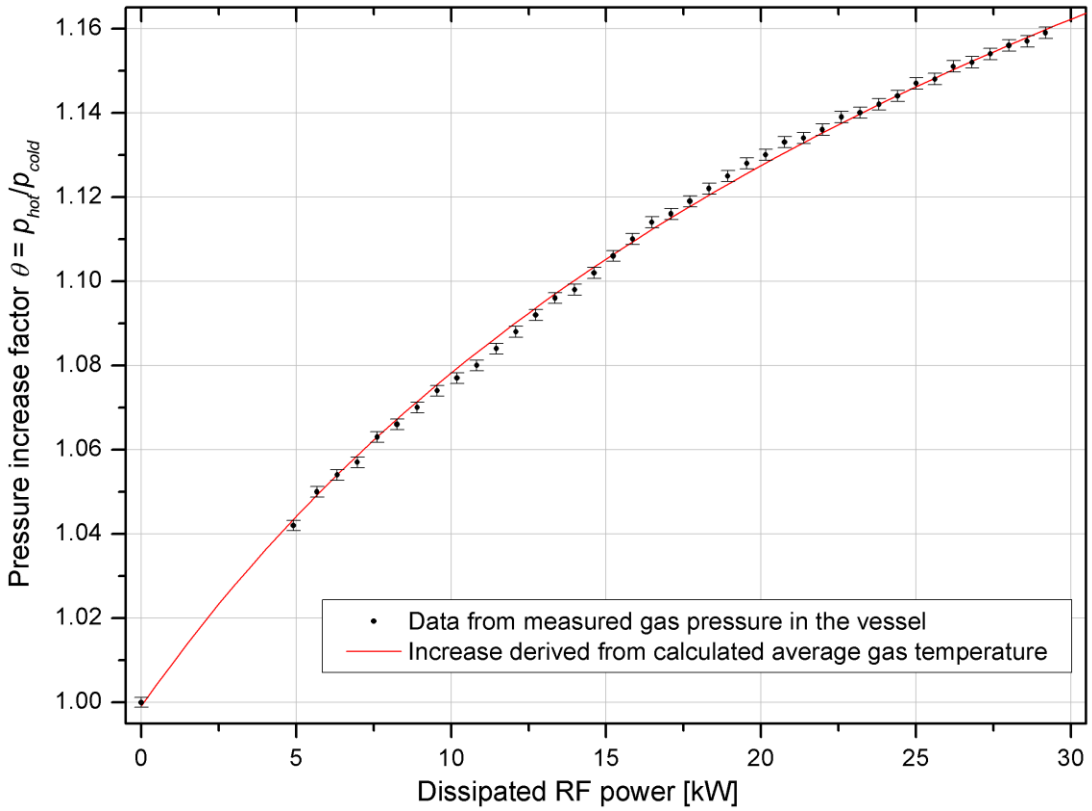

Figure 5.5 Measured pressure rise vs. RF power compared with calculated pressure rise ($V = 11.5\ l$, $V_{dis} = 3.8\ l$, $T_{cold} = 300$ K, $p_{cold} = 78.4$ hPa)

5.7 Lensing Effect due to Optical Path Curvature

As described previously, the refractive index n varies across the discharge gap due to the temperature gradient. This means the optical thickness of a discharge region of length L is also a function of the distance x of the beam travelling parallel to the optical axis. The optical thickness function $d_{opt}(x)$ can be expressed as a product of the discharge length L and the refractive index profile $n(x)$ as follows:

$$d_{opt}(x) = n(x)L \tag{5.26}$$

The goal is to calculate the radius of curvature of the optical thickness $d_{opt}(x)$, which would be the measure of the thermal lensing in the discharge region.

The radius of curvature $ROC(x)$ of a function $d_{opt}(x)$ can be calculated analytically [5.12]:

$$ROC(x) = \frac{\left[1 + d_{opt}'(x)^2\right]^{\frac{3}{2}}}{\left|d_{opt}''(x)\right|} \tag{5.27}$$

where $d_{opt}'(x)$ and $d_{opt}''(x)$ are first and second derivatives of $d_{opt}(x)$ after x.
This approach requires a continuous and derivative function $d_{opt}(x)$. However, the numerical calculation results in a number of discrete data points. The continuous function can be found by fitting a number of data points with a polynomial function, but taking a polynomial would already make assumptions about the behaviour of the numerical data. An alternative approach is to find a circle function through three neighbouring data points:

$$\left(x - x_c\right)^2 + \left(d_{opt}(x) - d_{opt}(x_c)\right)^2 = ROC(x)^2 \tag{5.28}$$

where the variables x_c and $d_{opt}(x_c)$ are the coordinates of the centre of the circle and $ROC(x)$ is the radius of curvature of the thermal lens at the point x. The results of these two approaches deviate by less than 0.5%, which leads to the conclusion that both approaches are legitimate solutions for the radius of curvature as a function of the position across the inter-electrode gap.

It is useful for applications, such as the ABCD matrix formalism, to represent the function $ROC(x)$ by a single effective thermal lensing radius of curvature R_{therm} or focal length f_{therm} with:

$$f_{therm} = \frac{R_{therm}}{2} \tag{5.29}$$

The calculated index profiles $n(x)$ (such as curve (b) in figure 5.6) reveal that $n(x)$ can be approximated by a circular function in the central region. The curvature of $n(x)$ increases rapidly towards the discharge walls, but on the other hand the laser beam intensity also decreases for the free space resonator configuration as indicated in figure 5.6 by curve (a).

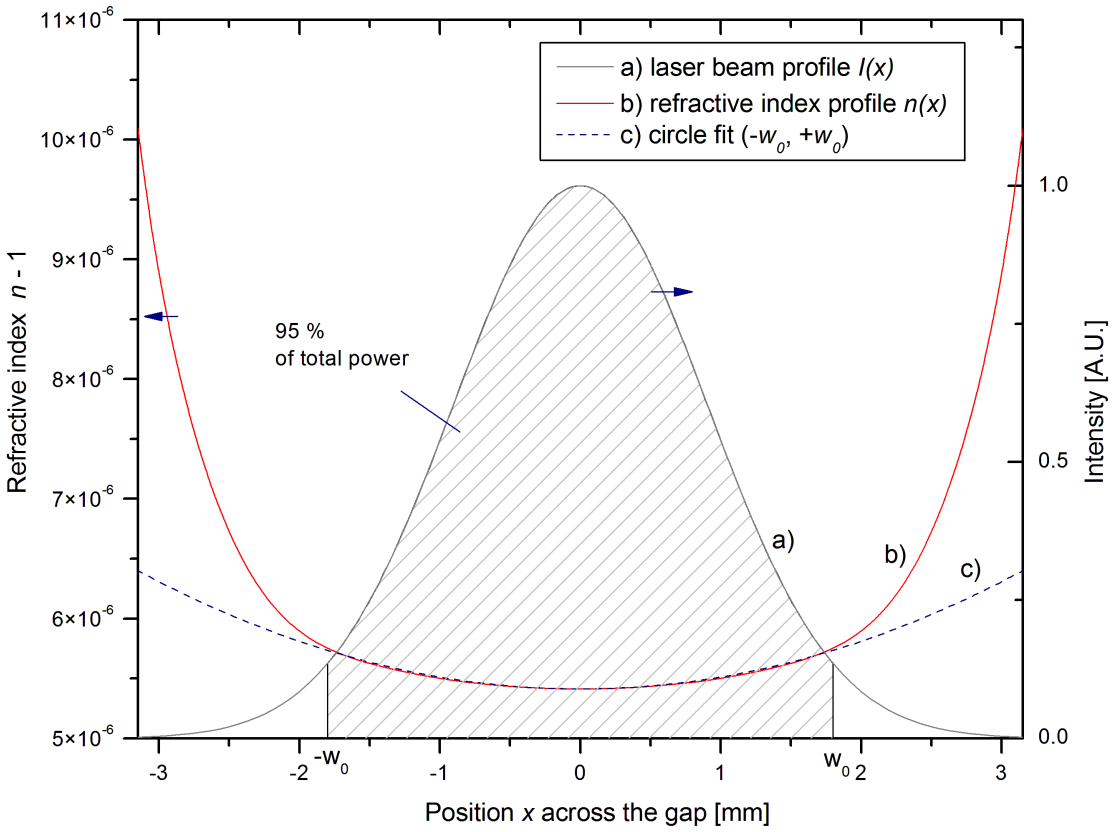

Figure 5.6 Approximation of the refractive index profile

a) Expected laser beam intensity

b) Refractive index profile (power density w = 7.6 W/cm^3, 91 hPa, dicharge gap d = 6.33 mm)

c) Circle fit of central region of refractive index profile (circle radius is 5.2 m)

As can be seen in figure 5.6, the refractive index and therefore the optical thickness is at minimum at the centre and increases towards the walls. The thermal lens becomes negative (de-focusing) for diffusion cooled gas lasers in contrast to a positive lens observed in solid state lasers.

5.8 Influence of Operating Parameters on Thermal Lensing

The procedure of thermal lens calculation is defined according to sections 5.1 - 5.7 and it enables now to qualify the influence of the many boundary conditions imposed on the system. Parameters such as the gas composition, which affects the thermal conductivity and RF excitation frequency of 27.12 MHz which affects the Joule heat profile, are kept fixed since they are not expected to be changed in the design phase. The impact of other parameters, such as the gap geometry, average power density and gas pressure can be tested in the model to find out which parameters needed to be included in the resonator design and which can be neglected.

The pulsing duty cycle of the RF input power is changed constantly during operation, because it is required to control the delivered average laser power. A commonly used pulsing frequency is 10 kHz. The pulse period at this frequency of 100 µs is much shorter than the thermal inertia of the laser gas which is in order of 2 - 3 ms. For this reason, the effect of the duty cycle on the thermal lens can be simulated by adjusting the average power load. The amount of gas inside the resonator remains the same when varying the duty cycle so that the operating pressure can be adjusted following the relationship investigated in section 5.5. The calculated thermal lensing results for 30 kW RF input power are shown in figure 5.7. The increase of thermal lensing is largest at low duty cycles up to about 60% duty cycle, which equals to a power density of about 4.7 W/cm^3. If the duty cycle is varied between 60% and 100%, the change of the thermal lensing effect is relatively small.

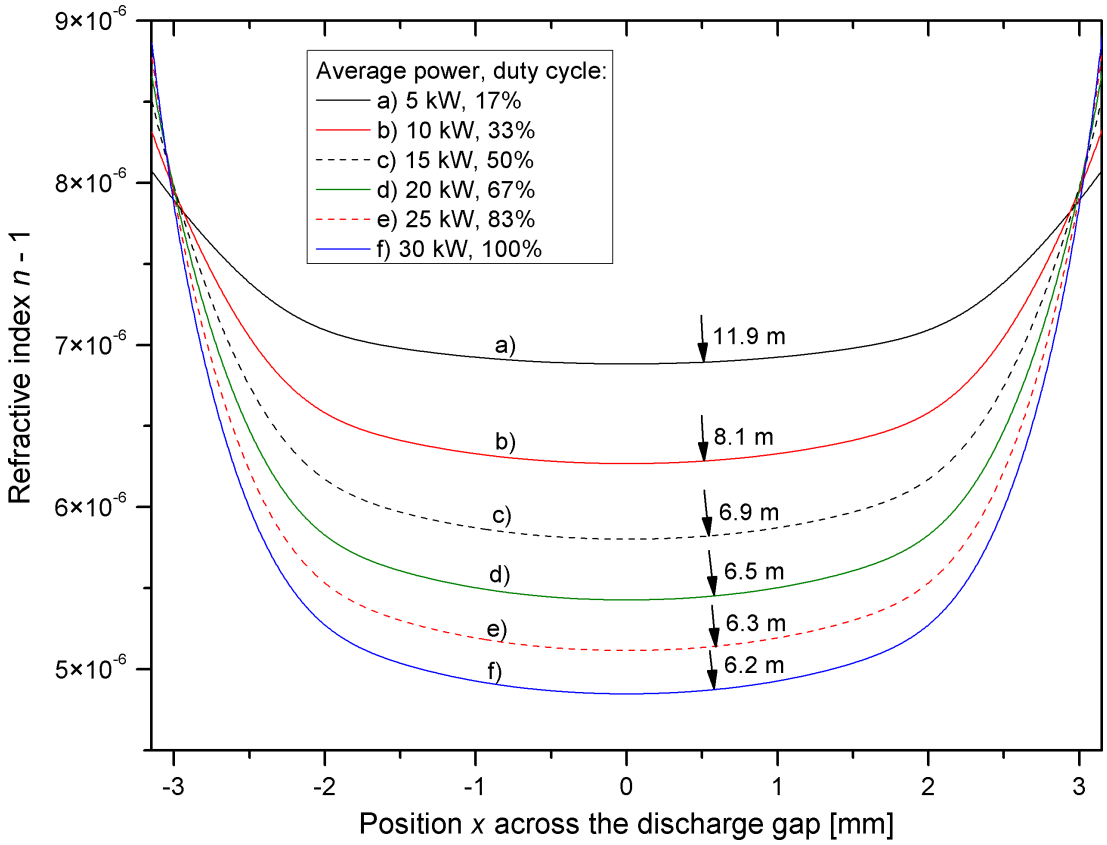

Figure 5.7 Refractive index profiles of the thermal lens as function of RF duty cycle for a discharge gap of 6.33 mm, power amplitude 30 kW (power density of 7.6 W/cm^3) and fill pressure 70 hPa in a TruCoax laser

The resonator can be operated at different values of RF input power and gas pressures. The radii of curvature of the thermal lensing element for two RF power levels (20 kW and

30 kW) and two operating pressures (70 hPa and 90 hPa) which is the typical bandwidth of the laser operation are shown in figure 5.8. It can be seen that the pressure setting plays a dominant role in the thermal lensing effect. The focal power of the thermal lens is linearly-dependent on the pressure (see equation (5.9)).

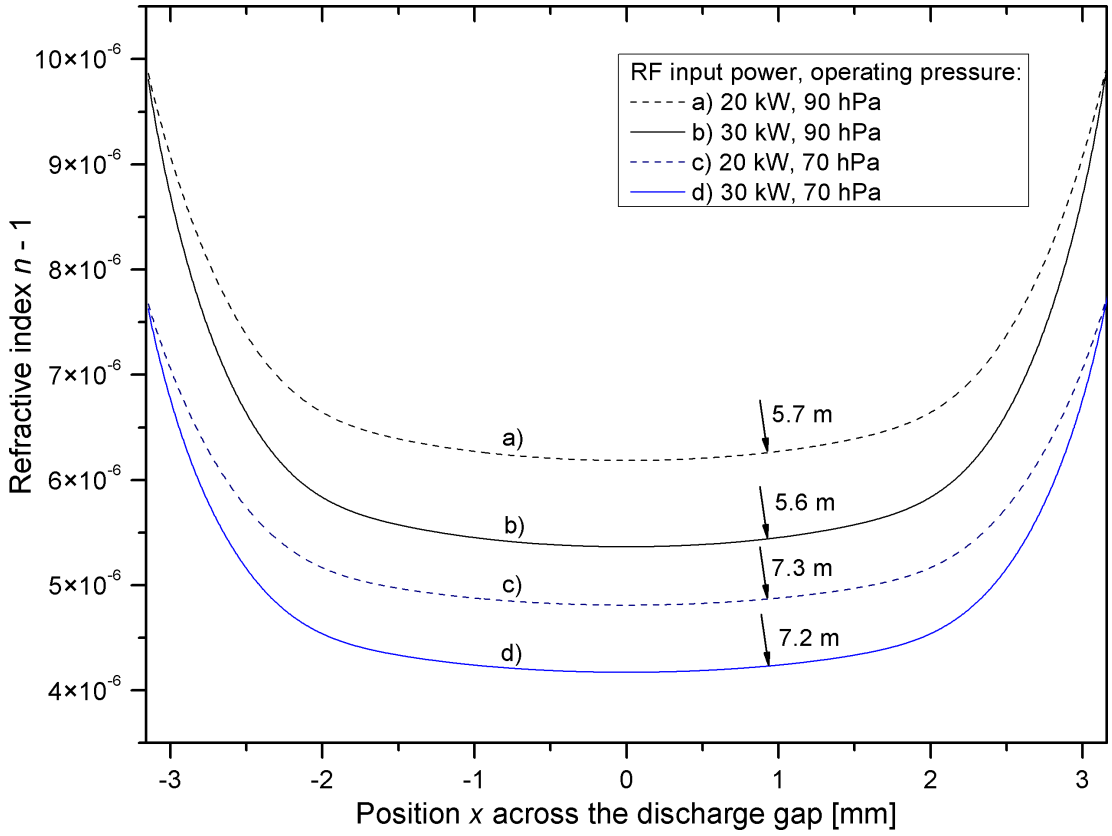

Figure 5.8 Refractive index profiles at two RF input powers (blue and black curves) and operating pressures (solid and dashed curves). The effective radius of curvature for 1.3 m discharge length as defined in figure 5.6 is shown for each curve.

The geometrical setup plays also an important role in the amount of thermal lensing generated by the discharge. The radius of curvature of the thermal lens was calculated for a range of different inter-electrode gaps. The operating pressure was kept constant while the gap size was changed to investigate the effect of thermal lensing in a caustic-shaped electrode setup. It was found to be necessary for the lateral power density profile *w(x)* to be adjusted for different discharge gaps, because according to the scaling laws the ion sheath thickness d_s does not change if the gas composition and excitation frequency remain the same [5.10]. The average power density is also scaled to keep the product of discharge volume *V* and power density *w* constant. The power density profiles and the resulting refractive index profiles of the thermal lensing for three discharge gaps are

shown in figure 5.9. The thermal lensing becomes more pronounced at smaller discharge gaps. The gas temperature in the discharge gap centre is lower for smaller gaps, but on the other hand the average power density is larger and the temperature gradient is similar throughout the scanning range of the discharge gaps.

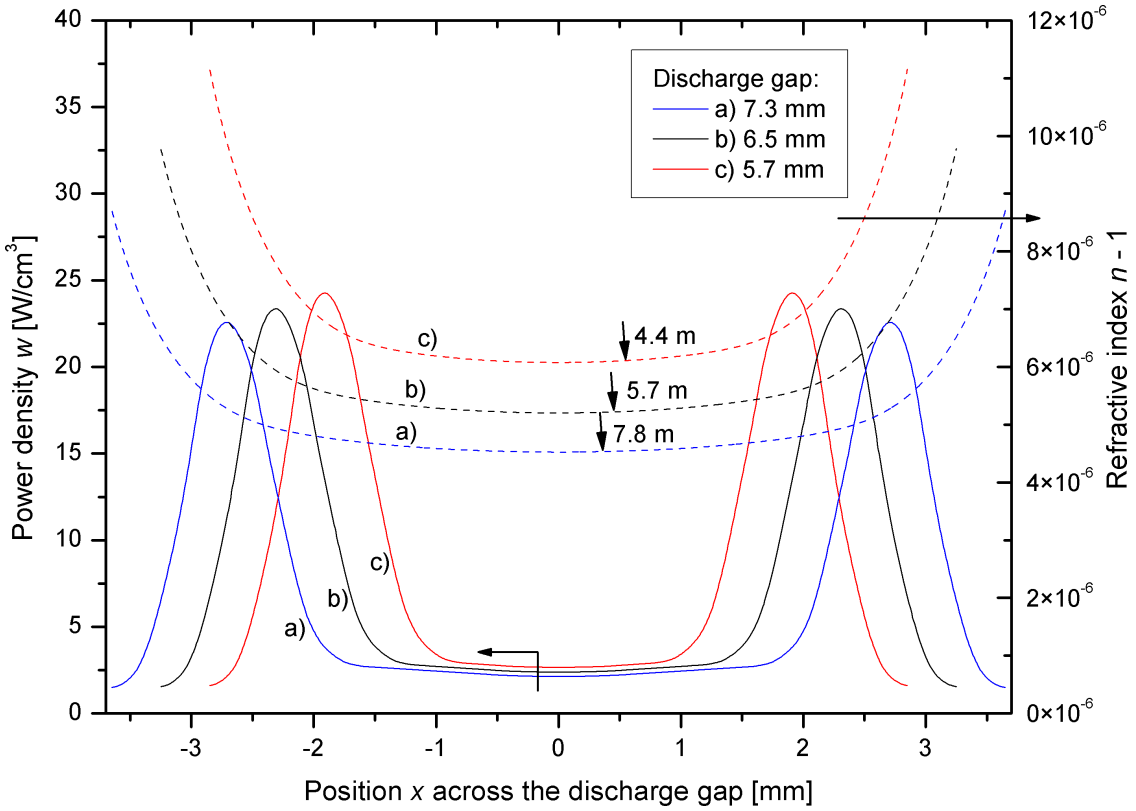

Figure 5.9 Refractive index and expected power density at three different discharge gaps for 30 kW RF input power. The operating pressure was adjusted according to RF discharge scaling laws for the refractive index profiles (78, 88 and 101 hPa for 5.7, 6.5 and 7.3 mm, respectively).

To conclude the investigation of thermal lensing as a function of the boundary conditions, the relative rank of the individual parameters was tested for a defined point of operation. Each of the parameters was modified by 1% of the original value and the resulting thermal lens effect was compared to the original state. The results of varying the duty cycle, pressure, discharge gap and RF input power are summarised in table 5.3. The parameters such as the excitation frequency and the gas mixture are not altered. The difference between the change of the duty cycle and the RF input power is the fact that when changing the duty cycle the amount of gas inside the resonator vessel remains constant. To achieve maximal power, the gas pressure is increased with RF input power. The increase of the pressure for this particular resonator design was found empirically to

be about 0.6 hPa per additional kW of RF input power. The calculation shows (table 5.3), that the discharge gap has the strongest impact on thermal lensing. By narrowing down the gap by 1%, the thermal lensing is increased by 1.21%. The next important factor is the gas pressure, which is linearly proportional to thermal lensing, as pointed out earlier. The change of either the duty cycle or RF input power by 1% make an insignificant contribution to the thermal lensing change if the laser head is operated at nominal power level as in case investigated here.

Table 5.3 Relative significance of changes in boundary conditions

Variable	Nominal value	1% variation	Relative change of f_{therm} or R_{therm}
Pressure *P*	70 hPa	+0.7 hPa	+1.00%
Duty cycle *dc*	95%	+0.95%	+0.04%
Gap *d*	6.3 mm	+63 µm	-1.21%
RF input power *P*	30 kW	+0.3 kW	+0.40%

5.9 Summary

In this chapter, the thermal lensing effect of the gas due to the temperature gradient perpendicular to the optical axis is investigated for typical operating conditions of a TruCoax CO_2 laser. The theoretical model developed here includes parameters such as the gas mixture, gas pressure and the lateral Joule heat release profile. The suggested model allowed an investigation of the thermal lensing effect as a function of the various boundary conditions, and provides valuable insights into what are the significant parameters to consider in terms of thermal lensing when designing a laser. The results gained from the calculation will serve as the foundation for Chapter 6 in which the effects of thermal lensing are included in the model of the stable optical resonator.

5.10 References

[5.1] N. B. Vargaftik “Справочник по теплофизическим свойствам газов и жидкостей” (Russian: “Handbook of thermo-physical properties of gases and fluids”), UDC 536.22+536.23 (1972)

[5.2] E. F. Plinski, J. S. Witkowski “Prediction of the thermal properties of CO_2, CO and Xe laser media”, Opt. Laser Technol., vol. 33, pp. 61-66 (2001)

[5.3] E. A. Mason, S. C. Saxena “Approximate formula for the thermal conductivity of gas mixtures”, Phys. Fluids, vol. 1, pp. 361-369 (1958)

[5.4] M. Born, E. Wolf “Principles of optics”, Cambridge University Press, ISBN 0-521642221 (1999)

[5.5] D. R. Lide “CRC Handbook of chemistry and physics, 85th edition”, CRC Press, ISBN 0-849-304857 (2004)

[5.6] R. J. Tilley “Understanding solids: the science of materials”, Willey, ISBN 0-470-85275-5 (2004)

[5.7] Yu.P. Raizer “Gas discharge physics”, Springer, ISBN 3-540-19462-2 (1997)

[5.8] Yu. P. Raizer, M. N. Shneider, N. A. Yatsenko “Radio-frequency capacitive discharges”, CRC Press, ISBN 0-8493-8644-6 (1995)

[5.9] R. E. Jacobson, S. F. Ray, G. G. Attridge, N. R. Axford “The manual of Photography”, Focal Press, ISBN 0-240-51574-9 (2000)

[5.10] P. P. Vitruk, H. J. Baker, D. R. Hall “Similarity and scaling in diffusion-cooled RF-excited carbon dioxide lasers”, IEEE J. Quant. Electron., vol. 30, pp. 1623-1634 (1994)

[5.11] J. Lienhard IV, J. Lienhard V “A heat transfer textbook”, Phlogiston Press Cambridge, ISBN 0-971-38352-9 (2002)

[5.12] L. Papula “Mathematik für Ingenieure und Naturwissenschaftler Band 1”, Vieweg, ISBN 3-528-94236-3 (2001)

Chapter 6

IMPACT OF THERMAL LENSING ON THE COAXIAL LASER RESONATOR

6.1 Introduction

In the previous chapter the thermal profile across the discharge gap in the TruCoax resonator was calculated based on the known operating parameters. The resulting refractive index profile leads to an interaction between the laser beam and the gas medium, which is termed as the thermal lensing effect.

The impact of the thermal lensing on the optical resonator in the stable direction is the subject of the investigation in this chapter. The predicted thermal lensing effect will be compared with experimental measurements to enable an estimate to be made of the error of the theoretical prediction, and corresponding possible over-simplification involved. The ABCD matrix formalism will be used as a tool to describe the thermal lensing in the medium, which will be incorporated into a model of the TruCoax laser optical resonator in the stable direction. The model of the laser resonator will then be used to estimate the beam expansion due to thermal lensing as a function of the position along the optical axis. The combined knowledge of thermal lensing and an accurate modelling of the beam propagation in the radial direction will produce a better optical representation of the TruCoax laser resonator.

6.2 Analytical Equation for Thermal Lensing Optical Element

As pointed out in the section 5.7, the refractive index profile can be approximated by a circular function around the centre of the discharge gap. These steps allow one to represent the lateral de-focusing power across the gap $f(x)$ in terms of a single parameter, the focal length, f_{therm} of the thermal lens medium over the discharge length L in the optical axis direction z. The spatial extent of the thermal lensing medium along the z-axis

can be represented by a series of diverging lenses. In figure 6.1(a) one approach is shown with three lenses separated by *L/2*. Generally this model can be described in the ABCD matrix formalism as:

$$M_{LPL} = \begin{pmatrix} 1 & 0 \\ -\dfrac{1}{f_{therm}(n+1)} & 1 \end{pmatrix} \cdot \left[\begin{pmatrix} 1 & \dfrac{L}{n} \\ 0 & 1 \end{pmatrix} \cdot \begin{pmatrix} 1 & 0 \\ -\dfrac{1}{f_{therm}(n+1)} & 1 \end{pmatrix} \right]^n \tag{6.1}$$

where f_{therm} is the focal length of the entire thermal lensing region and n is the number of subsections.

The product matrix can be further simplified if the thermal lensing element consists only of pairs of lens and free space propagation elements as shown in figure 6.1(b):

$$M_{LP} = \left[\begin{pmatrix} 1 & \dfrac{L}{n} \\ 0 & 1 \end{pmatrix} \cdot \begin{pmatrix} 1 & 0 \\ -\dfrac{1}{f_{therm}n} & 1 \end{pmatrix} \right]^n \tag{6.2}$$

The representation of the thermal lensing medium is less realistic in the case of $M_{LP,}$ since the results will be dependent on the propagation direction. However, for a sufficiently large number of subsections n, the two approaches will converge towards the same solution.

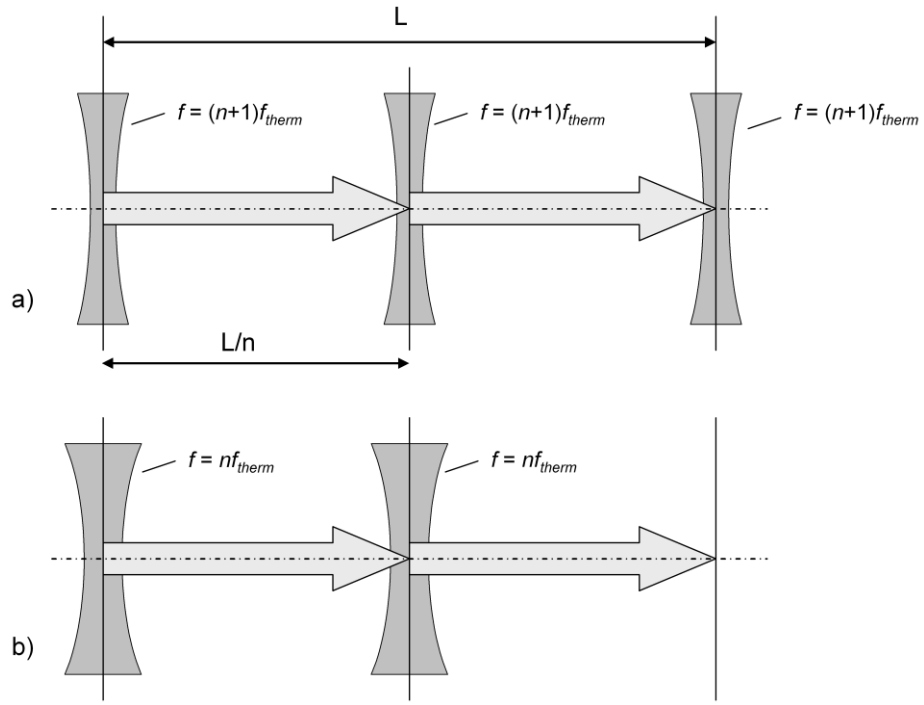

Figure 6.1 Approximation of the thermal lensing medium with a series of lenses, shown here for n = 2:
a) lens - propagation path - lens (LPL) model
b) lens - propagation path (LP) model

A matrix expression M_{therm} for a continuously beam-diverging medium of overall focal length f_{therm}, which extends over the length L, can be found by calculating the limit of the power of the matrix:

$$M_{therm} = \lim_{n\to\infty}\left[\begin{pmatrix} 1 & \frac{L}{n} \\ 0 & 1 \end{pmatrix}\cdot\begin{pmatrix} 1 & 0 \\ -\frac{1}{f_{therm}n} & 1 \end{pmatrix}\right]^n = \lim_{n\to\infty}\begin{pmatrix} 1-\frac{L}{f_{therm}n^2} & \frac{L}{n} \\ -\frac{1}{f_{therm}n} & 1 \end{pmatrix}^n = \lim_{n\to\infty} M^n \qquad (6.3)$$

The problem has to be solved in two steps. An analytical expression for the matrix to the n-th power needs to be derived in the first step, while the second step involves the computation of the convergence terms for an infinitely-large number of subsections n.

The method of eigenvalue decomposition can be used as showed in [6.1] to calculate the power of the matrix M, provided that the matrix is diagonalizable:

$$M^n = S\Lambda^n S^{-1} \qquad (6.4)$$

The matrix Λ is a diagonal matrix where its elements are the eigenvalues λ_1 and λ_2 of the matrix M, and where the matrix S is the eigenvector matrix. The columns of S are the eigenvectors v_1 and v_2, and the matrix S^{-1} is the inverse matrix of S. Since the matrix Λ consists only of diagonal values, its n-th power can be calculated very conveniently by raising each element to the n-th power.

The eigenvalues of matrix M are calculated from the characteristic equation with I_2 being a 2×2 identity matrix:

$$\det(M - \lambda I_2) = 0 \qquad (6.5)$$

The eigenvalues of matrix M are:

$$\lambda_1, \lambda_2 = \frac{\pm\sqrt{L^2 - 4n^2 L f_{therm}} + 2n^2 f_{therm} - L}{2n^2 f_{therm}} \qquad (6.6)$$

The eigenvectors v_1 and v_2 of eigenvalues λ_1 and λ_2, respectively, are those non-zero vectors that satisfy the equation [6.2]:

$$(M - \lambda I_2)\cdot v = 0 \qquad (6.7)$$

Solving equation (6.7) for eigenvalues of matrix M, we obtain the eigenvectors v_1 and v_2:

$$\nu_1, \nu_2 = \begin{pmatrix} \frac{1}{2n}\left(L \pm \sqrt{L^2 - 4n^2 L f_{therm}}\right) \\ 1 \end{pmatrix} \tag{6.8}$$

The two eigenvectors v_1 and v_2 define the eigenvector matrix S as:

$$S = \begin{pmatrix} \frac{1}{2n}\left(L + \sqrt{L^2 - 4n^2 L f_{therm}}\right) & \frac{1}{2n}\left(L - \sqrt{L^2 - 4n^2 L f_{therm}}\right) \\ 1 & 1 \end{pmatrix} \tag{6.9}$$

Inserting matrix S from equation (6.9) into equation (6.4) yields:

$$M^n = \begin{pmatrix} S_{11} & S_{12} \\ S_{21} & S_{22} \end{pmatrix} \cdot \begin{pmatrix} \lambda_1{}^n & 0 \\ 0 & \lambda_2{}^n \end{pmatrix} \cdot \left[\frac{1}{\det(S)} \begin{pmatrix} S_{22} & -S_{12} \\ -S_{21} & S_{11} \end{pmatrix} \right] \tag{6.10}$$

The expressions in each matrix cell are rather long, so to illustrate the subsequent procedure only the matrix element in the second line, first column, M_{21} will be demonstrated. The expression is found by multiplication of matrix elements in equation (6.10):

$$\left(M^n\right)_{21} = \frac{n}{r^*}\left[\left(\frac{2n^2 f_{therm} - L - r^*}{2n^2 f_{therm}} \right)^n - \left(\frac{2n^2 f_{therm} - L + r^*}{2n^2 f_{therm}} \right)^n \right] \tag{6.11}$$

with

$$r^* = \sqrt{L^2 - 4n^2 L f_{therm}} \tag{6.12}$$

For large number of sections ($n \to \infty$), the terms without n can be omitted. The equation (6.11) can then be simplified to:

$$\lim_{n\to\infty}\left(M^n\right)_{21} = \frac{1}{\sqrt{-4L f_{therm}}}\left[\left(1 - \frac{\sqrt{-4n^2 L f_{therm}}}{2n^2 f_{therm}} \right)^n - \left(1 + \frac{\sqrt{-4n^2 L f_{therm}}}{2n^2 f_{therm}} \right)^n \right] \tag{6.13}$$

The power terms are defined as exponential functions ([6.3], page 70):

$$\lim_{x\to\infty}\left(1 \pm \frac{k}{x}\right)^x = \exp\left(\pm k\right) \tag{6.14}$$

By applying the equation (6.13) we arrive at:

$$\lim_{n\to\infty}\left(M^n\right)_{21} = \frac{\exp\left(-\frac{\sqrt{-L f_{therm}}}{f_{therm}} \right) - \exp\left(\frac{\sqrt{-L f_{therm}}}{f_{therm}} \right)}{2\sqrt{-L f_{therm}}} \tag{6.15}$$

With the hyperbolic sine:

$$\sinh(x) = \frac{\exp(x) - \exp(-x)}{2} \tag{6.16}$$

The expression in equation (6.15) can be simplified using equation (6.16) to:

$$\lim_{n\to\infty}\left(M^n\right)_{1,2} = \frac{-\sinh\left(\frac{\sqrt{-Lf_{therm}}}{f_{therm}}\right)}{\sqrt{-Lf_{therm}}} \tag{6.17}$$

A similar procedure is applied to the other elements in the M_{therm} matrix, and the resulting analytical solution for the thermal lens matrix is:

$$M_{therm} = \begin{pmatrix} \cosh\left(\frac{b}{f_{therm}}\right) & \frac{Lf_{therm}}{b}\sinh\left(\frac{b}{f_{therm}}\right) \\ -\frac{1}{b}\sinh\left(\frac{b}{f_{therm}}\right) & \cosh\left(\frac{b}{f_{therm}}\right) \end{pmatrix} \tag{6.18}$$

where b denotes a repeating term in the matrix:

$$b = \sqrt{-Lf_{therm}} \tag{6.19}$$

The value of f_{therm} is negative, since the medium is de-focusing, making all the expressions real.

Verdeyen [6.4] derived a matrix expression for a continuous lens starting with a differential equation for ray trajectories. The expression is ([6.4], page 55):

$$T = \begin{pmatrix} \cosh\left(\frac{L}{F}\right) & F\sinh\left(\frac{L}{F}\right) \\ \frac{1}{F}\sinh\left(\frac{L}{F}\right) & \cosh\left(\frac{L}{F}\right) \end{pmatrix} \tag{6.20}$$

where L is the length of the medium as in equation (6.18) and F is a parameter describing the refractive index profile in lateral direction x ([6.4], page 55):

$$n(x) = n_0\left(1 + \frac{x^2}{2F^2}\right) \tag{6.21}$$

Matrix M_{therm} describes the de-focusing magnitude of the medium by a focal length f_{therm}, whereas the matrix T gets it directly from knowledge of the refractive index profile.

Comparison of the matrix elements in M_{therm} (equation 6.18) and T (equation 6.20) shows that the two matrix derivations are equivalent if:

$$f_{therm} = -\frac{F^2}{L} \tag{6.22}$$

The above equation also provides the link between the different notations.

The analytical solution in equation (6.18) can also be tested for correctness by comparing the results with a numerical calculation. The thermal lensing matrix can be calculated numerically for a number n of subsections using equation (6.1) or the simplified equation (6.2). The relative difference between the numerical and analytical results for f_{therm} = -3 m and L = 1.3 m, which are typical values for TruCoax laser, is plotted in figure 6.2. It can be seen that the numerical solution converges towards the analytical result with increasing number of subsections, as was expected. The plots also show that the numerical solution with the "lens-propagation path-lens" system is generally closer to the analytical solution compared to the "lens-propagation path" system (compare figure 6.1(a)) and 6.1(b)).

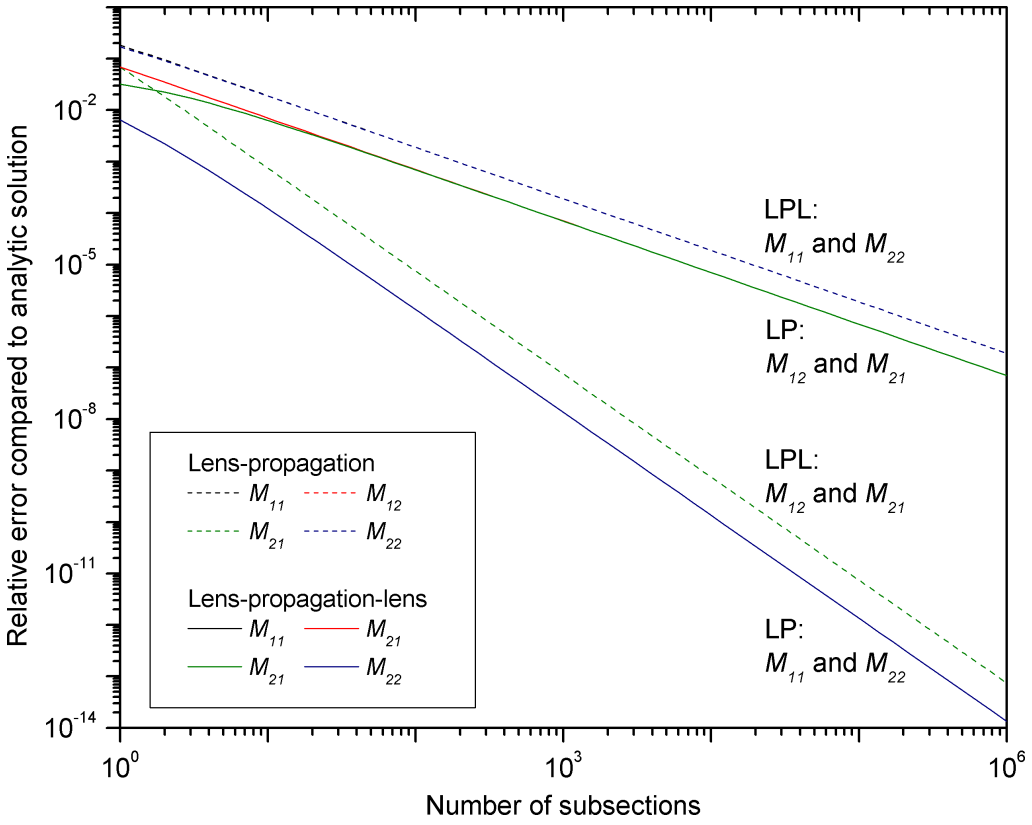

Figure 6.2 Relative difference between numerically calculated values and the solution from the analytical equation for individual matrix elements. Thermal lensing parameters are: f_{therm} = -3 m, L = 1.3 m.

6.3 Measurement of Thermal Lensing and Comparison with Calculations

The method for calculation of the ABCD matrix for a given discharge length L and thermal lensing focal length f_{therm} makes possible an indirect measurement of the thermal lensing in the TruCoax laser. The experimental setup is depicted schematically in figure 6.3(a). In this configuration the TruCoax optical resonator mirrors are replaced by optical grade silica windows with slightly wedged surfaces. A HeNe laser beam with a wavelength of 632.9 nm is aligned to be parallel to the optical axis in the centre of the RF discharge gap. The beam size of the HeNe laser is measured by evaluation of the data from a digital image of the beam profile. Examples of acquired images with the RF discharge turned on and off in the TruCoax discharge cell are shown in figure 6.3(b). The beam radius of the HeNe laser is measured by free space propagation over several distances throughout the measurement range and fitted with a Gaussian beam profile. The experimental configuration is modelled using the ABCD matrix formalism with the HeNe beam as input beam and the thermal lens matrix M_{therm} describing propagation through the discharge cell. The focal length of the thermal lensing region f_{therm} is deduced by adjusting the value of f_{therm} so that the resulting beam size at the point of observation equals the measured beam size.

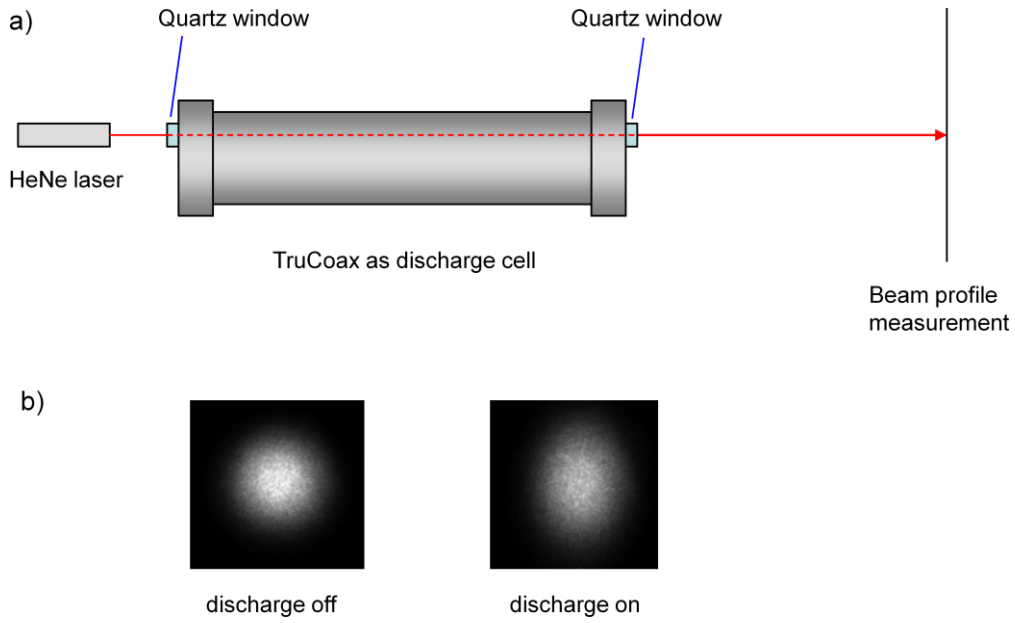

Figure 6.3 Measurement of thermal lensing:

a) schematic representation of experimental setup

b) typically recorded HeNe laser beam profile with and without thermal lensing

The beam profile was recorded with an acquisition rate of two images per second. The beam radius in the direction of the thermal lens is calculated using the method of "second moments". An example of beam size measurement in this experimental setup is shown in figure 6.4. We can see an abrupt beam size increase after the discharge is turned on to full power. After an initial stabilization phase of about five minutes, where the thermal lensing properties (RF discharge distribution, electrodes temperature, pressure due to dissociation degree) converge towards an equilibrium state, the pulsing duty cycle is reduced after one minute running time at each setting. As can be seen in figure 6.4, the measurement accuracy is clearly sufficient to resolve the beam size variations for duty cycle steps of 10%. It was noted that the RF discharge does not fill the entire discharge gap in the longitudinal direction for duty cycles below 30%. At these low duty cycles the measured beam size starts to drift, caused by slow shifting of the RF discharge boundary.

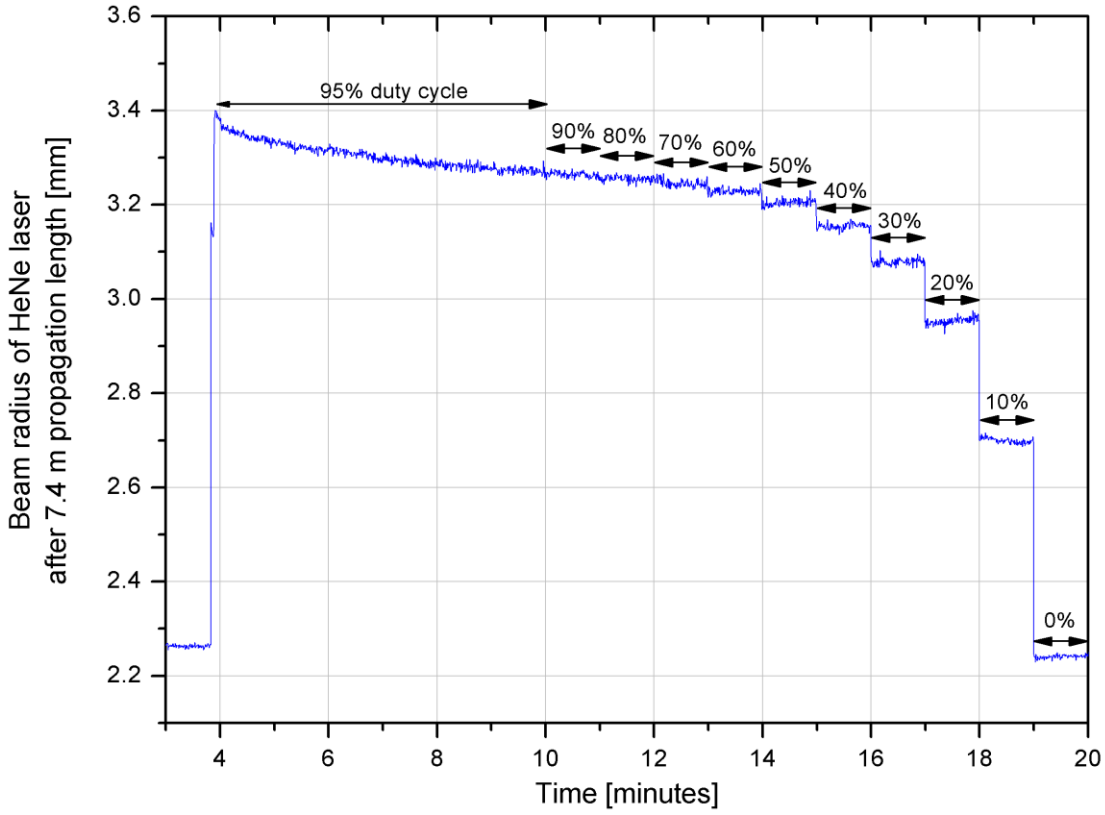

Figure 6.4 Measured beam size of HeNe laser after propagation through a TruCoax discharge cell. RF power amplitude is 30.5 kW, fill-up pressure is 77 hPa, average discharge gap is 6.6 mm. The pulsing duty cycles at 10 kHz are indicated for each setting.

The comparison of the indirect measurement of the thermal lensing focal length and the calculation is shown in figure 6.5. The measurement data (figure 6.4) was used to find the

thermal lensing values (dots (a) in figure 6.5). The procedure for the thermal lens calculation (curve (b) in figure 6.5) is described in Chapter 5. Constant longitudinal RF power density was assumed.

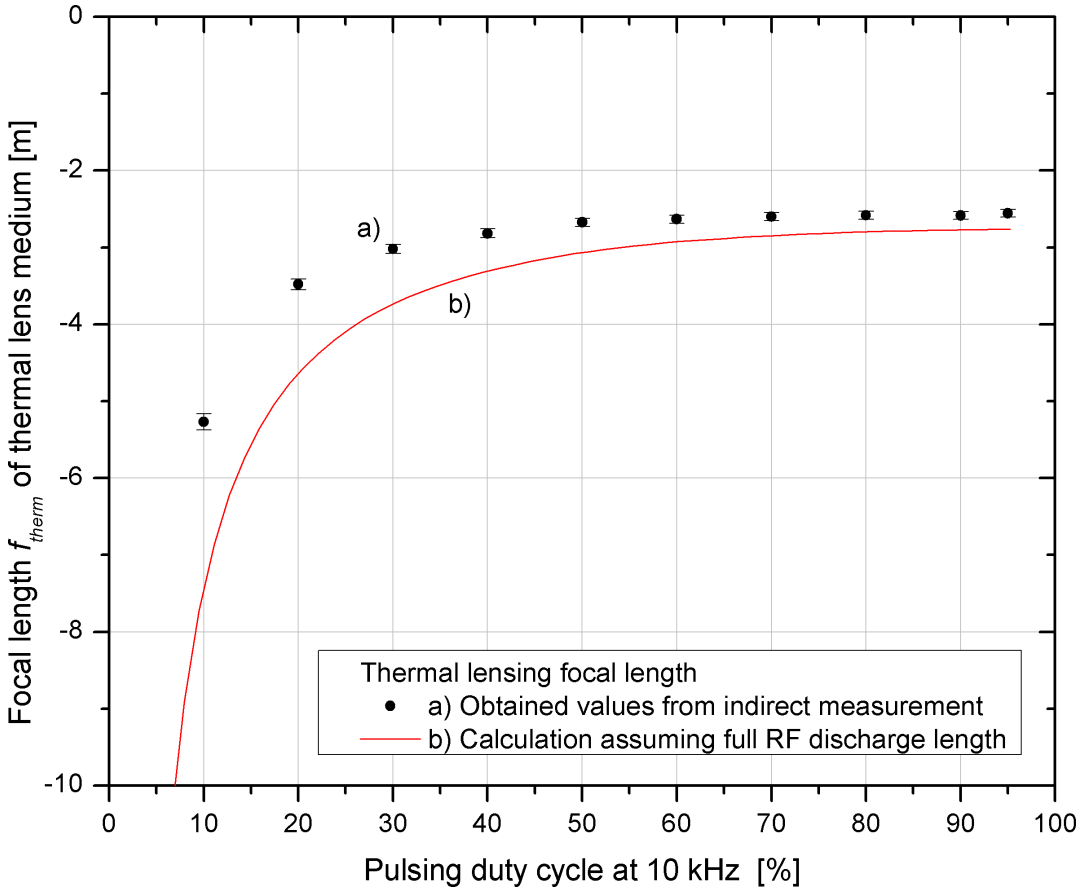

Figure 6.5 Comparison of indirectly measured thermal-lensing radii of curvatures (based on data shown in figure 6.4) and calculation as function of RF input power.

In general, the experimental results show that the effect of thermal lensing is consistently underestimated by the theoretical model.

It should be noted that the interaction of the beam with the thermal lensing medium in the regions close to the electrodes was neglected in the theoretical model, since the beam intensity is very low compared to that in the central region. However, it may be that this effect could be large enough to produce a noticeable increase in the overall thermal lensing power. The shrinkage of the RF discharge at lower duty cycles can also affect the overall thermal lensing, which was not addressed in the model. Nevertheless, at the maximal power level the relative difference of about 8% in thermal lensing values gives a

reasonable correlation between measurement and theory considering the number of calculation steps that are involved.

6.4 Beam Propagation in the Stable Direction of TruCoax Resonator

The mathematical representation of the thermal lensing in terms of an ABCD matrix and the accuracy of the model was discussed in the previous section. The goal of this section is to study the impact of applying this model to the beam propagation in the stable direction of the TruCoax laser resonator. Starting with a simple two mirror configuration, the resonator model will be further extended to represent impact of thermal lensing on beam propagation in the TruCoax laser resonator in the stable direction.

6.4.1 Thermal lensing in a symmetric two mirror resonator

The effect of thermal lensing can be studied for a simple resonator configuration consisting of two mirrors with the same focal length as shown in figure 6.6. The distance *d* between the mirrors and the thermal lensing region is equal for both mirrors, so making the resonator symmetric.

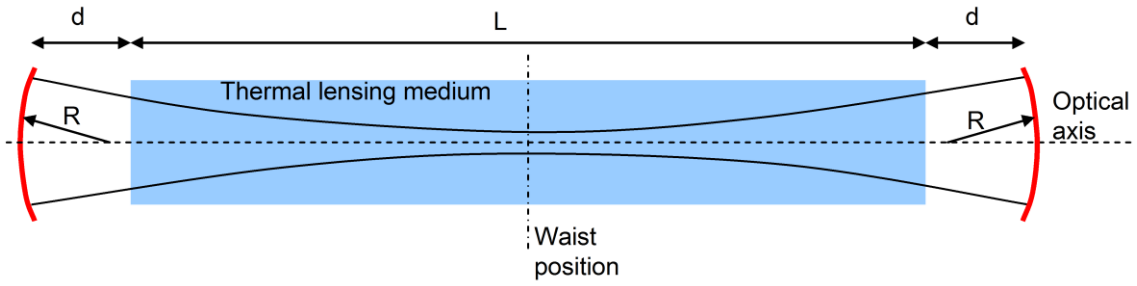

Figure 6.6 A symmetric stable two mirror resonator with a thermal lensing medium

The calculation procedure of intra-cavity beam propagation can be illustrated using the simple case of a symmetric two mirror configuration.

(a) Find transfer matrix of the optical system

The advantage of such a configuration is that the beam waist position will be constant regardless of the thermal lensing focal length f_{therm} and the radii of curvature R of the mirrors. Starting with the waist position, one beam round trip in the resonator is modelled by cascaded multiplication of the matrices. The resonator is symmetric so that

mathematically the resonator consists of propagation through two identical "half-resonators". It is therefore sufficient to describe the transfer matrix as:

$$\begin{pmatrix} A & B \\ C & D \end{pmatrix} = M_{therm}\left(2f_{therm}, \frac{L}{2}\right) \cdot \begin{pmatrix} 1 & d \\ 0 & 1 \end{pmatrix} \cdot \begin{pmatrix} 1 & 0 \\ -\frac{2}{R} & 1 \end{pmatrix} \cdot \begin{pmatrix} 1 & d \\ 0 & 1 \end{pmatrix} \cdot M_{therm}\left(2f_{therm}, \frac{L}{2}\right) \qquad (6.23)$$

where $M_{therm}(2f_{therm},L/2)$ is the thermal lensing matrix as defined in equation (6.18).

(b) Calculate the complex curvature of the resonator beam

The condition for the beam in the stable direction is to remain constant after any number of roundtrips. The Gaussian beam is described by a complex beam parameter (also complex radius of curvature) q as [6.5]:

$$q = z + jz_R \qquad (6.24)$$

The real part z is the distance to the beam waist and the argument of the imaginary number z_R is the Rayleigh range. The complex beam parameter q_t in the waist position after t roundtrips should be therefore the same as the complex beam parameter q_{t+1} after $t + 1$ round trips [6.6]:

$$\begin{pmatrix} q_{t+1} \\ 1 \end{pmatrix} \equiv \begin{pmatrix} A & B \\ C & D \end{pmatrix} \cdot \begin{pmatrix} q_t \\ 1 \end{pmatrix} \qquad (6.25)$$

The solution for the complex beam parameter q_{res} in a stable resonator can be found by inserting

$$q_{res} = q_t = q_{t+1} \qquad (6.26)$$

into the equation (6.23), setting the determinant of the transfer matrix to unity and solving for q_{res}.

The two solutions are:

$$q_{res1} = \frac{1}{2C}\left(A - D + \sqrt{A^2 + 2AD + D^2 - 4}\right) \qquad (6.27)$$

$$q_{res2} = \frac{1}{2C}\left(A - D - \sqrt{A^2 + 2AD + D^2 - 4}\right) \qquad (6.28)$$

The second solution in equation (6.28) delivers positive numbers for the Rayleigh range z_R and is used for further calculations.

(c) Calculate the beam size from complex radius

The final step is necessary if we need to know the Gaussian beam radius w at a point z in the resonator. The complex beam parameter q_{res2} in the centre of the resonator is known from equation (6.28). Multiplying the result with the thermal lensing matrix M_{therm} gives

a two-element matrix with two complex numbers c_1 and c_2 as a function of propagation distance z, starting from the beam waist position:

$$\begin{pmatrix} c_1(z) \\ c_2(z) \end{pmatrix} = M_{therm}(f_{therm}, z) \cdot \begin{pmatrix} q_{res2} \\ 1 \end{pmatrix} \tag{6.29}$$

The vector is normalised to the second element to obtain the complex beam parameter q at the propagation distance z:

$$\begin{pmatrix} q(z) \\ 1 \end{pmatrix} = \frac{1}{c_2(z)} \cdot \begin{pmatrix} c_1(z) \\ c_2(z) \end{pmatrix} \tag{6.30}$$

As mentioned earlier, the real part of the complex beam parameter q describes the distance z to the beam waist and the imaginary number value is the Rayleigh range. We can insert the complex beam parameter into the Gaussian beam propagation function to obtain the beam radius at propagation distance z, as follows:

$$w(z) = \sqrt{\mathrm{Im}(q(z)) \frac{\lambda}{\pi} \left[1 + \frac{\mathrm{Re}(q(z))}{\mathrm{Im}(q(z))} \right]^2} \tag{6.31}$$

The beam radii in the thermal lensing medium were calculated using the procedure described for L = 1.3 m, d = 59.5 mm and f_{therm} = -2.6 m (see figure 6.6). The radii of curvatures R were varied, whereas other values were kept constant to study the impact of the thermal lensing on the resonator design. The beam radii in the thermal lensing medium are shown for three configurations. The solid lines represent the beam radii for a free space propagation in the resonator (f_{therm} = -∞ m) for comparison. For short mirror focal lengths (R = 0.75 m in figure 6.7), the beam becomes larger in the beam waist region but smaller towards the mirrors. As the mirror curvature is decreased and moves from the concentric to the confocal stable resonator region, the beam becomes larger in the entire region due to thermal lensing. When we decrease the mirror curvature even more (R = 3.0 m in figure 6.7), we move towards a plano-plano resonator and the beam becomes expanded considerably due to the thermal lens.

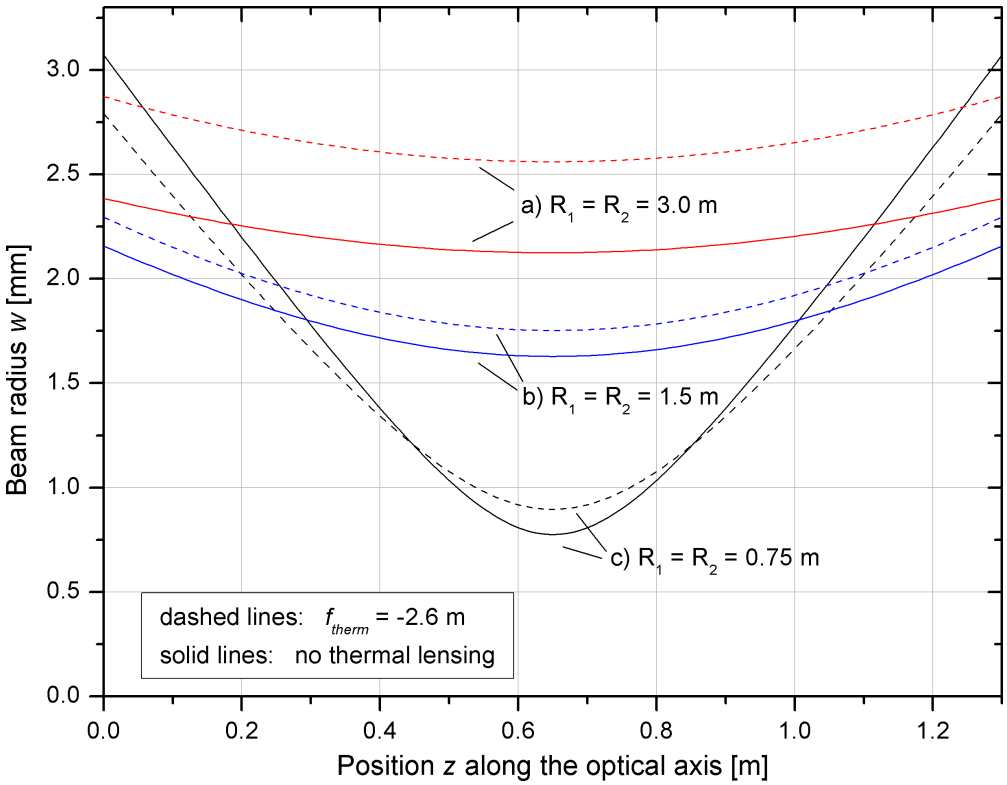

Figure 6.7 Beam radius in the thermal lensing region for L = 1.3 m, d = 59.5 mm for different symmetric mirror configurations

The trend described here can be seen when the relative increase of the beam size is plotted as a function of the mirror radii (figure 6.8). At around $R_1 = R_2 = 1$ m the beam increase is minimal in the waist position. The beam shrinks compared to free space beam for even shorter beam radii at distances closer to the mirror as shown for $R_1 = R_2 = 0.75$ m (figure 6.7(c)). For larger radii of curvature of the mirrors, the beam expands throughout the propagation distance. Not only does the expansion become larger for large mirror curvatures, but also the relative size increase is observed to grow, as can be seen in figure 6.8.

The edge of stability of a two mirror resonator is expected to be different with a thermal lensing medium compared to the well known case of free space propagation. In general, the optical resonator reaches the edge of stability when the mirror curvature exactly compensates for the defocusing thermal lens. The maximum radius of curvature at this edge of stability can be found by trial and error, or analytically. The analytical solution can be found by calculating the complex m value [6.6] from the ray transfer matrix of the resonator:

$$m = \frac{A + D}{2} \tag{6.32}$$

where A and D are the elements of the ray transfer matrix.

The m-value can be regarded as a ray matrix equivalent to the g-parameters of two mirror resonators. The resonator is stable, if [6.6]:

$$-1 \le m \le 1 \tag{6.33}$$

As for the g-parameters, the plano-plano stability edge is at $m = 1$. An analytical solution can be found if we solve the ray transfer matrix coefficients for $m = 1$ in equation (6.32). However, analytical terms become rather long for resonators with many matrix elements. In the simplified case of a resonator as shown in figure 6.6, where the thermal lens occupies the entire region between the mirrors ($d = 0$), a solution for the radii of curvatures in the stability limit can be found as follows:

$$R_{\max} = -b \coth\left(\frac{b}{2 f_{th}}\right) \tag{6.34}$$

where b is the repeating term as defined in equation (6.19).

For example, for a mirror separation of $L = 1.4$ m and a thermal lensing focal length of $f_{therm} = -2.6$ m, the maximal radii of curvature of the mirrors are $R_{max} \approx 5.43$ m. Larger radii of curvature yield an unstable resonator due to thermal lensing.

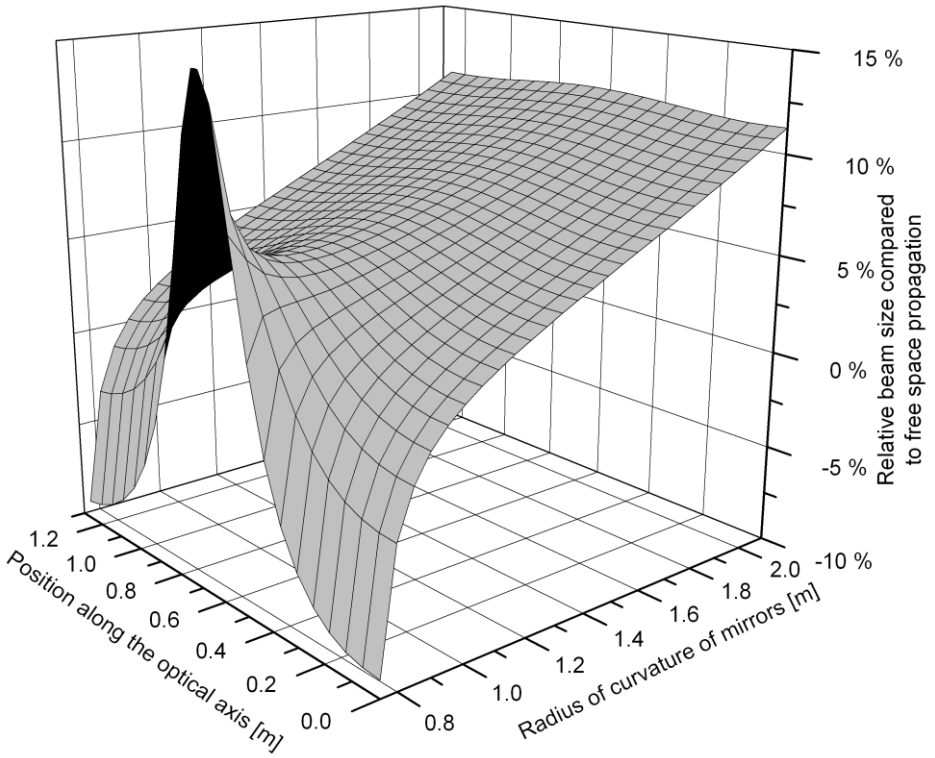

Figure 6.8 Relative beam size increase in the thermal lensing region for $L = 1.3$ m, $d = 59.5$ mm, $f_{therm} = -2.6$ m as function of the position and radii of curvature of resonator mirrors

6.4.2 ABCD-matrix model of TruCoax resonator in stable direction

A symmetric two-mirror resonator introduced in the previous section is sufficient to "trial" the calculation approach and to study the effect of mirror curvatures on the beam propagation. However, the beam propagation in the actual TruCoax resonator cannot be modelled faithfully with a two-mirror design, since as shown in figure 6.9, the two halves of the helix mirror are the two end mirrors, but the beam is refocused by propagation through the axicon mirror. Nevertheless, the model can be simplified mathematically, since the beam propagation is symmetric around the beam waist position in the middle of the axicon mirror, so one half of the propagation distance is sufficient to represent the beam propagation in the resonator.

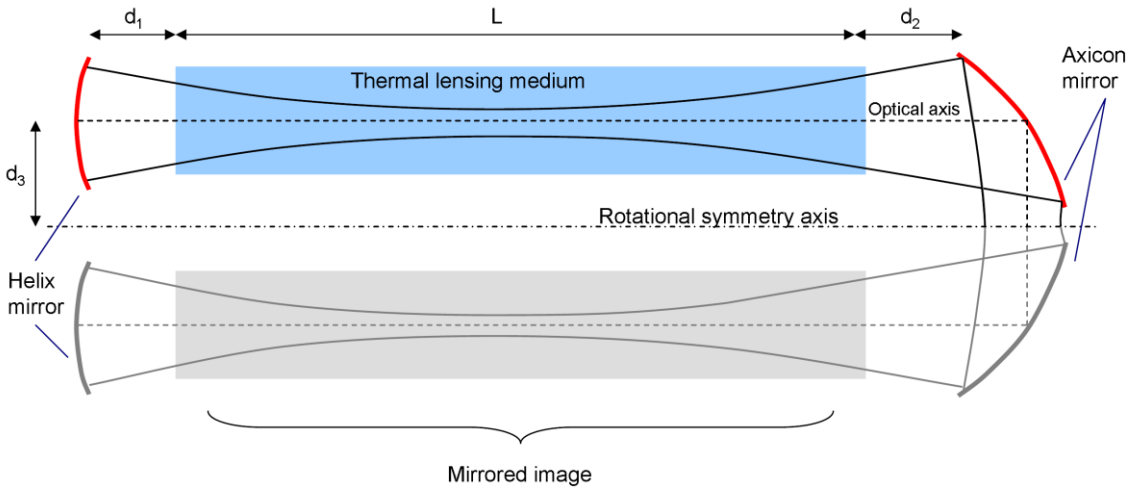

Figure 6.9 Stable direction model of the TruCoax resonator, where the propagation inside of axicon mirror is included

The same calculation method is applied to this improved model of the stable direction propagation. The ray transfer matrix is found by cascaded multiplication of 11 matrix elements, as compared to the 5 matrix elements model in the previous section. Figure 6.10 shows the resulting beam size due to thermal lensing (black curve) as a function of the *z*-position, as well as the beam size in the free space propagation direction (red curve). The mirrors of curvature (R_{he} = 2.000 m, R_{ax} = 3.668 m, where the value of R_{ax} is already corrected for 45º angle of incidence) are chosen in such a way that the beam size is the same at each end of the discharge region (see red curve in figure 6.10). The calculations show that the relative increase in the beam size due to lensing is inhomogeneous as a function of the *z*-position and varies between 8% and 11.5% for f_{therm}= -2.6 m. The beam size increase is generally larger at the axicon mirror end. The same data can also be

interpreted in term of the beam waist position. The results show a shift of beam waist towards the helix when the thermal lens is introduced. This shift is predicted to be of the order of 30 mm.

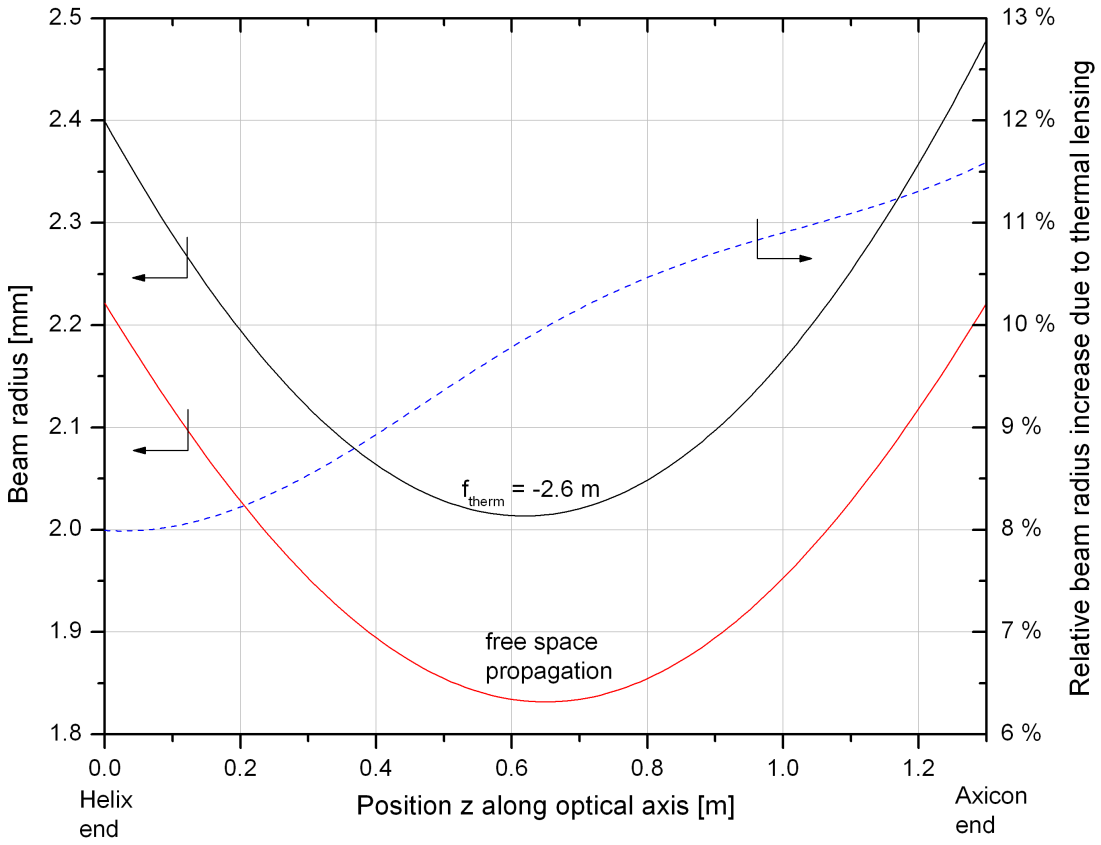

Figure 6.10 Beam radius along the optical axis with and without thermal lensing. The relative increase in beam size is shown by a dashed curve.

However, for the interpretation of results, it is necessary to keep in mind that the beam size can vary in the range between the cases of "free space propagation" and that of "maximal thermal lensing", depending on the pulsing duty cycle. The curvatures of manufactured resonator mirrors may also vary due to machining tolerances so that an exact fit of the mode volume and discharge geometry will be very difficult to achieve. A compromise solution would be to adjust the curvatures so that the beam size is symmetric in the medium range of RF input power. To achieve this situation, the radius of curvature of the axicon mirror (for example) should be increased by 2%.

6.4.3 Effect of longitudinal power distribution

The thermal lensing medium may be considered to be of constant defocusing power in the propagation direction *z*, and this assumption is sufficient to predict the expanded beam size as shown in section 6.3. It is known, however that there exists a longitudinal voltage variation along the electrodes due to transmission line effects which will lead to Joule heat variation, which in turn will show as a propagation distance-dependent thermal lens. In order to be able to calculate the effect of the varying thermal lensing effect, two tasks must be completed. The first is to extend the ABCD-matrix model, which includes the thermal lensing medium as a function of propagation direction *z*, while the second is to establish an electrical model, which allows us to estimate the longitudinal Joule heat distribution.

The thermal lensing matrix was derived based on the assumption, that each subsection has the same thermal lensing power. This condition does not apply here, but we can regard the varying thermal lensing medium as a series of thermal lensing sections, where each section *i* can have an individual focal length f_{therm}:

$$M_i = M_{therm}\left(f_{therm}(i) \times i_{\max}, \frac{L}{i_{\max}} \right) \tag{6.35}$$

In the above equation, *L* is the thermal lensing element length. The position *z* in the thermal lensing medium can be addressed by an index *i* or vice versa:

$$z = \frac{i}{i_{\max}} L \tag{6.36}$$

The number of sections i_{max} can be chosen to be as high as required to represent a thermal lens with a continuously varying focal length. In contrast to the analytical expression for M_{therm} in equation (6.18), the values of the overall thermal lensing matrix are found numerically by use of cascaded matrix multiplication. The matrices M_i are now not identical, and the matrix multiplication becomes not commutative. For forward and backward travelling beam the matrix values are:

$$M_{forward} = \prod_{i=i_{\max}}^{1} M_i \tag{6.37}$$

$$M_{backward} = \prod_{i=0}^{i_{\max}-1} M_i \tag{6.38}$$

We define the forward travelling direction as the one from the helix towards the axicon mirror, and after calculating the ray transfer matrix with these thermal lensing matrices, the beam size is obtained as described in the previous section. Now however, instead of the general term (equation (6.18)), the thermal lens matrix value must be calculated by multiplying M_i to the point z, where the beam size is probed. Two solutions for the beam size exist, depending whether the beam is travelling in the forward or the backward direction.

Having established the resonator model with varying thermal lensing power, we need now to estimate the thermal lensing focal length as a function of the longitudinal position. For this purpose, one-dimensional lossy transmission line theory will be applied in order to calculate the longitudinal RF voltage distribution from which the dissipated power can be deduced. The method described in the previous chapter (section 5.8) allows one to calculate the focal length of the thermal lensing as a function of the power density.

The relationship between the RF power density w and inter-electrode voltage V_{gap} is related to the current-voltage characteristics of the discharge structure. Experimental results [6.8] show, that above the normal current density (i.e. the discharge is filling the entire area on the electrodes) the inter-electrode voltage is increasing approximately linearly with increasing power density, until an abrupt transition from α- to γ-type discharge occurs at some threshold voltage. We know that during operation of the TruCoax laser at the nominal RF input power both conditions are met: the discharge has filled the entire volume and no γ-type discharge is present so that we can assume the linear power-voltage characteristic.

Vidaud *et al.* [6.9] have measured the power-voltage relationship for nitrogen with similar parameters (29.25 MHz, 73 hPa, 5.9 mm inter-electrode spacing) compared to the ones of the TruCoax laser. The data points of the inter-electrode voltage V_{gap} with the corresponding volumetric RF power densities w were taken from [6.9] and linearly interpolated to obtain:

$$w(V_{gap}) = 0.31 \times V_{gap} - 64.77 \tag{6.39}$$

where the unit of power density $w(V_{gap})$ is W/cm^3 and V_{gap} is given in Volts. The equation (6.39) was used to obtain the power density distribution $w(z)$ based on the voltage distribution $V(z)$ from the transmission line model (graph (b) in figure 3.16),

where the input voltage V_{in} is adjusted to achieve the known power density averaged over the discharge length.

The actual w-V_{gap} relationship for the laser gas mixture will be different to the experimental results in nitrogen, but the scope is to feed the transmission line data with best-guessed data to obtain a first impression of impact of the transmission line effect on the intra-cavity beam size.

The resulting power density distribution as shown in figure 6.11 is used as the input data to calculate the focal length of the thermal lens as function as position z along the longitudinal direction.

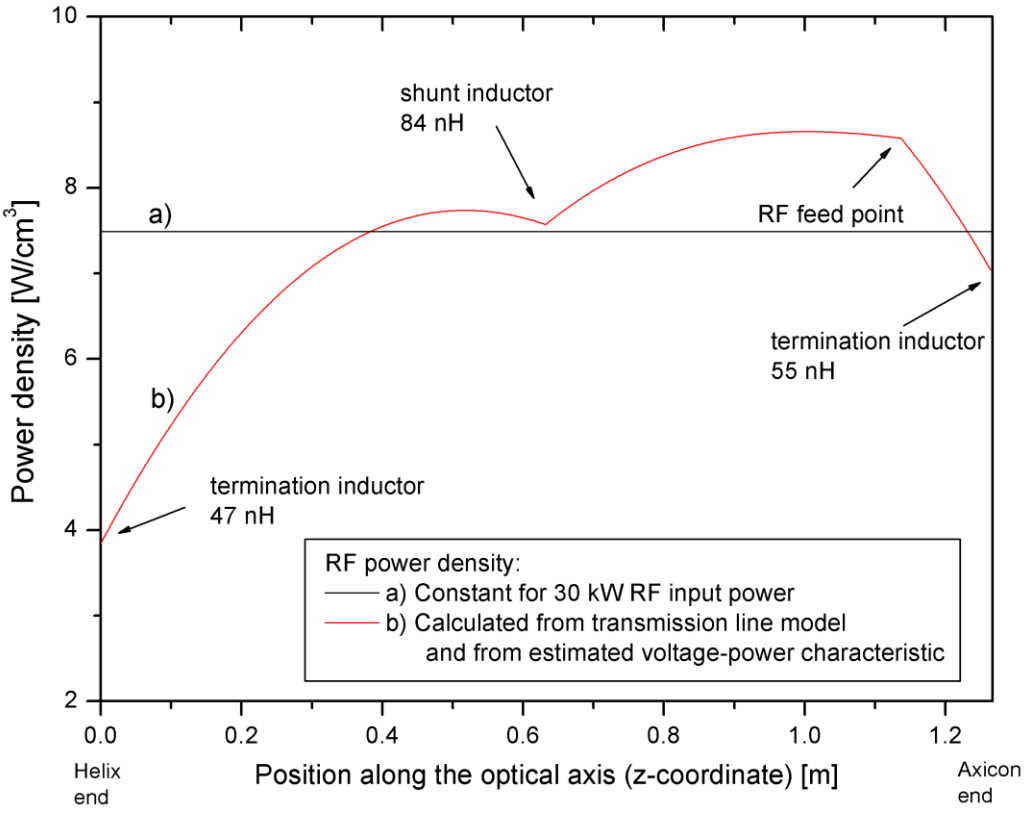

Figure 6.11 Calculated longitudinal discharge power density using transmission line model (see section 3.7). Parameters: TruCoax V6 with single 84 nH inductor with 30 kW RF input power

The RF discharge length L was split into sections with 1 mm length for each section. Each section i is characterised by a unique value of thermal lensing focal length f_i and matrix element M_i. After multiplying out the transfer matrix and finding the solution of a stable complex beam parameter q_{res}, we can calculate the beam size for both propagation directions. The results show that the effect on the beam size is very small when a varying

thermal lens is introduced into the model. This result is easier to demonstrate if one simply examines the beam size difference instead of plotting beam size for the cases (a) and (b) as depicted in figure 6.11. The resulting deviation of the beam radius compared to a beam radius with constant longitudinal power density is shown in figure 6.12. The curves (a) and (c) show the beam radius difference for beam propagation directions as indicated by the arrows. The average beam radius deviation is plotted as curve (b).

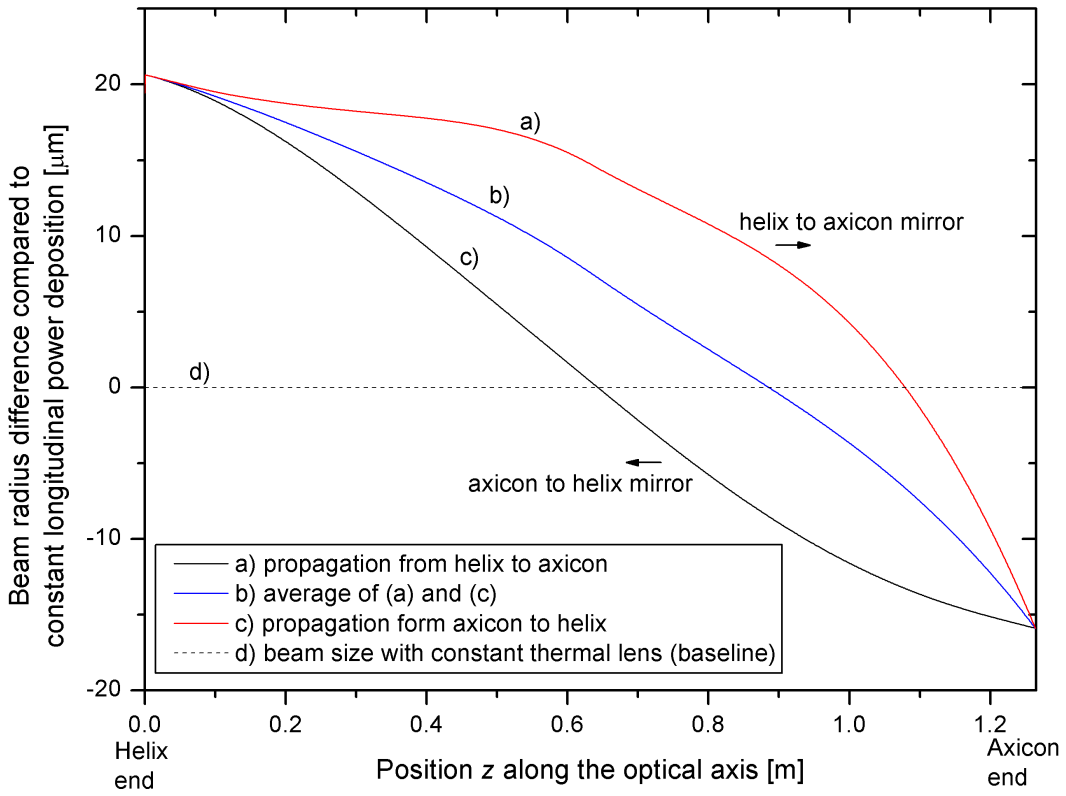

Figure 6.12 Beam radius deviation for a longitudinal power density distribution compared to constant power density

Comparing the plots in figures 6.11 and 6.12, we can see that the beam is smaller at the axicon mirror end. However, at this end there is a higher power density and therefore stronger thermal lensing, which appears counter-intuitive. The result is a consequence of the calculated self-reproducing beam (equation (6.25)), where it is necessary for the beam to be smaller in the region of stronger thermal lens in order to form a stable resonator solution.

The results show that the beam expansion is in the opposite direction compared to the beam expansion due to propagation inside the axicon (compare figures 6.10 and 6.12). The given voltage distribution has therefore a stabilizing effect on the asymmetric beam

expansion, but the effect is small. For comparison, the thermal lens increases the beam radius by about 200 μm (see figure 6.10), whereas the beam radius variation in figure 6.12 are in the range of ±30 μm. However, if the more extreme situation of discharge plasma shrinkage were to occur, the effect would be more noticeable as mentioned in section 6.3.

6.5 Inter-electrode Gap Spacing Design

The lateral dimension up to this point has not been considered, and a non-truncated Gaussian beam has been studied using the ABCD matrix formalism. However, in a free space resonator, as found in the stable direction of the TruCoax laser resonator, the lateral dimension of the active laser medium is important and needs to be limited to ensure fundamental transversal mode and high beam quality. The resonator Fresnel number N_f is a common indicator as to whether the resonator can operate multimode [6.7]:

$$N_f = \frac{a^2}{\lambda L_{cav}} \tag{6.40}$$

where a is the radius of an aperture, λ is the wavelength and L_{cav} is the cavity length.

Multimode operation occurs if the Fresnel number is larger than unity. In fact, the Fresnel number in the radial direction for the TruCoax laser resonator, where the separation between the electrodes acts as an aperture, is around unity. For such cases, a mixture of modes, notably the fundamental TEM_{00} mode and the TEM_{10} mode, is expected because it is possible that the aperture is too large to provide unambiguous discrimination against the TEM_{10} mode. On the other hand, an aperture which is too small is associated with more stringent requirements for the alignment of the electrodes to the mirrors, and therefore often results in reduced output power. A number of electrode gaps were tested on the TruCoax V5 and V6 resonators. An electrode gap of 7 mm at the ends and 6.2 mm in the centre delivers a good compromise of alignment sensitivity, power and beam quality under typical operating conditions. In order to determine experimentally the extent to which the thermal lens defines the beam in the radial direction, the pressure was reduced to 15 hPa in a TruCoax V5 resonator. The RF discharge was observed to fill the entire electrode length with an input power of 3 kW at this pressure. The beam profiles were acquired with a commercial beam scanner (Primes BeamScanner, model BS50) at 2 m propagation distance from the output coupling window. The comparison of profiles with reduced pressure and typical operating condition is shown in figure 6.13. In the case of 15 hPa fill pressure, the amount of thermal lensing is greatly reduced as thermal lensing is

approximately linearly proportional to the gas density. The beam in the radial direction is wider at the measured propagation distance and shows signs of a second peak next to the main peak at reduced pressure. For comparison, the beam at typical operating parameters (bottom plot in figure 6.13) is observed to operate in the fundamental mode in the radial direction.

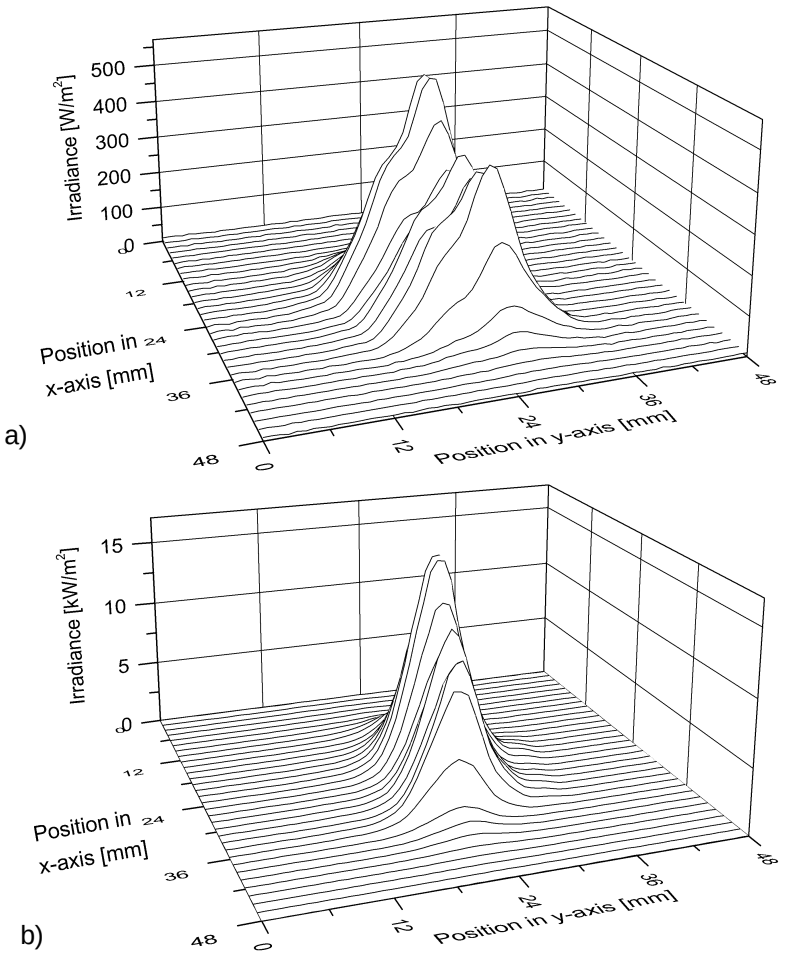

Figure 6.13 Suppression of higher order mode by thermal lensing. The beam profiles are measured at 2 m propagation distance:

a) 3 kW RF input power, 15 hPa fill pressure, f_{therm} ≈ -29 m

b) 27 kW RF input power, 70 hPa fill pressure, f_{therm} ≈ -3 m

The results have shown that the TruCoax electrode spacing has been optimised to include the beam expansion effect due to thermal lensing. The electrode spacing geometry is plotted in figure 6.14 together with estimated beam sizes for three cases. The calculated beam sizes for 70 hPa and 15 hPa fill pressures are plotted in curves indicated as (a) and (b) respectively. For comparison, the expected beam size for free space propagation is

plotted as curve (c). The beam sizes are calculated by multiplication of the beam radii from the ABCD matrix thermal lensing model by a factor of 3. The value for the multiplication factor is often deduced empirically. Siegman ([6.7], page 691) proposes a factor of 3.5 to 4.0 for low power lasers or value of π in general. It can be seen from the curves in figure 6.14, that the effective aperture size is increased when approaching free space propagation. As the ratio between the aperture size and fundamental mode size is increased, the diffraction losses for higher order modes are reduced to a point where they exceed the lasing threshold, since the mode size is approximately proportional to the square root of the transverse mode order ([6.7], page 690).

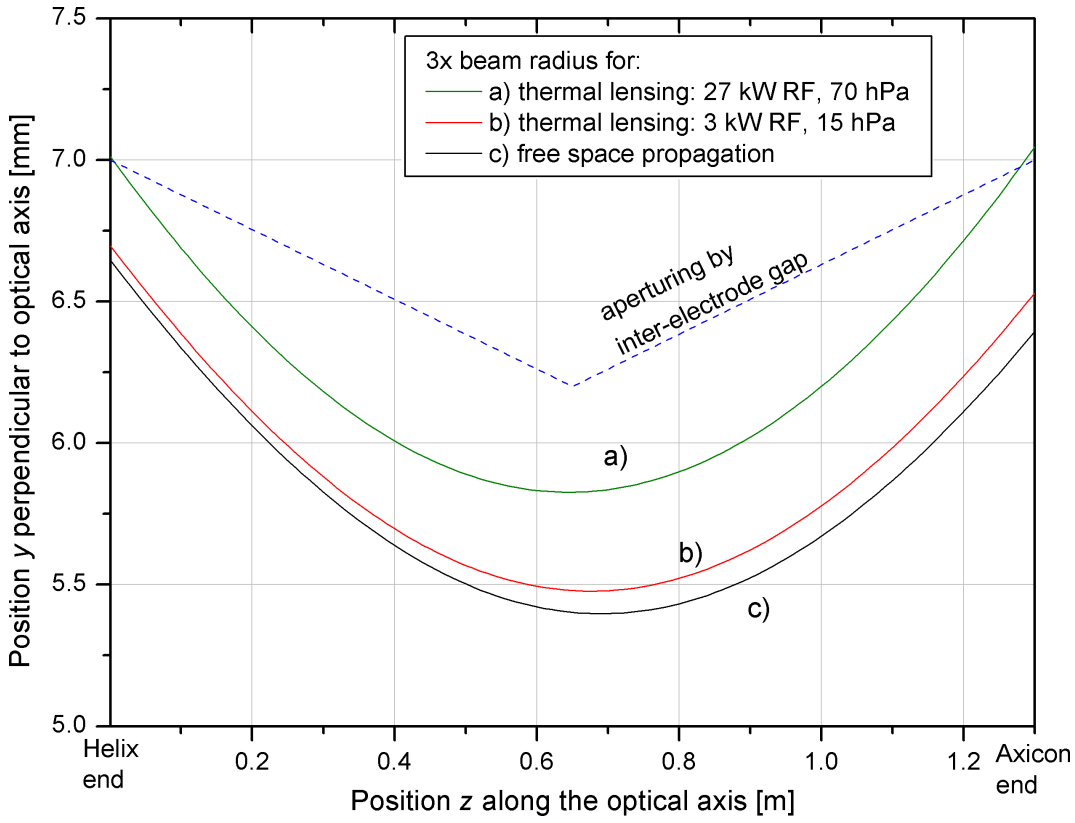

Figure 6.14 Expected interaction of the beam in the stable direction with the electrode gap in a TruCoax V6 resonator for:

a) typical operating conditions

b) condition of reduced thermal lensing effect

c) idealised free space propagation

6.6 Summary

The effect of the thermal lens in the TruCoax resonator in the stable direction was studied in this chapter. In the first sections, a mathematical expression was derived to represent the thermal lensing medium within the ABCD matrix formalism. The thermal lensing

matrix is shown to be the product of an infinitely-large number of diverging lenses, and this expression was then used to determine the magnitude of the thermal lensing for the case of a TruCoax laser discharge cell, allowing comparison to be made with the experimentally measured results. The theory is shown to agree within 8% with the measurements and provides confidence in the calculated thermal lensing magnitude in spite of the large number of steps in the calculation steps and the simplifications involved.

A model of the TruCoax resonator which includes thermal lensing was gradually introduced, starting with a simple symmetric two-mirror model and advancing towards a model which includes thermal lens variations due to transmission line effects along the electrodes. It was possible to deduce from the simplified symmetric model how thermal lensing has a different effect on the expansion of the intra-cavity optical beam depending on the resonator configuration (from concentric through to confocal to plano-plano).

With the addition of beam propagation inside the axicon mirror in the model it was shown that the beam expansion is asymmetric along the electrodes even if the beam size is matched to the electrode gap under the assumption of free space propagation. These results can be used to establish a set of mirror radii of curvature and electrode gaps that are specifically optimised to provide asymmetric expansion due to the thermal lens.

Variation in RF discharge power density along the electrodes is a well-established phenomenon caused by transmission line effects. The power density variation is shown to give rise to a variation of the thermal lensing power as function of the propagation distance. This effect has been included in the calculation, where the overall thermal lensing matrix is calculated by cascaded multiplication of a larger number thermal lensing sections with unique thermal lensing focal lengths. The results show that the beam is generally smaller in the regions with stronger defocusing power of the thermal lens, which is due to the stable resonator condition. However, the beam size variation is negligibly small compared to beam expansion in the helix-axicon resonator due to thermal lensing with constant optical power throughout the discharge length.

In the final part of the chapter, the amount of beam aperturing by the electrodes is mentioned. The effective aperture size, which defines the high beam quality of the resonator in the radial direction is strongly affected by the thermal lens and needs to be included in the resonator geometry optimization.

The thermal lensing effect in the lateral direction was assumed to be constant, which allows calculating the beam propagation with the standard ABCD matrix tools. The accuracy of calculation can be improved in the subsequent work, if the variation of thermal lensing magnitude is included in the lateral direction. This can be achieved by numerical methods based on the Fox and Li [6.10] algorithms.

The beam amplification is also not constant in the lateral direction. The effect of the laser gain variation, where the gain is lower in the centre of the discharge gap, is not related to thermal lensing but has a similar lensing effect. The lensing effect due to the transverse gain profile should be also included to provide the full picture for the optimization of a free space stable resonator.

6.7 References

[6.1] G. Strang "Introduction to linear algebra, 3rd edition", Wellesley-Cambridge, ISBN 0-09614088-9-8 (2003)

[6.2] K. Kuttler "Elementary linear algebra", lecture notes, Brigham Young University (2012)

[6.3] M. Abramowitz, I. A. Stegun, "Handbook of mathematical functions", National Bureau of Standards, USA (1972)

[6.4] J. T. Verdeyen, "Laser Electronics", Prentice Hall, ISBN 0-137-066-66X (1995)

[6.5] H. Kogelnik, T. Li "Laser beams and resonators", Proc. IEEE, vol. 54, pp. 1312-1329 (1966)

[6.6] L. W. Casperson "Mode stability of lasers and periodic optical systems", IEEE J. Quant. Electron., vol. 10, pp. 629-634 (1974)

[6.7] A. E. Siegman "Lasers", University Science Books, Mill Valley, ISBN 0-935-702-115 (1986)

[6.8] Yu. P. Raizer, M. N. Shneider, N. A. Yatsenko "Radio-frequency capacitive discharges", CRC Press, ISBN 0-8493-8644-6 (1995)

[6.9] P. Vidaud, S. M. A. Durani, D. R. Hall "Alpha and gamma RF capacitive discharges in N_2 at intermediate pressures", J. Phys. D: Appl. Phys., vol. 21, pp. 57-66 (1988)

[6.10] A. G. Fox, T. Li "Resonant modes in a maser interferometer", Bell Syst. Tech. J., vol. 40, pp. 453-488 (1961)

Chapter 7

CAUSALITY BETWEEN THE LASER SIGNATURE AND LASER POWER STABILITY

7.1 Introduction

Previous chapters dealt with instability processes that are intrinsically related to the gas discharge and the way it is operated, such as acoustic resonances and arcing in the region of the RF feed-through.

This chapter, however, focuses on the mechanisms that determine the temporal stability of the laser output power. Based on the CO_2 molecular kinetics and the optical mode-selection processes, an analytical model is developed that describes and predicts the temporal behaviour of the CO_2 laser output power.

The chapter is organised in four sections. The modelling of the laser signature (in section 7.2) takes up the largest part, and here the theory is introduced, since it is needed to describe the CO_2 laser spectrum, while in section 7.3 the theory is applied to the specific case of the TruCoax laser. Experimental results of the laser signature are then correlated with calculations (section 7.3), and measurements related to transverse mode discrimination are presented in section 7.4. The linkage between the laser emission spectrum and the corresponding output power is discussed in section 7.5.

7.2 Theoretical Background of Laser Signature Formation

7.2.1 Vibrational and rotational states

The carbon dioxide molecule is one of the first molecules whose infrared absorption spectrum was studied extensively, many decades before discovery and development of the CO_2 laser. The CO_2 molecule is a symmetric linear molecule with two oxygen atoms on either side of the carbon atom. The three possible vibrational modes are shown in figure 7.1. In the symmetric stretch mode v_1 the oxygen atoms move in opposite direction while

the carbon molecule stays stationary. This is the only optically inactive mode, since the dipole moment of the molecule does not change. In the bending mode v_2 the carbon atom and the two oxygen atoms move perpendicularly to the long axis of the molecule. The CO_2 molecule can also vibrate perpendicular to the direction shown in the drawing, so the bending mode is doubly degenerate. The carbon atom moves in the opposite direction to the two oxygen atoms in the asymmetric stretch vibrational mode v_3. The vibrational state of the CO_2 molecule, which can be a combination of the three vibrational modes or their overtones, can be described by the shorthand notation $(n_1\, n_2{}^l\, n_3)$. The integer numbers n_1, n_2, and n_3 indicate the vibrational quantum number of modes v_1, v_2, and v_3 respectively. The angular momentum quantum number l describes the state of the degenerate bending mode v_2.

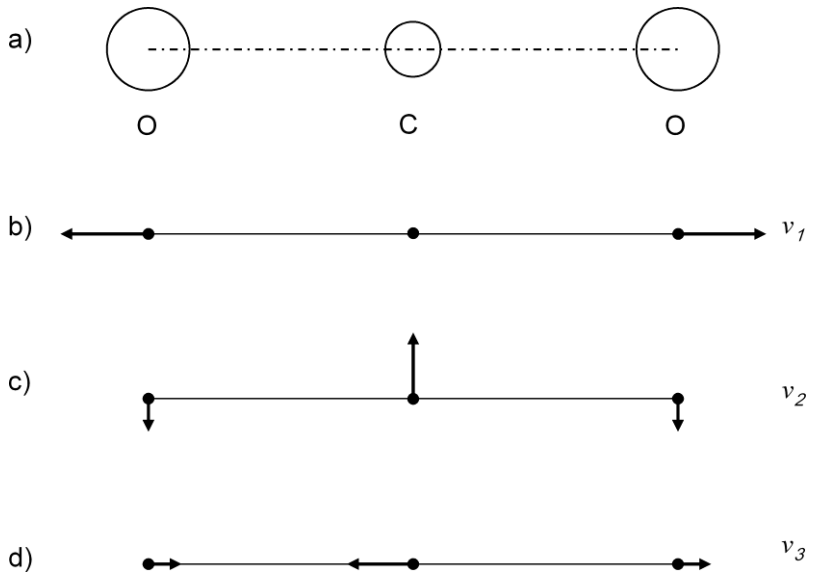

Figure 7.1 Schematic representation of the CO_2 molecule (based on [7.1]):
a) arrangement of the linear CO_2 molecule
b) symmetric stretch vibrational mode
c) one of two bending vibrational modes, the other mode is 90° rotated along the long axis
d) asymmetric stretch vibrational mode

The energy levels associated with these three fundamental vibrational modes were determined by Adel and Dennison [7.2] as: ω_1 = 1351.2 cm^{-1}, ω_2 = 672.2 cm^{-1} and ω_3 = 2496.4cm^{-1}.

The ω_1 and $2\omega_2$ energy levels are coincidentally only 7 cm^{-1} apart, however, the actual spectra of the two vibrational levels differ from the expected levels at $\hbar\omega_1$ and $2\hbar\omega_2$. Fermi [7.1] could explain the measured energy levels by the fact that the two states

interact with each other via the so-called Fermi resonance such that the spacing between the unperturbed 10^00 and the 02^00 energy levels increases, shifting the higher, 10^00 level up and the lower, 20^00 level further down. The resultant energy levels are denoted by (I) and (II) to indicate that they are modified due to the Fermi resonance. A simplified energy level diagram for a CO_2 laser is shown in figure 7.2.

Collisions with electrons cause nitrogen molecules to be excited from the ground state to the v = 1 vibrational level, and the excited N_2 molecules are metastable with very long relaxation times in the order of seconds. The vibrational-vibrational transfer between N_2 (v = 1) and CO_2 (00^01) is very likely during this time, since the energy difference is only 18 cm^{-1}. The two most pronounced laser transitions are from 00^01 to (I) emitting at 10.4 μm wavelength and from 00^01 to (II) at 9.4 μm.

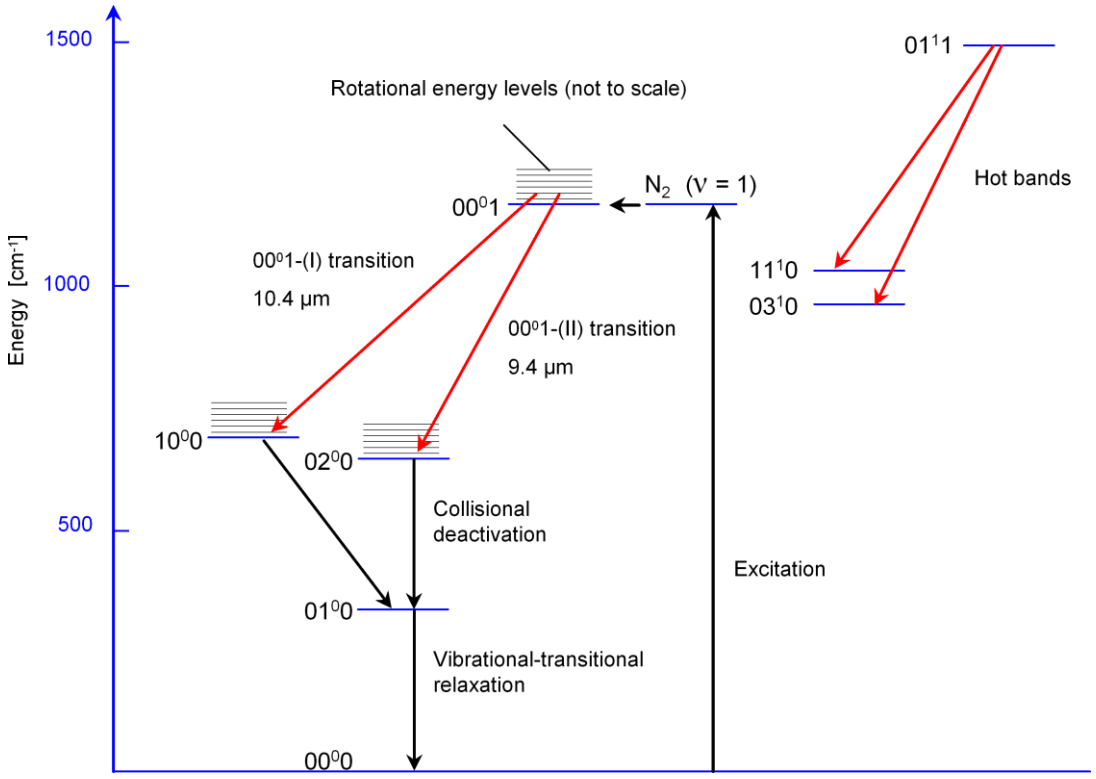

Figure 7.2 Simplified energy diagram of CO_2 and N_2 rotational-vibrational levels

In addition to vibrational excitation levels the rotational energy of the CO_2 molecules must also be considered. This is also quantised and described by the quantum number *J*. Such rotation is almost unperturbed by vibrational effects, so that the rotational-vibrational molecule energy can be described by a sum of vibrational and rotational energies as indicated in figure 7.2.

The rotational energy as function of quantum number J has been measured with increasing accuracy in [7.3], [7.4], [7.5], [7.6] by deduction from the heterodyne beat frequency derived from mixing the source with a known frequency (wavelength) beam. The authors fit the measured frequencies with a 4^{th} order polynomial of the form:

$$F(J) = G_\upsilon + B_\upsilon J(J+1) - D_\upsilon [J(J+1)]^2 + H_\upsilon [J(J+1)]^3 + L_\upsilon [J(J+1)]^4 \qquad (7.1)$$

where G_υ is the energy difference between the vibrational states and B, D, H, L are the fitted constants. The subscript υ is an index variable describing the vibrational transition, i.e. either $00^0 1$-(I) or $00^0 1$-(II).

The selection rule for the rotational-vibrational transition dictates that $\Delta J = \pm 1$. Transitions with $\Delta J = 1$ are located in the so-called P-branch, while the transition with $\Delta J = -1$ are located in the so-called R-branch. The convention for rotational energy transition nomenclature is to specify the rotational quantum number of origin at absorption, which is the 'destination' at emission. Thus, the transition [$00^0 1$, $J = 21$] → [(I), $J = 20$], for example, would be abbreviated as 10P20.

In addition to the $00^0 1$-(I) and $00^0 1$-(II) transitions, which are also called regular bands, there could be other transitions that have coincidentally a similar energy difference as the regular bands. These so-called "sequence bands" are $00^0 2 \rightarrow 10^0 1$ and $00^0 2 \rightarrow 02^0 1$ transitions, whereas "hot bands" are $01^1 1 \rightarrow 03^1 1$ transitions. The ten lines that have the closest frequency difference between the regular bands and hot bands are indicated in red in figure 7.3 based on frequency data provided in [7.5]. The frequency differences are shown in table 7.1. The proximity of these lines, combined with pressure broadening, can produce the merging of the spectral lines as is seen as an anomalous spectrum, as will be explained in further section.

Table 7.1 Frequency difference between regular and hot bands for ten closest lines

Regular Band Line	Hot Band Line	Frequency Difference Δv
$00^0$1-(II) R(24)	$00^0$1-$03^1$0 R(12)	26.4 MHz
$00^0$1-(I) P(56)	$00^0$1-$11^1$0 P(23)	41.2 MHz
$00^0$1-(I) P(20)	$00^0$1-$11^1$0 R(23)	47.4 MHz
$00^0$1-(II) P(10)	$00^0$1-$03^1$0 P(19)	108.6 MHz
$00^0$1-(II) R(62)	$00^0$1-$03^1$0 R(43)	140.8 MHz
$00^0$1-(II) P(22)	$00^0$1-$03^1$0 P(30)	191.5 MHz
$00^0$1-(II) P(58)	$00^0$1-$03^1$0 P(64)	425.4 MHz
$00^0$1-(I) P(48)	$00^0$1-$11^1$0 P(13)	437.6 MHz
$00^0$1-(II) R(40)	$00^0$1-$03^1$0 R(26)	552.1 MHz
$00^0$1-(I) P(34)	$00^0$1-$11^1$0 R(42)	781.5 MHz

7.2.2 Line broadening

The frequencies of the vibrational-rotational transitions are not discrete points in the spectrum range, but rather are broadened as a result of various effects. Generally, five broadening mechanisms are described by Mitchell *et al.* [7.7]: natural broadening, Doppler Effect broadening, Lorentz, Holtsmark and Stark effect broadening. The different broadening mechanisms can generally be classified to two groups: homogeneous and inhomogeneous broadening.

Line broadening type is classified as "inhomogeneous" if the molecules are characterised in different groups based on their properties where the line broadening depends on these properties. One of the most important inhomogeneous broadening mechanisms is Doppler broadening, where the molecules experience a shift in the transition frequency due to their thermally-generated motion relative to the electromagnetic wave. For a Maxwellian velocity distribution the lineshape is described by a Gaussian profile where the linewidth at half maximum is given by [7.8]:

$$\Delta \nu_D = 2\nu_{12}\sqrt{\frac{2kT}{Mc^2}\ln 2} \tag{7.2}$$

where ν_{12} is the frequency difference between lower and upper laser state, k is the Boltzmann constant, T is the gas temperature, M is the mass number of the CO_2 molecule.

For homogeneous broadening, molecules are indistinguishable from each other, and the lineshape of each molecule is identical to the lineshape for the whole group of molecules. The lineshape of homogeneously broadened lines is Lorentzian. Lorentz and Holtsmark broadening were historically regarded as distinct broadening mechanisms, where the first occurs due to collisions between different molecule species, while the later involves collisions between identical molecular species. Collectively, such transitions are often described as collision or pressure broadened. The width of the collision broadened line is expressed in the literature as function of pressure *p* in form [7.9]:

$$\Delta\omega = A + Bp \tag{7.3}$$

where *A* and *B* fitting coefficients, which should not be confused with Einstein coefficients. The coefficients can be determined by measuring the linewidth as a function of the gas mixture and pressure, and the most frequently cited equation is the one found by Abrams [7.10]:

$$\Delta\nu_P[MHz] = 7.58\times\left(\psi_{CO_2} + 0.73\psi_{N_2} + 0.64\psi_{He}\right)\times p[torr]\times\sqrt{\frac{300}{T}} \tag{7.4}$$

where ψ_n is the fraction of gas species *n*. Natural broadening relates to the decay of emission due to limited lifetime of the emitting level. However, natural or lifetime broadening effect is negligible compared to pressure broadening for gas conditions appropriate for CO_2 lasers, as the measured linewidth approaches zero at low pressure [7.10], [7.11], as pointed out by Siegman [7.9].

When, as is frequently the case, the spectral line is broadened by various effects independently, then in the time domain the net lineshape is the product of the lineshapes, while in the frequency domain the net result is obtained from the convolution. For convoluted homogeneous lines the net result is given by [7.12]:

$$\Delta\nu_L = \sum\Delta\nu_{Li} \tag{7.5}$$

where $\Delta\nu_{Li}$ are widths of individual Lorentzian lines.

For convoluted inhomogeneous lines the overall linewidth is given by [7.12]:

$$\Delta\nu_G = \sqrt{\sum\left(\Delta\nu_{Gi}\right)^2} \tag{7.6}$$

In general for the CO_2 laser (which may run over a wide range of gas pressures), the dominant line broadening mechanisms are pressure and Doppler broadening, which are of homogeneous and inhomogeneous types respectively, but where the convolution integral

cannot be solved analytically. The lineshape based on this convolution integral is termed as the Voigt profile [7.9].

7.2.3 Gain coefficient of regular bands

The frequency difference between individual rotational-vibrational lines is about 55 GHz, which is small enough, such that the populations of lines with different rotational number *J* are in thermal equilibrium. The probability of finding a molecule with a vibrational state *n* and rotational transition *j* can be found using the Maxwell-Boltzmann distribution [7.8] as follows:

$$n_{\upsilon,j} \propto (2J+1)\exp\left(-F(J)\frac{hc}{kT}\right) \tag{7.7}$$

where *F(J)* is the rotational energy as function of *J*. The capital letter *J* denotes the rotational *state* of the molecule in contrast to the small letter *j* which denotes the rotational *transition*.

For collision-broadening-dominated gas laser conditions, Witteman [7.8] has derived an equation for the gain (or absorption) coefficient α [7.8]. For the *P*-branch the gain coefficient is given by:

$$\alpha_P(j) = \frac{\lambda^2 hcB}{4\pi kT}(2J-1)A_P \frac{2}{\pi\Delta\nu_P}\left\{N_{\upsilon'}\exp\left[-F(J)\frac{hc}{kT}\right] - N_{\upsilon}\exp\left[-F(J-1)\frac{hc}{kT}\right]\right\} \tag{7.8}$$

where *B* is the rotational energy constant, λ is the emission wavelength, *F(J)* is the rotational energy, $N_{\upsilon'}$ and N_{υ} are the vibrational state density of upper and lower laser levels, respectively, and A_P is the spontaneous transition probability.

Similarly, the gain coefficient for the *R*-branch [7.8] is given by:

$$\alpha_R(j) = \frac{\lambda^2 hcB}{4\pi kT}(2J+3)A_R \frac{2}{\pi\Delta\nu_R}\left\{N_{\upsilon'}\exp\left[-F(J+1)\frac{hc}{kT}\right] - N_{\upsilon}\exp\left[-F(J)\frac{hc}{kT}\right]\right\} \tag{7.9}$$

The spontaneous transition probabilities A_P and A_R are given in [7.8] as function of *J* and based on experimental measurements. The state densities $N_{\upsilon'}$ and N_{υ} are of the order 10^{14} cm^{-3} for DC excited CO_2 lasers [7.13], though the exact values depend on the operating conditions of the particular system. In figure 7.3 the gain coefficient has been calculated for the 00^01-(II) and 00^01-(I) bands with *P*- and *R*-transitions according for equations

(7.8) and (7.9) assuming a value of the ratio of the densities $N_{v'}/N_v$ of 1.6 and gas temperature of 400 K.

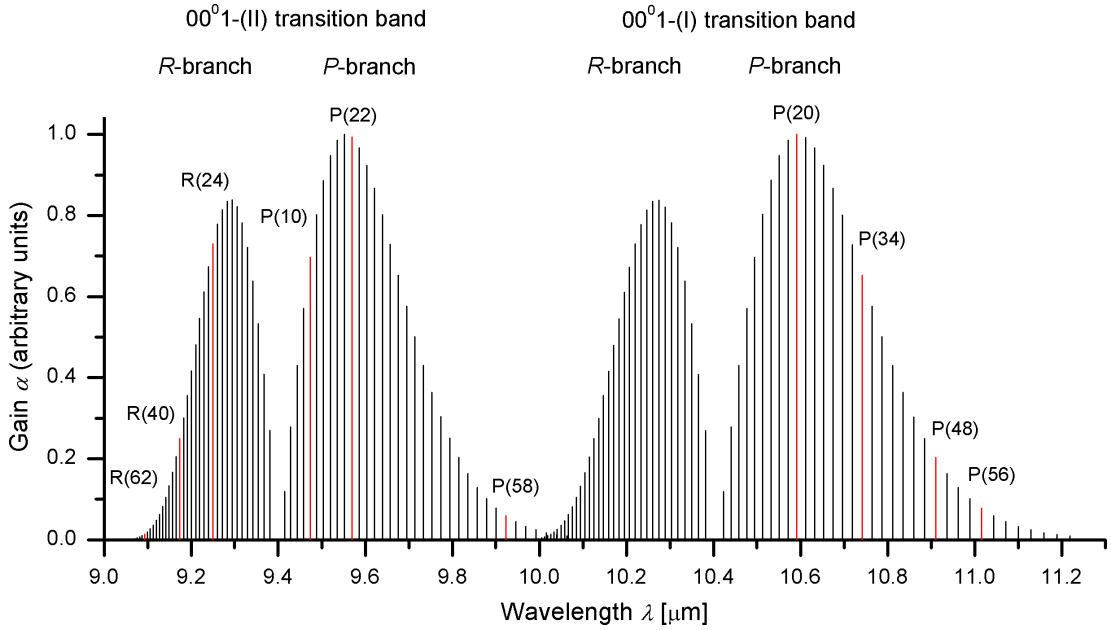

Figure 7.3 Calculated relative gain for $N_{v'}/N_v$ = 1.6, T = 400 K. The highlighted lines are the ones overlapping with hot band lines from table 7.1.

The coefficient values were scaled to the maximum value of unity. The wavelength values (abscissa in figure 7.3) were calculated based on equation (7.1) and data from [7.4].

7.2.4 Laser signature

In the earlier sections, the lineshape and the vibrational-rotational spectrum of the CO_2 molecule were briefly described. The third condition is that an optical resonator is formed if the cavity length L is set equal to an integer number q of half-wave $\lambda/2$:

$$L = q\frac{\lambda_0}{2} \tag{7.10}$$

where λ_0 is the wavelength in vacuum, since the difference between wavelength in vacuum and the wavelength in the gas medium is negligibly small in this context.

Combining these three conditions, it is apparent that for a given cavity length L there will be a broadened rotational line which is closest to the longitudinal standing wave condition (7.10).

The longitudinal mode number q is large for typical cavity lengths; it is in the order of hundreds of thousands. Even if the relative frequency difference between the lines is small, the phase difference builds up of the many longitudinal mode orders. If the optical cavity length is varied over several wavelengths, for example by using a voltage-controlled piezoelectric actuator to control the longitudinal position of one of the resonator mirrors, or by thermal expansion of the resonator, a certain pattern or sequence of rotational lines is observed using a spectrometer. This observed spectral variation is often referred to as the laser signature. An example of how the signature of a CO_2 laser can be reconstructed was reported by Schiffner [7.14], and a theoretical model was developed to enable prediction of the signature, with the lineshapes being approximated by parabolas (see figure 7.4).

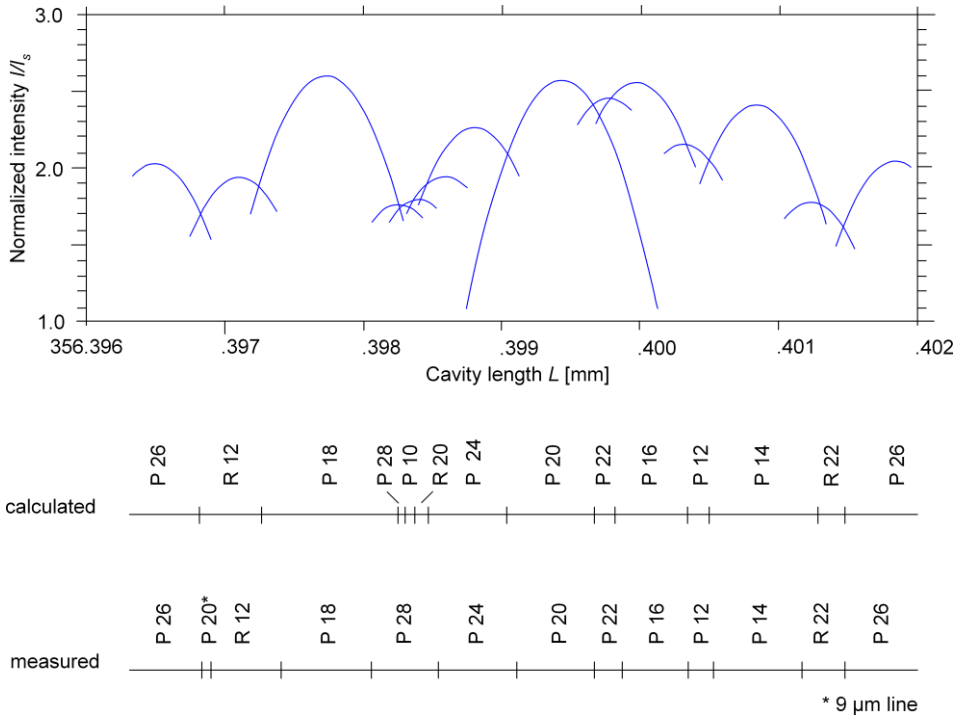

Figure 7.4 Signature modelling and comparison to results (adapted from [7.14])

7.3 Measurement of Laser signature and Correlation to Theory

After establishing the theoretical background, the focus of this section is to report work performed to develop a model which can reproduce the experimentally-observed laser signature of TruCoax laser. Since the signature depends on a set of boundary conditions, the objective is to find a close estimate of these conditions which can be refined to reflect the measurement data.

7.3.1 Numerical solution of the Voigt profile

The operating pressure in the TruCoax laser, which is approximately 70 hPa, dictates that neither the homogeneous nor the inhomogeneous broadening mechanism can be neglected. The solution of the convolution integral results in the Voigt profile *V(ν)* [7.15]:

$$V(\nu) = \frac{\alpha_P}{\alpha_D{}^2} \frac{1}{\pi^{3/2}} \int_{-\infty}^{\infty} \frac{\exp(-\chi^2)}{\left(\frac{\nu - \nu_0}{\alpha_P} - \chi\right)^2 + \left(\frac{\alpha_P}{\alpha_D}\right)^2} d\chi \tag{7.11}$$

In equation (7.11), α_P is half-width of the pressure broadened Lorentz profile, α_D is the half-width of Doppler broadened Gaussian profile and ν_0 is the frequency at the peak of the profile; χ is a dimensionless auxiliary integration variable.

No analytical solution of the Voigt integral has been found. The focus for the calculation is to integrate the function $f(\chi)$ numerically after simplifying the constants in equation (7.11):

$$V(\nu) = K \int_{-\infty}^{\infty} f(\chi) d\chi \tag{7.12}$$

In figure 7.5 the Voigt integral was calculated numerically for typical operating conditions appropriate for the TruCoax laser.

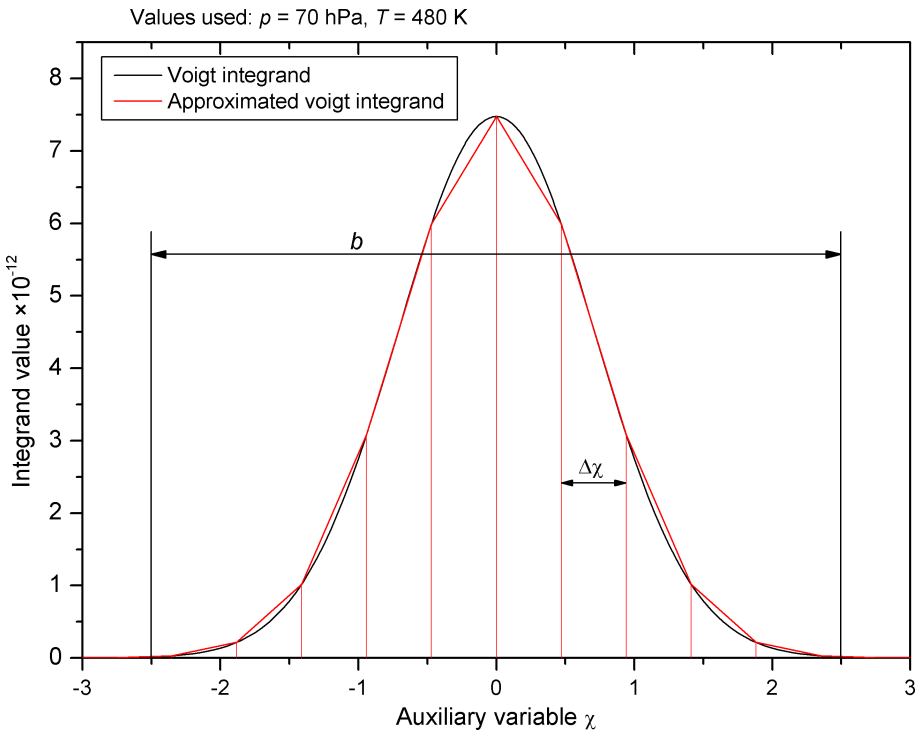

Figure 7.5 Approximated integration by taking discrete trapezoidal sections

It is necessary to calculate the Voigt lineshape for a large number of data points, so that the update of the signature being modelled is as rapid as possible if the boundary conditions are modified. This is achieved by applying the linearised approximation as shown in red in figure 7.5. The continuous integral is replaced by a number n of trapezoidal sections:

$$\int_{-\infty}^{\infty} f(\chi)d\chi \approx \frac{f(\chi_1)+f(\chi_2)}{2}\Delta\chi + \frac{f(\chi_2)+f(\chi_3)}{2}\Delta\chi + \ldots + \frac{f(\chi_{n-1})+f(\chi_n)}{2}\Delta\chi \qquad (7.13)$$

The advantage of the integral is that the integrand converges towards zero for large arguments in the positive and negative directions:

$$\lim_{\chi\to\pm\infty} f(\chi) \to 0 \qquad (7.14)$$

Based on the limit (7.14), the terms at the boundaries y_0 and y_n can be omitted without introducing a significant error, if the integration region is large enough. The terms in equation (7.13) can then be simplified to a computationally simple algorithm:

$$\int_{-b/2}^{b/2} f(\chi)d\chi \approx \Delta\chi \sum_{i=2}^{n-1} f(\chi_i) \qquad (7.15)$$

where $\Delta\chi$ is the spacing between the data points and b is the integration range as shown in figure 7.5.

The Voigt integral can be approximated based on (7.11) and (7.15) as:

$$V_{appr}(\nu) = \frac{\alpha_P}{{\alpha_D}^2}\frac{h}{\pi^{3/2}}\sum_{i=2}^{n-1}\frac{\exp(-{\chi_i}^2)}{\left(\frac{\nu-\nu_0}{\alpha_P}-\chi_i\right)^2+\left(\frac{\alpha_P}{\alpha_D}\right)^2} \qquad (7.16)$$

The choice of the number n of data points and spacing $\Delta\chi$ between them determine the accuracy of the approximation. The results in figure 7.6 show the dependency of the parameters on the accuracy and the computation speed. The accuracy is calculated from the difference between the calculated result as a function of integration range of χ and data point density against the result at highest range and density (top right corner in figure 7.6). The results show that at a range of 5 and data point density of 36 points per unit of χ (b = 5; $\Delta\chi$ = 1/36), the accuracy reaches its limit, which is the rounding error of a floating point variable with double precision.

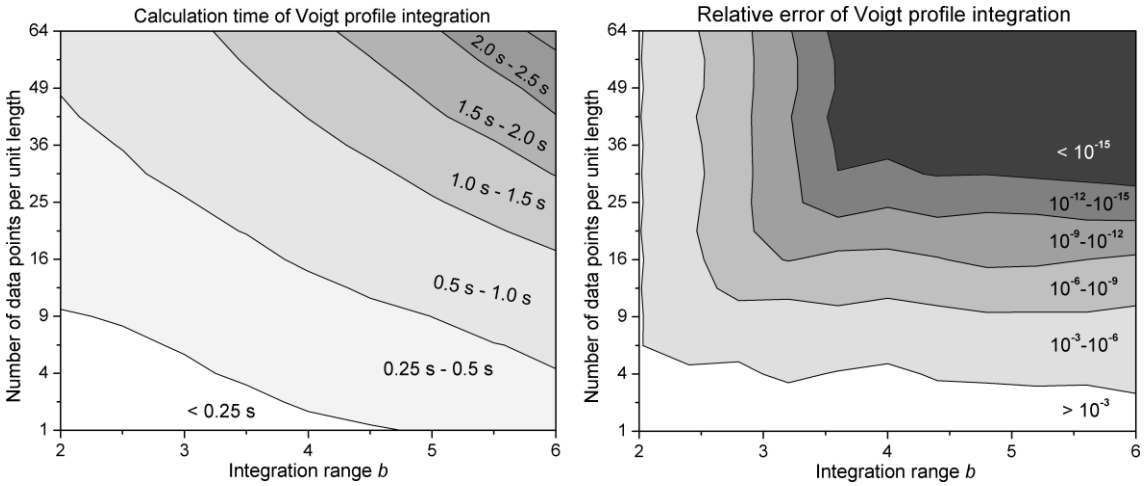

Figure 7.6 Calculation time for 10000 calculations (left) and accuracy of the numerical Voigt profile integration (right) to determine the optimal trade off parameters

The width of the integrand $f(\chi)$ is a function of the gas pressure p and temperature T. The parameters were scanned in the expected operating region for a time consuming, high quality integration and the trade-off parameters (b = 5, $\Delta\chi$ = 1/8). The results show (figure 7.7), that the relative error does not exceed 0.05%.

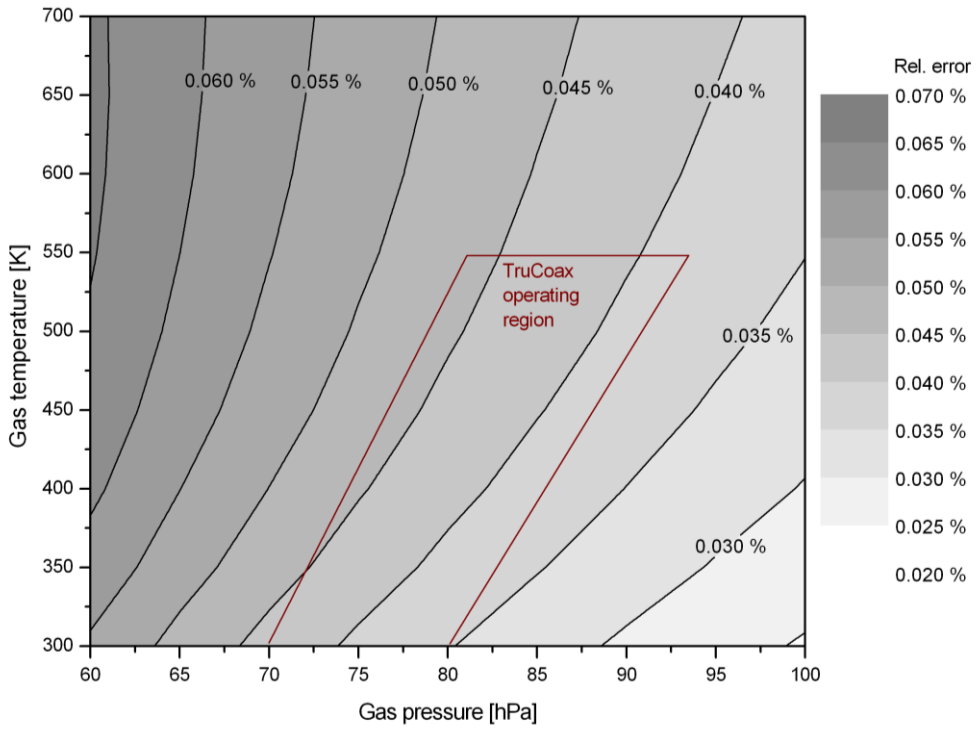

Figure 7.7 Error of Voigt integral approximation with b = 5 and $\Delta\chi$ = 1/8 in the operating range of the TruCoax laser

7.3.2 Laser signature in dependence of cavity length

The laser resonator length variation is the dependent variable defining the laser signature. Therefore the lineshape, which is a function of the detuning frequency $\Delta\nu$ from the line centre frequency ν_0, needs to be expressed in terms of detuning of the resonator length ΔL. Assuming that the frequency (or wavelength) shift is small enough so that the longitudinal mode number q remains constant, we can state from equation (7.10):

$$\Delta L = q\frac{\Delta\lambda}{2} \tag{7.17}$$

Inserting equation (7.17) into (7.10) and after rearranging for frequency, the dependence for cavity length detuning ΔL can be written as:

$$\Delta L = -L\frac{\Delta\nu}{\nu_0 + \Delta\nu} \tag{7.18}$$

where $\Delta\nu$ is the detuning frequency, ν_0 is the centre frequency of the transition. The relation (7.18) together with the approximation (7.16) allows one to calculate the relative gain for a Voigt lineshape as a function of an arbitrary cavity length $L + \Delta L$. Equation (7.18) can be further simplified acknowledging that the frequency of the transition is several magnitudes larger than the linewidth:

$$\nu_0 >> \Delta\nu \tag{7.19}$$

By using the assumption (7.19) the equation becomes:

$$\Delta L = -\frac{L}{\nu_0}\Delta\nu \tag{7.20}$$

Direct measurement of length variation ΔL in micrometer-range in a mechanical structure of over one metre is not trivial, but indirect measurement based on thermal expansion is straightforward, as both inner and outer electrodes are water cooled. The relative change of the cavity length is obtained by:

$$\Delta L(t) = L\kappa\ \Delta T(t) \tag{7.21}$$

where L is the nominal cavity length, κ is the linear expansion coefficient for the electrode material, $\Delta T(t)$ is the measured deviation of water temperature from the set point temperature.

The temperature measurement provides sufficient accuracy to be able to calculate the laser signature. The limitation of this method was observed for high temperature gradients which result in cavity length changes of 0.4 μm per second or more. At these

fast temperature changes the signature seems to change more slowly in the experiment than expected. A possible explanation is that the mechanical system cannot immediately assume the temperature of the water due to thermal inertia.

Temperature measurements provide information about the relative change of the cavity length, and the absolute length of the mechanical assembly is known within tenths of a millimetre. However, the length uncertainty of the entire assembly accuracy is too large to be able to be used directly for laser signature evaluation. The cavity length L_{cav} at nominal temperature of 298 K used for the signature calculation can be expressed as:

$$L_{cav} = L_0 + s\frac{\lambda}{2} \tag{7.22}$$

where L_0 is the assumed cavity length from manufacturing drawings of the TruCoax laser, s is a real number defining a small cavity length offset and λ is the CO_2 laser wavelength.

The line selection mechanism was applied based on available recorded temperature data for 10 minutes to obtain a laser signature plot over the measurement duration as shown in figure 7.8. The largest variation in the result is observed if the nominal cavity length is modified within a fraction of the half-wavelength. The results show that this parameter is one of the most critical variables, which influences the correlation between the measurement and calculation. The modification of the nominal length by an integer number of half-wavelength also shows a variation of produced signature, but the extent of the variant is much less. The wavelength difference between the neighbouring rotational lines is small, but for a large enough shift of multiples of the half-wavelengths the order of the appearing lines starts to alter.

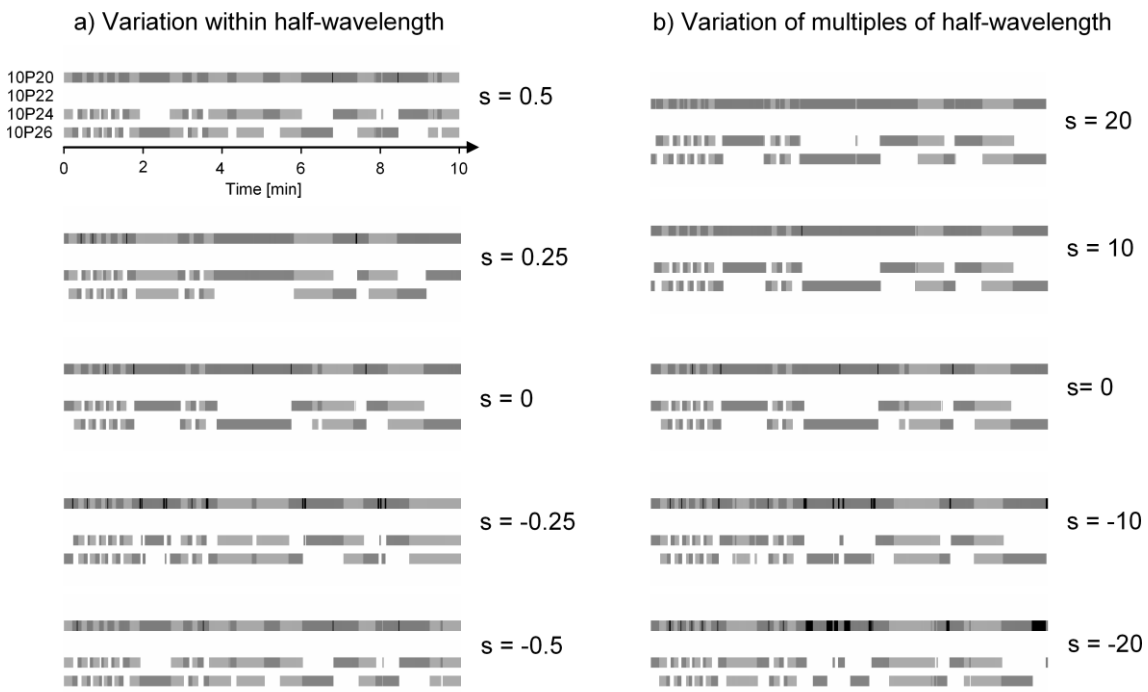

Figure 7.8 Influence of starting cavity length on calculated signature, where parameter *s* is defined in equation (7.22). The shades of grey indicate the strength of the line, dark being high.

7.3.3 Anomalous gain for P(20) line

The P(20) line in the $00^0 1$ - (I) transition band is only separated by 41.7 MHz from the $00^0 1$ - $11^1 0$ hot band transition in the R(23) line (see table 7.1). For the pressures employed in the TruCoax laser, or in RF excited CO_2 lasers in general, the linewidth due to homogeneous broadening becomes larger that the spacing of the two mentioned lines and the P(20) becomes the dominant lasing line. Singer [7.16] was one of the first researchers to measure the gain of each of the lines at 770 hPa for 4:1:1 He:N_2:CO_2 gas mixture. The additional gain for the P(20) line was 10%. At these pressures the linewidth is large enough so that the amplitude of the R(23) of the hot band can be approximated to be 10% of the P(20) line. For the lineshape found in the TruCoax laser the additional gain can be calculated based on this information to be 9.4%.

7.3.4 Adjustment of the lasing threshold

The gain of the electromagnetic wave amplitude is offset by the losses in the optical cavity, and so lasing occurs at certain lines when the gain is larger than the losses. The cavity losses may have different causes such as transmission or absorption at the mirrors, diffraction losses due to finite size of the mirrors etc. An analytical solution based only

on losses associated with losses at the mirrors defined to have reflectivity R_1 and R_2 and a cavity length L can be estimated using [7.13]:

$$Loss_{mirror} = \frac{1}{2L}\ln\left(\frac{1}{R_1 R_2}\right) \tag{7.23}$$

The loss in the mirrors is minimal for highly reflective coatings, and according to (7.23), the losses are of the order of 0.1%.

Diffraction losses as the beam propagates from one mirror which become projected onto the other mirror can be calculated numerically using the Fox and Li methods. A useful resonator parameter in estimating the diffraction losses is the Fresnel number N_f, which is defined as [7.9]:

$$N_f = \frac{a^2}{\lambda L} \tag{7.24}$$

with the mirror radius a, wavelength λ and cavity length L. For a = 3.5 cm and L = 1.4 m the Fresnel number N_f is 0.815. For a TEM_{00} mode with this Fresnel number, Fox and Li calculated [7.17] a power loss of 0.4%. The diffraction losses in the annular helical-axicon resonator using the Fox and Li approach were reported by Ehrlichmann in [7.18]. The loss mechanism due to interaction of the beam with the curved electrode wall appears to be the dominating factor and amounts to 2% - 3% [7.18].

The overall losses in the TruCoax laser were set to 6% in order for the calculations to match the measured signature. Possible explanation for the higher-than-expected losses might be due not only to the resonator design but also due to the measurement accuracy of the equipment used. For example, there is some uncertainly in the precise identification of the laser emission lines, since the phosphor sensor-screen of the spectrum analyzer (Macken 16A) is also somewhat sensitive to stray light (IR/visible) with which it is partially illuminated (as well as the laser light), so that the screen may display spurious signal (in addition to that produced by the laser radiation), for stray input light over a certain threshold.

7.3.5 Estimation of the population inversion value

The laser gain in equations (7.8) and (7.9) were derived as a function of the spectroscopic constants and also of the translational temperature T and the population density probability of the lower and upper vibrational levels N_v and $N_{v'}$. The gas temperature can

be estimated from a solution of the heat equation. For the TruCoax laser at 30 kW RF input power it was calculated to be 520 K. On the other hand, the values for the population probabilities depend on a large number of factors, such as the number of gas species and free electrons as collision partners. The energy transfer for vibrational and rotational excitation and relaxation also depends on their translational energy.

An approach to estimate the vibrational level populations is to apply the results of a "temperature model". The individual vibrational states are described in this model as temperatures, assuming that the molecules with the same vibrational quantum state are in thermal equilibrium because the energy exchange between these molecules is considered to happen instantaneously. The first temperature model by Witteman [7.8] comprised of five temperatures: T_1 for the symmetric stretch mode (10^00), T_2 for the bending mode (01^10), T_3 for the asymmetric stretch mode (00^01), T_4 for the vibrational mode of nitrogen and T_5 for the translational mode. The computation can be reduced to a three temperature model if the asymmetric stretch and bending modes of the CO_2 molecule are assumed to be close to the translational temperature [7.19]:

$$T_1 = T_2 = T \tag{7.25}$$

The populations of the two remaining CO_2 vibrational modes were derived by Smith and Thomson [7.20]. The population of the asymmetric stretch mode is:

$$N_{00^01} = \frac{n_{CO_2}}{Z}\exp\left(-\frac{h\nu_3}{kT_3}\right) \tag{7.26}$$

The population of the symmetric stretch mode is:

$$N_{10^00} = \frac{n_{CO_2}}{Z}\exp\left(-\frac{h\nu_1}{kT_1}\right) \tag{7.27}$$

where n_{CO2} is the CO_2 molecule density, ν_n is the vibrational frequency and Z is the vibrational partition function [7.20]:

$$Z = \left[1-\exp\left(-\frac{h\nu_1}{kT_1}\right)\right]^{-1}\left[1-\exp\left(-\frac{h\nu_2}{kT_1}\right)\right]^{-2}\left[1-\exp\left(-\frac{h\nu_3}{kT_3}\right)\right]^{-1} \tag{7.28}$$

The population inversion ΔN can be calculated from the populations of the two vibrational states in the upper and lower laser levels as given in equations (7.26) and (7.27) [7.20]:

$$\Delta N = N_{00^01}F(J') - \frac{\theta(J)}{\theta(J')}N_{10^00}F(J) \tag{7.29}$$

where $\theta(J)$ is the degeneracy factor $2J+1$, $F(J)$ is the energy at rotational level J, where the prime symbol is used to differentiate between the states before (J') and after the transition (J). For P(20) line the states are $J' = 20$ and $J = 19$.

The actual values of the populations $N_{00}{}^{0}{}_{1}$ and $N_{10}{}^{0}{}_{0}$, or in general $N_{v'}$ and N_{v} are not vital for the functional relationship of the gain $\alpha(J)$. It is sufficient to evaluate the population ratio η which we define as:

$$\eta = \frac{N_{10^0 0} + \Delta N}{N_{10^0 0}} \tag{7.30}$$

Sazhin *et al.* [7.19] measured the vibrational temperature T_3 in a fast-flow DC excited CO_2 laser with a 1:11:28 CO_2:N_2:He gas mixture as a function of the gas pressure and volumetric power density as shown in figure 7.9.

The results for the 75 hPa curve shown in figure 7.9 together with the equations (7.25) to (7.30) were used to estimate the population ratio η in the TruCoax resonator at 30 kW RF input power, giving a value of input power density of 8 W/cm^3. The calculated population ratio as a function of the temperature $T_1 = T_2 = T$ is plotted as curve (a) in figure 7.10. As expected, the pumping efficiency decreases with increasing temperature.

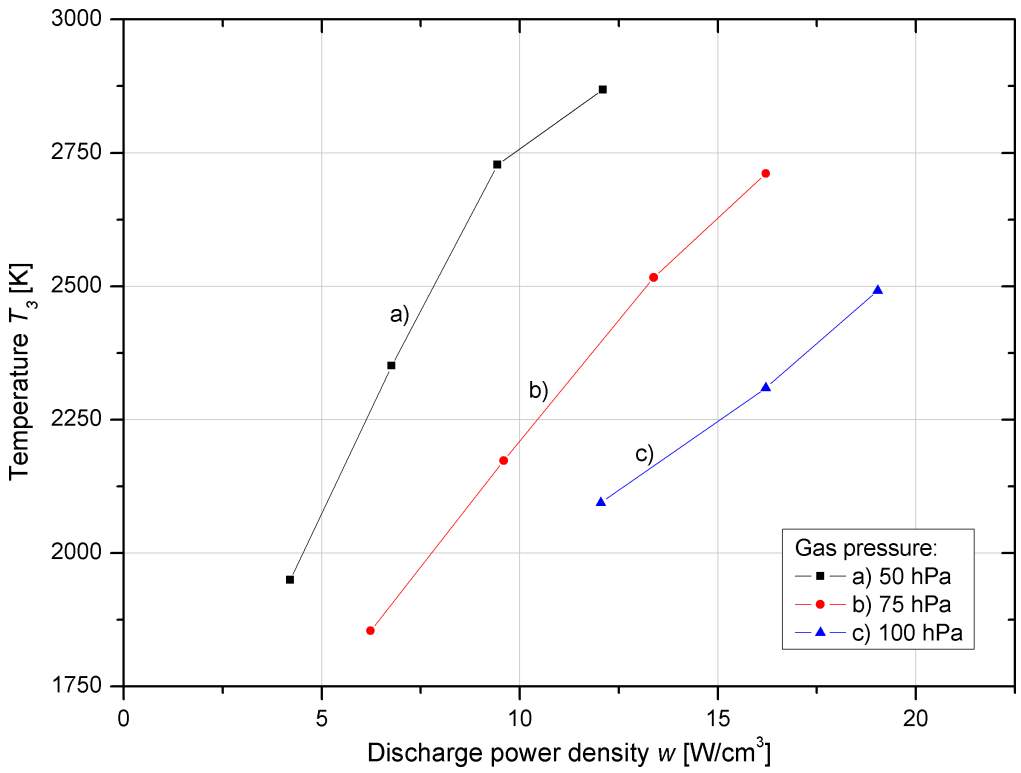

Figure 7.9 Measured asymmetric stretch mode temperature T_3 [7.19]

The measured lines in the TruCoax laser operating at 30 kW RF input power are P(20), P(22), P(24) and P(26). The temperature T and the population ratio η were adjusted in the function $\alpha(J)$ (equation 7.8) so that the relative gain of the lowest and highest observed rotational lines, which are P(20) and P(26) respectively, remain constant. By doing this, the calculated laser signature remains similar in appearance regardless of gas temperature. The result of this method of evaluation of the population ratio η is plotted as curve (b) in figure 7.10. The intersection point lies at 507 K, which is remarkably close to the calculated average gas temperature of 520 K, probably because the E/N ratio was very similar for two relevant laser types, namely the TruCoax and the fast-flow DC laser in [7.19].

Another degree of uncertainty is the function of the population ratio from the 3-temperature model in figure 7.10(a). The actual values in the case of the TruCoax laser are not expected to be identical since the results in [7.19] are based on a setup with a different gas mixture.

The evaluation, however, is able to provide a useful orientation and starting point for the values of the population ratio as function of gas temperature.

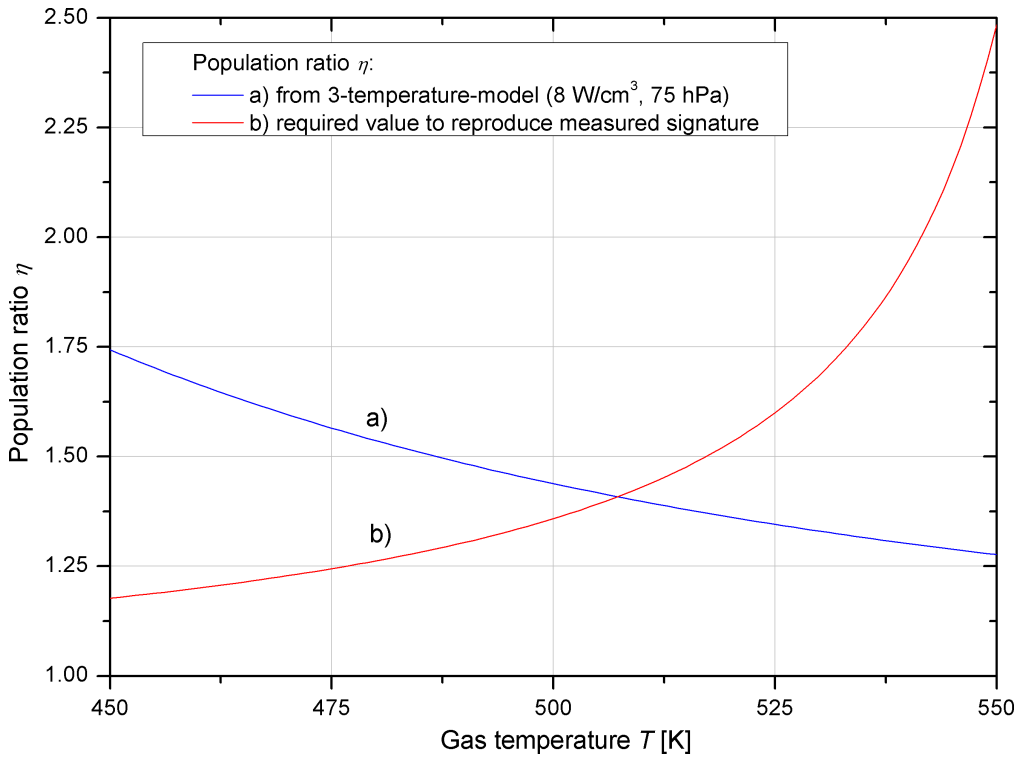

Figure 7.10 Population ratio η as function of gas temperature

a) calculation based on three-temperature model with data from [7.19]

b) population ratio which yields similar TruCoax laser signature ($\alpha_P(20) = \alpha_P(26)$)

7.3.6 Prediction of laser signature

An example of a comparison between the calculated laser signature and measurement of the spectrum of the TruCoax laser running at 30 kW RF input power over a period of about 10 minutes is shown in figure 7.11. The laser was left running for more than one hour before starting the measurement to ensure that the mechanical structure is in thermal equilibrium. The cooling water temperature in 7.11(a) is converted into the electrode thermal expansion as described in the previous section, and the calculated gain values for individual rotational lines are shown in 7.11(b). The rotational lines are drawn in the laser signature result in 7.11(c), if the gain value is above the threshold value. A typical feature that was observed in this configuration is that the line P(22) is missing in the signature. The overall gain of the P(20) line is, due to its anomaly, larger than the highest gain lines P(24) - P(26), which are described by the Maxwell-Boltzmann distribution at the operating temperature of 500 K.

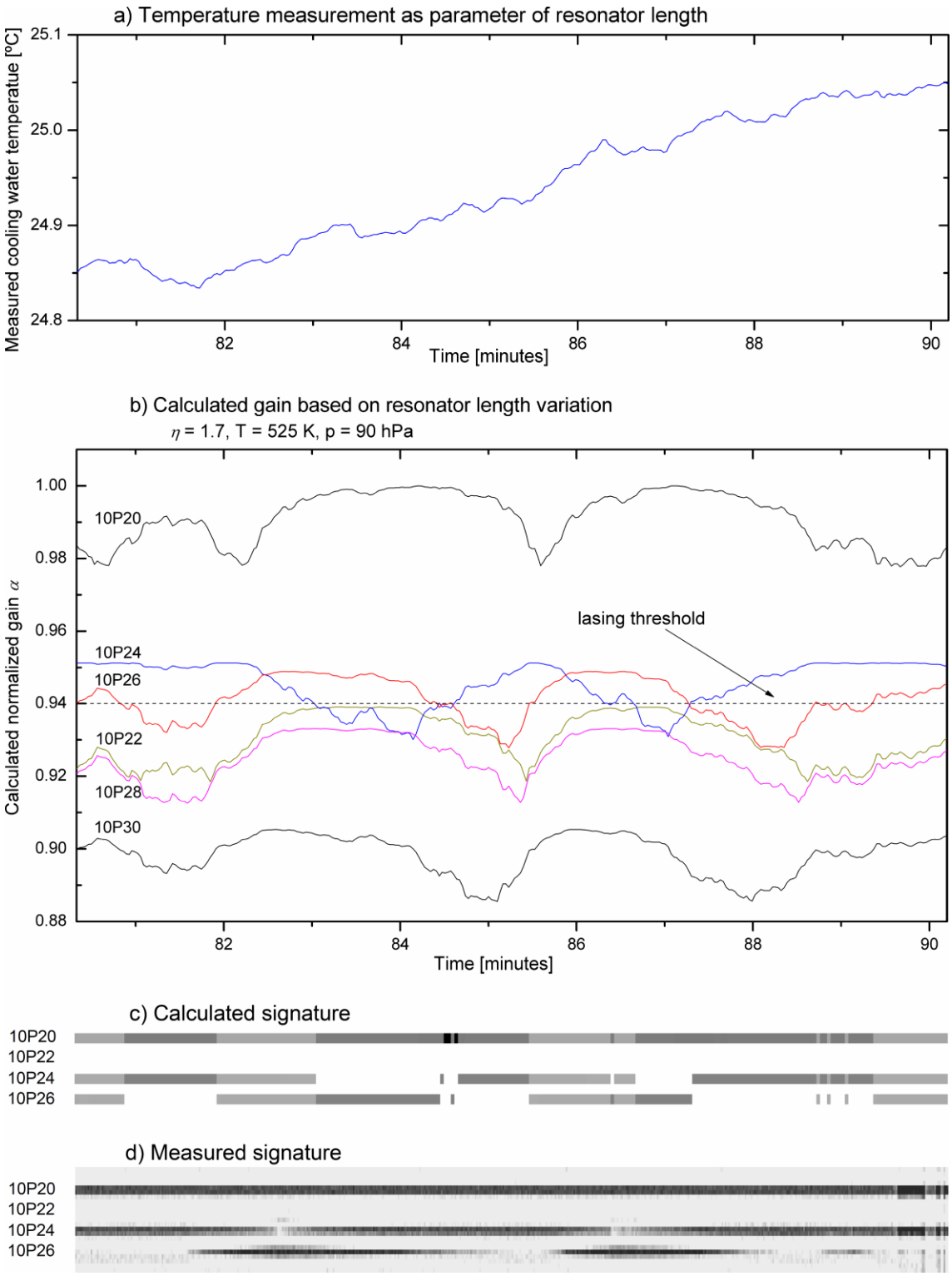

Figure 7.11 Calculation of laser signature based on temperature measurement shown in (a). The gain of individual rotational lines is shown in (b). The calculated laser signature as result of (b) is compared with the measured laser signature in graphs (c) and (d)

7.4 Mode Discrimination by Aperturing the Beam in the Radial Direction

The interaction with the electrodes in a free space resonator is minimal compared to the case of a waveguide laser, but it is not negligible. The electrodes in the TruCoax resonator define the beam in the stable direction, in which the electrode spacing is adjusted to provide a trade-off of minimal interaction with the fundamental mode in one hand and as the loss mechanism for higher order modes on the other hand.

The scattered infrared light inside the axicon mirror block, which appears due to coupling losses of the beam into the gap between the electrodes, is measured in a setup as shown in figure 7.12. A fraction of the scattered light escapes after multiple bounces inside the axicon mirror block. The light is then picked up by a power meter.

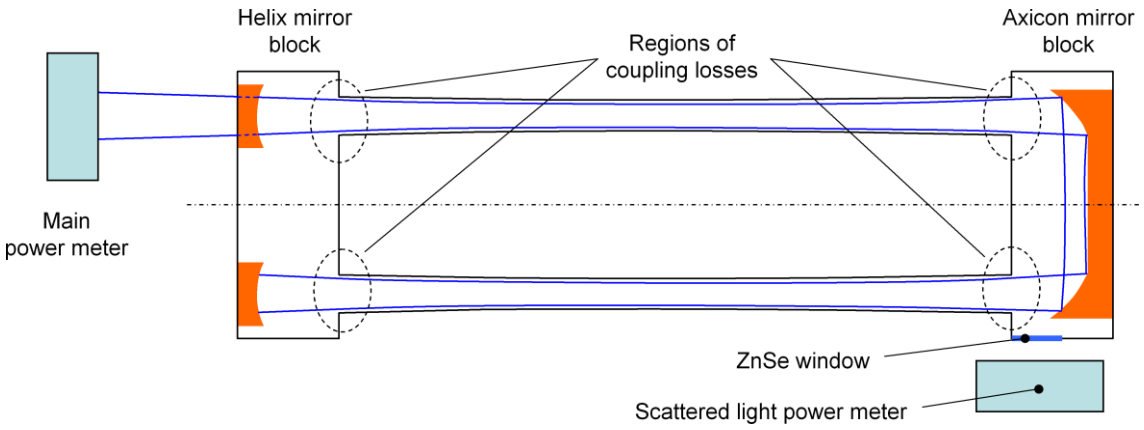

Figure 7.12 Setup to measure the resonator coupling losses

The results of a simultaneous measurement of the laser output power, the scattered light power and the laser signature is shown in figure 7.13. The red vertical lines are inserted for orientation. It was observed that the laser experiences drops in output power when higher order lines lase, which is best seen in the case of the P(26) line as indicated by the red vertical lines. At the same time the scattered light power is at its maximal value so that the laser output power and the scattered light power seem to be indirectly proportional to each other. The measured scattered light power increases by about 10% comparing the scattered light for P(20) and P(26) lines.

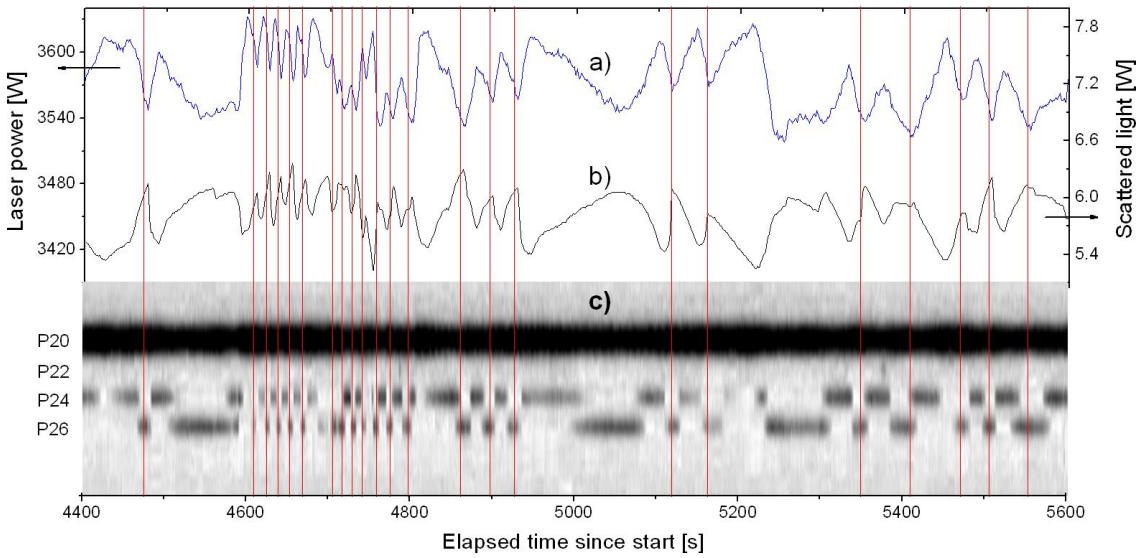

Figure 7.13 Correlation of measured losses (a) with laser output power drops (b) and appearance of higher rotational lines (c)

The explanation for this phenomenon is likely to be the variation of the fundamental mode size of the beam in the stable direction for different rotational lines. The wavelength difference between the rotational lines is relatively small, with about 0.2% per ΔJ of 2. The increase of power in the tail of the fundamental mode profile in the region outside the gap increases, however, by 3.6% if we calculate the beam size in the stable direction in the position of the electrode end at the axicon side. The deflection of the beam by the strong thermal lens near the electrodes and diffraction on the electrode edges is expected to increase the variation of the amount of the scattered light due to longer wavelength even more.

7.5 Correlation between Laser Signature and Output Power

The measurements (figures 7.11 and 7.13) show that the typical TruCoax laser signature with 30 kW RF input power consists of P(20), P(24) and P(26) lines, with the P(20) being the dominating line. As soon as the cavity length changes away from the P(20) optimum, lines with higher J values start to appear as can be observed in the calculated gain curves in figure 7.14. In the previous section it was stated that the higher order lines are associated with higher internal scattering losses. The output power for the given setup therefore simplifies to a response which is proportional to the gain of the P(20) line:

$$P_{out} \propto 1 - \alpha_P(20) \tag{7.31}$$

The gain for the P(20) line can be obtained from the set of parameters that are able to reproduce the laser signature. An example of such a calculation is shown in figure 7.14.

The laser power fluctuation has, according to this model, maximal amplitude that will not exceed ±25 W (see curve (b) in figure 7.14). This prediction is true for most of the measurements. However, the occurrence of some fluctuations with about 3x the expected amplitude has no apparent reason from only a consideration of the spectral properties.

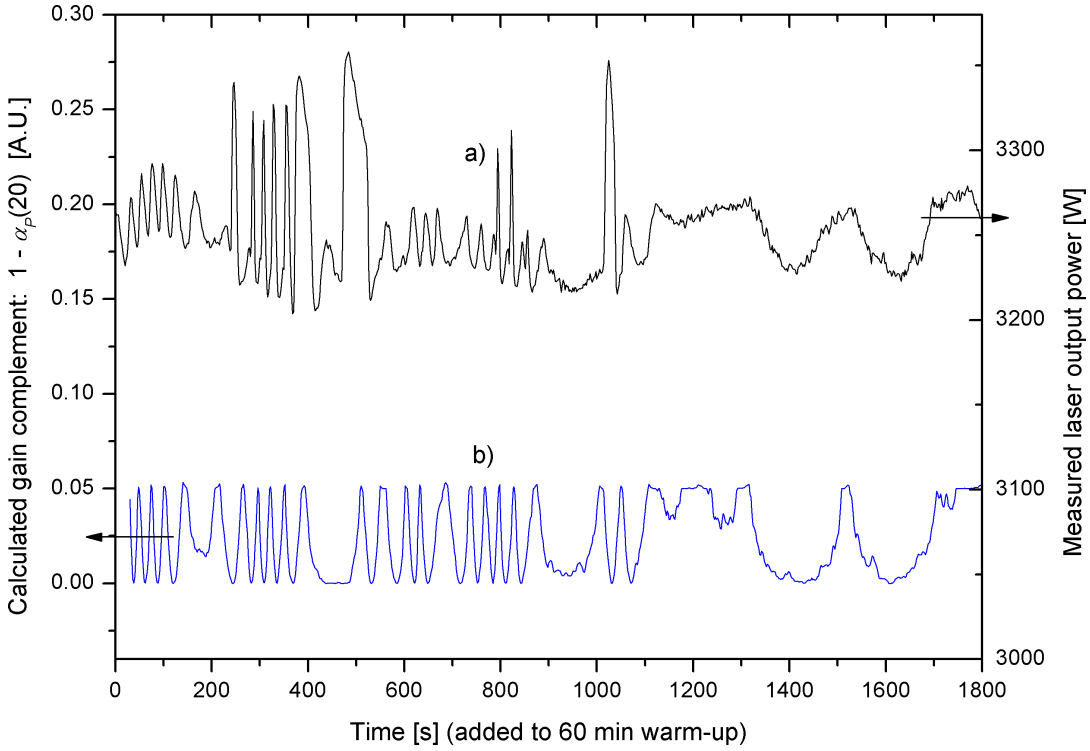

Figure 7.14 Comparison of (a) measured laser output power and (b) signal proportional to 1 - α_P(20)

The approach of deducing the gain of individual rotational lines from the laser signature gives a good insight of the laser output power behaviour and could explain the power fluctuations within some boundaries. We can refer to these power fluctuations as laser *signature* power fluctuations, and these fluctuations produce a measured power stability of about ±25 W, a value that is fully acceptable for the intended application. The suggested model is not able to describe the mechanism of seemingly random power fluctuations larger than the "laser signature fluctuations" without incorporating further properties, such as the fluctuations of the optical flux.

7.6 Summary

An extensive model has been developed which describes the vibrational-rotational spectrum of a CO_2 laser within a laser resonator. The specific dimensions and boundary conditions relevant to the TruCoax laser were applied to the model so as to be able to reproduce the laser signature. The excellent correlation that was observed between the

measured laser signature and the calculation was used as a key to gain insight into the detailed operation of the TruCoax laser system. For example, the results obtained could be used to determine the values of the relative gain of the individual rotational lines. Also typical observed laser power fluctuation could be explained in terms of the laser signature calculations. The model could also be expanded to include other band transitions.

However, the model also showed its limitations in not providing a full explanation of the larger-than-expected fluctuations in laser output power. A possible approach to being able to explain and tackle these fluctuations has recently been developed by optimizing the resonator design in the unstable direction, and a study of this topic was conducted by Deile [7.21]. In addition, an experimental setup, where the effective magnification of the TruCoax laser in the unstable direction was varied by masking part of the beam in the azimuthal direction, showed a significant improvement in the output power stability [7.22].

7.7 References

[7.1] E. Fermi, "Über den Ramaneffekt des Kohlendioxyds", Z. Phys., vol. 71, pp. 250-259 (1931)

[7.2] A. Adel, D. M. Dennison, "The infrared spectrum of carbon dioxide. Part I", Phys. Rev., vol. 43, pp. 716-723 (1933)

[7.3] L. Freed, L. C. Bradley, R. G. O'Donnell, "Absolute frequencies of lasing transitions in seven CO_2 isotopic species", IEEE J. Quantum Electron., vol. 16, pp. 1195-1206 (1980)

[7.4] L. C. Bradley, K. L. Soohoo, C. Freed, "Absolute frequencies of lasing transitions in nine CO_2 isotopic species", IEEE J. Quantum Electron., vol. 22, pp. 234-266 (1986)

[7.5] A. G. Maki, Che-Chung Chou, K. M. Evenson, L. R. Zink, Jow-Tsong Shy, "Improved molecular constants and frequencies for the CO_2 laser from new high-J regular and hot-band frequency measurements", J. Mol. Spectrosc., vol. 167, 211-224 (1994)

[7.6] A. Amy-Klein, H. Vigué, C. Chardonnet, "Absolute frequency measurement of $^{12}C^{16}O_2$ laser lines with a femtosecond laser comb and new determination of the $^{12}C^{16}O_2$ molecular constants and frequency grid", J. Mol. Spectrosc., vol. 228, pp. 206-212 (2004)

[7.7] A. C. G. Mitchell, M. W. Zemansky, “Resonance radiation and excited atoms”, Cambridge Press, ISBN 0-521-084334 (1961)

[7.8] W. J. Witteman “The CO_2 laser”, Springer, Berlin, ISBN 3-540-17657-8 (1987)

[7.9] A. E. Siegman “Lasers”, University Science Books, Mill Valley, ISBN 0-935-702-115 (1986)

[7.10] R. L. Abrams “Broadening coefficients for P(20) CO_2 laser transition”, Appl. Phys. Lett., vol. 25, pp. 609-611 (1972)

[7.11] L. Rosenmann, M. Y. Perrin, J. Taine “Collisional broadening of CO_2 IR lines. I. Diode measurements for CO_2-N_2 mixtures in the 295-815 K temperature range”, J. Chem. Phys., vol. 88, pp. 2995-2998 (1988)

[7.12] O. Svelto “Principles of lasers”, Springer, New York, ISBN 978-1-4419-1301-2 (1998)

[7.13] J. T. Verdeyen, “Laser Electronics”, Prentice Hall, ISBN 0-137-066-66X (1995)

[7.14] G. Schiffner “Prediction of CO_2 laser signatures”, IEEE J. Quant. Electron., vol. 8, pp. 877-882 (1972)

[7.15] Xianglei Huang, Yuk Ling Yung, “A common misunderstanding about the Voigt line profile”, J. Atm. Sci., vol. 61, pp. 1630-1632 (2003)

[7.16] S. Singer “Observations of anomalous gain coefficients in TEA double-discharge CO_2 lasers”, IEEE J. Quantum Electron., vol. 10, pp. 829-831 (1974)

[7.17] A. G. Fox, T. Li “Resonant modes in a maser interferometer”, Bell Syst. Tech. J., vol. 40, pp. 453-488 (1961)

[7.18] D. Ehrlichmann “Azimuthal instabile Resonatoren und Ringresonatoren für Hochleistungslaser”, diss. RWTH Aachen (1994)

[7.19] S. Sazhin, P. Wild, C. Leys, D. Toebaert and E. Sazhina “The three temperature model for the fast-axial-flow CO_2 laser”, J. Phys. D: Appl. Phys., vol. 26, pp. 1872-1883 (1993)

[7.20] K. Smith, R. M. Thomson “Computer modeling of gas lasers”, Plenum Press New York, ISBN 0-306-31-0996 (1978)

[7.21] J. Deile “Power scaling of high brightness multi-kilowatt coaxial CO_2 lasers”, dissertation HWU Riccarton (2012)

[7.22] V. Granson, F. J. Villarreal, J. Deile, J. F. Monjardin, S. Sumrain “Optimization of the intra-cavity optical flux in the unstable direction in RF excited annular CO_2 laser in terms of power stability”, Proc. SPIE 8600, 86004 (2013)

Chapter 8

CONCLUSIONS AND FUTURE OUTLOOK

8.1 Introduction

The main objective of the work presented here was to minimise or eliminate entirely various instability processes in the TruCoax V6, an annular RF discharge high-power CO_2 laser intended for industrial applications. The topics covered include RF discharge instabilities, laser output-power instabilities and the effect of thermal lensing on the optical resonator design. The RF discharge instabilities covered in the study were further divided in terms of the cause of their occurrence, whether thermal instabilities and ionic instabilities in the RF feed region, or instabilities caused by acoustic resonances.

A systematic treatment of each of these topics included a review of the underlying physics fundamentals, establishing numerical or analytical models to describe the problem and experimental confirmation of the theory. As outcome of each section, a safe operation regime or an improved design were implemented to counteract the instability issues.

The body of work presented in this thesis is a significant contribution to the design and subsequent release of the TruCoax V6 laser platform with both 2.5 kW and 3.2 kW versions. One key feature of this research is that the enhanced laser design enables manufacturing costs to be driven down by 40% compared to the previous V5 laser, which is a major enhancement in terms of market competitiveness. Moreover, the improved control of RF discharge and optical power instabilities has led to higher production yield and longer product life-time.

The thesis chapters are laid out as relatively independent units, so it is appropriate in this chapter to discuss the overall conclusions and future outlook individually relating to each chapter. The contents of the topics are summarized in table 8.1 emphasising the common approach for problem solving.

Table 8.1 Summary of topics covered in the thesis

	RF discharge instabilities (RF feed)	Acoustic resonances	Thermal lensing	Laser signature
Theoretical background	Electrostatics Electric breakdown with RF voltage	Acoustic wave Speed of sound Helmholtz equation	Heat equation Gas mixture properties ABCD matrix formalism	Vibrational-rotational IR spectrum of CO_2 CO_2 laser gain Lineshape
Calculation and simulation	Laplace's equation El. Breakdown based of diffusion theory	Acoustic eigenmodes (FEA) Transient heat equation (FEA)	Temperature, refractive index profiles across the gap Thermal lensing matrix	Optical gain for individual rotational lines
Experiments	Analysis of failures with different RF feed designs	Frequency sweep with harmonic excitation Pressure wave response	RF discharge luminosity profile Single pass propagation with HeNe laser	Spectrum and power measurements Scattered light power
Significant improvement	Modified design eliminated damage	Defined allowed frequency band Laser control options	Verified thermal lensing magnitude with experiments Studied dependency of thermal lensing on operating parameters	Shown two regimes of instabilities: <25 W is due to laser signature

8.2 Suppression of Discharge Instabilities in the RF Feed Region (Chapter 3)

The development of a RF feed-through assembly capable of delivering 30 kW of RF power through the vacuum envelope to the discharge region was the subject of Chapter 3.

An electric breakdown model for RF voltages using diffusion theory was established based on the literature and a Boltzmann function solver [8.1], and a second model was set up to determine the electric field distribution for a given RF feed-through design, using a commercial FEM package [8.2]. The electric potential distribution derived from the Poisson's equation allows one to locate the region where arc-occurrence is most probable, where, as expected, this region coincides with areas of shortest electric field lines. An early confidence-booster for validity of the model came when predictions of the location

of the electric breakdown site in an early RF feed design proved to be accurate. The shape and location of the dielectric insulator and the geometry of the RF feed shaft were redesigned (aided by the electrostatic model), and when the new RF feed assembly was implemented no signs of subsequent arcing damage were observed.

As an additional complication at higher RF input power (~30 kW compared to 20 kW in the Model TruCoaxV5 laser), was that an "instability" in the RF discharge was observed when a transition from the α-type to the γ-type RF discharge occurs in the vicinity of the RF feed-through. A transmission line model was applied to the RF discharge structure of the annular laser to reveal any unfavourable voltage distribution immediately before RF discharge ignition. In order to minimise high electric fields, an optimised inner-electrode geometry was proposed which makes use of the Euler spiral shape, based on the results from an electrostatic model and subsequently implemented in the system. The redesigned RF feed design successfully turned what had been a high-risk component, which was often the initiator of discharge instabilities into a reliable feature of the TruCoax V6 laser design.

Regarding possible *future developments*, a useful improvement of the model could be achieved by adding an algorithm to find the shortest field line automatically so as to identify regions that are particularly susceptible to arcing. Moreover, the procedure as described can also be adapted for use with other components in the system, such as the inductors used to even out the longitudinal voltage distribution. With the formation of the RF discharge, the voltage across the discharge gap is regulated by the current-voltage characteristics of the α-type discharge, and the electrostatic model can be modified to include a discharge structure with a conducting plasma column. This modification is useful for the evaluation of the high electric fields of the "hot" mechanical structure.

The transition from α-type to γ-type RF discharge mentioned above is related to electric breakdown, a phenomenon which is especially important for the TruCoax laser, which is excited by RF fields at a frequency of 27.12 MHz, at which value the transition threshold is relatively low, thereby increasing the risk of the transition instability occurring. We can modify the electric breakdown model based on Townsend's criterion to estimate the α-γ transition as a breakdown of the ion sheath. This modified model is useful to investigate the occurrence of the γ-type discharge as a function of operating parameters such as gas mixture and pressure, discharge gap and inter-electrode voltage.

A logical solution to increase the threshold of the transition to γ-type discharge is to apply higher RF excitation frequencies as pointed out in section 2.3.1. However, this step involves switching to a different (higher cost) RF power supply and requires a redesign of electrical components which was not within the scope of the thesis.

8.3 Acoustic Resonances in the Laser Vacuum Vessel (Chapter 4)

The objective of the research discussed in this chapter was to mitigate the effects of acoustic resonances which can interrupt stable operation of the RF discharge under pulsed excitation conditions. In order to describe the laser cavity as an acoustic device, the basic underlying acoustic theory from elementary sound wave propagation to the Helmholtz differential equation were introduced to provide the required physics background.

The values of resonant frequencies of the TruCoax laser cavity were determined using an FEM model. Specific to the given geometry, the Helmholtz resonance, where the kinetic energy is stored by compression of the gas in either the helix or axicon mirror block turns out to be lower than the first standing wave eigenmode in the longitudinal direction. The Helmholtz and the first order modes in the axial direction at 90 Hz and 200 Hz respectively are the two strongest resonant frequencies with the largest regions of low and high gas pressure, which are dangerous as possible "triggers" for RF discharge instabilities.

Two experimental setups were used to test the validity of the FEM model. In the first experiment, an acoustic wave was excited harmonically in the cavity by a loudspeaker. The sound excitation frequency was swept to obtain the acoustic wave amplitude as a function of frequency. The transient microphone signal following an acoustic pressure wave excitation was used in the second experiment to measure resonant frequencies. The measurement results were observed to agree with the calculated predictions within the limits of the details of the model and the accuracy of the measurements.

Laser operation at specific laser pulsing frequencies are required by laser users for the optimization of the laser metal cutting applications, which are dependent on parameters such as material type and thickness. Stemming from the fact that it is unacceptable for the design to be optimised for only a certain range of pulsing frequencies, and since acoustic resonances will always be present in a rigidly walled vessel, a duty cycle-frequency map was prepared based on measurement data and a time-dependent numerical solution of the

heat equation. This map provides an overview of the severity of the acoustic resonances in the operational range of the TruCoax laser.

Two methods to minimise the resonances with software are proposed. The first method is the use of a double-frequency modulation, where the low frequency gating signal consists of a train of high frequency pulses, which was shown to be capable of successfully diminishing the standing wave patterns. The *second* proposed method would involve frequency dithering and is predicted to provide a similar positive effect, though experimental verification is not included here. Although acoustics is a classical and well studied discipline in physics and engineering, detailed treatment applying to a specific gas laser, as presented in this thesis is hard to find in the literature.

It should be mentioned here that, unfortunately, it was not possible to carry out some potentially interesting and beneficial work due to time and hardware-access constraints. Nevertheless, the research that was completed can be grouped into two categories; the first category was aimed at improving the accuracy of the acoustical model while the second was geared towards suppression of resonances by software logic.

The accuracy of resonant frequency values generated from an FEM model depends on how closely the mesh of the model represents the actual structure, and the accuracy of the results obtained, especially at higher order modes where small features become more important, can be improved by importing a more refined model from a solid (3-dimensional) CAD drawing. The import feature could not be realised with the FEM package that was available in this work [8.2].

A harmonic excitation model was used which allows a steady state solution for the pressure or particle velocity distribution to be determined. However, we can move to a transient analysis model, which is more appropriate to describe the pressure wave experiments described in section 4.5, since it can, for example, be used to investigate the unfavourable frequency transitions that create high pressure amplitudes that threaten to cause interruptions in the stable α-type RF discharge operation. Also, the Transmission Line Matrix method (TLM) [8.3] may be a suitable approach to investigate time-dependent pressure variations.

Regarding the task of suppressing acoustic resonances with software algorithms, we can introduce a timer that restricts operation so as to avoid certain pulsing parameters based

on data provided in the acoustic resonance severity map (section 4.6). In this way, the pulsing frequency can be shifted towards less harmful frequencies before a standing wave patterns have the time to be built up in the vessel.

Similarly, the frequency dithering algorithm (section 4.7.2) reduces the magnitude of acoustic resonances by pulsing with a slightly different frequency for each period. However, the frequency dither did not fully deliver the anticipated positive results in the preliminary experiments, and further tests need to be carried out to improve the parameters for the algorithm.

Developing a better understanding of acoustic resonances in the laser vessel has also resulted in some other (synergistic) effects, and two examples are mentioned here, namely acoustic cleaning and discharge stabilization.

Currently, one of the steps in the laser production process involves running the discharge in pulsing mode where the pressure wave from the discharge ignition "shakes loose" small metallic particles left on the electrode surface following machining. This procedure is referred as the cleaning step. In the proposed modification of this procedure, a loudspeaker is used at atmospheric pressure instead of the RF discharge. In this case it is desired to actually choose resonant frequencies during acoustic excitation, since there is no RF discharge present. The advantage of using the loudspeaker is higher effectiveness of the cleaning step due to the higher gas pressure which are usable, and also the much smaller electricity consumption.

In another example, the RF discharge pulsing frequency and the duty cycle were modulated with a sinusoidal function similar to the frequency dithering reported above (section 4.7.2). The idea behind this modulation is to prevent the build-up of even partial standing wave patterns, which can occur even if the pulsing frequency is not in resonance. In these circumstances, preliminary tests have shown that the more homogeneous pressure wave distribution that this modulation produces results in an increased value of the threshold for α-γ discharge transition.

8.4 Fundamentals of Thermal Lensing in Gas Lasers (Chapter 5)

Thermal lensing is an especially important topic in diffusion-cooled free space optical resonators because of the large gas temperature gradients that can be established across

the discharge gap. It is therefore necessary to estimate the magnitude of this thermal lensing effect during the resonator optimization process.

The proposed calculation procedure includes several steps, where some can be carried out in parallel while some results are fed into the next step. The calculations took into account properties particular to the annular laser (thermal conductivity, viscosity, refractive index as a function of temperature) and the Joule heating profile of the α-type discharge structure. Based on the input parameters (pressure, discharge gap, power density), the radius of curvature of the thermal lens so-generated was evaluated as a function of position across the electrode gap. For the typical operating conditions in the TruCoax laser, the effective radius of curvature of the thermal lensing was determined to be between -5 m and -6 m in the centre and becoming rapidly much shorter towards the walls, due to the large local rate of change of the temperature gradient. For example, at 77 hPa operating pressure and 6.6 mm average inter-electrode spacing the measured and calculated thermal lensing radii amounted to -5.5 m and -5.1 m, respectively, which is significant when compared to the helix mirror, which has a radius of curvature of 2 m. The calculation procedure allowed an investigation to be carried out of the impact of the various boundary conditions on the magnitude of thermal lensing, so as to provide some design rules for laying out the optical resonator. It was shown that gas pressure and discharge gap variation have a large effect on thermal lensing, whereas relevant values of power density variation cause only marginal changes in the thermal lensing generated.

An attempt was made to avoid approximations in the modelled-phenomena in order to retain the highest possible accuracy in the predictions, e.g. the thermal conductivity of the gas mixture was not assumed to be constant or even linearly-dependent on temperature. However, the discharge structure was derived from the luminosity profile, where a model of the RF discharge structure would allow us to investigate the impact of changes in parameters such as excitation frequency, pressure, applied voltage or RF power density on the thermal lensing produced.

The apparent beam focusing which is caused by the transverse gain profile is not related to thermal lensing. Nevertheless, this effect is also of interest since we want to describe beam interaction with the gain medium. The approach for the calculation of the CO_2 laser gain profile has been shown in the literature such as in [8.4]. This effect is expected to

compensate for the thermal lensing to some extent, and it would be beneficial to apply the gain profile modelling to the specific case of the annular resonator.

Overall, the results show that the magnitude of thermal lensing is significant for the TruCoax laser. Moreover, the calculation procedure as described here could also be applied to other high power gas lasers such as fast flow resonators and amplifiers or waveguide gas lasers, recognizing that the actual optical configuration in these lasers may differ from the configuration predicted by free space propagation.

8.5 Impact of Thermal Lensing on the Coaxial Laser Resonator (Chapter 6)

Having established the magnitude of thermal lensing, the results can be used to estimate the magnitude of beam expansion in the stable direction inside the TruCoax optical resonator.

The ABCD matrix formalism was used as a tool to study the internal beam propagation, where the refractive index profile was approximated with a quadratic function. This simplification allows the magnitude of thermal lensing to be represented by a single value of radius of curvature or focal length.

An analytical formula for an ABCD matrix representing a continuously diverging medium was derived, which is similar in form to the ABCD matrix representation of a continuous lens (see [8.5], page 55). The advantage of the analytical formula is that it can be used to develop further analytical solutions of the resonator. Moreover, this method is easy to apply and provides optimal accuracy compared to numerical matrix multiplication.

The analytical formula was used to compare the indirectly-measured thermal lensing magnitude with the results of calculations as described in the previous chapter. The relative difference between the calculation and the indirect measurement is about 8%, which is a reasonable agreement considering the number of calculation steps.

A stable resonator model of the TruCoax laser was established, which includes the thermal lensing medium with a four-mirror-resonator. The model showed that due to the propagation path between the two axicon mirror surfaces, the beam expands along the RF discharge length, which is the thermal lensing medium. The results indicate that the beam

radius is 8% larger at the helix and 11.5% larger at the axicon end of the RF discharge length, as compared to free-space propagation in the same four-mirror-resonator.

The variation of the thermal lensing magnitude along the length as a result of RF power density variation was estimated from the transmission line model from Chapter 3 and data available in the literature. The results show an insignificant variation of beam size, leading to the overall conclusion that it is the thermal lensing magnitude that is the key defining factor.

The results presented in Chapter 6 show that thermal lensing is a significant factor in the specific case of the TruCoax resonator. Thus the characteristics of the resonator in the stable direction are defined not only by the curvatures of the resonator mirrors, but also by the thermal lens, and both factors need to be included in resonator geometry optimization to provide the discharge gap designed for only the fundamental mode operation, as confirmed by the experimental results.

Other effects can be studied with the ABCD matrix approach, including the effect on the beam size caused by a partially-filled RF discharge gap in the longitudinal direction, which is sometimes the case at low pulsing duty cycles.

However, the results show a stronger thermal lens in the vicinity of the electrodes, and the validity of the parabolic approximation of the refractive index profile could be verified even if the irradiance of the laser beam is small close to the electrode walls. Nevertheless, it should be noted that the thermal lensing profile can be better represented by numerical analysis in commercial packages such as VirtualLab [8.6], or GLAD [8.7] or by means of proprietary software as shown by Deile [8.8].

8.6 Causality Between the Laser Signature and the Laser Power Stability (Chapter 7)

A model to simulate the laser signature as a function of the laser cavity length was setup in order to study the relationship between output power and laser signature. This model features the rotational-vibrational spectrum of the CO_2 molecule in the regular $00^0 1$-(I) and $00^0 1$-(II) transition bands and the laser gain as a function of the rotational quantum number, the translational temperature and the population inversion ratio.

In the pressure range of 60-90 hPa and the temperature range 300-500 K that are typical for the TruCoax laser, the spectral widths of homogenous and inhomogeneous line broadening mechanisms are of similar magnitudes. Typical simplification, where lineshape is assumed to be purely either Lorentzian or Gaussian (depending on the dominant broadening mechanism) could not be applied there. Instead, a numerical algorithm to convolute both lineshapes, which is a numerical summation of the Voigt integral, was optimised to be executed with a trade-off between accuracy and execution time.

The model could be used to confirm the estimated operational parameters of lasing threshold, gas temperature, population inversion ratio, and the anomalous gain of the 10P(20) line, so as to be able to compare the measured laser signature with the simulated signature. It was found that coupling losses, which describe the lost optical power when the intra-cavity beam is re-entering the discharge gap, are proportional to the wavelength, i.e. the emission with rotational lines with higher order have the higher coupling losses which in turn leads to lower output power. Power fluctuations in the order of only ±25 W could be attributed to the line-selection mechanism caused by cavity-length variation, whereas no indication of any correlation with the laser signature was found for any larger or sudden power fluctuations that were observed experimentally. Since the results showed that the laser emission spectrum and the coupling losses are not responsible for the observed sudden power fluctuations, another factor, namely the beam amplification path in the unstable resonator direction was investigated in subsequent work (see [8.9] and not covered in this thesis). The intra-cavity beam propagation, which is governed by the resonator configuration in the azimuthal direction, was studied there using the ray-tracing method. The inverse proportionality of total propagation length and net gain threshold for lasing is considered to be the main trigger for output power instabilities. Experiments showed that by blocking a part of the mirror in the azimuthal direction and thus reducing the number of roundtrips the relative power stability improved from over 50 W to less than 25 W [8.9], which are the remaining power fluctuations generated by "laser signature" effects.

The accuracy of the signature calculation was sufficient in terms of the quality of the results and the computational time. Better correlation with the measured spectra can only be expected with direct and accurate measurement data of the actual cavity length, which

was not available at the time of thesis preparation. However, it was shown that the measurement of the cooling water temperature is sufficient to enable a good estimate of the cavity length and therefore the laser signature. The water temperature can be taken as an easily obtainable input parameter to actively adjust the cavity length with piezoelectric-element actuators, for example. In this way, the laser output power and the emission spectrum can be stabilised within static operating conditions.

The mechanism for the relationship between the measured scattered light and the output power does need to be further investigated. At this point it is not certain whether the wavelength-dependent coupling losses are beneficial and which modification to the laser geometry will minimise the coupling losses.

In the concluding chapter we have seen that there are still many unknowns in the annular resonator mechanisms even 15 years after the first demonstration and continuing research and development in this topic is needed to further improve its performance.

8.7 References

[8.1] BOLSIG, "Electron Boltzmann equation solver", version 1.05, CPAT Toulouse & Kinema Software (1996)

[8.2] FlexPDE, "A flexible solution system for partial differential equations", version 6.14, PDE Solutions Inc. (2010)

[8.3] D. de Cogan, W. J. O'Connor, S. Pulko "Transmission Line Matrix (TLM) in computational mechanics", CRC Press Boca Raton, ISBN 041-532-7172 (2005)

[8.4] V. N. Ochkin, W. J. Witteman, B. I. Ilukhin, I. V. Kochetov, P. J. M. Peters, Yu. B. Udalov, S. N. Tskhai "Influence of the electric field frequency on the performance of a RF excited CO_2 waveguide laser", Appl. Phys. B, vol. 63, pp. 575-583 (1996)

[8.5] J. T. Verdeyen, "Laser Electronics", Prentice Hall, ISBN 0-137-066-66X (1995)

[8.6] VirtualLab "Laser resonator toolbox", LightTrans GmbH (2013)

[8.7] GLAD "General Laser Analysis and Design", Applied Optics Research (2012)

[8.8] J. Deile "Power scaling of high brightness multi-kilowatt coaxial CO_2 lasers", dissertation Heriot-Watt University (2012)

[8.9] V. Granson, F. J. Villarreal, J. Deile, J. F. Monjardin, S. Sumrain "Optimization of the intra-cavity optical flux in the unstable direction in RF excited annular CO_2 laser in terms of power stability", Proc. SPIE 8600, 86004 (2013)

Appendix I: RF breakdown voltage calculation (MathCad)

Input data from BOLSIG:

$dat := READPRN("He77\_N2\_13\_CO210.txt")$

Continous functions by linearly interpolating input data

$\mu_{in}(x) := linterp(dat^{\langle 0 \rangle}, dat^{\langle 2 \rangle}, x)$ $\alpha_{in}(x) := linterp(dat^{\langle 0 \rangle}, dat^{\langle 5 \rangle}, x)$ $D_{in}(x) := linterp(dat^{\langle 0 \rangle}, dat^{\langle 3 \rangle}, x)$

Conversion from data units (cm, Torr) to metric units:

$conv := \frac{cm \cdot torr}{Pa \cdot m}$ $Volt := V$ $hPa := 100 \cdot Pa$

$\mu(V,p,d) := \mu_{in}\left(\frac{V}{p \cdot d} \cdot \frac{Pa \cdot m}{Volt} \cdot conv\right) \cdot \frac{1}{p} \cdot \left(\frac{torr \cdot cm^2}{Volt \cdot s}\right)$

$\alpha(V,p,d) := \alpha_{in}\left(\frac{V}{p \cdot d} \cdot \frac{Pa \cdot m}{Volt} \cdot conv\right) \cdot p \cdot \frac{1}{cm \cdot torr}$

$D(V,p,d) := D_{in}\left(\frac{V}{p \cdot d} \cdot \frac{Pa \cdot m}{Volt} \cdot conv\right) \cdot \frac{1}{p} \cdot \frac{torr \cdot cm^2}{s}$

Boundary conditions:

$\nu_{RF} := 27.12 \cdot MHz$ $p := 60 \cdot hPa$ $d := 6.6 \cdot mm$

Kihara's RF breakdown equation:

$$f(V,p,d) := \frac{1}{\pi^2} \cdot \left(d - \frac{2 \cdot \mu(V,p,d) \cdot \frac{V}{d}}{2 \cdot \pi \cdot \nu_{RF}}\right)^2 \cdot \frac{\alpha(V,p,d) \cdot \mu(V,p,d) \cdot \frac{V}{d}}{D(V,p,d)}$$

Find breakdown voltage:

$V_{init} := 350 \cdot Volt$ $V_{br2} := root(f(V_{init}, p, d) - 1, V_{init})$ $V_{br2} = 334.872\,Volt$

Plot :

$V := 100 \cdot Volt, 110 \cdot Volt .. 10000 \cdot Volt$

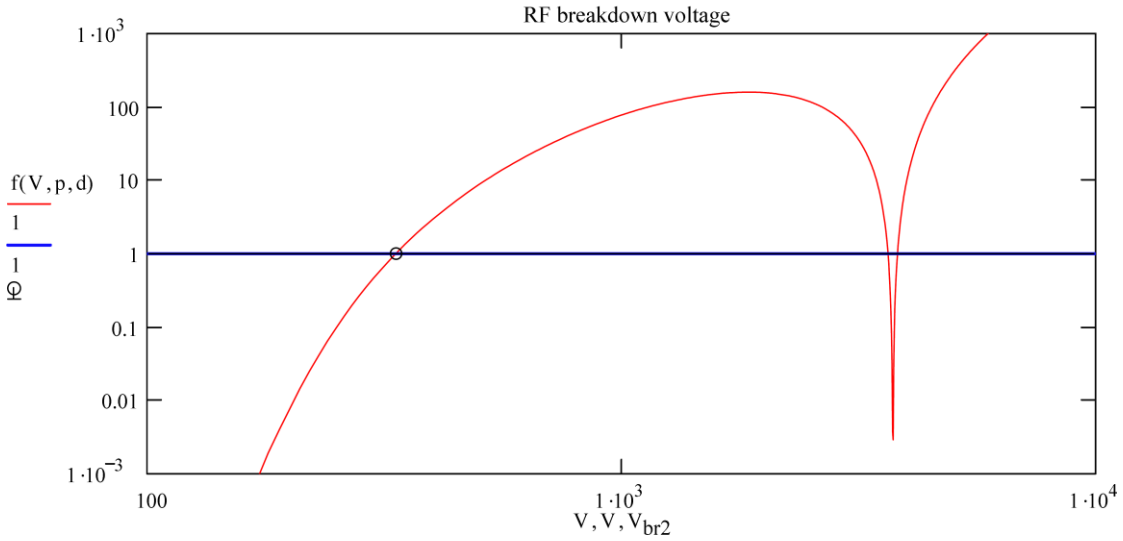

Appendix II: Laplace's equation calculation (FlexPDE)

```
TITLE 'RF feed'
     ! based on electrostatic problem description in FlexPde 6 help file
VARIABLES
     phi
     q

COORDINATES
     ycylinder( 'r', 'y')

 SELECT
     errlim=1
     threads=3
     ngrid =25

DEFINITIONS
    epsilon0=1
    epsilonr
    s=20.106194690265486
    E= - grad(phi)

EQUATIONS
   phi: div(epsilonr*epsilon0*grad(phi)) = 0
   q: div(grad(q)/(epsilonr*epsilon0)) = 0 !Adjoint equation as shown in FlexPDE help

BOUNDARIES

     ! entire region
    region 1
    epsilonr = 1
    start (0.000/s,0.000/s)  natural(phi) = 0 natural(q ) = tangential(grad(phi))
    line to (0.000/s, 0.000/s) natural(phi) = 0 natural(q) = tangential(grad(phi))
    line to (1.020/s,0.000/s) natural(phi) = 0 natural(q) = tangential(grad(phi))
    line to (1.020/s,1.289/s) natural(phi) = 0 natural(q) = tangential(grad(phi))
    line to (0.000/s,1.289/s) natural(phi) = 0 natural(q) = tangential(grad(phi))
    line to close

    ! ground
    start (1.020/s,0.310/s) value(phi) = 0
    line to (0.368/s,0.311/s) line to (0.362/s,0.318/s) line to (0.362/s,0.444/s)
    line to (0.365/s,0.444/s) line to (0.365/s,0.464/s) line to (0.463/s,0.464/s)
    line to (0.463/s,0.444/s) line to (0.467/s,0.444/s) line to (0.473/s,0.450/s)
    line to (0.473/s,0.826/s) line to (1.020/s,0.826/s)
    line to close

     ! live
    start (1.020/s,0.000/s) value(phi) = 400
    line to (0.000/s,0.000/s) line to (0.000/s,1.289/s)  line to (0.322/s,1.289/s)
    line to (0.322/s,1.208/s) line to (0.329/s,1.208/s)  line to (0.329/s,1.188/s)
    line to (0.276/s,1.188/s) line to (0.276/s,1.093/s)  line to (0.179/s,0.969/s)
    line to (0.101/s,0.677/s) line to (0.101/s,0.052/s)  line to (0.543/s,0.052/s)
    line to (0.543/s,0.110/s) arc to (0.546/s,0.119/s)  to (0.554/s,0.126/s)
    line to (0.616/s,0.162/s) arc to (0.641/s,0.173/s)  to (0.664/s,0.177/s)
    line to (1.020/s,0.177/s) line to (1.020/s,0.000/s)
    line to close

    !dielectric
     region 2
     epsilonr = 9.6
     start(0.464/s,0.474/s)    line to (0.454/s,0.464/s) line to (0.368/s,0.464/s)
     line to (0.362/s,0.458/s) line to (0.362/s,0.331/s) line to (0.101/s,0.331/s)
     line to (0.101/s,0.592/s) line to (0.453/s,0.592/s) line to (0.464/s,0.581/s)
     line to close

  PLOTS
    contour (magnitude(E))  painted nominmax contours=25  fixed range=(0,8.7e4)
             zoom(0, 0, 3.8e-2 ,3.8e-2 )
    contour ( q ) black nominmax notags notips contours=25
             zoom(5e-3, 2.5e-3, 40e-3,15e-3 )

 END
```

Appendix III: Lossy transmission line (MathCad)

General parameters:

$\varepsilon_0 := 8.854 \cdot 10^{-12} \cdot \frac{F}{m}$ $\mu_0 := 4 \cdot \pi \cdot 10^{-7} \cdot \frac{H}{m}$ $j := \sqrt{-1}$ $nH := 10^{-9} \cdot H$

$R_{avg} := 77.5 \cdot mm$ $dh := 3.5 \cdot mm$ $f := 27.12 \cdot MHz$ $\omega := 2 \cdot \pi \cdot f$

Transmission line lump components:

$L := \frac{\mu_0}{2 \cdot \pi} \cdot \ln\left(\frac{R_{avg} + dh}{R_{avg} - dh}\right)$ $C := 1.42 \cdot \frac{nF}{m}$ $R := 0 \cdot \frac{\Omega}{m}$ $G := 0.2334 \cdot \frac{1}{\Omega \cdot m}$

$Z_0 := \sqrt{\frac{R + j \cdot \omega \cdot L}{G + j \cdot \omega \cdot C}}$ $\gamma := \sqrt{(R + j \cdot \omega \cdot L) \cdot (G + j \cdot \omega \cdot C)}$

Transmission line impedance and voltage reflection coefficient:

$Z_{TL}(Z_{term}, d) := Z_0 \cdot \frac{Z_{term} + Z_0 \cdot \tanh(\gamma \cdot d)}{Z_0 + Z_{term} \cdot \tanh(\gamma \cdot d)}$ $Z_{par}(Z_1, Z_2) := \frac{Z_1 \cdot Z_2}{Z_1 + Z_2}$ $\Gamma(Z) := \frac{Z - Z_0}{Z + Z_0}$

Transmission line section lengths:

$d_1 := 632 \cdot mm$ $d_2 := 505 \cdot mm$ $d_3 := 127 \cdot mm$ $L_z := d_1 + d_2 + d_3$

Termination impedances and inductor value:

$Z_{he} := 0.8 \cdot \Omega + j \cdot \omega \cdot 47 \cdot nH$ $Z_{ind} := 0 \cdot \Omega + j \cdot \omega \cdot 84 \cdot nH$ $Z_{ax} := 0.8 \cdot \Omega + j \cdot \omega \cdot 55 \cdot nH$ $V_{in} := 400 \cdot V$

Caculation of input impedance:

$Z_{right} := Z_{TL}(Z_{ax}, d_3)$ $Z_{he\_TL1} := Z_{TL}(Z_{he}, d_1)$ $Z_{he\_TL1\_ind} := Z_{par}(Z_{TL}(Z_{he}, d_1), Z_{ind})$

$Z_{left} := Z_{TL}(Z_{he\_TL1\_ind}, d_2)$ $Z_{in} := Z_{par}(Z_{right}, Z_{TL}(Z_{he\_TL1\_ind}, d_2))$

Comparison between calculated and measured input impedances:

$Z_{in} = 3.19 + 0.691i\Omega$ $Zin_{meas} := (3.19 + 0.69 \cdot j) \cdot \Omega$

Voltage in a transmission line section:

$V_{TL}(V_{in}, Z_{in}, Z_{out}, d, z) := \frac{V_{in}}{1 + \Gamma(Z_{in})} \cdot e^{-\gamma \cdot z} \cdot \left[1 + \Gamma(Z_{out}) \cdot e^{2 \cdot \gamma \cdot (z - d)}\right]$

Voltage in a series of transmission line sections:

$$V(z) := \begin{cases} V_{TL}(V_{in}, Z_{right}, Z_{ax}, d_3, -z + d_3) & \text{if } 0 \le z < d_3 \\ V_{TL}(V_{in}, Z_{left}, Z_{he\_TL1\_ind}, d_2, z - d_3) & \text{if } d_3 \le z < d_3 + d_2 \\ V_{TL}(V_{TL}(V_{in}, Z_{left}, Z_{he\_TL1\_ind}, d_2, d_2), Z_{he\_TL1}, Z_{he}, d_1, z - d_3 - d_2) & \text{if } d_3 + d_2 \le z \le L_z \end{cases}$$

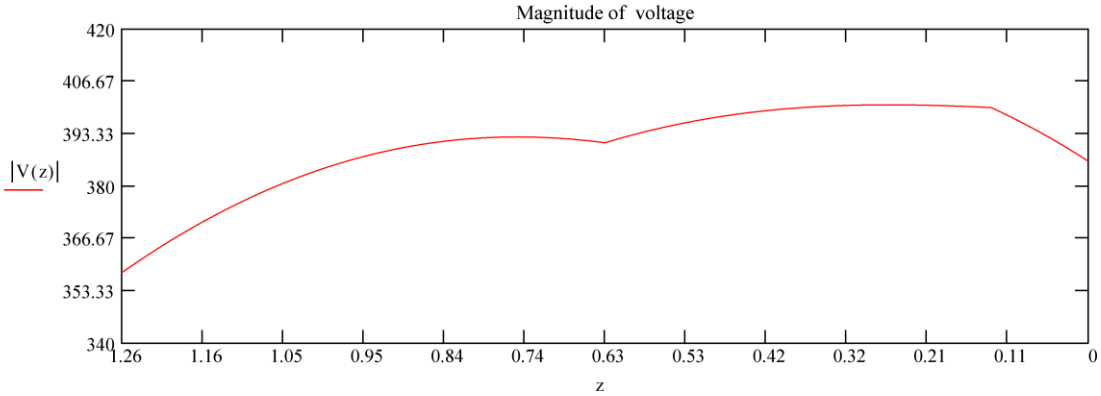

Appendix IV: 3-dimensional eigenmode calculation (FlexPDE)

```
TITLE     'Cylindrical Resonator'
    ! based on 2-d description in "mex175.pde" in [4.9]
SELECT
    errlim = 0.0001    modes = 3
    ngrid = 150        threads = 3

COORDINATES
    cartesian3

VARIABLES
    phi

DEFINITIONS
   ! speed of sound
   Temp = 300
   gamma = 1.564     r = 594.66
   cmix = sqrt(gamma*r*Temp)

   ! geometry
   R2 = 120e-3       R1 = 77.5e-3
   d = 6.33e-3       L1 = 82.5e-3
   L = 1.25          L2 = 82.5e-3

   ! wave equation conversion
   uz = -dz(phi)
   shift = 1
   omega = sqrt((lambda + shift) * cmix^2)
   p = omega*phi

EXTRUSION
   surface 'bottom' z = 0
   layer '1'
   surface 'midbottom'  z = L1
   layer '2'
   surface 'top' z = L1 + L
   layer '1'
   surface 'top' z = L1 + L + L2

EQUATIONS
   div(grad(phi)) + lambda*phi + shift*phi = 0

BOUNDARIES
   region '1'
   layer '1'
   surface 'top'
   start (-R2,0) natural(phi)=1
   arc (center = 0,0) angle=360 to close
   region '2'
   layer '2' void
   surface 'midbottom'
   surface 'bottom'
   start (-R2,0)
   arc (center = 0,0) angle=360 line to (-R1-d/2,0)
   arc (center = 0,0) angle=360 line to (-R1+d/2,0)
   arc (center = 0,0) angle=360 line to (-R1-d/2,0) to close


PLOTS
   elevation( p/500, uz) from (0, R1,0)
         to (0,R1,L1+L+L2) report(omega/(2*Pi))

END
```

Appendix V: Intra-cavity beam size with thermal lensing (MathCad)

Dimensions and defintions:

$R := 100\cdot mm$

$R_{ax} := 3.6\cdot m$

$R_{he} := 2\cdot m$

$d_1 := 100\cdot mm$

$d_2 := 100mm$

$L := 1.2\cdot m$

$\lambda := 10.6\cdot 10^{-6} m$

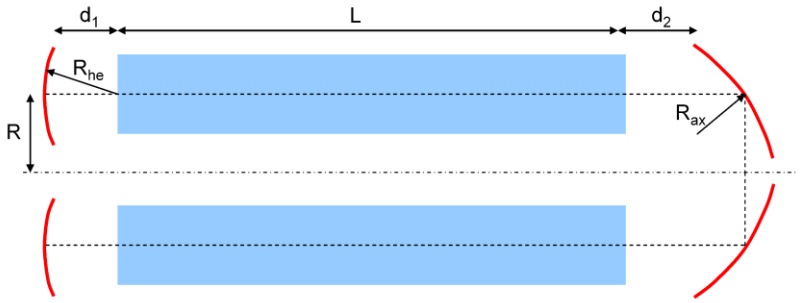

Matrices:

$$M_{therm}(f_{therm}, L) := \begin{pmatrix} \cosh\left(\frac{\sqrt{-L\cdot f_{therm}}}{f_{therm}}\right) & L\cdot\frac{f_{therm}}{\sqrt{-L\cdot f_{therm}}}\cdot\sinh\left(\frac{\sqrt{-L\cdot f_{therm}}}{f_{therm}}\right) \\ -\frac{1}{\sqrt{-L\cdot f_{therm}}}\cdot\sinh\left(\frac{\sqrt{-L\cdot f_{therm}}}{f_{therm}}\right) & \cosh\left(\frac{\sqrt{-L\cdot f_{therm}}}{f_{therm}}\right) \end{pmatrix} \qquad M_L(R) := \begin{pmatrix} 1 & 0 \\ -\frac{2}{R} & 1 \end{pmatrix} \qquad M_P(d) := \begin{pmatrix} 1 & d \\ 0 & 1 \end{pmatrix}$$

System transfer matrix:

$$M(f_{therm}, R_{he}, R_{ax}) := M_P(R)\cdot M_L(R_{ax})\cdot M_P(d_2)\cdot M_{therm}(f_{therm}, L)\cdot M_P(d_1)\cdot M_L(R_{he})\cdot M_P(d_1)\cdot M_{therm}(f_{therm}, L)\cdot M_P(d_2)\cdot M_L(R_{ax})\cdot M_P(R)$$

Complex radius of resonator:

$$q_{res}(f_{th}, R_{he}, R_{ax}) := \frac{1}{\frac{M(f_{th}, R_{he}, R_{ax})_{1,1} - M(f_{th}, R_{he}, R_{ax})_{0,0}}{2\cdot M(f_{th}, R_{he}, R_{ax})_{0,1}} - \frac{1}{M(f_{th}, R_{he}, R_{ax})_{0,1}}\cdot\sqrt{\left(\frac{M(f_{th}, R_{he}, R_{ax})_{0,0} + M(f_{th}, R_{he}, R_{ax})_{1,1}}{2}\right)^2 - 1}}$$

Propagate from center of the axicon to thermal lensing element at axicon end:

$i_m := 1200 \qquad i := 1 .. i_m$

$$V(f_{th}, i) := M_{therm}\left(\frac{i_m}{i}\cdot f_{th}, \frac{i}{i_m}\cdot L\right)\cdot M_P(d_2)\cdot M_L(R_{ax})\cdot M_P(R)\cdot\begin{pmatrix} q_{res}(f_{th}, R_{he}, R_{ax}) \\ 1 \end{pmatrix}$$

Beam size as function of position:

$$q(f_{th}, i) := \left(\frac{V(f_{th}, i)}{V(f_{th}, i)_1}\right)_0 \qquad w(f_{th}, i) := \left|\sqrt{Im(q(f_{th}, i))\cdot\frac{\lambda}{\pi}}\right|\cdot\sqrt{1 + \left(\frac{Re(q(f_{th}, i))}{Im(q(f_{th}, i))}\right)^2}$$

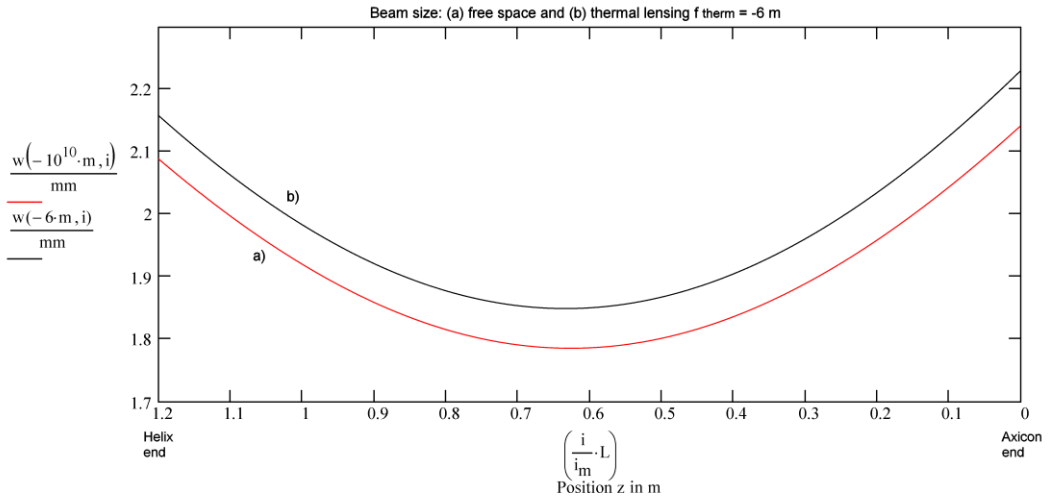

Appendix VI: Gain/Absorption for pressure-broadened lineshape (MathCad)

$h := 6.626068\cdot10^{-34}\,J\cdot s$ $\quad k_B := 1.38065\cdot10^{-23}\,\frac{J}{K}$ $\quad c_0 := 2.997926\cdot10^{8}\,\frac{m}{s}$ $\quad \mu m := 10^{-6}\cdot m$ $\quad hPa \equiv 10^{2}\cdot Pa$

Constants taken from A. G. Maki et al., J Mol Spectrosc 167 211 (1994)

$$\begin{pmatrix} B_0 & D_0 & H_0 & L_0 & x \\ B_I & D_I & H_I & L_I & \nu_I \\ B_{II} & D_{II} & H_{II} & L_{II} & \nu_{II} \end{pmatrix} := \begin{pmatrix} 11606.2069330121 & .0039880239163 & 0.42345763\cdot10^{-9} & 0.207115\cdot10^{-14} & 1 \\ 11697.5694304130 & .0034458963179 & 5.59420870\cdot10^{-9} & 1.69581353\cdot10^{-14} & 28808813.82164 \\ 11706.3646162132 & .0047114508178 & 6.99727785\cdot10^{-9} & -2.97801111\cdot10^{-14} & 31889960.171417 \end{pmatrix}\cdot\frac{MHz}{c_0}$$

$B := \frac{B_0 + B_I + B_{II}}{3}$ $\quad N_0 := 10^{16}\cdot\frac{1}{cm^3}$ $\quad \Delta N(\eta) := (\eta - 1)\cdot N_0$ $\quad J := 2, 4 .. 80$

Einstein A coefficients from W. J. Witteman "The CO2 laser", ISBN 3-540-17567-8

$A_{PI}(J) := (0.19015 - 8.875\cdot10^{-4}\cdot J)\cdot\frac{1}{s}$ $\quad A_{RI}(J) := (0.15423 + 0.00112\cdot J)\cdot\frac{1}{s}$

$A_{PII}(J) := (0.20353 - 9.5\cdot10^{-4}\cdot J)\cdot\frac{1}{s}$ $\quad A_{RII}(J) := (0.15675 + 0.00142\cdot J)\cdot\frac{1}{s}$

$$\begin{pmatrix} \psi_{CO2} \\ \psi_{N2} \\ \psi_{He} \end{pmatrix} := \begin{pmatrix} 12.5\% \\ 12.5\% \\ 75\% \end{pmatrix}$$

$\Delta\nu_P := 7.58\cdot(\psi_{CO2} + 0.73\cdot\psi_{N2} + 0.64\psi_{He})\cdot\frac{p}{torr}\cdot\sqrt{\frac{300\cdot K}{T}}\cdot MHz$

$f(J) := J\cdot(J+1)$

$E_0(J) := B_0\cdot f(J) - D_0\cdot f(J)^2 + H_0\cdot f(J)^3 + L_0\cdot f(J)^4$

$E_{II}(J) := B_{II}\cdot f(J) - D_{II}\cdot f(J)^2 + H_{II}\cdot f(J)^3 + L_{II}\cdot f(J)^4$

$E_I(J) := B_I\cdot f(J) - D_I\cdot f(J)^2 + H_I\cdot f(J)^3 + L_I\cdot f(J)^4$

$\lambda_{PI}(J) := \left(E_0(J-1) - E_I(J) + \nu_I\right)^{-1}$ $\quad \lambda_{RI}(J) := \left(E_0(J+1) - E_I(J) + \nu_I\right)^{-1}$

$\lambda_{RII}(J) := \left(E_0(J+1) - E_{II}(J) + \nu_{II}\right)^{-1}$ $\quad \lambda_{PII}(J) := \left(E_0(J-1) - E_{II}(J) + \nu_{II}\right)^{-1}$

$$\alpha_{PI}(J) := \frac{\lambda_{PI}(J)^2\cdot h\cdot c_0\cdot B}{4\cdot\pi\cdot k_B\cdot T}\cdot(2\cdot J-1)\cdot A_{PI}(J)\cdot\frac{2}{\pi\cdot\Delta\nu_P}\cdot\left[\left(N_0+\Delta N(\eta)\right)\cdot\exp\left(-E_0(J-1)\cdot\frac{h\cdot c_0}{k_B\cdot T}\right) - N_0\cdot\exp\left(-E_I(J)\cdot\frac{h\cdot c_0}{k_B\cdot T}\right)\right]$$

$$\alpha_{RI}(J) := \frac{\lambda_{RI}(J)^2\cdot h\cdot c_0\cdot B}{4\cdot\pi\cdot k_B\cdot T}\cdot(2\cdot J+3)\cdot A_{RI}(J)\cdot\frac{2}{\pi\cdot\Delta\nu_P}\cdot\left[\left(N_0+\Delta N(\eta)\right)\cdot\exp\left(-E_0(J+1)\cdot\frac{h\cdot c_0}{k_B\cdot T}\right) - N_0\cdot\exp\left(-E_I(J)\cdot\frac{h\cdot c_0}{k_B\cdot T}\right)\right]$$

$$\alpha_{PII}(J) := \frac{\lambda_{PII}(J)^2\cdot h\cdot c_0\cdot B}{4\cdot\pi\cdot k_B\cdot T}\cdot(2\cdot J-1)\cdot A_{PII}(J)\cdot\frac{2}{\pi\cdot\Delta\nu_P}\cdot\left[\left(N_0+\Delta N(\eta)\right)\cdot\exp\left(-E_0(J-1)\cdot\frac{h\cdot c_0}{k_B\cdot T}\right) - N_0\cdot\exp\left(-E_{II}(J)\cdot\frac{h\cdot c_0}{k_B\cdot T}\right)\right]$$

$$\alpha_{RII}(J) := \frac{\lambda_{RII}(J)^2\cdot h\cdot c_0\cdot B}{4\cdot\pi\cdot k_B\cdot T}\cdot(2\cdot J+3)\cdot A_{RII}(J)\cdot\frac{2}{\pi\cdot\Delta\nu_P}\cdot\left[\left(N_0+\Delta N(\eta)\right)\cdot\exp\left(-E_0(J+1)\cdot\frac{h\cdot c_0}{k_B\cdot T}\right) - N_0\cdot\exp\left(-E_{II}(J)\cdot\frac{h\cdot c_0}{k_B\cdot T}\right)\right]$$